MAPPING DIFFUSE SOLAR RADIATION FROM SATELLITE DATA FOR THAILAND

By
MR. Danuch PHAISATHIT

A Thesis Submitted in Partial Fulfillment of the Requirements
for Doctor of Philosophy PHYSICS
Department of PHYSICS
Silpakorn University
Academic Year 2024
Copyright of Silpakorn University

การจัดทำแผนที่รังสีกระจายจากภาพถ่ายดาวเทียมสำหรับประเทศไทย



โดย
นายดนุช พลายสถิตย์

วิทยานิพนธ์นี้เป็นส่วนหนึ่งของการศึกษาตามหลักสูตรปรัชญาดุษฎีบัณฑิต
สาขาวิชาฟิสิกส์ แบบ 1.1
ภาควิชาฟิสิกส์
มหาวิทยาลัยศิลปากร
ปีการศึกษา 2567
ลิขสิทธิ์ของมหาวิทยาลัยศิลปากร

MAPPING DIFFUSE SOLAR RADIATION FROM SATELLITE DATA FOR THAILAND

By
MR. Danuch PHAISATHIT



A Thesis Submitted in Partial Fulfillment of the Requirements
for Doctor of Philosophy PHYSICS
Department of PHYSICS
Academic Year 2024
Copyright of Silpakorn University

Title	Mapping diffuse solar radiation from satellite data for Thailand
By	MR. Danuch PHAISATHIT
Field of Study	PHYSICS
Advisor	Assistant Professor Dr. Korntip Tohsing
Co advisor	Professor Dr. Serm Janjai

Faculty of Science, Silpakorn University in Partial Fulfillment of the Requirements for the Doctor of Philosophy

.....Dean of Faculty of Science
(Assistant Professor Dr. Korakot Chanjirakul)

Approved by

.....Chair person
(Assistant Professor Dr. Pranomkorn Choosri)

.....Advisor
(Assistant Professor Dr. Korntip Tohsing)

.....Co advisor
(Professor Dr. Serm Janjai)

.....Committee
(Assistant Professor Dr. Somjet Pattarapanitchai)

.....Committee
(Associate Professor Dr. Sumaman Buntoung)

650730020 : Major PHYSICS
Keyword : Diffuse solar radiation, Atmospheric parameter, Diffuse fraction, Mathematical model, Machine learning, Satellite-based data

MR. Danuch PHAISATHIT : Mapping diffuse solar radiation from satellite data for Thailand Thesis advisor : Assistant Professor Dr. Korntip Tohsing

This study aims to develop a model for estimating monthly average daily diffuse solar radiation and to generate spatial maps over Thailand. Ground-based observations were collected from four stations located in different regions (Chiang Mai, Nakhon Pathom, Ubon Ratchathani, and Songkhla) during 2012-2024. The diffuse and global radiation were measured using pyranometers with 2-axis sun trackers. Additionally, the validation data for the generated maps were collected in 2024 from indirect measurements at four other stations (Phayao, Uthai Thani, Udon Thani, and Nakhon Si Thammarat).

Ground-based atmospheric parameters were retrieved from two sources, AERONET (aerosol optical depth, precipitable water, and total ozone column) and Thai Meteorological Department (cloud cover, air temperature, relative humidity, and wind speed) Satellite-based atmospheric parameters were derived from multiple sources: MODIS MCD18A1 (global radiation), MODIS MYD08 (aerosol optical depth, precipitable water, ozone, cloud cover), NCEP/NCAR (air temperature, relative humidity), and CCMP (wind speed).

To align the satellite-based data with ground observations, quantile mapping (QM) was applied for improving an agreement between two data sources. A model development used the relationship between diffuse fraction and clearness index. Parameters were selected using t-statistics and p-values, identifying clearness index, air temperature, and relative humidity as significant inputs for the baseline model (M1). Additional variables were incorporated through the subset selection (M2-M32) by using the multiple linear regression, which the model M6 adding wind speed achieved the highest accuracy with a mean bias difference (MBD) of 4.71%, a root mean square difference (RMSD) of 14.15%, and the index of agreement (IOA) of 0.933. Subsequently, the diffuse fraction derived from model M6 was compared with that obtained from other modeling approaches including k-fold cross-validation (M6A) and artificial neural networks (M6B), as well as with models from previous studies (models O1–O11). The model M6A demonstrated the best performance with the MBD of 2.81%, RMSD of 13.49%, and IOA of 0.957.

After that, for generating spatial maps of the diffuse solar radiation across Thailand, all satellite-based atmospheric parameters were preprocessed into the same format and calculated the diffuse solar radiation at each pixel using the cross-validation model of M6A. These data were validated against the independent ground data and showed a good agreement between both datasets with the discrepancy by MBD of 2.58%, RMSD of 16.77%, and IOA of 0.886. This confirmed the reliability of the diffuse solar radiation maps purposed from this work.

ACKNOWLEDGEMENTS

In the pursuit of this Degree of Doctor of Philosophy (Physics) thesis, the researcher was supported by a scholarship from the Development and Promotion of Science and Technology Talents Project (DPST). The researcher would like to express sincere gratitude to the DPST for this opportunity.

I would like to express my sincere thanks to Assistant Professor Dr. Korntip Tohsing, advisor, for invaluable guidance and support throughout this research.

Gratitude is also extended to Professor Dr. Serm Janjai, co-advisor, for providing insightful academic advice.

The researcher would also like to thank all faculty members and staff of the Solar Radiation Laboratory, Department of Physics, Faculty of Science, Silpakorn University, for their support and collaboration throughout the course of this study.

I am grateful to the Thai Meteorological Department for providing meteorological data and taking care of the instruments installed at its regional offices.

Finally, the researcher expresses deep appreciation to all family members and friends, as well as all instructors, for their constant encouragement, which contributed significantly to the successful completion of this study.

Danuch PHAISATHIT

มหาวิทยาลัยศิลปากร

TABLE OF CONTENTS

Page

ABSTRACT ..... D

ACKNOWLEDGEMENTS ..... E

TABLE OF CONTENTS ..... F

LIST OF TABLES ..... H

LIST OF FIGURES I

Chapter 1 Introduction 1

1.1 Rationale of the study 1

1.2 Objectives 2

1.3 Scope of the study 2

Chapter 2 Theory and literature review 3

2.1 Solar radiation 3

2.1.1 Nature and components of solar radiation 3

2.1.2 Solar geometry 5

2.1.2.1 The path of the Sun 5

2.1.2.2 Determination of the Sun's position 7

2.1.2.3 Solar time and hour angle 10

2.2 Extraterrestrial solar irradiance 14

2.2.1 Extraterrestrial solar radiation spectrum 14

2.2.2 Solar constant 15

2.2.3 Extraterrestrial solar radiation 15

2.2.3.1 Hourly solar radiation 15

2.2.3.2 Daily and monthly average daily solar radiation 18

2.3 Effect of atmospheric parameters to the diffuse solar irradiance 19

2.3.1 The effect of aerosols on solar radiation 19

2.3.2 The effect of precipitable water on solar radiation 21

2.3.3 The effect of ozone layers on solar radiation 24
2.3.4 The effect of cloud on solar radiation 25
2.3.5 The Effect of indirect atmospheric parameters on solar radiation 26
2.4 Literature review 28
Chapter 3 Methodology and results 33
3.1 Equipment and atmospheric data 33
3.1.1 Ground-based data 33
3.1.1.1 Solar radiation equipment 33
3.1.1.2 Atmospheric data 60
3.1.2 Satellite-based data 66
3.2 Diffuse fraction model 68
3.2.1 Atmospheric parameter preparation and selection 70
3.2.2 Evaluation of atmospheric parameters for model selection 79
3.2.3 Model development and performance evaluation 80
3.3 Satellite-based diffuse solar radiation map 90
3.3.1 Preparation of satellite-based data 90
3.3.2 Mapping diffuse solar radiation 94
Chapter 4 Conclusions 102
Appendices 104
Appendix A: Diffuse fraction model results 105
Appendix B: Input data for generating diffuse solar radiation maps 128
REFERENCES 180
VITA 186

LIST OF TABLES

Page

Table 1 Details of solar radiation monitoring stations. 34

Table 2 Description of satellite-derived datasets and their corresponding ground parameters. 66

Table 3 t-statistics and p-values of each atmospheric parameter. 80

Table 4 Summary of regression models (M1–M32) using satellite-derived parameters corresponded to different input variables and evaluation statistics (MBD, RMSD and IOA). 84

Table 5 Performance comparison of diffuse fraction models with previous studies and different methods. 88

มหาวิทยาลัยศิลปากร

LIST OF FIGURES

Page

Figure 1 The spectrum of the board band solar radiation presenting the extraterrestrial solar radiation (yellow graph) and the solar radiation at the Earth's surface (red graph). Adapted from Petty (2006). 3

Figure 2 The components of solar radiation on the Earth's surface..... 5

Figure 3 The Earth's elliptical orbit around the Sun. Adapted from Petty (2006). 6

Figure 4 Solar path diagram on solstices and equinoxes. Adapted from Meeus (1991). 6

Figure 5 Determination of the Sun's position using the horizontal coordinate system. Adapted from Iqbal (2012). 8

Figure 6 Determining the position of the Sun using the equatorial coordinate system. Adapted from Iqbal (2012). 9

Figure 7 Variation of the Sun's declination angle (δ) throughout the year. Adapted from Benard et al. (1980)..... 9

Figure 8 Annual variation of the difference between true solar time and mean solar time (Et). Adapted from Iqbal (2012). 11

Figure 9 Variation of the correction factor for Earth-Sun distance (E0) over the course of a year. Adapted from Duffie et al. (2020). 13

Figure 10 Spectrum of extraterrestrial solar radiation. Adapted from Iqbal (2012). .. 14

Figure 11 Solar irradiance incident on a horizontal plane (Io) and on a perpendicular plane to the direction of extraterrestrial solar irradiance (Ion). Adapted from Iqbal (2012). 16

Figure 12 Characteristics of aerosols produced by biomass burning. Adapted from Boucher (2015). 20

Figure 13 Representation of Atmospheric Water Vapor Content. 22

Figure 14 The absorption spectra of water vapor (H_2O) and oxygen (O_2) (van Dijk et al., 2003). 23

Figure 15 Representation of Total Ozone column. 25

Figure 16 Absorption spectra of cloud (Petty, 2006). 26

Figure 17 Example diffuse solar radiation map across Zimbabwe in August from Hove and Göttsche (1999). 32

Figure 18 Solar monitoring stations used in this work star labels are main stations and dot labels are indirect station for obtaining the diffuse solar radiation. 33

Figure 19 Pyranometer CM21 (global solar radiation) at Chiang Mai station. 35

Figure 20 Pyranometer CM11 (diffuse solar radiation) at Chiang Mai station. 35

Figure 21 Pyrheliometer sNIP (direct solar radiation) at Chiang Mai station. 36

Figure 22 Datalogger DX2000 at Chiang Mai station. 36

Figure 23 Pyranometer CM21 (global solar radiation) at Nakhon Pathom station. ... 37

Figure 24 Pyranometer CM11 (diffuse solar radiation) at Nakhon Pathom station. .. 37

Figure 25 Pyrheliometer NIP (direct solar radiation) at Nakhon Pathom station. 38

Figure 26 Datalogger DX2000 at Nakhon Pathom station. 38

Figure 27 Pyranometer CM21 (global solar radiation) at Ubon Ratchatani station. .. 39

Figure 28 Pyranometer CM11 (diffuse solar radiation) at Ubon Ratchatani station. .39

Figure 29 Pyrheliometer sNIP (direct solar radiation) at Ubon Ratchatani station. ... 40

Figure 30 Datalogger DX2000 at Ubon Ratchatani station. 40

Figure 31 Pyranometer CM21 (global solar radiation) at Songkhla. 41

Figure 32 Pyranometer CM11 (diffuse solar radiation) at Songkhla. 41

Figure 33 Pyrheliometer NIP (direct solar radiation) at Songkhla. 42

Figure 34 Datalogger DX2000 at Songkhla. 42

Figure 35 Pyranometer CMP11 (global solar radiation) at Phayao station. 43

Figure 36 Pyrheliometer CH1 and suntracker (direct solar radiation) at Phayao station. 43

Figure 37 Datalogger GM10 and control box at Phayao station. 44

Figure 38 Pyranometer CMP11 (global solar radiation) at Uthai Thani station. 44

Figure 39 Pyrheliometer CH1 and suntracker (direct solar radiation) at Uthai Thani station. 45

Figure 40 Datalogger GM10 and control box at Uthai Thani station. 45

Figure 41 Pyranometer CMP11 (global solar radiation) at Udon Thani station. 46

Figure 42 Pyrheliometer CH1 and suntracker (direct solar radiation) at Udon Thani station. 46

Figure 43 Datalogger GM10 and control box at Udon Thani station. 47

Figure 44 Pyranometer CMP11 (global solar radiation) at Nakhon Si Thammarat station. 47

Figure 45 Pyrheliometer CH1 and suntracker (direct solar radiation) at Nakhon Si Thammarat station. 48

Figure 46 Datalogger GM10 and control box at Nakhon Si Thammarat station. 48

Figure 47 Example of a calibration graph for the global solar radiation measurement at Nakhon Pathom station. 50

Figure 48 Example of a calibration graph for the diffuse solar radiation measurement at Nakhon Pathom station. 50

Figure 49 Example of a calibration graph for the direct solar radiation measurement at Nakhon Pathom station. 51

Figure 50 Example of a calibration of a global solar radiation instrument at Chiang Mai station. 51

Figure 51 Example of a calibration of a global solar radiation instrument at Nakhon Pathom station. 52

Figure 52 Example of a calibration of a global solar radiation instrument at Ubon Ratchatani station. 52

Figure 53 Example of a calibration of a global solar radiation instrument at Songkhla station. 53

Figure 54 Example of a calibration of a global solar radiation instrument at Phayao station. 53

Figure 55 Example of a calibration of a global solar radiation instrument at Uthai Thani station. 54

Figure 56 Example of a calibration of a global solar radiation instrument at Udon Thani station. 54

Figure 57 Example of a calibration of a global solar radiation instrument at Nakhon Si Thammarat station. 55

Figure 58 The distribution of global solar radiation at Chiang Mai station. 56

Figure 59 The distribution of diffuse solar radiation at Chiang Mai station. 56

Figure 60 The distribution of global solar radiation at Nakhon Pathom station. 57

Figure 61 The distribution of diffuse solar radiation at Nakhon Pathom station. 57

Figure 62 The distribution of global solar radiation at Ubon Ratchathani station. 58

Figure 63 The distribution of diffuse solar radiation at Ubon Ratchathani station.....58

Figure 64 The distribution of global solar radiation at Songkhla station.....59

Figure 65 The distribution of diffuse solar radiation at Songkhla station. 59

Figure 66 Psychrometer, dry-bulb thermometer (left), relative humidity table (mid), and wet-bulb thermometer (right). (Earth Science Stack Exchange, 2021). 61

Figure 67 Cup anemometer used for measuring the wind speed. (Munro Instruments, 2024). 62

Figure 68 AERONET Monitoring Stations around the world. (https://aeronet.gsfc.nasa.gov/, 2025). 63

Figure 69 Sun photometer at Chiang Mai station. 64

Figure 70 Sun photometer at Nakhon Pathom station. 64

Figure 71 Sun photometer at Ubon Ratchathani station. 65

Figure 72 Sun photometer at Songkhla station. 65

Figure 73 The relationship between diffuse fraction and clearness index at Chiang Mai station. 68

Figure 74 The relationship between diffuse fraction and clearness index at Nakhon Pathom station.....69

Figure 75 The relationship between diffuse fraction and clearness index at Ubon Ratchathani station.....69

Figure 76 The relationship between diffuse fraction and clearness index at Songkhla station.....70

Figure 77 Comparison of ground-based global solar radiation and MODIS downward shortwave solar radiation. 71

Figure 78 Comparison of AERONET aerosol optical depth and MODIS aerosol optical depth.....71

Figure 79 Comparison of AERONET precipitable water and MODIS precipitable water.....72

Figure 80 Comparison of AERONET total ozone column and MODIS total ozone column.....72

Figure 81 Comparison of TMD cloud cover and MODIS cloud fraction.....73

Figure 82 Comparison of TMD air temperature and NCEP/NCAR air temperature..73

Figure 83 Comparison of TMD relative humidity and NCEP/NCAR relative humidity. 74

Figure 84 Comparison of TMD wind speed and NCEP/NCAR wind speed. 74

Figure 85 Comparison of ground-based global solar radiation and MODIS downward shortwave solar radiation after applying quantile mapping. 75

Figure 86 Comparison of AERONET aerosol optical depth and MODIS aerosol optical depth after applying quantile mapping. 76

Figure 87 Comparison of AERONET precipitable water and MODIS precipitable water after applying quantile mapping. 76

Figure 88 Comparison of AERONET total ozone column and MODIS total ozone column after applying quantile mapping. 77

Figure 89 Comparison of TMD cloud cover and MODIS cloud fraction after applying quantile mapping. 77

Figure 90 Comparison of TMD air temperature and NCEP/NCAR air temperature after applying quantile mapping. 78

Figure 91 Comparison of TMD relative humidity and NCEP/NCAR relative humidity after applying quantile mapping. 78

Figure 92 Comparison of TMD wind speed and NCEP/NCAR wind speed after applying quantile mapping. 79

Figure 93 Comparison between observed and estimated diffuse fraction using Model M6. 85

Figure 94 The structure of 10-fold cross-validation model (M6A). 86

Figure 95 The structure of Artificial neuron network model (M6A). 87

Figure 96 Comparison between observed and estimated diffuse fraction using Model M6A from k-fold cross-validation method. 89

Figure 97 Example of satellite image from MODIS MCD18A1. 90

Figure 98 Reprojection image by WGS84 (EPSG:4326) system. 90

Figure 99 Cropped image of the study domain for this study. 91

Figure 100 Interpolated image for filling the gap of filled the missing data. 92

Figure 101 Resampled image with the resolution of 0.01°×0.01°. 93

Figure 102 Monthly global solar radiation maps from MODIS for the year 2024. 95

Figure 103 Monthly air temperature maps from NCEP/NCAR for the year 2024. 96

Figure 104 Monthly relative humidity maps from NCEP/NCAR for the year 2024..97

Figure 105 Monthly wind speed and wind direction maps from CCMP for the year 2024.....98

Figure 106 Monthly average daily diffuse solar radiation maps for the year 2023.....99

Figure 107 Monthly average daily diffuse solar radiation maps for the year 2024..100

Figure 108 The validation of diffuse solar radiation from the map generated against indirectly measured values from ground-based measurement.....101

Figure 109 Comparison between observed and estimated diffuse fraction using Model M1.....105

Figure 110 Comparison between observed and estimated diffuse fraction using Model M2.....105

Figure 111 Comparison between observed and estimated diffuse fraction using Model M3.....106

Figure 112 Comparison between observed and estimated diffuse fraction using Model M4.....106

Figure 113 Comparison between observed and estimated diffuse fraction using Model M5.....107

Figure 114 Comparison between observed and estimated diffuse fraction using Model M6.....107

Figure 115 Comparison between observed and estimated diffuse fraction using Model M7.....108

Figure 116 Comparison between observed and estimated diffuse fraction using Model M8.....108

Figure 117 Comparison between observed and estimated diffuse fraction using Model M9.....109

Figure 118 Comparison between observed and estimated diffuse fraction using Model M10.....109

Figure 119 Comparison between observed and estimated diffuse fraction using Model M11.....110

Figure 120 Comparison between observed and estimated diffuse fraction using Model M12.....110

Figure 121 Comparison between observed and estimated diffuse fraction using Model M13.....111

Figure 122 Comparison between observed and estimated diffuse fraction using Model M14.....111
Figure 123 Comparison between observed and estimated diffuse fraction using Model M15.....112
Figure 124 Comparison between observed and estimated diffuse fraction using Model M16.....112
Figure 125 Comparison between observed and estimated diffuse fraction using Model M17.....113
Figure 126 Comparison between observed and estimated diffuse fraction using Model M18.....113
Figure 127 Comparison between observed and estimated diffuse fraction using Model M19.....114
Figure 128 Comparison between observed and estimated diffuse fraction using Model M20.....114
Figure 129 Comparison between observed and estimated diffuse fraction using Model M21.....115
Figure 130 Comparison between observed and estimated diffuse fraction using Model M22.....115
Figure 131 Comparison between observed and estimated diffuse fraction using Model M23.....116
Figure 132 Comparison between observed and estimated diffuse fraction using Model M24.....116
Figure 133 Comparison between observed and estimated diffuse fraction using Model M25.....117
Figure 134 Comparison between observed and estimated diffuse fraction using Model M26.....117
Figure 135 Comparison between observed and estimated diffuse fraction using Model M27.....118
Figure 136 Comparison between observed and estimated diffuse fraction using Model M28.....118
Figure 137 Comparison between observed and estimated diffuse fraction using Model M29.....119
Figure 138 Comparison between observed and estimated diffuse fraction using Model M30.....119

Figure 139 Comparison between observed and estimated diffuse fraction using Model M31 120

Figure 140 Comparison between observed and estimated diffuse fraction using Model M32 120

Figure 141 Comparison between observed and estimated diffuse fraction using Model O1 from Oliveira et al. (2002) and El-Sebaii and Trabea (2003). 121

Figure 142 Comparison between observed and estimated diffuse fraction using Model O2 from Barbaro et al. (1981). 121

Figure 143 Comparison between observed and estimated diffuse fraction using Model O3 from Ulgen and Hepbasli (2009). 122

Figure 144 Comparison between observed and estimated diffuse fraction using Model O4 from Bamiro (1983). 122

Figure 145 Comparison between observed and estimated diffuse fraction using Model O5 from Lealea and Tchinda (2013). 123

Figure 146 Comparison between observed and estimated diffuse fraction using Model O6 from Boukelia et al. (2014) 123

Figure 147 Comparison between observed and estimated diffuse fraction using Model O7 from Bailek et al. (2018) 124

Figure 148 Comparison between observed and estimated diffuse fraction using Model O8 from Bailek et al. (2018) 124

Figure 149 Comparison between observed and estimated diffuse fraction using Model O9 from (Lealea & Tchinda, 2013). 125

Figure 150 Comparison between observed and estimated diffuse fraction using Model O10 from Mubiru and Banda (2007). 125

Figure 151 Comparison between observed and estimated diffuse fraction using Model O11 from Li et al. (2011). 126

Figure 152 Comparison between observed and estimated diffuse fraction using Model M6A from k-fold cross-validation method. 126

Figure 153 Comparison between observed and estimated diffuse fraction using Model M6B from artificial neurons network method. 127

Figure 154 Monthly global solar radiation maps from MODIS for the year 2012 ... 128

Figure 155 Monthly global solar radiation maps from MODIS for the year 2013 ... 129

Figure 156 Monthly global solar radiation maps from MODIS for the year 2014 ... 130

Figure 157 Monthly global solar radiation maps from MODIS for the year 2015…131
Figure 158 Monthly global solar radiation maps from MODIS for the year 2016…132
Figure 159 Monthly global solar radiation maps from MODIS for the year 2017…133
Figure 160 Monthly global solar radiation maps from MODIS for the year 2018…134
Figure 161 Monthly global solar radiation maps from MODIS for the year 2019…135
Figure 162 Monthly global solar radiation maps from MODIS for the year 2020…136
Figure 163 Monthly global solar radiation maps from MODIS for the year 2021…137
Figure 164 Monthly global solar radiation maps from MODIS for the year 2022…138
Figure 165 Monthly global solar radiation maps from MODIS for the year 2023…139
Figure 166 Monthly global solar radiation maps from MODIS for the year 2024…140
Figure 167 Monthly air temperature maps from NCEP/NCAR for the year 2012…141
Figure 168 Monthly air temperature maps from NCEP/NCAR for the year 2013…142
Figure 169 Monthly air temperature maps from NCEP/NCAR for the year 2014…143
Figure 170 Monthly air temperature maps from NCEP/NCAR for the year 2015…144
Figure 171 Monthly air temperature maps from NCEP/NCAR for the year 2016…145
Figure 172 Monthly air temperature maps from NCEP/NCAR for the year 2017…146
Figure 173 Monthly air temperature maps from NCEP/NCAR for the year 2018…147
Figure 174 Monthly air temperature maps from NCEP/NCAR for the year 2019…148
Figure 175 Monthly air temperature maps from NCEP/NCAR for the year 2020…149
Figure 176 Monthly air temperature maps from NCEP/NCAR for the year 2021…150
Figure 177 Monthly air temperature maps from NCEP/NCAR for the year 2022…151
Figure 178 Monthly air temperature maps from NCEP/NCAR for the year 2023…152
Figure 179 Monthly air temperature maps from NCEP/NCAR for the year 2024…153
Figure 180 Monthly relative humidity maps from NCEP/NCAR for the year 2012. 154
Figure 181 Monthly relative humidity maps from NCEP/NCAR for the year 2013. 155
Figure 182 Monthly relative humidity maps from NCEP/NCAR for the year 2014. 156

Figure 183 Monthly relative humidity maps from NCEP/NCAR for the year 2015. 157
Figure 184 Monthly relative humidity maps from NCEP/NCAR for the year 2016. 158
Figure 185 Monthly relative humidity maps from NCEP/NCAR for the year 2017. 159
Figure 186 Monthly relative humidity maps from NCEP/NCAR for the year 2018. 160
Figure 187 Monthly relative humidity maps from NCEP/NCAR for the year 2019. 161
Figure 188 Monthly relative humidity maps from NCEP/NCAR for the year 2020. 162
Figure 189 Monthly relative humidity maps from NCEP/NCAR for the year 2021. 163
Figure 190 Monthly relative humidity maps from NCEP/NCAR for the year 2022. 164
Figure 191 Monthly relative humidity maps from NCEP/NCAR for the year 2023. 165
Figure 192 Monthly relative humidity maps from NCEP/NCAR for the year 2024. 166
Figure 193 Monthly wind speed and wind direction maps from CCMP for the year 2012.....167
Figure 194 Monthly wind speed and wind direction maps from CCMP for the year 2013.....168
Figure 195 Monthly wind speed and wind direction maps from CCMP for the year 2014.....169
Figure 196 Monthly wind speed and wind direction maps from CCMP for the year 2015.....170
Figure 197 Monthly wind speed and wind direction maps from CCMP for the year 2016.....171
Figure 198 Monthly wind speed and wind direction maps from CCMP for the year 2017.....172
Figure 199 Monthly wind speed and wind direction maps from CCMP for the year 2018.....173

Figure 200 Monthly wind speed and wind direction maps from CCMP for the year 2019.....174

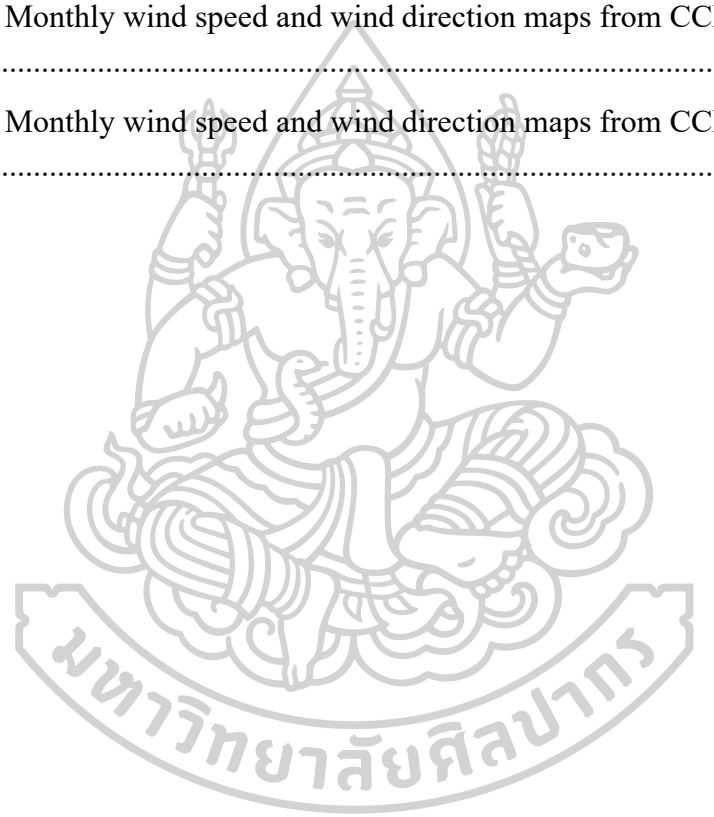
Figure 201 Monthly wind speed and wind direction maps from CCMP for the year 2020.....175

Figure 202 Monthly wind speed and wind direction maps from CCMP for the year 2021.....176

Figure 203 Monthly wind speed and wind direction maps from CCMP for the year 2022.....177

Figure 204 Monthly wind speed and wind direction maps from CCMP for the year 2023.....178

Figure 205 Monthly wind speed and wind direction maps from CCMP for the year 2024.....179



Chapter 1
Introduction

1.1 Rationale of the study

The Sun is the main source of energy resulting from thermonuclear reactions. It emits energy into space in the form of electromagnetic waves of various wavelengths, which are referred to as solar radiation. The solar radiation that reaches the Earth's surface is called broadband radiation that is in the wavelength range of 300 to 3,000 nm. The broadband solar radiation includes ultraviolet radiation (UV) in the wavelengths between 100 and 400 nm. However, most of the short wavelength of UV was absorbed by the atmosphere, so the UV that can reach the earth's surface is in the range of 280 to 400 nm. It also includes visible light with wavelengths of 400 to 700 nm and infrared radiation (IR) with wavelengths between 760 and 3,000 nm, which consists of near-infrared (NIR) and mid-infrared (MIR). Solar radiation that enters the Earth's atmosphere can be separated into three types: direct solar radiation is radiation that directly travels to the Earth's surface; diffuse solar radiation is radiation that was reflected and scattered due to interactions with various components in the atmosphere before reaching the surface; and global solar radiation is the total solar radiation received from the hemisphere, summarizing both direct and diffuse components.

Diffuse solar radiation is important in various fields such as solar energy, agriculture, and climate research because it can reach the Earth's surface even under cloudy conditions. In Thailand, although there are many stations measuring the global solar radiation, only a few have ground-based measurements of the diffuse solar radiation resulting in limited data availability. This lack of diffuse radiation measurements makes it necessary to explore alternative methods such as using mathematical models and satellite data.

This study focuses on the diffuse solar radiation, which is important to understand how it forms in the atmosphere. Before reaching the Earth's surface, some solar radiation is absorbed and scattered by different components in the atmosphere. This produces diffuse solar radiation. The main things that cause scattering are clouds and aerosols, which are opaque objects. Other parameters namely, water vapor and ozone also absorb specific types of radiation. Water vapor can attenuate the infrared radiation, while ozone blocks the ultraviolet radiation. Other atmospheric factors such as air temperature, relative humidity, and wind speed can also affect the diffuse solar radiation in an indirect way.

As mentioned above, the model was widely used for estimating the diffuse solar radiation, based on the relationship between a diffuse fraction and clearness index. The diffuse fraction is a ratio between the diffuse solar radiation to the global solar radiation representing the information of the sky condition at a specific time. The clearness index is a ratio of global solar radiation to extraterrestrial solar radiation, which indicates the transparency of the atmosphere. In this study, the

diffuse fraction model is combined with satellite data to generate spatial maps of the diffuse solar radiation over Thailand.

The spatial distribution of solar radiation derived from the maps can support the strategic planning of solar energy technology deployment. For instance, areas with lower diffuse solar radiation are more suitable for technologies that primarily utilize direct solar radiation. In contrast, regions with higher diffuse solar radiation may benefit from technologies designed to capture diffuse light, such as curved (Moruno et al., 2024), tube-shaped (Bempah et al., 2019) and bifacial solar panels (Salloom et al., 2018).

Therefore, the aims of this research are to develop a model for estimating diffuse solar radiation and to generate the map that shows spatial distribution over Thailand by using satellite data. The resulting map can be used to fill data gaps in areas without ground measurements and support future researches related to solar energy and atmospheric studies.

1.2 Objectives

1. To measure and collect the diffuse solar radiation at 8 monitoring stations across Thailand.

2. To develop and evaluate a model for estimating the diffuse solar radiation in Thailand.

3. To generate diffuse solar radiation maps for Thailand using satellite data.

1.3 Scope of the study

This research investigates the diffuse solar radiation over Thailand using solar radiation data from ground-based monitoring stations that directly measure both global and diffuse solar radiation. These stations are located at the Faculty of Science, Silpakorn University in Nakhon Pathom (13.82°N, 100.04°E) for the central region, Chiang Mai (18.78°N, 98.98°E) in the North, Ubon Ratchathani (15.25°N, 104.87°E) for the Northeast, and Songkhla (7.20°N, 100.60°E) for the South. To validate the generated radiation maps, this study also used data from stations that indirectly measure the diffuse radiation based on observations of global and direct solar radiation. These stations include Phayao (19.19°N, 99.88°E) in the North, Uthai Thani (15.35°N, 100.01°E) in the central region, Udon Thani (17.38°N, 102.81°E) in the Northeast, and Nakhon Si Thammarat (8.43°N, 99.50°E) in the South. Additional atmospheric data were obtained from the Thai Meteorological Department (TMD) and the AERONET network. Moreover, to generate the diffuse solar radiation map, satellite data from the Moderate Resolution Imaging Spectroradiometer (MODIS) aboard Aqua and Terra satellites along with reanalysis data from the Cross-Calibrated Multi-Platform (CCMP) and NCEP/NCAR Reanalysis Project, were used to provide atmospheric parameters for estimating and visualizing the spatial distribution of the diffuse solar radiation.

Chapter 2
Theory and literature review

2.1 Solar radiation

2.1.1 Nature and components of solar radiation

Solar radiation is created by thermonuclear fusion at the core of the Sun, which acts as a massive energy source. At extremely high temperatures and pressures, hydrogen atoms fuse to form helium through a series of nuclear reactions. This process releases an enormous amount of energy in the form of electromagnetic wave. The energy generated in the core travels outward through radiative and convective zones of the Sun, eventually reaching the photosphere, where it is emitted into space. This emitted energy, known as solar radiation.

The spectrum of broadband solar radiation, which spans wavelengths from 300 to 3,000 nanometers, consists of three main components: ultraviolet (UV) radiation, visible light, and infrared (IR) radiation. Approximately 5 percent of the solar energy is in the UV range, 43 percent in the visible range, and 52 percent in the infrared range. The spectrum of solar radiation is shown in figure 1.

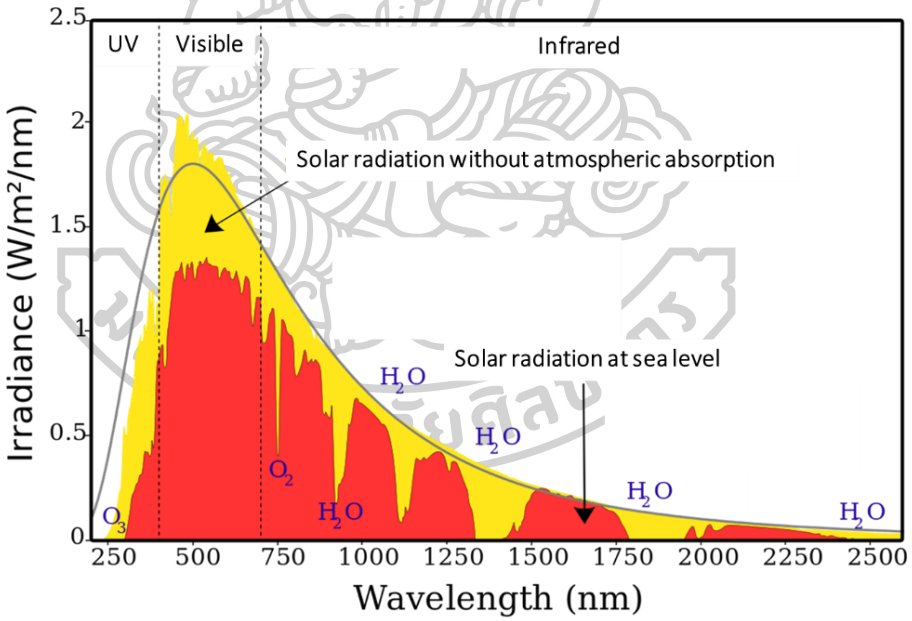


Figure 1 The spectrum of the board band solar radiation presenting the extraterrestrial solar radiation (yellow graph) and the solar radiation at the Earth's surface (red graph). Adapted from Petty (2006).

UV is a component of solar radiation with wavelengths ranging from 100 to 400 nanometers. It is classified into three types: UVA (315–400 nm), UVB (280–315 nm), and UVC (100–280 nm). Although the Sun emits all three types, most UVC and some UVB are absorbed by the Earth's atmosphere, particularly by the ozone layer. As a result, only UVA and a small amount of UVB reach the Earth's surface. UV

radiation plays an important role in atmospheric chemistry and biological processes. While exposure to UVB is beneficial for vitamin D synthesis in humans, excessive exposure can lead to harmful effects such as skin cancer, eye damage, and degradation of materials.

Visible light is the portion of solar radiation that the human eyes can detect with wavelengths ranging from 400 to 700 nanometers. Although it makes up a small part of the electromagnetic spectrum, it represents a major portion of the solar energy that reaches the Earth. Visible light is divided into colors based on wavelength from violet at the shortest to red at the longest. This part of the spectrum plays a vital role in natural and technological processes including photosynthesis in plants, human vision, and optical sensing. Most visible light passes through the Earth's atmosphere with minimal absorption, although it is partially scattered by air molecules and aerosols. This scattering, especially of blue light, explains why the sky appears blue. Because of its energy and interaction with biological systems, visible light is essential for solar energy applications and environmental studies.

IR is a significant component of solar radiation with wavelengths longer than visible light, typically ranging from 700 to 3,000 nanometers. It is often divided into three regions: near-infrared (NIR, 700–1,400 nm), mid-infrared (MIR, 1,400–3,000 nm), and far-infrared (beyond 3,000 nm, though primarily of terrestrial origin). The majority of IR falls within the NIR and MIR range. IR carries a substantial portion of the Sun’s energy and plays a vital role in the Earth's energy balance and surface heating. As IR radiation travels through the atmosphere, some of it is absorbed by water vapor, carbon dioxide, and other greenhouse gases, which contribute to the warming of the atmosphere. Infrared radiation is also used in various applications, such as remote sensing, thermal imaging, and solar energy systems. Understanding the behavior of IR radiation and its interaction with atmospheric components is essential for climate modeling, energy budget analysis, and environmental monitoring.

When solar radiation reaches the Earth’s atmosphere and surface, it is commonly divided into three components based on its path and interaction with the atmosphere. Direct solar radiation refers to radiation that travels in a straight line from the Sun to the Earth's surface. It is the most intense form of solar radiation and occurs under clear-sky conditions. Diffuse solar radiation, on the other hand, is the radiation that has been scattered by air molecules, aerosols, clouds, and other atmospheric particles before reaching the ground. Although less intense than direct radiation, diffuse radiation can reach the surface even when the sky is overcast or partly cloudy sky. Global solar radiation is the total amount of solar energy received on a horizontal surface and is the sum of both direct and diffuse radiation. The global, diffuse and direct solar radiation are shown in figure 2.

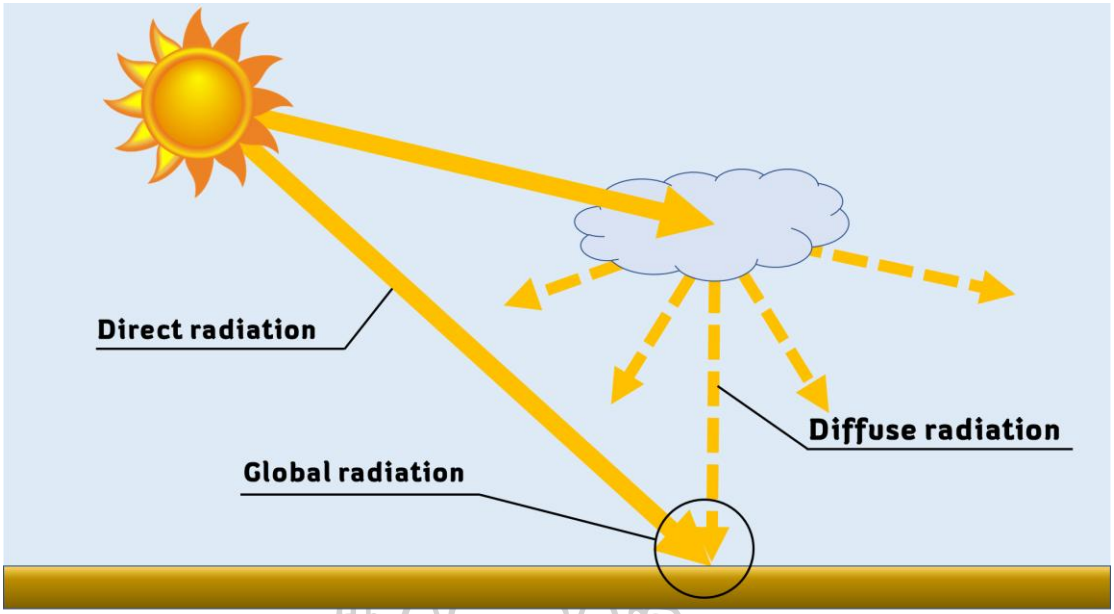


Figure 2 The components of solar radiation on the Earth's surface.

Global solar irradiance on a horizontal surface (GHI) is the sum of direct solar irradiance projected onto the surface and diffuse solar irradiance from the sky. The direct component must be adjusted based on the solar zenith angle. This relationship can be expressed as:

$$GHI = DNI \cdot \cos(\theta_z) + DHI \quad (1)$$

where GHI is global horizontal irradiance, DNI is direct normal irradiance, DHI is diffuse horizontal irradiance, and θ_z is the solar zenith angle.

2.1.2 Solar geometry

2.1.2.1 The path of the Sun

In general, the positions of stars appear fixed relative to a celestial equator because stars are so far away from the Earth that their movement cannot be observed over short periods. Therefore, we perceive stars as remaining on the same plane, which is parallel to the celestial equator. However, in the case of planets and the Sun, their apparent paths across the sky change throughout the year. This is because these celestial objects are much closer to the Earth and their positions continuously shift relative to the Earth's equatorial plane. It is well known that the Earth orbits the Sun in an elliptical path with the Sun located at one of the focus points of the ellipse. Moreover, the Earth's rotational axis is tilted at an angle of 23.5 degrees from the perpendicular to the plane of its orbit as illustrated in Figure 3.

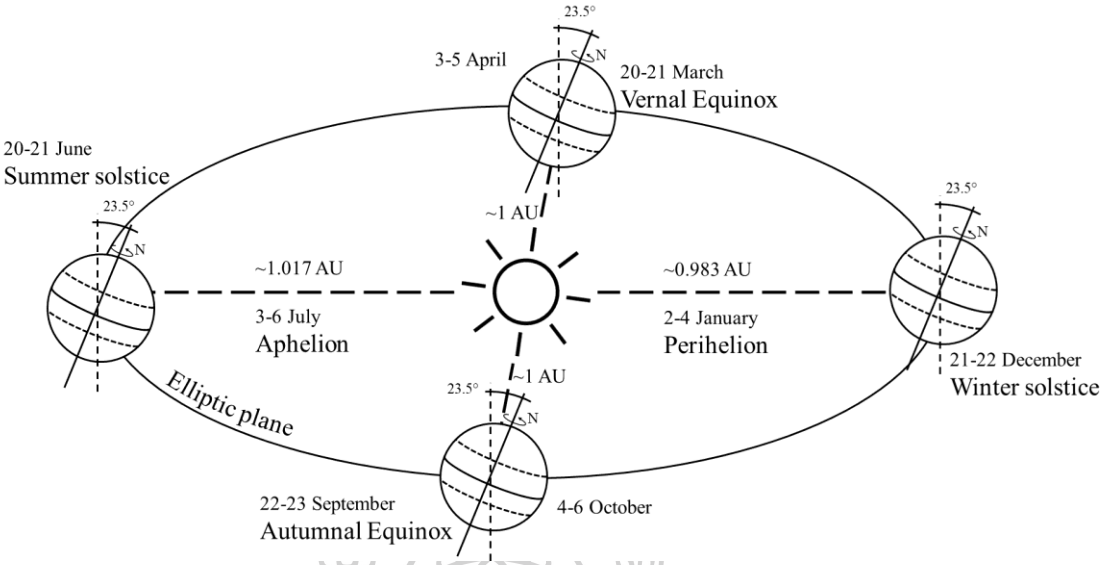


Figure 3 The Earth's elliptical orbit around the Sun. Adapted from Petty (2006).

As shown in Figure 3, on June 21 or 22, the Earth's North Pole is tilted most directly toward the Sun, while on December 21 or 22, the South Pole is tilted most directly toward the Sun. On March 20 or 21 and September 22 or 23, the Sun lies along the Earth's equatorial plane. On these dates, the Sun appears to move along the celestial equator. On June 21 or 22, the Sun reaches its northernmost position relative to the celestial equator and on December 21 or 22, it reaches its southernmost position as illustrated in Figure 4.

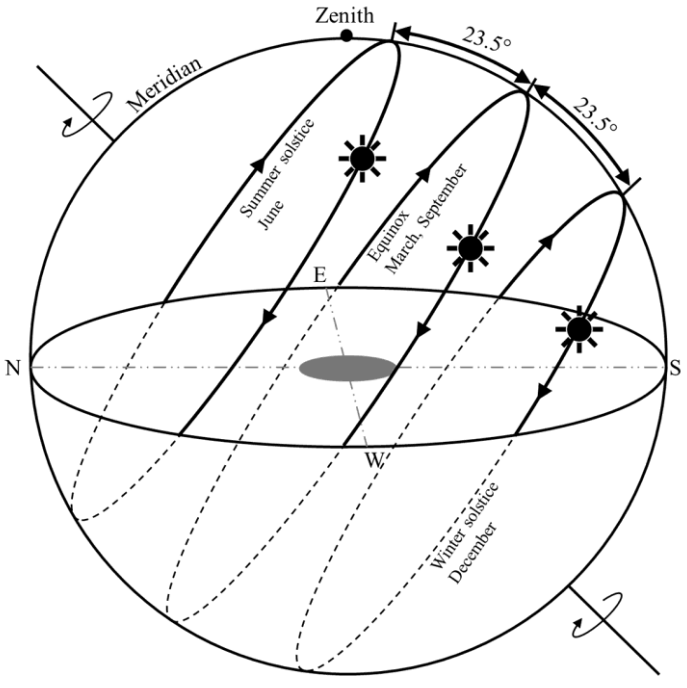


Figure 4 Solar path diagram on solstices and equinoxes. Adapted from Meeus (1991).

The orbital planes of celestial objects in the sky, including the Sun, are parallel to the celestial equator. However, since the celestial equator is perpendicular to the celestial rotation axis and this axis is inclined relative to the horizontal plane by an angle equal to the observer's latitude, the apparent path of the Sun across the sky varies depending on the observer's latitude on the Earth's surface.

2.1.2.2 Determination of the Sun's position

To calculate the solar radiation on planes, both outside the Earth's atmosphere and at the Earth's surface, it is necessary to determine the position of the Sun in the sky. The position of the Sun is described by assuming the sky as a hemisphere of an imaginary sphere called a celestial sphere with the observer at its center. Since the sky has an infinite radius the position of the Sun can be defined using only two angles on the celestial sphere. In the field of solar radiation, the position of the Sun can be determined using two main coordinate systems as follows:

1) Horizontal Coordinate System, this system determines the position of the Sun using two angular measurements (as shown in Figure 5) based on the observer's local horizon:

a. Azimuth angle (ψ) is the angle measured from the south direction (OS in Figure 5) to the projection of the line connecting the observer and the Sun onto the horizontal plane (OB). The value is positive if the projection lies in the eastern half of the sky and negative if it lies in the western half. The azimuth angle typically ranges from -180 degrees to 180 degrees.

b. Altitude angle (α) also known as the elevation angle, is the angle between the line from the observer to the Sun (OA) and its projection on the horizontal plane (OB). This angle ranges from 0 to 90 degrees. The angle between the line from the observer to the Sun (OA) and the line from the observer to the solar zenith point (OZ), the highest point in hemisphere is called the zenith angle (θ_z), which is also commonly used to define the Sun's position. The zenith angle is related to the altitude by the equation:

$$\theta_z = 90° - \alpha \tag{2}$$

The horizontal coordinate system is easy to understand. However, a limitation is that both the azimuth and altitude angles change continuously throughout the day and vary from one day to another throughout the year.

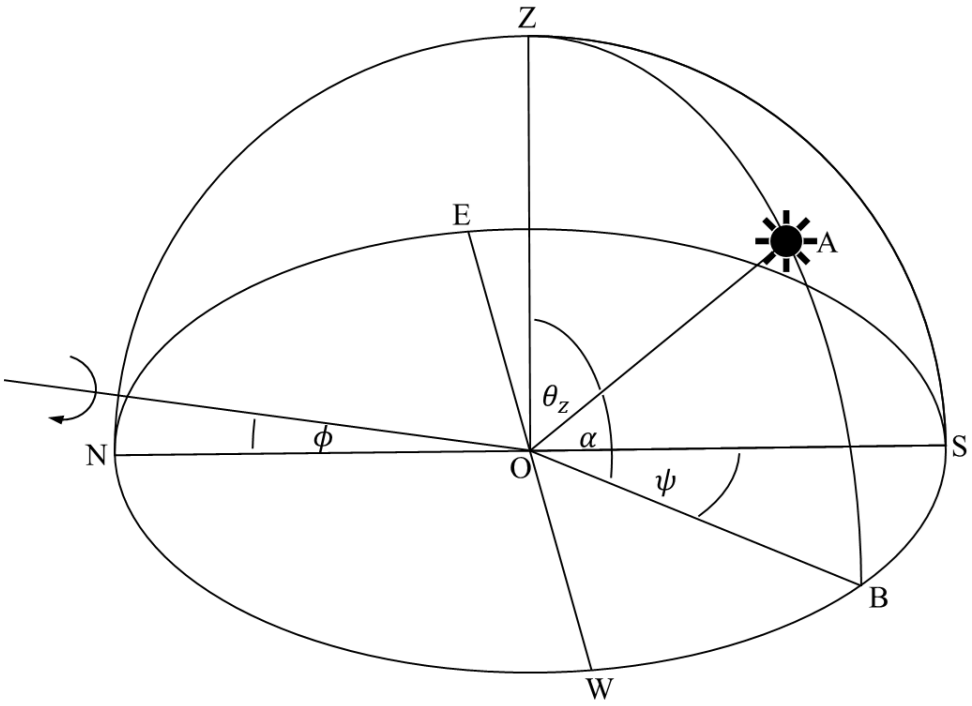


Figure 5 Determination of the Sun's position using the horizontal coordinate system. Adapted from Iqbal (2012).

2) Equatorial Coordinate System, in this system, the celestial equator is used as the reference plane. Since the apparent path of the Sun on the celestial sphere is nearly parallel to the celestial equator, and changes in this path over the course of a single day are minimal, it can be considered nearly constant. Therefore, the equatorial system determines the position of the Sun by drawing a great circle from one celestial pole through the Sun to the opposite pole (as shown in Figure 6). The first parameter used to define the Sun's position is the angular distance between the Sun and the celestial equator along this great circle, which is known as a declination (δ). The second parameter is the angular distance on the celestial sphere between the great circle that passes through the Sun and the observer's meridian. This angle is referred to as an hour angle (ω).

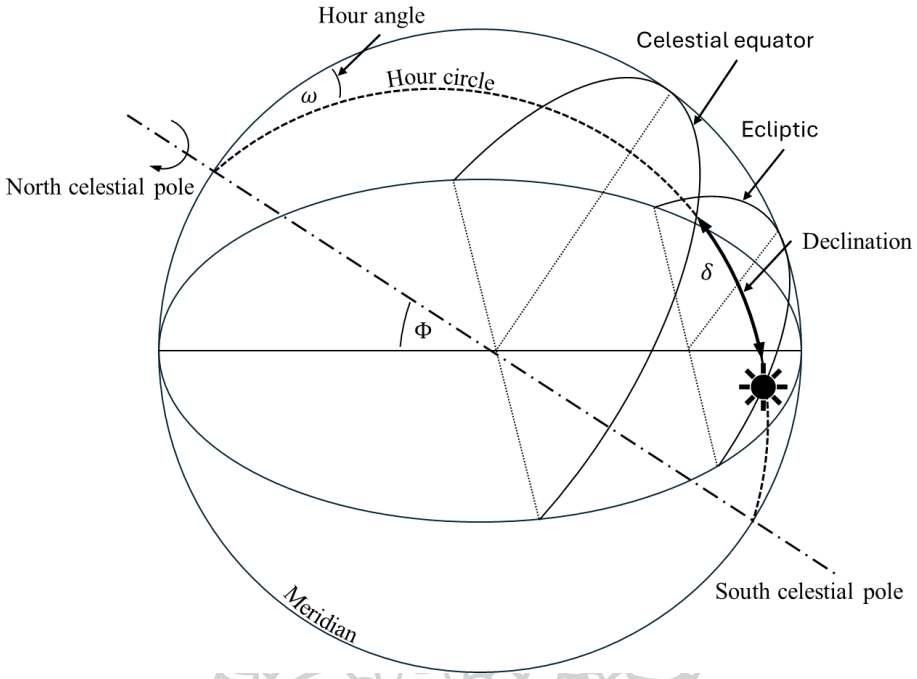


Figure 6 Determining the position of the Sun using the equatorial coordinate system. Adapted from Iqbal (2012).

The declination angle (δ) varies between $-23.5°$ and $23.5°$. Observations show that the declination changes throughout the year as illustrated in Figure 7.

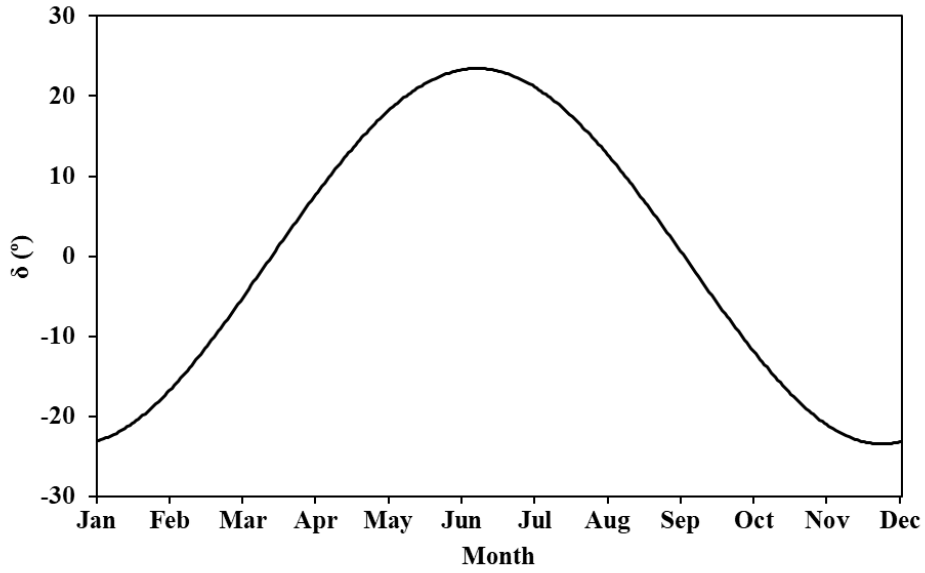


Figure 7 Variation of the Sun's declination angle (δ) throughout the year. Adapted from Benard et al. (1980).

From the graph in Figure 7, the data can be represented by an empirical equation as shown in Equation (3).

$$\delta = (0.006918 - 0.399912\cos\Gamma + 0.070257\sin\Gamma - 0.006758\cos 2\Gamma + 0.000907\sin 2\Gamma - 0.002697\cos 3\Gamma + 0.00148\sin 3\Gamma)\left(\frac{180}{\pi}\right) \quad (3)$$

When δ is the declination angle (º) and Γ is a day angle (rad).

The day angle can be calculated from Equation (4).

$$\Gamma = \frac{2\pi(d_n - 1)}{365} \quad (4)$$

Where d_n is a number day of the year with $d_n = 1$ on January 1 and $d_n = 365$ on December 31. For February, it is assumed to have 28 days.

Equation (3) provides a highly accurate estimation of the solar declination angle with a maximum error of no more than 3 arcminutes. However, using this equation can be rather complex. Therefore, Cooper (1969) proposed a simpler equation that, although slightly less accurate, is more convenient for general solar radiation energy applications. This equation can be expressed as follows:

$$\delta = 23.45\sin\left[\frac{360}{365}(d_n + 284)\right] \quad (5)$$

In the case of the hour angle (ω), it varies according to solar time, which is based on the Sun's position. As the Sun moves from the observer's local meridian westward and returns to the same position, it completes a cycle in 24 hours. During this time, the hour angle also completes a full rotation of 360 degrees. This means the Sun appears to move at a rate of 15 degrees per hour. Therefore, the relationship between the hour angle and solar time can be expressed as follows:

$$\omega = 15(12 - ST) \quad (6)$$

Where ω is the hour angle of the Sun (º) and ST is a solar time (hours).

The solar time can be calculated from the local standard time (LST) or the clock time used in daily life. The details of this calculation will be explained in the following section.

2.1.2.3 Solar time and hour angle

The solar time is not uniform meaning that the length of each day varies throughout the year. This is because the Earth's orbit is elliptical causing the Earth's

speed in its orbit to change depending on its position. When the Earth is closer to the Sun, it moves faster than at other points. This irregularity makes it difficult to compare events using solar time. Therefore, scientists established a more uniform time system by dividing the solar time on January 1, 1900, into 86,400 equal parts, each called one second. This system is known as mean solar time Benard et al. (1980) and Smart and Green (1977).

Since the mean solar time is consistent, it can be measured using constant periodic events, such as the swing of a pendulum or the vibration of a quartz crystal. The mean solar time at Greenwich, England, is defined as Universal Time (UT) or Greenwich Mean Time (GMT). Countries around the world divide their time zones relative to GMT. Each zone is defined by a standard longitude (LS), which differs from Greenwich by multiples of 15 degrees. For example, Thailand's standard longitude is 105° (15 × 7) meaning that Thailand is 7 hours ahead of GMT. Typically, each zone uses local standard time (LST), which is the clock time used in daily life. Large countries like the United States have multiple standard time zones to match local day and night patterns more accurately.

The solar time and the mean solar time differ throughout the year, as shown in the graph in Figure 8. This difference can be represented by the equation of time as follows:

$$E_t = 229.18(0.000075+0.001868\cos\Gamma - 0.032077\sin\Gamma - 0.014615\cos 2\Gamma - 0.04089\sin 2\Gamma) \quad (7)$$

Where E_t is the difference between solar time and mean solar time (minutes) and Γ is is the day angle (rad)

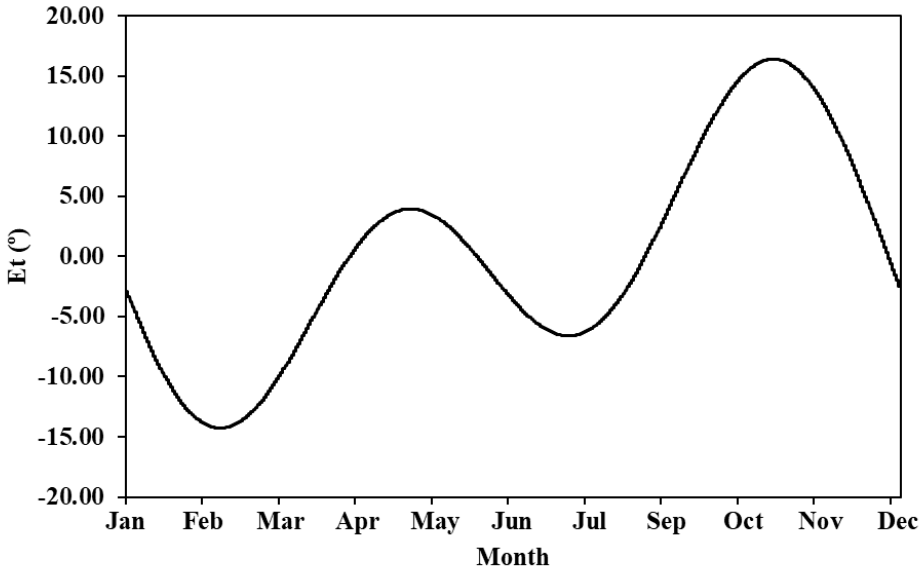


Figure 8 Annual variation of the difference between true solar time and mean solar time (E_t). Adapted from Iqbal (2012).

The solar time is directly related to the position of the Sun. For example, when the solar time is 12:00 PM, the hour angle (ω) is 0°. If the solar time is 11:00 AM, the hour angle is 15°. The solar time can be calculated from the local standard time by incorporating the equation of time and the difference between the standard meridian and the local longitude. This relationship can be expressed by the following equation:

$$ST = LST+4(L_s - L_{loc})+E_t \tag{8}$$

Where ST is the solar time (hours: minutes), LST is the local solar time (hours: minutes), L_s is the standard longitude (º), L_s is the local longitude (º), and E_t is the difference between solar time and mean solar time (minutes).

The value of $4 \times (L_s - L_{loc})$ is in minutes and both L_s and L_{loc} are negative, when located east of Greenwich and positive in the west. Therefore, if the local standard time (LST) is known, the solar time can be calculated. This solar time can then be substituted into Equation (6) to obtain the desired hour angle.

Since the Earth orbits the Sun is an elliptical path with the Sun located at one of the ellipse's foci, the distance between the Earth and the Sun varies throughout the year. This variation affects the intensity of solar radiation received by the Earth because solar radiation intensity is inversely proportional to the square of the distance. This intensity can be calculated using the Equation (9) where I_{sc} is the solar constant (i.e., the intensity of solar radiation outside the Earth's atmosphere on a plane perpendicular to the radiation direction at the average Earth-Sun distance, r_o), and I_{on} is the extraterrestrial solar radiation on a plane perpendicular to the radiation direction at a given Earth-Sun distance r.

$$I_{on} = \left(\frac{r_o}{r}\right)^2 I_{sc} \tag{9}$$

If E_0 is represented of $\left(\frac{r_o}{r}\right)^2$, then Equation (9) can be rewritten as follows:

$$I_{on} = E_0 I_{sc} \tag{10}$$

In general, E_0 is referred to the correction factor for variations in the distance between the Earth and the Sun. Based on astronomical knowledge. The values of r_o and r can be determined allowing E_0 to be calculated for each day of Earth's orbit around the Sun. The E_0 throughout the year against time is shown in Figure 9.

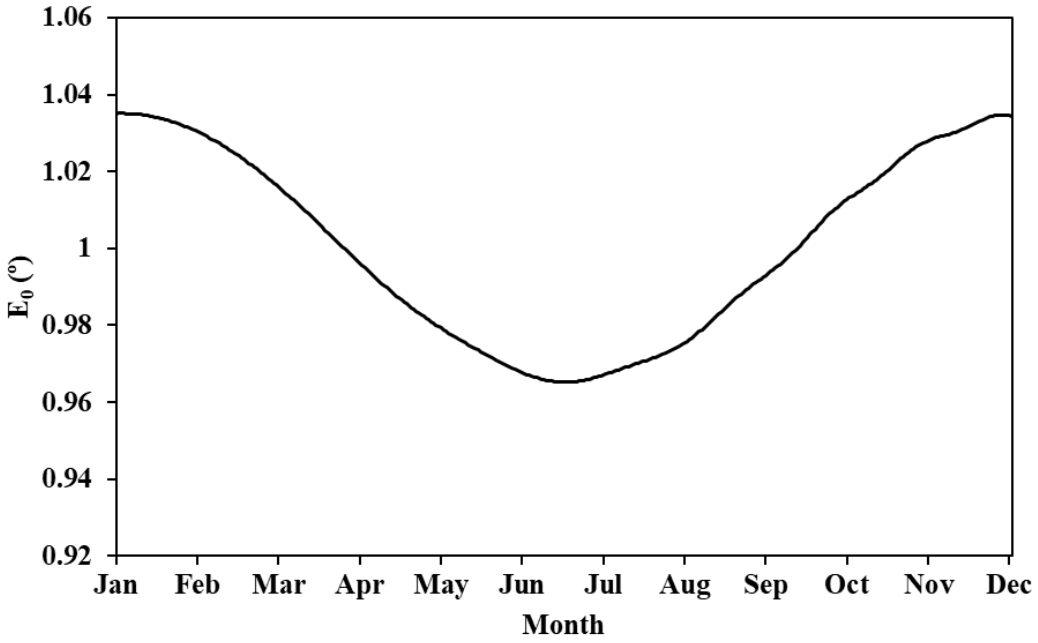


Figure 9 Variation of the correction factor for Earth-Sun distance (E_0) over the course of a year. Adapted from Duffie et al. (2020).

For case of applying the E_0 values in various calculations, Spencer (1971) represented the graph in Figure 9 using an empirical equation, which can be written as follows:

$$E_0 = 1.000110+0.034221\cos\Gamma +0.001280\sin\Gamma +0.000719\cos 2\Gamma +0.000077\sin 2\Gamma \quad (11)$$

Where Γ is the day angle (rad), which can be calculated using Equation (4).

The value of E_0 calculated from Equation (11) provides high accuracy, which is suitable for applications requiring high precision. However, for general engineering purposes, Duffie et al. (2020) suggested using a less complex equation written as follows:

$$E_0 = 1+0.033\cos\left[\frac{2\pi d_n}{365}\right] \quad (12)$$

The value of E_0 can be used to correct for the variation in the Earth–Sun distance for calculating solar radiation energy at any point from the Sun, even in broadband radiation (0.3–3.0 microns) or specific spectral bands such as visible light or ultraviolet radiation.

2.2 Extraterrestrial solar irradiance

The extraterrestrial solar radiation is essential information for designing solar cells used in satellites and spacecraft. It also serves as a fundamental input for calculating solar radiation at Earth's surface. This section discusses the solar spectrum outside the Earth's atmosphere, the solar constant, methods for determining extraterrestrial radiation on various planes, and the conversion factors for transforming the radiation values from a horizontal to a tilted surface.

2.2.1 Extraterrestrial solar radiation spectrum

The radiation emitted by the Sun is electromagnetic waves with a wide range of wavelengths from gamma rays to radio waves, each having different intensities. The solar radiation spectrum refers to the intensity of solar radiation at various wavelengths. Since solar cells and materials used for the outer walls of spacecraft respond differently to solar radiation at different wavelengths, spectral data of solar radiation are crucial for designing solar cells and spacecraft materials. In addition, the extraterrestrial solar radiation spectrum is used as an input data for calculating the solar radiation spectrum at the Earth's surface. By combining theoretical calculations with data measured by ground-based instruments, the extraterrestrial solar radiation spectrum can be obtained as shown in Figure 10.

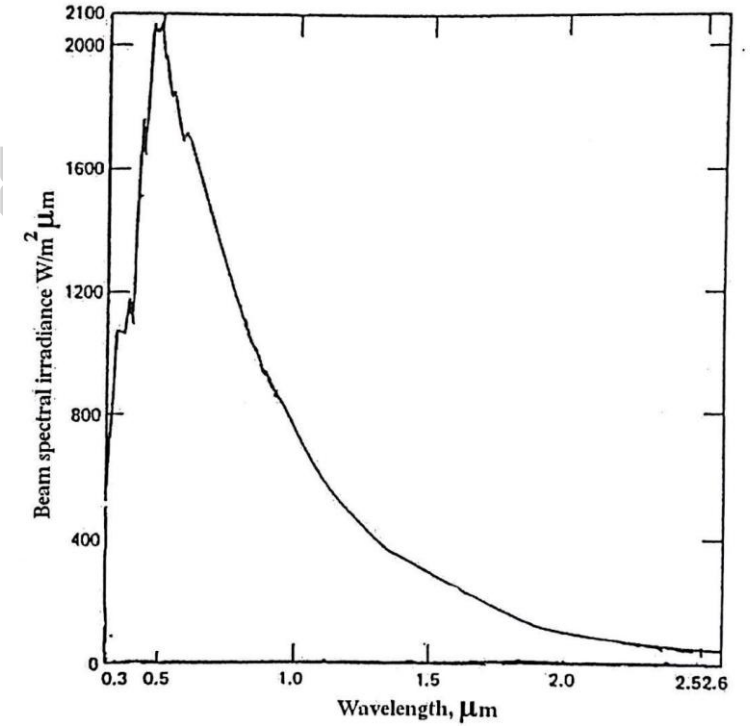


Figure 10 Spectrum of extraterrestrial solar radiation. Adapted from Iqbal (2012).

2.2.2 Solar constant

The solar constant (I_{sc}) refers to the total solar radiation energy across all wavelengths perpendicularly incident on a unit area per unit time at the mean distance between the Earth and the Sun (1.495×10^{11} m) called 1 AU outside the Earth's atmosphere. The solar constant is crucial for calculating the amount of solar energy reaching the Earth's surface. It has been determined through ground-based measurements as well as measurements taken using high-altitude balloons and aircraft. Initially, the solar constant was found to be 1353 W/m². Later, further measurements and corrections for various errors resulted in a revised value of 1366.1 W/m² (Iqbal, 2012) equivalent to 4921 kJ/m²/hr. This corrected value has been accepted by the World Meteorological Organization (WMO).

2.2.3 Extraterrestrial solar radiation

2.2.3.1 Hourly solar radiation

The amount of solar radiation at a given moment (solar irradiance) outside the Earth's atmosphere incident on a plane perpendicular to the direction of the solar rays depends on the distance between the Earth and the Sun as expressed by the following equation:

$$I_{on} = I_{sc}E_0 \tag{13}$$

Where I_{on} is the solar irradiance incident on a plane perpendicular to the direction of the solar radiation (W/m²) as illustrated in Figure11, I_{sc} is the solar constant (1,366.1 W/m²), and E_0 is the correction factor accounting for the variation in the Earth-Sun distance (–).

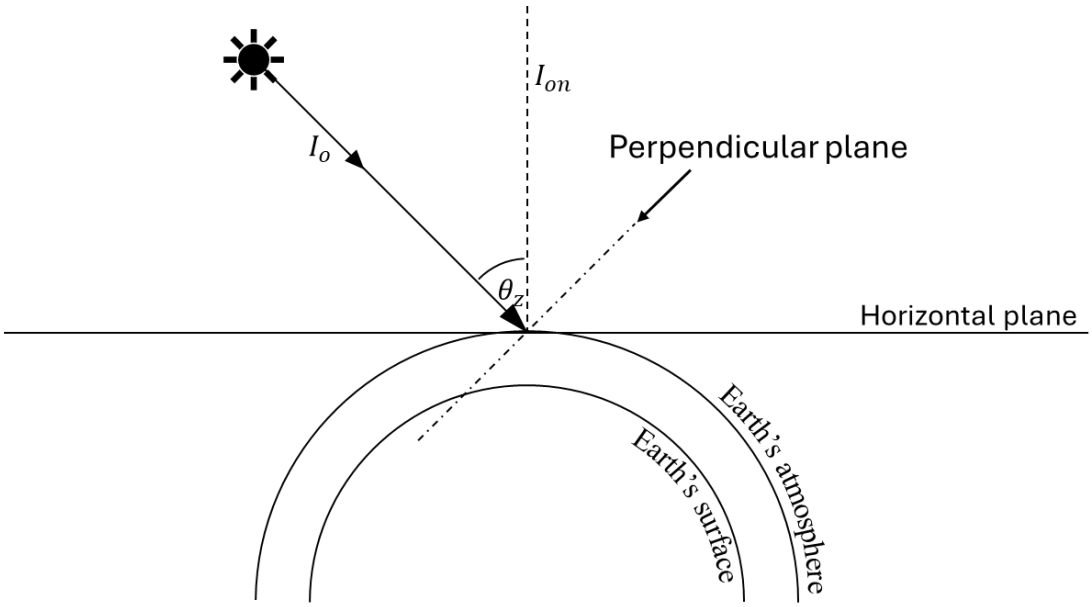


Figure 11 Solar irradiance incident on a horizontal plane (I_o) and on a perpendicular plane to the direction of extraterrestrial solar irradiance (I_{on}). Adapted from Iqbal (2012).

For the horizontal plane, the solar irradiance on the horizontal plane (I_o) follows the Equation (14).

$$I_o = I_{sc} E_0 \cos\theta_z \tag{14}$$

The cosine of solar zenith angle, $\cos\theta_z = \sin\delta\sin\phi + \cos\delta\cos\phi\cos\omega$, the Equation (14) can be written as:

$$I_o = I_{sc} E_0 (\sin\delta\sin\phi + \cos\delta\cos\phi\cos\omega) \tag{15}$$

In the case where we want to determine the amount of solar radiation, dI_o incident over a time interval, dt, and calculate the solar energy over a specific time, Equation (15) is written in the form of the following equation.

$$dI_o = 3600 I_{sc} E_0 \cos\theta_z \, dt \tag{16}$$

Where dt is the time interval in hours, and I_{sc} is the solar constant expressed as the amount of energy over 1 hour (4,917.96 × 10^3 J/m^2). From Equation (16), it can be seen that $\cos\theta_z$ depends on the hour angle (ω). For convenience in determining I_o, dt is converted into $d\omega$ because when the Earth completes one full rotation (24 hours), the hour angle changes by 2π radians. This can be written in equation form as follows:

$$dt = \left(\frac{12}{\pi}\right) d\omega \tag{17}$$

By substituting dt from Equation (17) and substituting the value of $\cos\theta_z$ into Equation (16), the following equation is obtained.

$$dI_o = \left(\frac{12x3600}{\pi}\right) I_{sc}E_0(\sin\delta\sin\phi + \cos\delta\cos\phi\cos\omega)d\omega \tag{18}$$

The solar radiation energy over a one-hour period can be obtained by integrating dI_o over that one-hour period as shown in Equation 19.

$$I_o = \left(\frac{12x3600}{\pi}\right) I_{sc}E_0 \int_{\omega_i-\frac{\pi}{24}}^{\omega_i+\frac{\pi}{24}} (\sin\delta\sin\phi + \cos\delta\cos\phi\cos\omega)d\omega \tag{19}$$

Where ω_i is the hour angle at the midpoint of the hour. The result of the integration is shown in Equation (20).

$$I_o = \left(\frac{12x3600}{\pi}\right) I_{sc}E_0(\sin\delta\sin\phi + \cos\delta\cos\phi\cos\omega_i) \tag{20}$$

In case where solar radiation is to be calculated for a time interval shorter or longer than 1 hour that is over the period when the sun's hour angle is between ω_1 and ω_2, the corresponding radiation can be computed by integrating Equation (20) from ω_1 to ω_2 as follows:

$$I_o = \left(\frac{12x3600}{\pi}\right) I_{sc}E_0[\frac{\pi}{180}(\omega_2 - \omega_1)\sin\delta\sin\phi + \cos\delta\cos\phi(\sin\omega_2 - \sin\omega_1)] \tag{21}$$

ω_1 and ω_2 in Equation (21) are expressed in degrees, and the factor $\pi/180$ is used to convert the units of ω_1 and ω_2 to radians.

2.2.3.2 Daily and monthly average daily solar radiation

The daily solar radiation H_o can be obtained by integrating the hourly solar radiation from sunrise to sunset. As expressed in Equation (22) or Equation (23)

$$H_0=\left(\frac{12x3600}{\pi}\right) I_{sc} E_0 \int \left(\begin{matrix}\sin\delta\sin\phi \\ +\cos\delta\cos\phi\cos\omega_i\end{matrix}\right) d\omega \quad (22)$$

or

$$H_0=\left(\frac{12x3600}{\pi}\right) I_{sc} E_0 \left[\frac{\pi}{180}\left(\begin{matrix}(\omega_{ss})\sin\delta\sin\phi \\ +\cos\delta\cos\phi\cos\omega_{ss}\end{matrix}\right)\right] \quad (23)$$

Where H_o is the daily extraterrestrial solar radiation on a horizontal surface (J/m^2), ω_{ss} is the hour angle at sunset (°), and I_{sc} is the solar constant for hourly energy ($4{,}917.96 \times 10^3$ J/m^2).

The monthly average daily solar radiation $\bar{H}_0$ can be obtained by integrating the daily solar radiation H_0 shown in Equation (24).

$$\bar{H}_0=\frac{1}{N}\sum_{n=1}^{N} H_{0,n} \quad (24)$$

Where $\bar{H}_0$ is monthly average daily extraterrestrial solar radiation (J/m^2), N is the last day of month.

มหาวิทยาลัยศิลปากร

2.3 Effect of atmospheric parameters to the diffuse solar irradiance

Solar radiation emitted by the Sun travels through the Earth's atmosphere before reaching the surface. Along the way, it is scattered and absorbed by various atmospheric components. To calculate solar irradiance and the resulting diffuse radiation, it is essential to understand the composition of the atmosphere and how each component affects solar radiation. These wavelength ranges interact differently with various atmospheric constituents. The main atmospheric components that significantly influence the diffuse solar radiation include aerosols (dust particles), precipitable water, clouds, and gases accumulated in the atmosphere. Among these, ozone is the gas that has the most substantial impact on solar radiation as clarified by Matsumi and Kawasaki (2003) and Inn and Tanaka (1953). In addition, some of the remaining atmospheric components indirectly influence the diffuse solar radiation, include air temperature, relative humidity and wind speed.

2.3.1 The effect of aerosols on solar radiation

Aerosols or atmospheric dust particles are solid or liquid particles suspended in the atmosphere excluding clouds and fog. These include smoke from fuel combustion, dust from the ground or deserts, sea salt spray, pollen, and chemical liquid droplets. Typically ranging in size from 0.1 to 1000 microns, aerosols vary in shape and chemical compositions depending on their source (Iqbal, 2012). Aerosols affect the solar radiation by both scattering and absorbing incoming sunlight. When solar radiation encounters these particles, part of it is scattered in various directions increasing diffuse radiation, while another part is absorbed reducing the total amount of radiation that reaches the Earth’s surface. The degree of this effect depends on aerosol concentration, size, and composition. In regions with high aerosol levels, such as urban or desert areas, direct solar radiation is significantly reduced, while diffuse radiation tends to increase. An example of aerosols from biomass burning is illustrated in Figure 12.

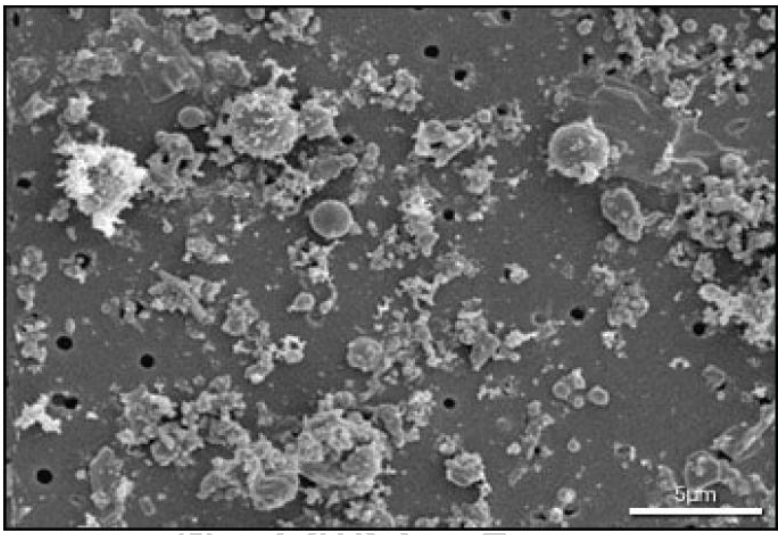


Figure 12 Characteristics of aerosols produced by biomass burning. Adapted from Boucher (2015).

Most aerosols are found in the troposphere locating from the Earth's surface up to about 2 km in altitude and are carried by wind currents. Generally, aerosols in this atmospheric layer remain about 1–2 weeks before settling to the ground due to gravity or being washed out by rain. A small number of aerosols can also be found in the stratosphere, mainly originating from volcanic ash, which can spread globally. These aerosols may remain in the atmosphere for several years because the stratosphere lacks rainfall to wash them out and lies at a higher altitude, where the influence of gravity is weaker.

In general, atmospheric aerosols can be categorized into two types: anthropogenic aerosols and natural aerosols. Examples of anthropogenic aerosols include particles from the combustion of fossil fuels and biomass burning. Natural aerosols arise from various natural processes, such as dust from deserts, soil particles, sea salt spray, and pollen.

Typically, the atmosphere always contains aerosols. As solar radiation passes through the atmosphere, it is scattered by these particles resulting in diffuse radiation and a portion is also absorbed by the aerosols. The proportion of scattering and absorption depends on the types of aerosols. For example, aerosols from fossil fuel combustion, which contain black carbon, can absorb up to 20 percent of solar radiation, while desert dust absorbs less than 5 percent (Kondrat′ev, 1999).

Since the attenuation of solar radiation by aerosols results from both absorption and scattering processes, separating the individual contributions from each is difficult. Therefore, Ångström (1929) proposed quantifying the attenuation capacity of aerosols using the aerosol optical depth, which is a function of the turbidity coefficient and the wavelength exponent as expressed in the following equation.

$$AOD = \beta\lambda^{-\alpha} \tag{25}$$

Where AOD is the aerosol optical depth (–), β is Angstrom's turbidity coefficient (–), α is Angstrom's wavelength exponent (–), and λ is the wavelength of solar radiation (microns).

The value of β is related to the concentration of aerosol particles or the number of aerosol particles per unit volume of air. In other words, a higher β indicates a higher aerosol concentration in the atmosphere. The value of α is inversely related to the particle size of the aerosols, when α is less, the aerosol particles are high, and when α is large, the particles are small. In general, atmospheric aerosols have an α value of approximately $\alpha = 1.3 \pm 0.5$ (Iqbal, 2012).

2.3.2 The effect of precipitable water on solar radiation

In general, water in the atmosphere exists in all three states: solid, liquid, and gas. Atmospheric water vapor refers to water in its gaseous state, intermixed with other gases in the atmosphere. Most water vapor is found from the Earth's surface up to about 2 kilometers in altitude. While in the atmosphere, water vapor can change state into liquid or solid, depending on the atmospheric temperature.

Water vapor forms primarily through the evaporation of water, especially from seas and oceans. It also comes from evaporation from soil surfaces and plant transpiration. The amount of water vapor present depends on climatic conditions. Equatorial regions typically have higher water vapor content than mid-latitude and high-latitude regions.

In solar radiation studies, the amount of water vapor is commonly represented as a precipitable water (w), which refers to the height of water that would result if all the water vapor in a vertical column of atmosphere with a base area of one unit were condensed into liquid water at the Earth's surface. The unit is typically centimeters (see Figure 13).

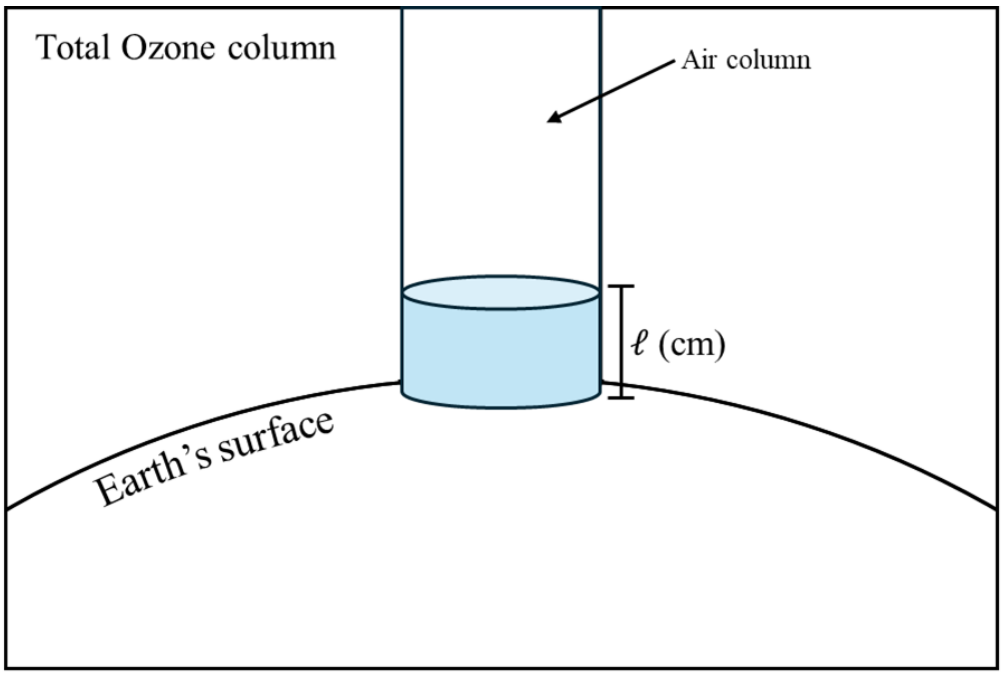


Figure 13 Representation of Atmospheric Water Vapor Content.

As solar radiation travels through the atmosphere, it is absorbed and scattered by water vapor resulting in a reduction of the radiation reaching the Earth's surface. The reduction caused by the scattering of water vapor molecules is considered negligible compared to absorption. Therefore, calculations of solar radiation passing through the atmosphere typically consider only the effects of absorption.

Water vapor absorbs solar radiation at various wavelengths in the form of wavelength bands, most of which lie in the infrared region. The amount of solar radiation absorbed depends on the quantity of water vapor in the atmosphere and the air mass that the radiation traverses. This absorption effect can be represented by the spectral transmittance coefficient of water vapor, which is the ratio of the extraterrestrial solar spectrum to the solar spectrum at the Earth's surface.

An example of the spectral transmittance coefficient for an atmosphere containing 2 cm of precipitable water is shown in Figure 14. The figure clearly illustrates the significant role of water vapor played in absorbing solar radiation within the infrared wavelength range.

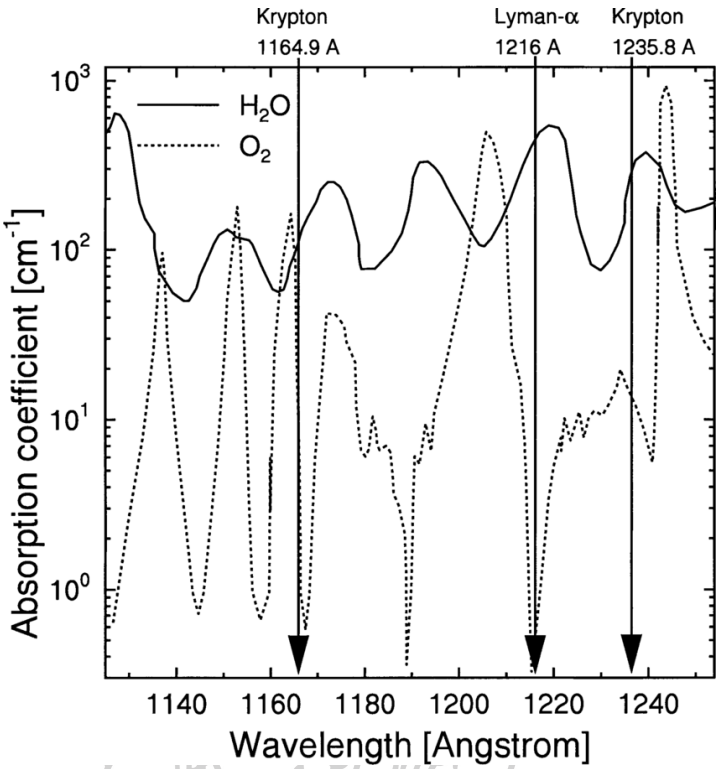


Figure 14 The absorption spectra of water vapor (H_2O) and oxygen (O_2) (van Dijk et al., 2003).

To calculate the solar radiation spectrum at the Earth's surface, it is necessary to know the transmittance coefficients of solar radiation at each wavelength. These coefficients depend on the amount of water vapor and the extinction coefficient of water vapor, which can be calculated using Leckner's equation (Leckner, 1978) as follows:

$$\tau_{w\lambda} = \exp[-0.2385 k_{w\lambda} w m_r / (1+20.07 k_{w\lambda} w m_r)^{0.45}] \quad (26)$$

Where $\tau_{w\lambda}$ is the transmittance coefficient of solar radiation at wavelength λ due to water vapor (–), $k_{w\lambda}$ is the extinction coefficient of solar radiation by water vapor (cm^{-1}), and m_r is the air mass (–).

For broadband transmittance of solar radiation due to water vapor, the coefficient can be determined using the formula by Lacis and Hansen (1974) as expressed:

$$\tau_w = 1 - \frac{2.9U_1}{(1+141.5U_1)^{0.635}+5.92U_1} \quad (27)$$

when $$U_1 = w m_r \quad (28)$$

2.3.3 The effect of ozone layers on solar radiation

Most ozone layers are found in the stratosphere with smaller amounts presenting in the troposphere. Tropospheric ozone is produced by certain industrial activities, such as drinking water treatment that uses ozone for disinfection, as well as by lightning. In the stratosphere, ozone is formed through a photodissociation reaction involving oxygen molecules (O_2). Ultraviolet (UV) photons from the sun break apart oxygen molecules into individual oxygen atoms (O). These atoms then combine with other oxygen molecules (O_2) to form ozone (O_3). This process can be written as a chemical reaction as follows (Frederick, 2008):

$$O_2+h\nu \rightarrow O+O \tag{29}$$

$$O+O_2+M \rightarrow O_3+M \tag{30}$$

Where $h\nu$ is the energy of a photon of ultraviolet radiation from the Sun (J), ν is the frequency of ultraviolet radiation (Hz), h is Planck's constant, and M is another atom or molecule that acts as a catalyst in the reaction.

To maintain balance, ozone in the stratosphere is also destroyed by photolysis reactions. In this process, an ozone molecule is struck by an ultraviolet photon and breaks down into an oxygen molecule and an oxygen atom as shown in this equation (Frederick, 2008):

$$O_3+h\nu \rightarrow O_2+O \tag{31}$$

The measurement of ozone layer is similar to that of water vapor. It is commonly expressed as the height of ozone in a vertical column of the atmosphere with a unit base area (see Figure 15). This assumes that all the ozone within the atmospheric column is brought down to the Earth's surface under Normal Temperature and Pressure (NTP) conditions, i.e., at a temperature of 15°C and a pressure of 101.325 kilopascals Rathakrishnan (2019) and Flowers et al. (2019). The amount of ozone is then expressed as the height (in centimeters) of this compressed ozone column, and the measured quantity is referred to as the total ozone column (O_3).

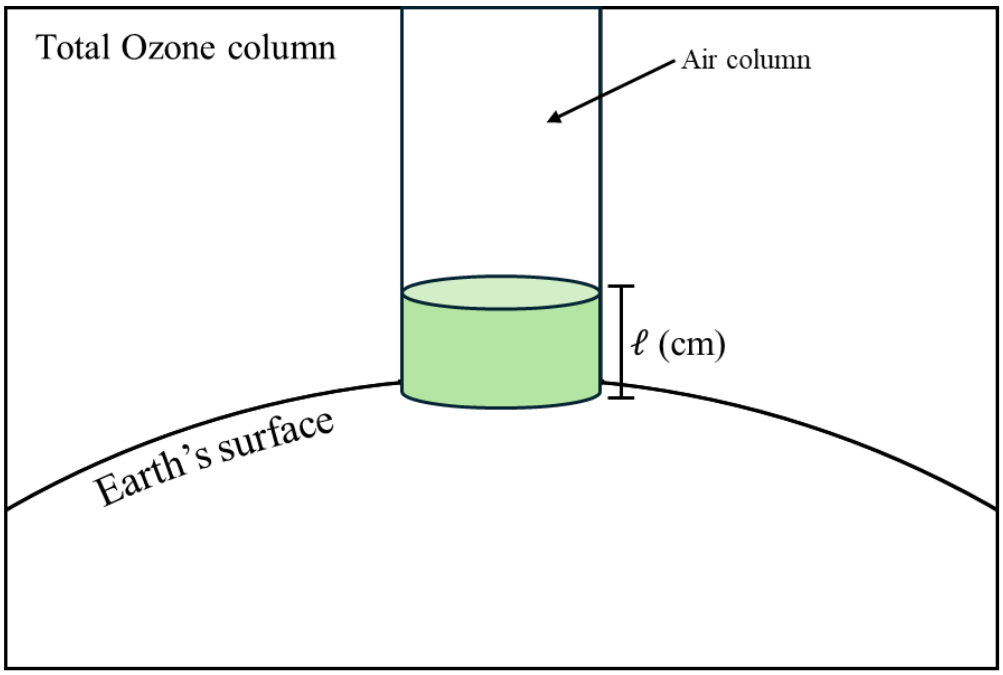


Figure 15 Representation of Total Ozone column.

We can also express the amount of ozone in Dobson Units (DU), which represent the total amount of ozone in an atmospheric column. One Dobson Unit is defined as the amount of ozone that would form a layer 0.01 cm thick under standard temperature and pressure (NTP). Therefore, 1 DU = 1000 × the total ozone column in centimeters.

2.3.4 The effect of cloud on solar radiation

Clouds are composed of tiny water droplets, ice crystals, or a combination of both. They can be classified by altitude into three levels: low-level clouds, mid-level clouds, and high-level clouds. Low-level clouds are found at altitudes below 2 kilometers above the Earth's surface, mid-level clouds occur between 2 and 7 kilometers, and high-level clouds are found above 7 kilometers. Additionally, there are vertically developed clouds, such as cumulonimbus clouds, which have bases at low levels and can extend vertically for several kilometers. Generally, low- and mid-level clouds consist primarily of water droplets, while high-level clouds are mainly composed of ice crystals.

Clouds play a significant role in attenuating the amount of solar radiation that reaches the Earth's surface. They scatter part of the solar radiation back into space and another part toward the Earth's surface as diffuse radiation. In general, clouds absorb very little solar radiation in the ultraviolet and visible light wavelength ranges but absorb more significantly in the infrared range.

Key optical properties of clouds include optical depth and the single scattering albedo, which refers to the ratio of scattered radiation to the total incident radiation. These properties depend on the characteristics of the cloud's components, particularly the phase (liquid or ice) and the size of the droplets. An example of the absorption coefficient of solar radiation by clouds composed of 20-micron water droplets is shown in Figure 16.

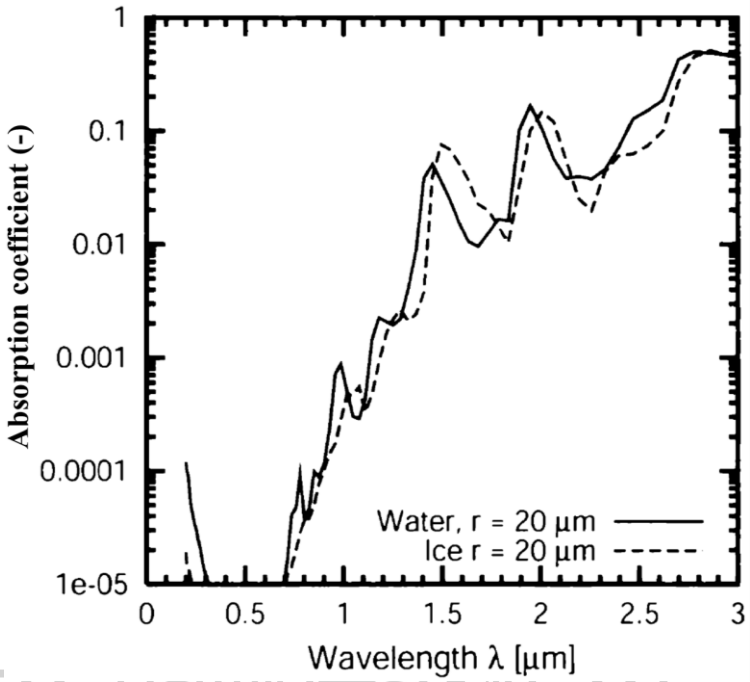


Figure 16 Absorption spectra of cloud (Petty, 2006).

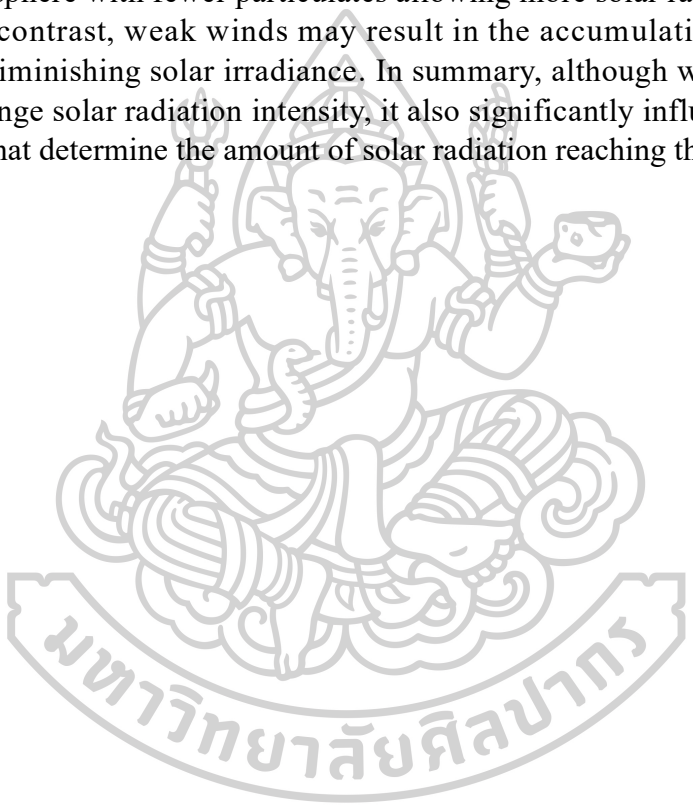
2.3.5 The Effect of indirect atmospheric parameters on solar radiation

The previous section presented the atmospheric parameters that directly affect solar radiation intensity. In contrast, some remaining atmospheric parameters influence solar radiation indirectly by affecting the key parameters.

Air temperature does not directly affect solar radiation. However, it indirectly influences solar radiation through several atmospheric processes. Higher temperatures can enhance water evaporation, leading to increased water vapor and cloud formation, both of which reduce solar radiation reaching the Earth's surface. Water vapor is a strong absorber in the infrared (IR) region of the solar spectrum. In hot and dry conditions, aerosols are often more abundant contributing to the attenuation of solar radiation through scattering and absorption. Moreover, a study in Germany found a strong correlation between air temperature and solar radiation with correlation coefficients reaching up to 0.93 (Behr, 2022).

The high relative humidity level can lead to the formation of haze and water droplets in the atmosphere, which scatter and absorb incoming solar radiation, also leading to increase cloud formation, which can further attenuate solar radiation. In Nigeria (Ayegba et al., 2017), Britain (Bett & Thornton, 2016), and Republic of Croatia (Falkoni & Krajačić, 2015), a study of utilizing the Hargreaves-Samani model (Hargreaves & Samani, 1985) found a negative correlation between RH and global solar radiation. This suggests that higher RH is associated with lower solar radiation.

Wind speed affects atmospheric stability, which in turn influences solar radiation. Stronger winds promote mixing in the atmosphere, dispersing the formation of particles that can scatter or absorb solar radiation. This mixing can lead to a more stable atmosphere with fewer particulates allowing more solar radiation to reach the surface. In contrast, weak winds may result in the accumulation of aerosols and pollutants diminishing solar irradiance. In summary, although wind speed does not directly change solar radiation intensity, it also significantly influences atmospheric conditions that determine the amount of solar radiation reaching the Earth's surface.



2.4 Literature review

In recent years, the diffuse solar radiation has become increasingly recognized as an important component of solar radiation and has been the subject of extensive research. Due to the challenges in directly measuring diffuse radiation, many studies have focused on using mathematical methods to estimate the diffuse radiation in areas where direct observations were not available.

Since the 1960s, numerous studies have aimed to estimate diffuse the solar radiation by establishing a linear relationship between the diffuse fraction and the clearness index. Liu and Jordan (1960) proposed one of the earliest models, which provided relationships for determining diffuse solar radiation on a horizontal surface under clear-sky conditions. Their study was based on long-term average hourly and daily diffuse radiation data collected from 98 locations across the United States and Canada.

Later, Orgill and Hollands (1977) conducted a detailed analysis of hourly diffuse radiation on a horizontal surface using measured total and diffuse solar radiation data obtained from Toronto Airport between September 1967 and August 1971. The models proposed in both studies follow the general form in terms of the hourly diffuse fraction (k_d) and the hourly clearness index (k_t).

Similarly, Exell and Santibuppakul (1984) developed empirical models to estimate mean daily diffuse solar radiation in Thailand using observed data from five meteorological stations (Chiang Mai, Ubon Ratchathani, Nakhon Ratchasima, Bangkok (Don Muang), and Songkhla) covering the period from 1968 to 1972. Their study analyzed the relationship between the clearness index and the diffuse fraction, proposing site-specific quadratic regression equations to represent this relationship. The results highlighted the decreasing trend of the diffuse fraction with increasing clearness index, consistent with atmospheric scattering behavior. This work provided one of the first comprehensive estimations of diffuse radiation patterns in Thailand and has served as a reference point for later solar energy modeling studies in the region. The expression proposed in their study is shown in Equation (32).

$$k_d = a_0 + a_1 k_t \tag{32}$$

Thereafter, Erbs et al. (1982) established polynomial model using a relationship between the hourly diffuse fraction and the hourly clearness index. These data were recorded at the four U.S. during 1974–1976 including Fort Hood, Livermore, Raleigh, and Maynard. The diffuse solar radiation calculated from the direct normal radiation was measured with a pyrheliometer and the total radiation was measured with a pyranometer. The test dataset was recorded in Highett, Victoria, Australia during the years 1966–1969.

Moreover, several other studies have also applied polynomial models but conducted experiments at different stations including Italy (Barbaro et al., 1981; Coppolino, 1990), China (Yin et al., 2023; Zhou et al., 2019), Libya (Ahwide et al., 2013; Said et al., 2003), Egypt (El-Sebaii & Trabea, 2003; Elminir, 2007; Trabea, 1999), Turkey (Bakirci, 2015, 2021; Ulgen & Hepbasli, 2002, 2009), and Saudi Arabia (Elhadidy & Abdel-Nabi, 1991) some parameterized models are shown as Equations (33)–(35).

$$k_d = a_0 + a_1 k_t + a_2 k_t^2 \tag{33}$$

$$k_d = a_0 + a_1 k_t + a_2 k_t^2 + a_3 k_t^3 \tag{34}$$

$$k_d = a_0 + a_1 k_t + a_4 k_t^2 + a_3 k_t^3 + a_4 k_t^4 \tag{35}$$

The model was later further developed using logistic equations. Lealea and Tchinda (2013) investigated the diffuse solar radiation in the northern and far northern regions of Cameroon. This study utilized 20 years of recorded data (1985–2005) on monthly mean diffuse solar radiation. The proposed models related the diffuse fraction to the clearness index and were presented in exponential and logarithmic forms as shown in Equations (36) and (37), respectively.

$$k_d = a_0 + \exp\,(a_1 k_t) \tag{36}$$

$$k_d = \ln(a_0 + a_1 k_t) \tag{37}$$

Boukelia et al. (2014) developed correlations for estimating monthly mean daily diffuse solar radiation and analyzed the relationship between the diffuse fraction and the clearness index. The study used data from six Algerian stations (Algiers, Constantine, Ghardaia, Bechar, Adrar, and Tamanrasset) covering approximately the period from 1990 to 2010. The proposed models were expressed in exponential and logarithmic forms, as shown in Equations (38) and (39), respectively.

$$k_d = a_0 \exp\,(a_1 k_t) \tag{38}$$

$$k_d = a_0 + a_1 \log(k_t) \tag{39}$$

Bailek et al. (2018) showed a systematic approach for diffuse solar radiation estimation over the Algerian Sahara. The data cover a period of six years approximate from 2005–2015 measured in the Adrar, Ghardaïa, and Tamanrasset were used. The model presented the monthly average daily diffuse fraction and clearness index on the logarithm model expressed in Equations (40) and (41), respectively.

$$k_d = a_0 + a_1 \log(k_t) \tag{40}$$

$$k_d = \log(a_0 + a_1 k_t) \tag{41}$$

Subsequently, the model based on the diffuse fraction and clearness index was further developed using a multiple linear regression equation, combining with additional atmospheric parameters. Mubiru and Banda (2007) also developed the linear relation of the diffuse fraction and clearness index by adding the relative humidity as expressed in the Equation (42). The study site was situated in Kampala, Uganda. The period of measurement for both diffuse and global solar irradiation was 2003–2005.

$$k_d = a_0 + a_1 k_t + a_2 RH \tag{42}$$

Janjai (2012) developed a monthly average daily diffuse fraction model by incorporating air temperature as an additional parameter and found that the model performance was improved. The data collected from four solar monitoring stations located at different parts of Bangkok, Thailand with the data collection period ranging from 4 to 8 years. The expression was shown in Equation (42). Li et al. (2011) also developed the model by adding air temperature and relative humidity. Using the data covering 30 years between 1971 and 2000 at Guangzhou station, China as expressed in Equation (43).

$$k_d = a_0 + a_1 k_t + a_2 T_a + a_3 RH \tag{43}$$

Pattarapanitchai and Janjai (2012) proposed a semi-empirical model for estimating clear-sky diffuse solar irradiance specifically tailored to tropical environments. The model was formulated by combining radiative transfer principles with empirical adjustments based on local atmospheric conditions. It expresses the diffuse irradiance (I_d) as a function of solar zenith angle and key atmospheric parameters such as Linke turbidity factor (T_L), aerosol optical depth (AOD), and precipitable water vapor (PW). The model was validated using ground-based pyranometer measurements collected at four stations in Thailand, namely Nakhon Pathom, Chiang Mai, Ubon Ratchathani, and Songkhla. The validation results showed a high correlation coefficient ($R^2 = 0.96$) and a mean bias error of less than 5%,

indicating good agreement between observed and estimated diffuse irradiance. This approach effectively integrates physical understanding with empirical calibration, making it a practical and accurate tool for estimating diffuse solar radiation in data-sparse tropical regions. The expression presented in Equation (44).

$$I_d = aI_{sc}E_0COS^{a_1}\theta_z(a_2AOD_{500} + a_3w + a_4O_3) \quad (44)$$

Furthermore, Zhu et al. (2021) conducted a study on daily diffuse solar radiation across 17 locations in such as China with each station situated in one of five distinct climatic zones Mountain Plateau Climatic Zone (MPZ), Temperate Continental Climatic Zone (TCZ), Temperate Monsoon Climatic Zone (TMZ), Subtropical Monsoon Climatic Zone (SMZ), and Tropical Monsoon Climatic Zone (TMPZ). The researchers then developed and compiled models to estimate the diffuse radiation intensity in terms of the diffuse fraction (the ratio of diffuse to global radiation). These models were based on six atmospheric parameters namely clearness index (k_t), sunshine fraction (S/S_0), total cloud cover (CC), relative humidity (RH), air temperature (T_a), and wind speed (ws).

This study first examined the correlation between the daily diffuse radiation and each of the six atmospheric parameters using correlation coefficients. It was found that clearness index, sunshine fraction, and cloud cover had strong correlations with the diffuse radiation intensity, while the other three parameters (relative humidity, air temperature and wind speed) showed relatively weak correlations.

Based on this analysis, the models were categorized into five groups according to the parameters with the strongest influence:

(1) models based on the clearness index,

(2) models based on the sunshine fraction,

(3) models based on the cloud cover,

(4) models based on all three key parameters (clearness index, sunshine fraction, and cloud cover)

(5) models based on all three key parameters developed using artificial neural networks (ANN).

These models were evaluated and compared across all five climatic zones. The results indicated that the most accurate and reliable model was the one developed using ANN by applying all six atmospheric parameters. The study also found that although the latter three parameters (RH, T_a, ws) had low individual correlations with the diffuse radiation, including them in the model enhanced its overall predictive accuracy.

Furthermore, models have been developed to utilize satellite data for generating spatial distribution maps of the diffuse solar radiation aiming to fill data gaps and support future research. Hove and Göttsche (1999) presented a study to estimate a long-term monthly solar radiation over Zimbabwe. Initially, they compiled monthly average daily global horizontal radiation data from 20 stations directly

measured by the Department of Meteorological Services of Zimbabwe (Met. Dept.). For an additional 9 stations, indirect estimation, were obtained from sunshine duration measurements using a linear relationship between the clearness index and sunshine duration derived from the original 20 stations. Satellite data from METEOSAT-2 and spatial interpolation were used to estimate radiation at 6 grid points across Zimbabwe resulting in long-term global solar radiation data for 35 locations.

To adjust these long-term values to the study period (1985–1986), time-series adjustment factors were applied. The diffuse solar radiation was then estimated using the relationship between the diffuse fraction and the clearness index. These estimates were compared against the measured diffuse radiation at Harare and Bulawayo, where 13 years of observations were available using pyranometers with shadow rings. The results showed strong agreement between the modeled and measured values as illustrated by the correlation between the diffuse fraction and clearness index. The final model was used to generate diffuse solar radiation maps across Zimbabwe as example presented in Figure 17.

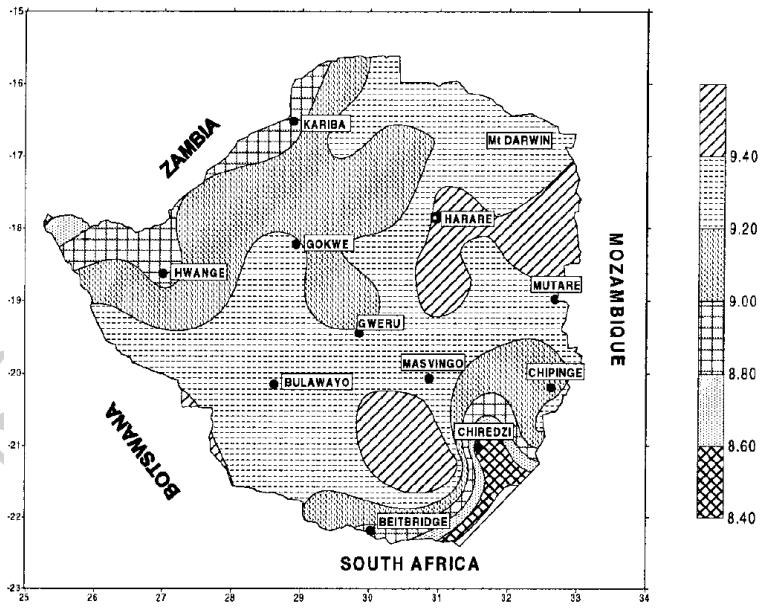


Figure 17 Example diffuse solar radiation map across Zimbabwe in August from Hove and Göttsche (1999).

Previous studies have demonstrated that the development of diffuse solar radiation models commonly started with the fundamental relationship between the diffuse fraction and the clearness index. Incorporating additional atmospheric parameters that significantly influence on the diffuse radiation has been shown to enhance model accuracy. Moreover, including parameters with low statistical significance can still contribute to improv model performance. The application of machine learning techniques further enhances model capability. These models can be employed to generate diffuse solar radiation maps effectively illustrating spatial distribution patterns.

Chapter 3
Methodology and results

3.1 Equipment and atmospheric data

3.1.1 Ground-based data

3.1.1.1 Solar radiation equipment

This study uses solar radiation data from the Silpakorn University network, which is installed at meteorological stations across different regions of Thailand. The data covers the period from 2012 to 2024. The data are divided into two sets: the training dataset for model development and the testing dataset for model and map evaluation. Data from the main stations during 2012–2022 are used as the training dataset, while data from 2023–2024 are used for testing the model. Additionally, data from stations that do not directly measure diffuse solar radiation are only used for validating the map. The study stations used in this work are shown in Figure 18.

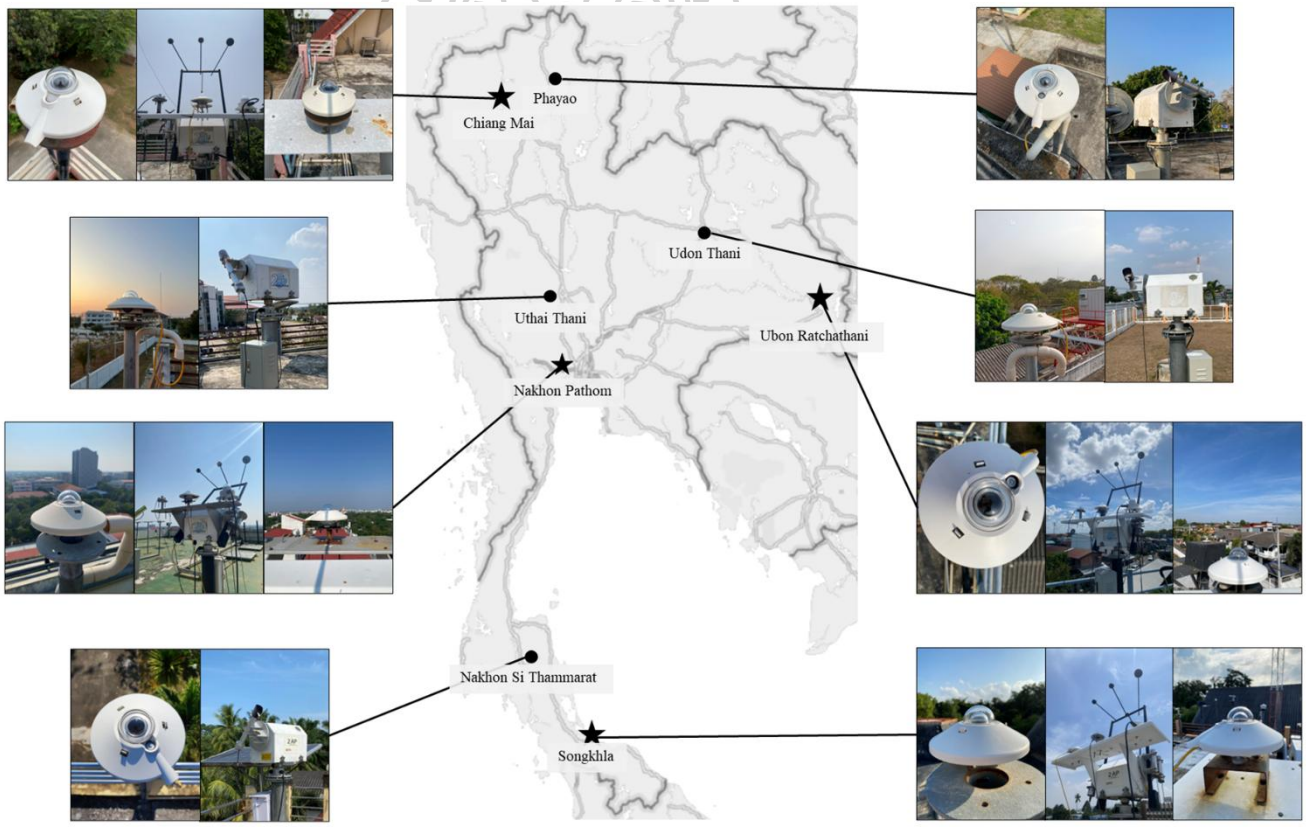


Figure 18 Solar monitoring stations used in this work star labels are main stations and dot labels are indirect station for obtaining the diffuse solar radiation.

From Figure 18, the four stations marked with stars are the primary stations that directly measure the diffuse solar radiation. These include Chiang Mai station (18.78°N, 98.98°E) in the northern region, Nakhon Pathom station (13.82°N, 100.04°E) in the central region, Ubon Ratchathani station (15.25°N, 104.87°E) in the

northeastern region, and Songkhla station (7.20°N, 100.60°E) in the southern region. The remaining four stations, marked with dots, estimate diffuse radiation indirectly by calculating from global horizontal irradiance and direct normal irradiance. These stations are Phayao station (19.19°N, 99.88°E) in the north, Uthai Thani station (15.35°N, 100.01°E) in the central region, Udon Thani station (17.38°N, 102.81°E) in the northeast, and Nakhon Si Thammarat station (8.43°N, 99.50°E) in the south. The information of the data from each station is shown in Table 1.

Table 1 Details of solar radiation monitoring stations.

Stations	latitude (°N)	longitude (°E)	Region	period (years)	Solar radiation data		
					Diffuse	Global	Direct
Chiang Mai	18.78	98.98	North	2012-2024	✓	✓	✓
Nakhon Pathom (Silpakorn University)	13.82	100.04	Central	2012-2024	✓	✓	✓
Ubon Ratchathani	15.25	104.87	Northeast	2012-2024	✓	✓	✓
Songkhla	7.20	100.60	South	2012-2024	✓	✓	✓
Phayao	19.19	99.88	North	2024	x	✓	✓
Uthai Thani	15.35	100.01	Central	2024	x	✓	✓
Udon Thani	17.38	102.81	Northeast	2024	x	✓	✓
Nakhon Si Thammarat	8.43	99.50	South	2024	x	✓	✓

At the main stations, the global solar radiation is measured using CM21 pyranometers from Kipp & Zonen. The diffuse solar radiation is measured using CM11 pyranometers, also from Kipp & Zonen mounted on a two-axis positioning system (2AP sun tracker) equipped with a shading ball. Direct solar radiation is measured using pyrheliometers model sNIP and NIP from Eppley mounted on the same sun tracker. All data are recorded using DX2000 data loggers from Yokogawa Electric Corporation. For the indirect measurement stations, the global solar radiation is measured using CMP11 pyranometers from Kipp & Zonen, while direct solar radiation is measured using CH1 pyrheliometers, also from Kipp & Zonen. Data at these stations are recorded using GM10 data loggers from Yokogawa Electric Corporation. The measuring instruments used at these stations are shown in Figures 19 to 46.



Figure 19 Pyranometer CM21 (global solar radiation) at Chiang Mai station.



Figure 20 Pyranometer CM11 (diffuse solar radiation) at Chiang Mai station.



Figure 21 Pyrheliometer sNIP (direct solar radiation) at Chiang Mai station.

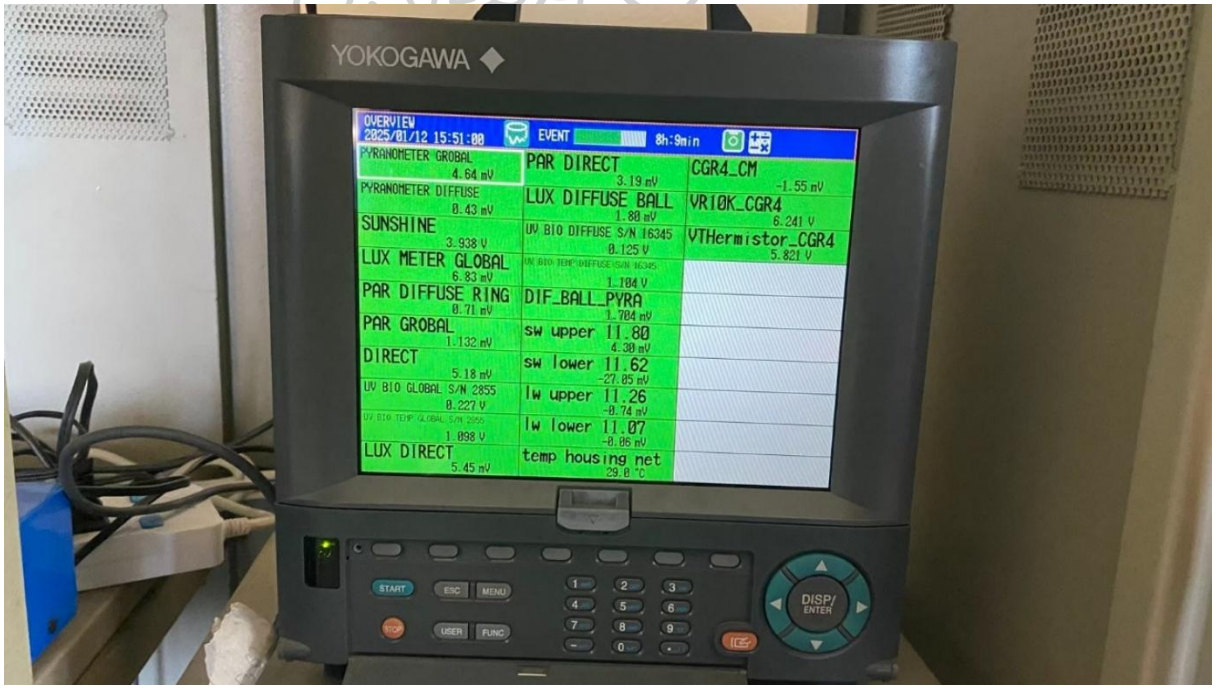


Figure 22 Datalogger DX2000 at Chiang Mai station.



Figure 23 Pyranometer CM21 (global solar radiation) at Nakhon Pathom station.



Figure 24 Pyranometer CM11 (diffuse solar radiation) at Nakhon Pathom station.



Figure 25 Pyrheliometer NIP (direct solar radiation) at Nakhon Pathom station.

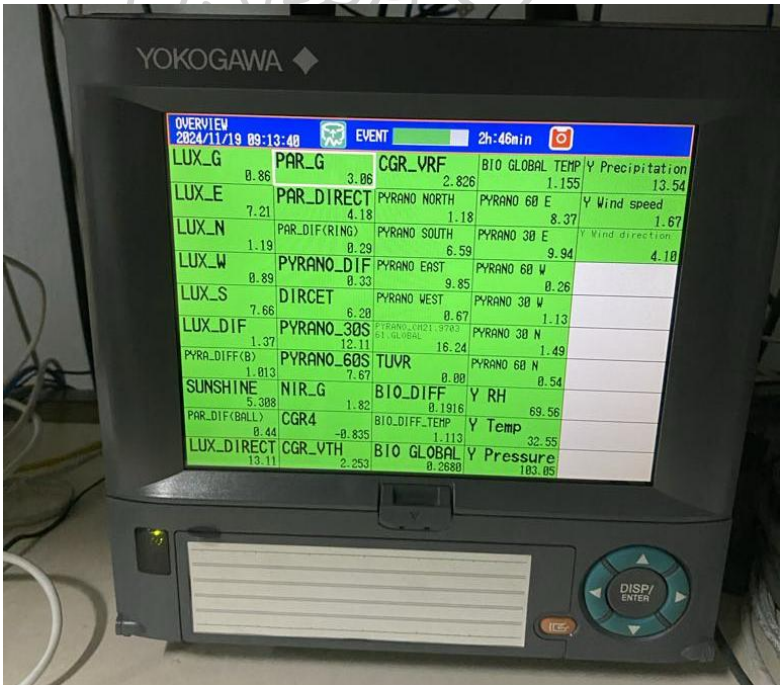


Figure 26 Datalogger DX2000 at Nakhon Pathom station.



Figure 27 Pyranometer CM21 (global solar radiation) at Ubon Ratchatani station.



Figure 28 Pyranometer CM11 (diffuse solar radiation) at Ubon Ratchatani station.



Figure 29 Pyrheliometer sNIP (direct solar radiation) at Ubon Ratchatani station.

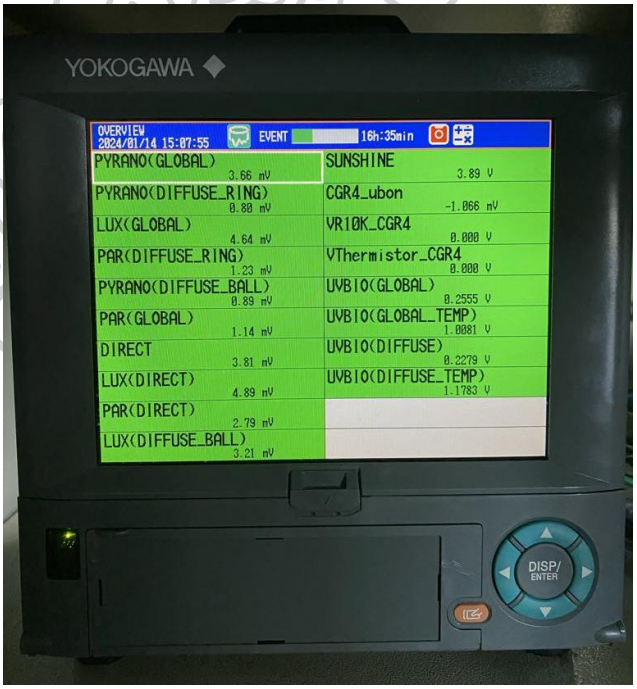


Figure 30 Datalogger DX2000 at Ubon Ratchatani station.



Figure 31 Pyranometer CM21 (global solar radiation) at Songkhla.



Figure 32 Pyranometer CM11 (diffuse solar radiation) at Songkhla.



Figure 33 Pyrheliometer NIP (direct solar radiation) at Songkhla.

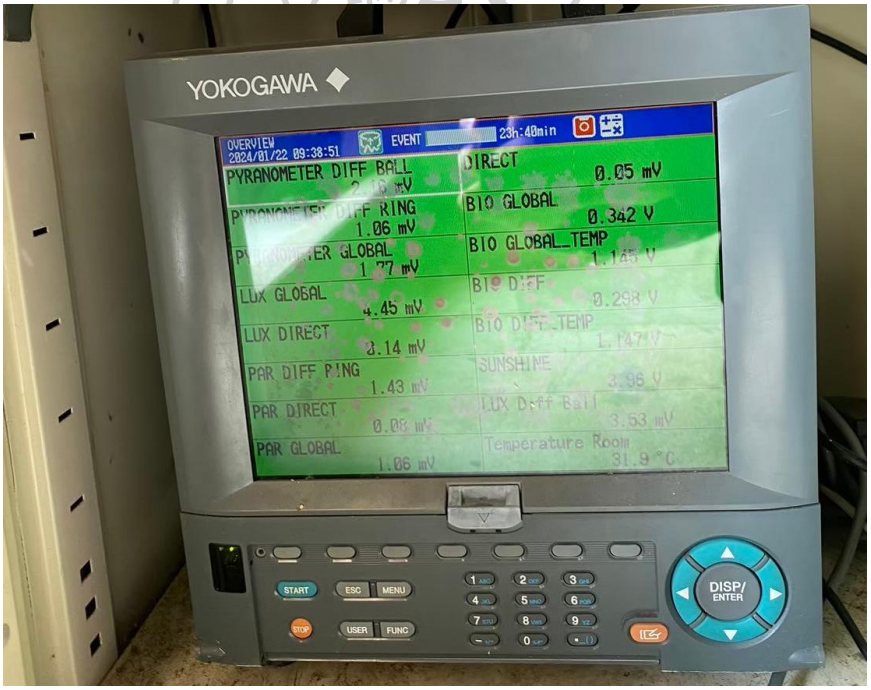


Figure 34 Datalogger DX2000 at Songkhla.



Figure 35 Pyranometer CMP11 (global solar radiation) at Phayao station.



Figure 36 Pyrheliometer CH1 and suntracker (direct solar radiation) at Phayao station.

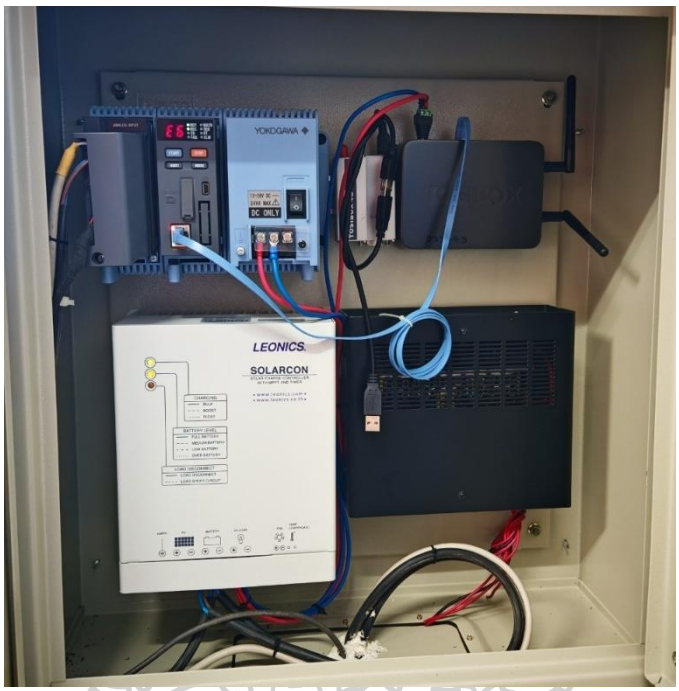


Figure 37 Datalogger GM10 and control box at Phayao station.



Figure 38 Pyranometer CMP11 (global solar radiation) at Uthai Thani station.



Figure 39 Pyrheliometer CH1 and suntracker (direct solar radiation) at Uthai Thani station.



Figure 40 Datalogger GM10 and control box at Uthai Thani station.



Figure 41 Pyranometer CMP11 (global solar radiation) at Udon Thani station.



Figure 42 Pyrheliometer CH1 and suntracker (direct solar radiation) at Udon Thani station.



Figure 43 Datalogger GM10 and control box at Udon Thani station.



Figure 44 Pyranometer CMP11 (global solar radiation) at Nakhon Si Thammarat station.



Figure 45 Pyrheliometer CH1 and suntracker (direct solar radiation) at Nakhon Si Thammarat station.

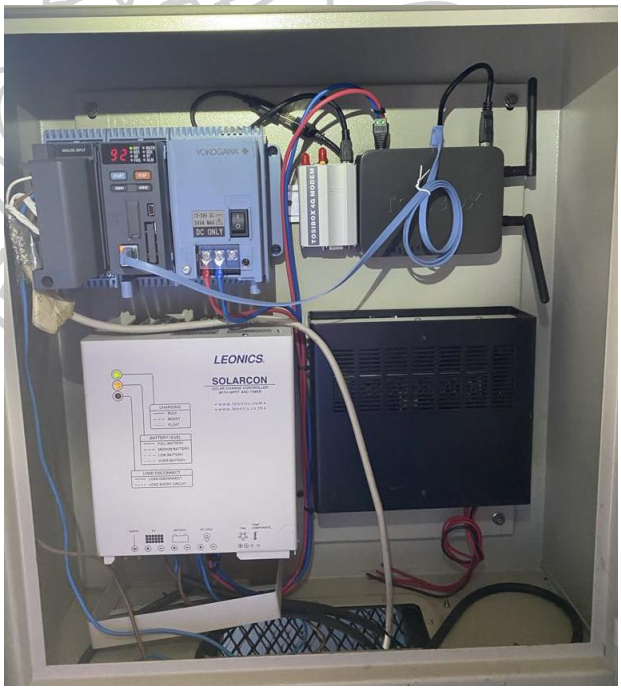


Figure 46 Datalogger GM10 and control box at Nakhon Si Thammarat station.

Each type of solar radiation instrument is always installed outdoors to ensure accurate measurement of solar radiation intensity. However, prolonged exposure to various weather conditions causes gradual degradation of the instruments, which leads to changes in their sensitivity over time. This can result in measurement errors making the data unreliable for further utilization. Therefore, regular calibration of the instruments is essential, ideally at least once a year.

The calibration process for pyranometers follows the ISO 9847 standard (ISO, 1992), while pyrheliometers are calibrated according to ISO 9059 (ISO, 1990). During calibration, a reference pyranometer and a reference pyrheliometer, both of which must be of equal or higher classification than the field instruments and already calibrated against a primary reference, are placed near the field instruments and aligned at the same level. Measurements are taken simultaneously on a clear, cloudless day.

The electrical output (voltage) from both the reference and field instruments is recorded and plotted to determine the relationship between the solar radiation intensity from the reference instrument and the voltage output from the field instrument. The slope of this graph represents the sensitivity of the field instrument being calibrated and can be expressed by Equation (45).

$$S = \frac{V_{field}}{I_{ref}} \tag{45}$$

Where S is the sensitivity of the solar radiation instrument ($V/\ W/m^2$), I_{ref} is the solar radiation intensity measured by the reference instrument (W/m^2), and V_{field} is the voltage output from the field solar radiation instrument need to be calibrated (V).

After calibrating the instrument, we obtain the voltage data from the field instrument and compare it with the solar radiation values measured by the reference instrument. Since the sensitivity of the reference instrument is already known, the solar radiation intensity measured by the reference instrument can be calculated. Then, by using the voltage output from the field instrument and the solar radiation intensity from the reference instrument, we can apply Equation (44). This is done by plotting a graph where the horizontal axis represents the solar radiation intensity measured by the reference instrument, and the vertical axis represents the voltage output from the field instrument to be calibrated. The slope of the graph indicates the sensitivity of the instrument being calibrated.

This calibration process can be applied to instruments measuring global radiation, diffuse radiation, and direct radiation. Examples of calibration graphs for all three types of instruments at the Nakhon Pathom station are shown in Figures 47–49, respectively. Examples of pyranometer calibrations from all nine stations are shown in Figures 50–57.

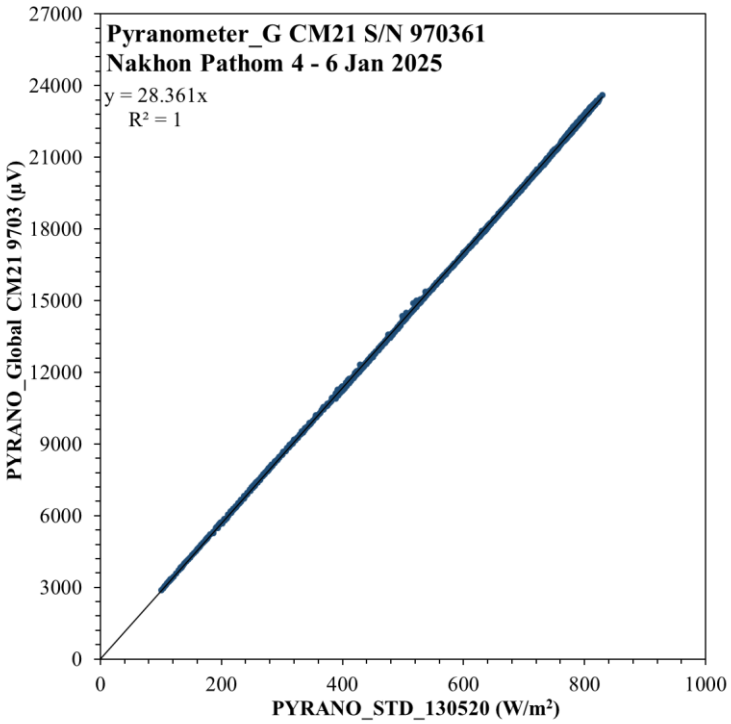


Figure 47 Example of a calibration graph for the global solar radiation measurement at Nakhon Pathom station.

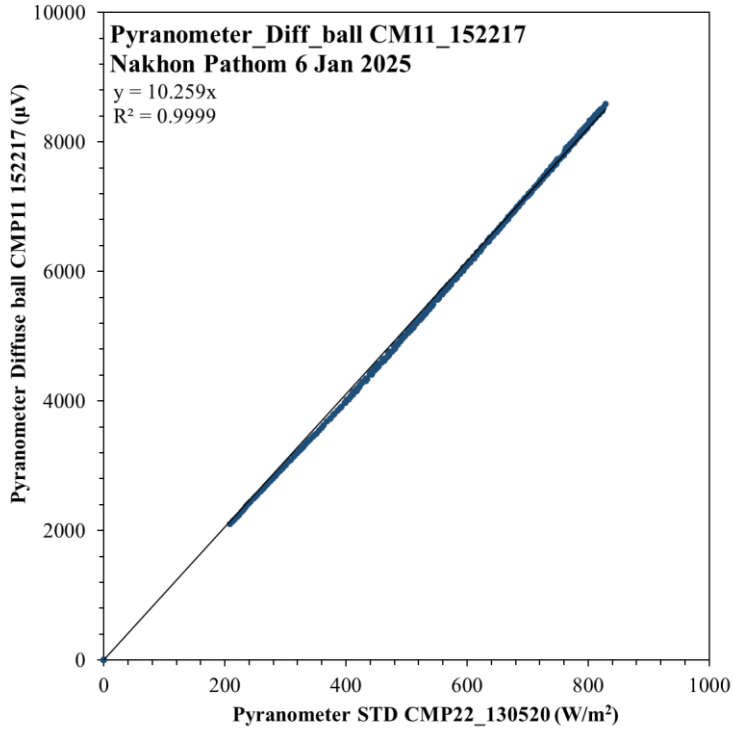


Figure 48 Example of a calibration graph for the diffuse solar radiation measurement at Nakhon Pathom station.

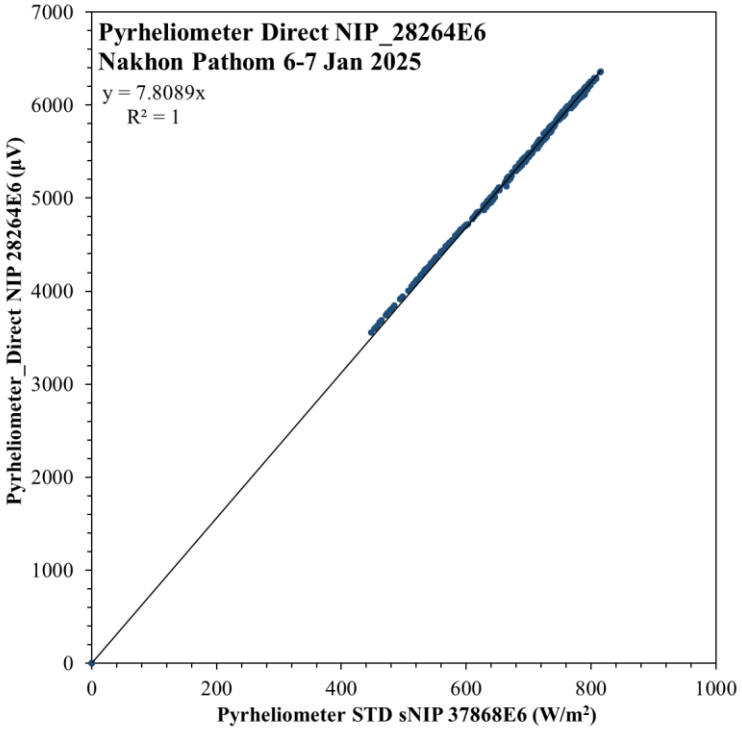


Figure 49 Example of a calibration graph for the direct solar radiation measurement at Nakhon Pathom station.



Figure 50 Example of a calibration of a global solar radiation instrument at Chiang Mai station.



Figure 51 Example of a calibration of a global solar radiation instrument at Nakhon Pathom station.



Figure 52 Example of a calibration of a global solar radiation instrument at Ubon Ratchatani station.



Figure 53 Example of a calibration of a global solar radiation instrument at Songkhla station.



Figure 54 Example of a calibration of a global solar radiation instrument at Phayao station.



Figure 55 Example of a calibration of a global solar radiation instrument at Uthai Thani station.



Figure 56 Example of a calibration of a global solar radiation instrument at Udon Thani station.



Figure 57 Example of a calibration of a global solar radiation instrument at Nakhon Si Thammarat station.

Although the solar radiation data was maintained by experienced meteorologists and researchers, quality control procedures were still required to remove potentially inaccurate values. Such errors may arise from sensor limitations, such as the cosine response error, or other technical issues. To ensure data reliability, the hourly irradiance values were screened using a procedure adapted from Abal et al. (2017) as outlined below:

1) Global and diffuse horizontal irradiance was greater than 0 W/m^2.
2) The cosine of the solar zenith angle was more than 0.1219 (solar altitude greater than 7°).
3) Global horizontal irradiance was greater than 5 W/m^2.
4) Global horizontal irradiance was greater than diffuse horizontal irradiance.
5) Global solar radiation was less than extraterrestrial solar radiation.
6) Diffuse solar radiation was less than or equal to half of extraterrestrial solar radiation.
7) Direct horizontal irradiance was less than extraterrestrial solar irradiance on the horizontal plane.

After the instruments are regularly maintained and calibrated annually, along with proper data screening, the resulting solar radiation data is high quality and ready for use in further studies.

The distribution of monthly average daily diffuse solar radiation in Thailand during the year 2012–2024 at Chiang Mai, Nakhon Pathom, Ubon Ratchathani, and Songkhla station are presented in Figures 58–65.

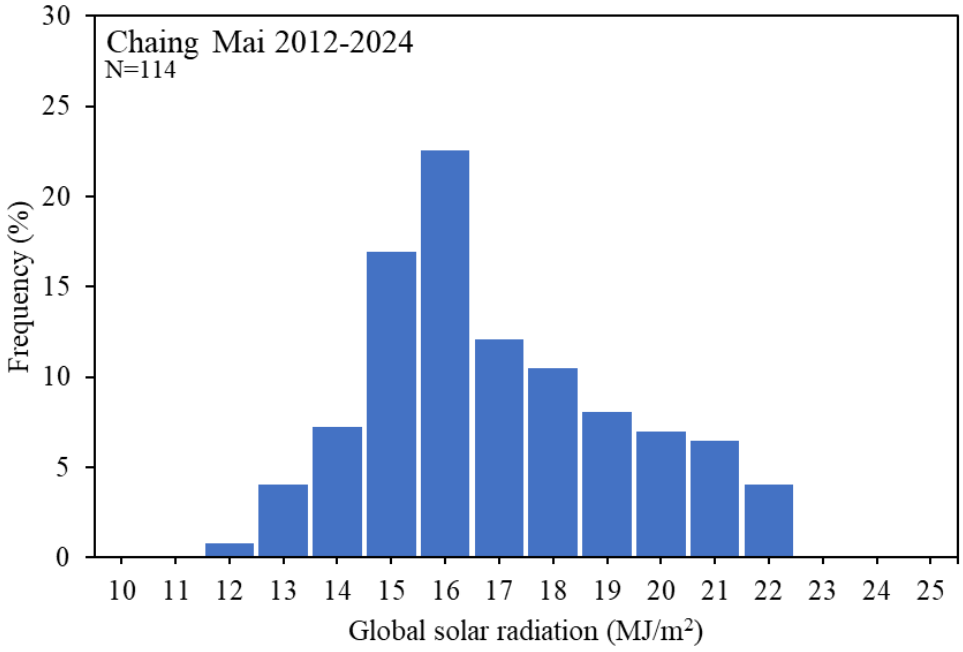


Figure 58 The distribution of global solar radiation at Chiang Mai station.

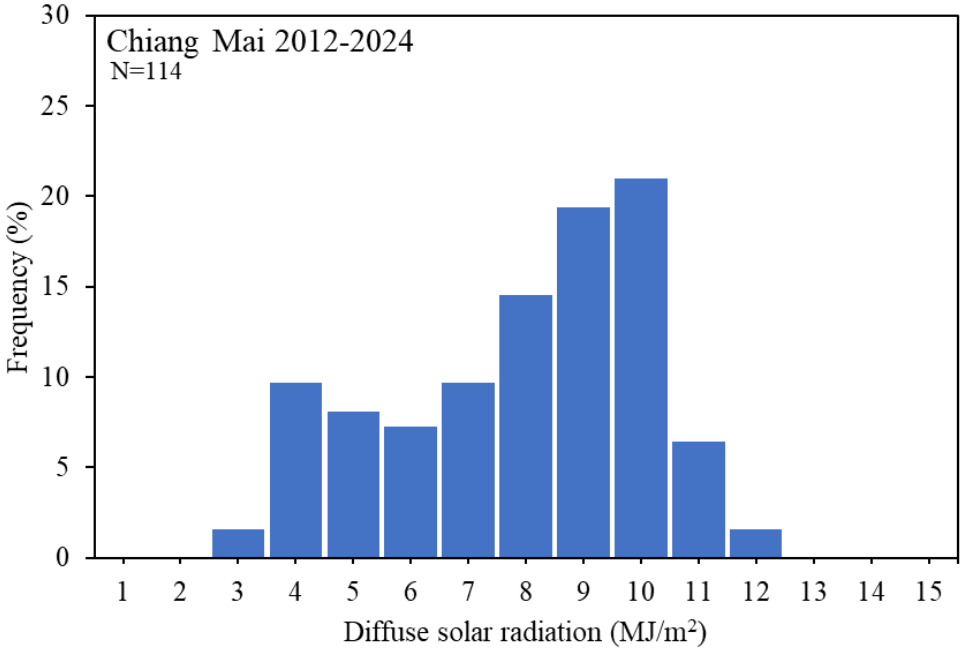


Figure 59 The distribution of diffuse solar radiation at Chiang Mai station.

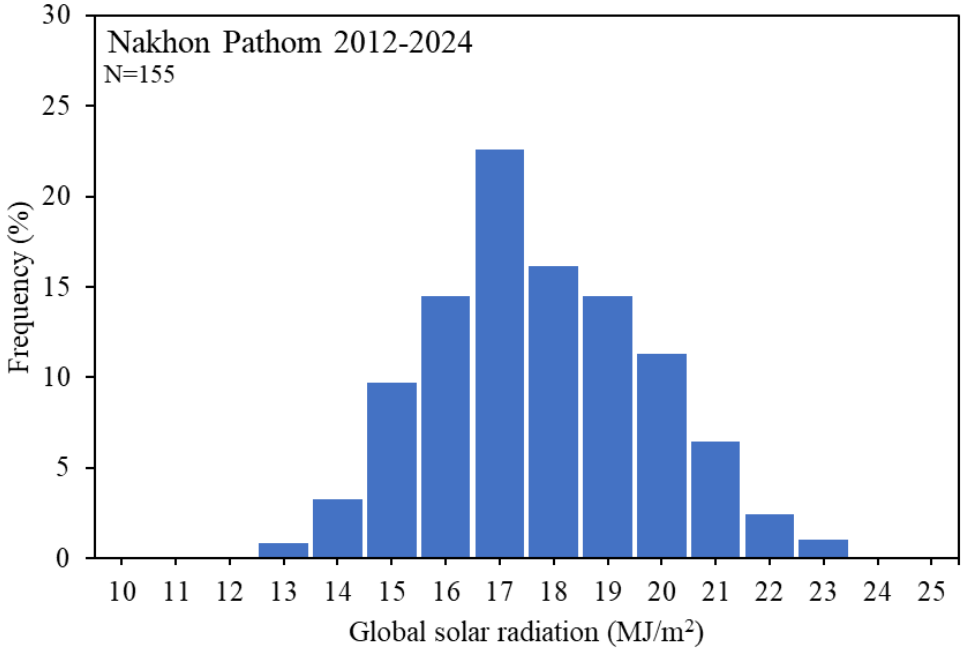


Figure 60 The distribution of global solar radiation at Nakhon Pathom station.

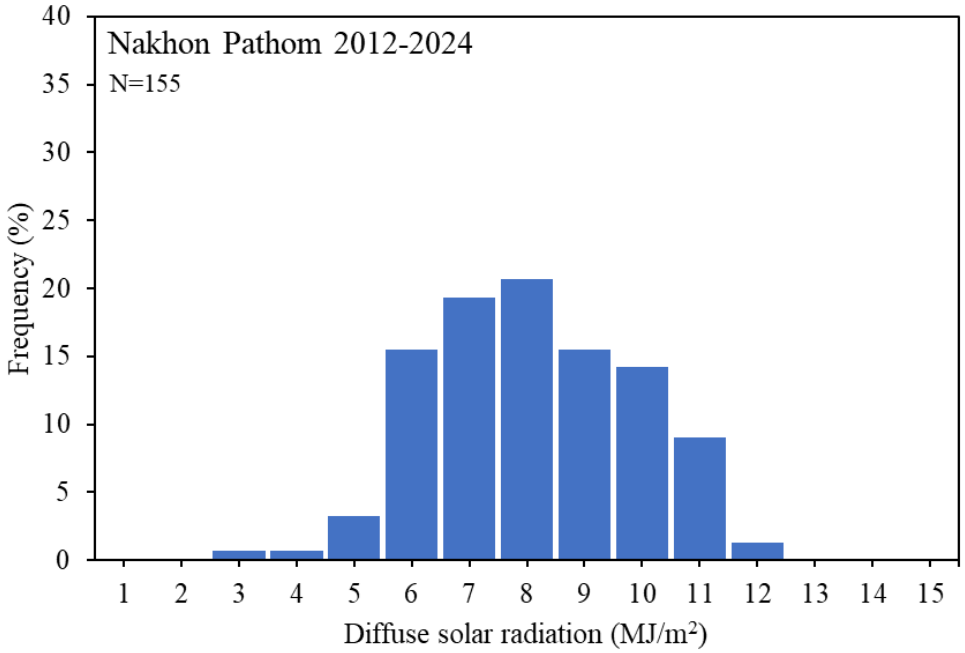


Figure 61 The distribution of diffuse solar radiation at Nakhon Pathom station.

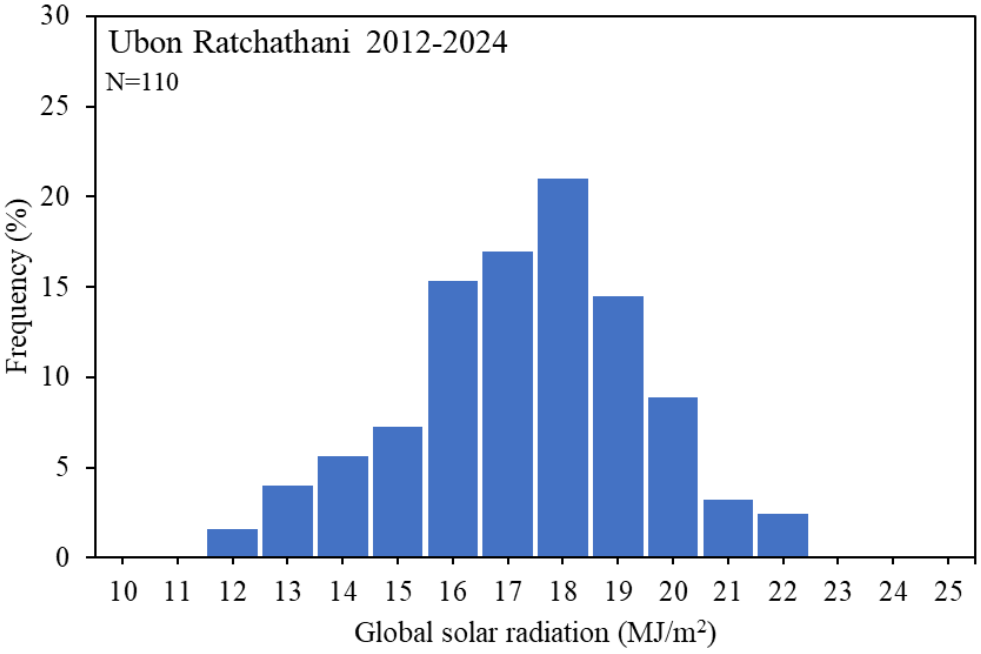


Figure 62 The distribution of global solar radiation at Ubon Ratchathani station.

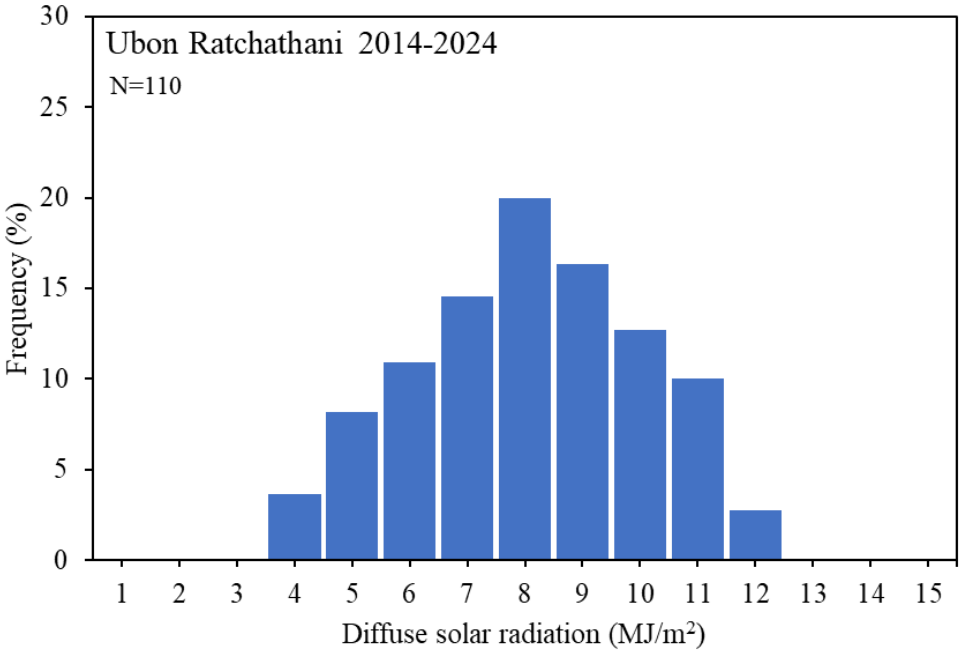


Figure 63 The distribution of diffuse solar radiation at Ubon Ratchathani station.

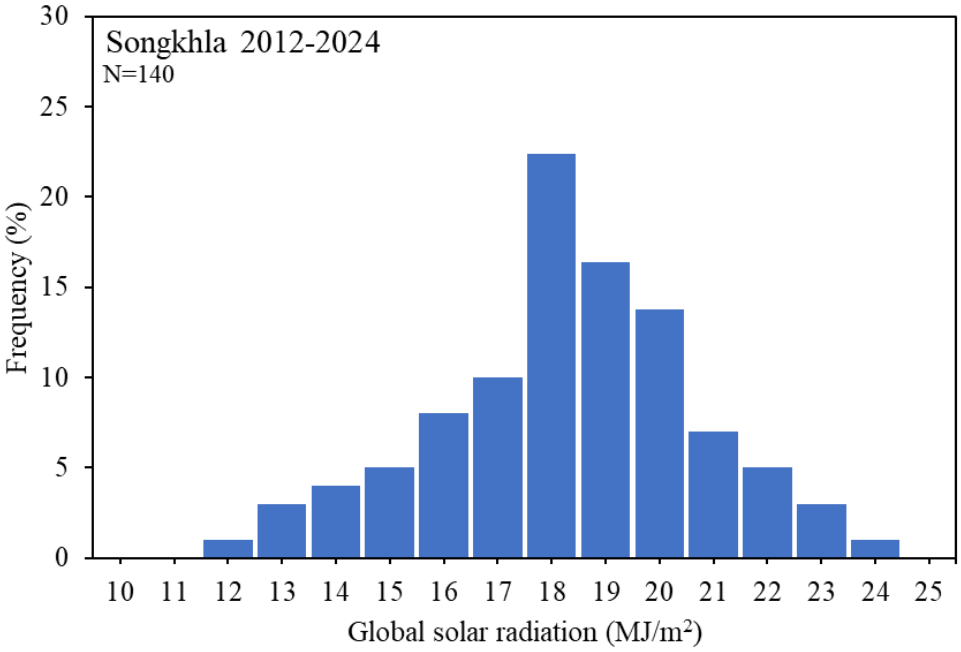


Figure 64 The distribution of global solar radiation at Songkhla station.

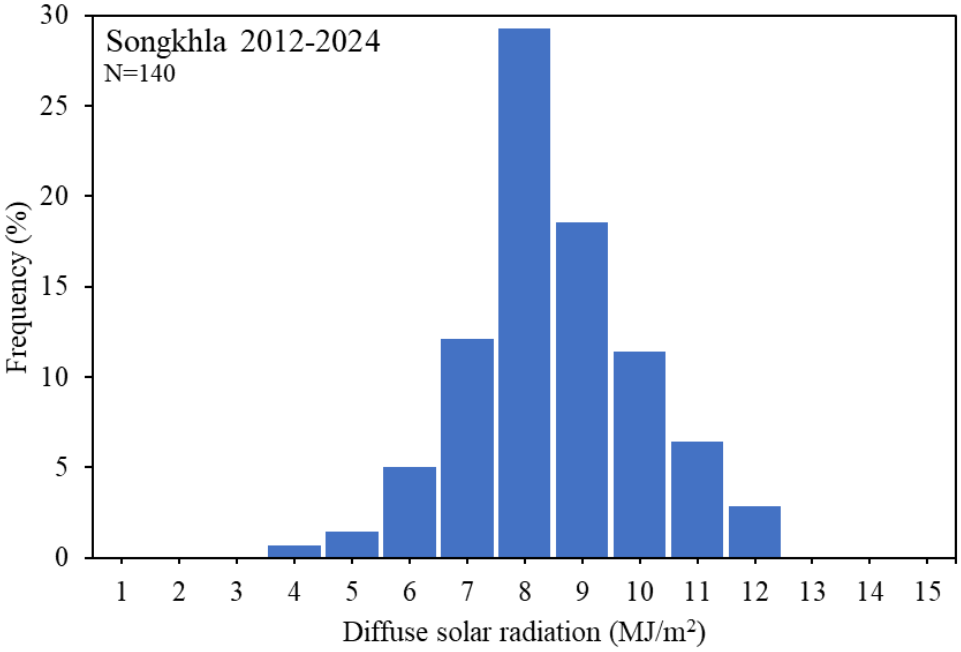


Figure 65 The distribution of diffuse solar radiation at Songkhla station.

The results shown in Figures 58 to 65 indicate that most of the distributions follow a normal distribution pattern. The global solar radiation generally shows the highest frequency around 17–18 MJ/m², while diffuse solar radiation peaks at approximately 8 MJ/m². However, Chiang Mai station shows a different, the peak

frequency of global solar radiation is slightly lower, around 16 MJ/m², and the diffuse solar radiation shows a higher peak at about 10 MJ/m². This difference may be due to the high amount of aerosols in the Chiang Mai area.

3.1.1.2 Atmospheric data

In this study, atmospheric parameters are collected from two sources of ground-based measurements. The dataset includes a total of seven variables: aerosol optical depth (AOD), precipitable water, total ozone column, cloud cover, air temperature, relative humidity, and wind speed. The data were collected from the same stations during the period 2012–2024 and 2024 only for Indirect-measurement stations.

The first source is Thai Meteorological Department (TMD), the national authority responsible for meteorological, climatological, and atmospheric observations and services in Thailand. TMD provides weather forecasts, warnings, and climate-related data for public safety, agricultural planning, and environmental research. The department manages a nationwide network of meteorological stations and operates observational tools such as weather radars, satellites, and solar radiation monitoring instruments. In this work, four parameters provided by TMD including cloud cover, air temperature, relative humidity, and wind speed are used.

TMD uses a traditional and widely accepted method to measure cloud cover at ground-based stations. Human observers visually estimate the fraction of the sky covered by clouds using the naked eye. The observations are recorded on a scale from 0 to 10, where 0 represents a completely clear sky and 10 indicates a fully overcast sky. These observations are typically made every hour during daylight.

The air temperature and relative humidity was measured by psychrometer as shown in the Figure 66.

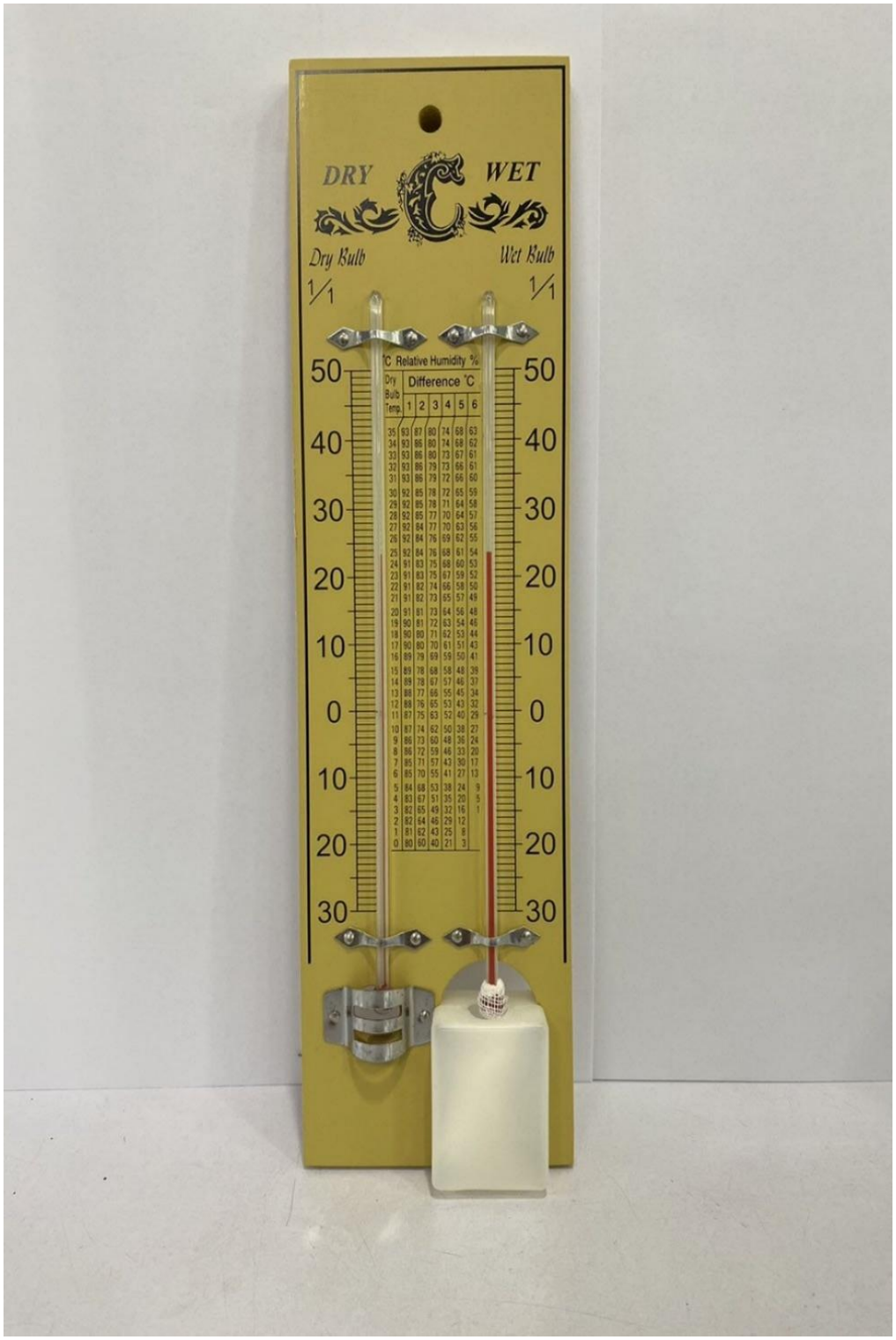


Figure 66 Psychrometer, dry-bulb thermometer (left), relative humidity table (mid), and wet-bulb thermometer (right). (Earth Science Stack Exchange, 2021).

The wind speed was measured by a cup anemometer as shown in Figure 67.



Figure 67 Cup anemometer used for measuring the wind speed. (Munro Instruments, 2024).

The second source is AERONET (AErosol RObotic NETwork), a ground-based network that measures atmospheric aerosol properties using remote sensing techniques. It was established by NASA in collaboration with PHOTONS. The measurements are conducted using the CIMEL Electronique Model 318A Sun photometer designed to observe the spectral direct solar radiation. These instruments are installed at various locations around the world as shown in Figure 68. Data from these stations can be accessed and downloaded from the website https://aeronet.gsfc.nasa.gov. The data collected can be used to analyze the characteristics of atmospheric constituents.



Figure 68 AERONET Monitoring Stations around the world.
(https://aeronet.gsfc.nasa.gov/, 2025).

In this study, Sun photometers were also installed at the main stations, which include Chiang Mai, Nakhon Pathom, Ubon Ratchathani, and Songkhla. The Sun photometers at these stations are shown in Figures 69 to 72, respectively. This work compiles hourly atmospheric parameter data from the AERONET network focusing on three variables: aerosol optical depth (AOD) at a wavelength of 500 nm, representing the concentration of aerosols that most strongly affect visible light, precipitable water, and the total ozone column, which represents the amount of ozone accumulated in the atmospheric column.



Figure 69 Sun photometer at Chiang Mai station.



Figure 70 Sun photometer at Nakhon Pathom station.



Figure 71 Sun photometer at Ubon Ratchathani station.



Figure 72 Sun photometer at Songkhla station.

3.1.2 Satellite-based data

This study uses satellite-based data on atmospheric parameters that affect the solar radiation. Satellite remote sensing is especially useful because it can cover large areas, which is important in places where ground measurements are limited or unavailable. The selected parameters include global solar radiation, aerosol optical depth, precipitable water, total ozone column, cloud cover, air temperature, relative humidity, and wind speed. Each dataset is described in the following sections, along with its role and justification for delivering in the diffuse solar radiation modeling framework. The details of the satellite data are shown in Table 2.

Table 2 Description of satellite-derived datasets and their corresponding ground parameters.

Satellite parameter	Ground parameter	Source	Resolution	Interval	Period
Downward shortwave radiation	Global solar radiation	MODIS MCD18A1	5 km	3-hourly	2012–2024
Aerosol optical depth	Aerosol optical depth	MODIS MYD08_M3	1°×1°	Monthly	2012–2024
Precipitable water	Precipitable water	MODIS MYD08_M3	1°×1°	Monthly	2012–2024
Total ozone column	Total ozone column	MODIS MYD08_M3	1°×1°	Monthly	2012–2024
Cloud fraction	Cloud cover	MODIS MYD08_M3	1°×1°	Monthly	2012–2024
Air temperature	Air temperature	NCEP/NCAR	2.5°×2.5°	Monthly	2012–2024
Relative humidity	Relative humidity	NCEP/NCAR	2.5°×2.5°	Monthly	2012–2024
Wind speed	Wind speed	CCMP V2.1	0.25°×0.25°	Monthly	2012–2024
Extraterrestrial radiation	Extraterrestrial radiation	Calculation	0.01°×0.01°	Monthly	2012–2024
Diffuse solar radiation	Diffuse solar radiation	Model (result)	0.01°×0.01°	Monthly	2023–2024

The downward shortwave radiation dataset used in this study was obtained from the MODIS in product code MCD18A1, which provides the surface solar irradiance derived from satellite observations and radiative transfer models. This product offers 3-hourly data of shortwave radiation expressed in units of W/m² at a 5 km spatial resolution. The MCD18A1 product represents all downward solar radiation in the range of 300 to 4000 nm including both direct and diffuse components. However, since most of the global solar radiation is typically measured in the range of 300 to 3000 nm, the MCD18A1 shortwave radiation is considered a suitable and reliable proxy for the global solar radiation in this study. Furthermore, the downward shortwave radiation from MCD18A1 was validated against ground-level global solar radiation measurements from Baseline Surface Radiation Network (BSRN) sites, (Liang & Wang, 2017; Wang et al., 2020). Therefore, the MCD18A1 downward

shortwave radiation are used as the satellite-derived global solar radiation input for the diffuse fraction modeling.

The next product from the MODIS is product code MYD08_M3, which is a monthly Level 3 atmospheric dataset collected by the Aqua satellite. It provides a 1°×1° spatial resolution and is averaged to monthly data. For this investigation, four parameters from this product were chosen: aerosol optical depth, total ozone column, water vapor, and cloud fraction. Satellite-derived atmospheric parameters have shown good agreement with ground-based observations. Aerosol optical depth (AOD) was validated using Sunphotometer measurements (Antuña-Marrero et al., 2018; Schaap et al., 2008; Wu et al., 2022), while precipitable water also showed strong consistency with the ground precipitable from Sunphotometer (Holben & Eck, 1990; Prasad & Singh, 2009). Total ozone column was validated by (Bilbao et al., 2014) and (Sharma et al., 2018). and cloud cover was assessed by Fontana et al. (2013) and Werkmeister et al. (2015). The cloud fraction is used as cloud cover, but instead of measuring clouds in the sky from the ground, it shows how much of the Earth's surface is covered by clouds from a satellite view. These selected parameters from the MYD08_M3 dataset are integrated into the model to improve the estimation of the diffuse solar radiation across the study area.

The monthly average Level 4 wind speed at 10 m above ground is provided by the Cross-Calibrated Multi-Platform CCMP, which uses data combined from several satellites (QuikSCAT, ASCAT, WindSat, SSMI/SSMIS) and reanalysis sources. It was created by Remote Sensing Systems (RSS) using a variational analysis technique to generate a global wind field and correct for sensor differences. In this study, the CCMP wind speed is used as surface wind input. The development methodology is detailed following Atlas et al. (2009).

The NCEP/NCAR Reanalysis Project, which integrates historical observations with numerical weather prediction models providing the air temperature and relative humidity used in this investigation. The data were extracted at the 0.995 sigma level representing near-surface conditions and provided as monthly averages with a spatial resolution of 2.5°×2.5°. The accuracy of these variables in the NCEP/NCAR reanalysis has been evaluated in Raziei and Parehkar (2021).

3.2 Diffuse fraction model

After examining the variation patterns and frequency distributions of the diffuse solar radiation at monitoring stations across different regions of Thailand, the researcher developed a model for estimating diffuse solar radiation to generate spatial distribution maps. As a starting point, the relationship between the diffuse fraction and the clearness index was utilized. The diffuse fraction is defined by Equation (46) and the clearness index by Equation (47). Prior to model development, the relationships the diffuse fraction and clearness index for at each station is shown in Figure 73–76.

$$\overline{K}_D = \frac{\overline{H}_D}{\overline{H}} \tag{46}$$

Where $\overline{K}_D$ is monthly diffuse fraction (–), $\overline{H}_D$ is monthly average daily diffuse solar radiation (MJ/m^2), and $\overline{H}$ is monthly average daily global solar radiation (MJ/m^2).

$$\overline{K}_T = \frac{\overline{H}}{\overline{H}_0} \tag{47}$$

Where $\overline{K}_T$ is monthly clearness index (–), $\overline{H}_0$ is monthly average daily extraterrestrial solar radiation (MJ/m^2).

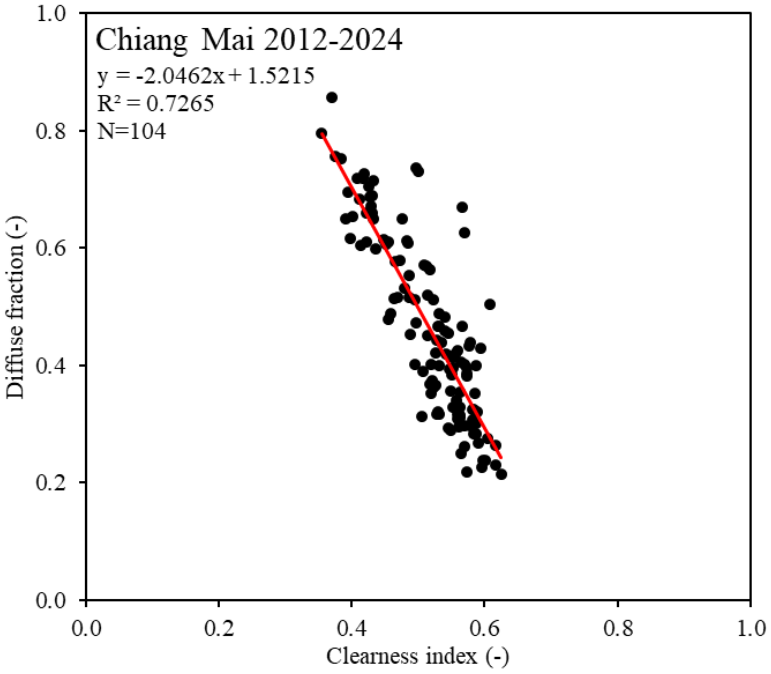


Figure 73 The relationship between diffuse fraction and clearness index at Chiang Mai station.

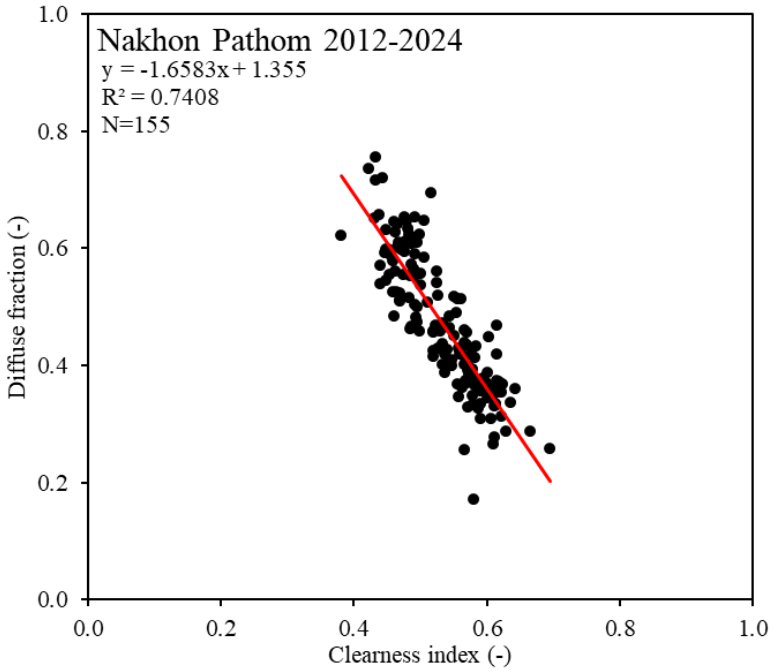


Figure 74 The relationship between diffuse fraction and clearness index at Nakhon Pathom station.

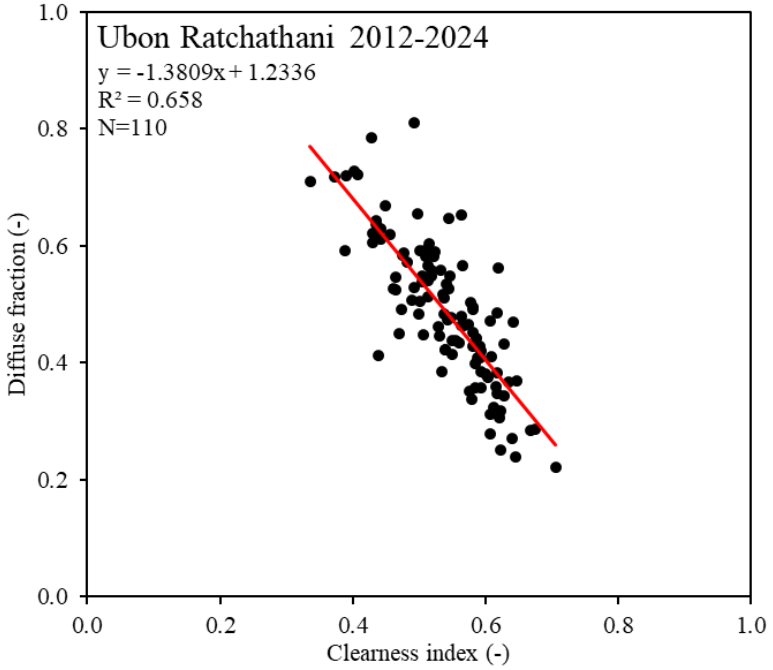


Figure 75 The relationship between diffuse fraction and clearness index at Ubon Ratchathani station.

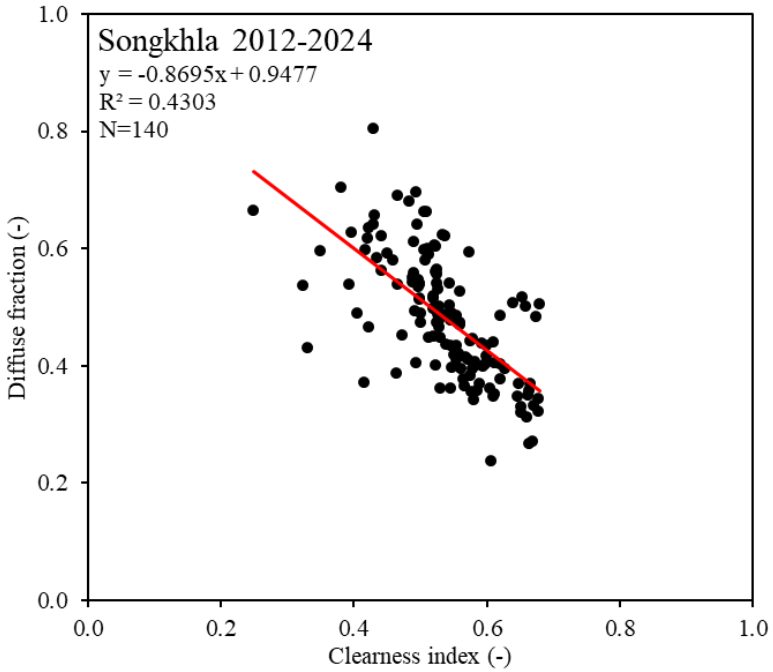


Figure 76 The relationship between diffuse fraction and clearness index at Songkhla station.

The results from the Figures 73–76 show the perfect identity of the relationship between diffuse fraction and clearness index.

3.2.1 Atmospheric parameter preparation and selection

This study aims to develop a model for estimating diffuse solar radiation, with the goal of applying the model to generate diffuse radiation maps over Thailand. The model is primarily designed to utilize satellite-based parameters to generate spatial maps in subsequent stages. However, satellite-derived and ground-based parameters often differ due to variations in measuring techniques and observational perspectives. After collecting atmospheric parameters from both ground-based stations and satellite observations, a comparative analysis between satellite-based and ground-based data are shown in Figures 77–84.

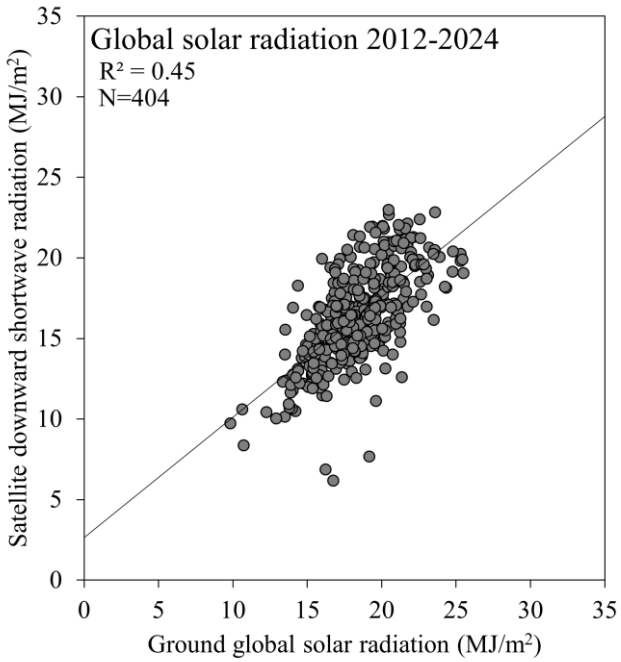


Figure 77 Comparison of ground-based global solar radiation and MODIS downward shortwave solar radiation.

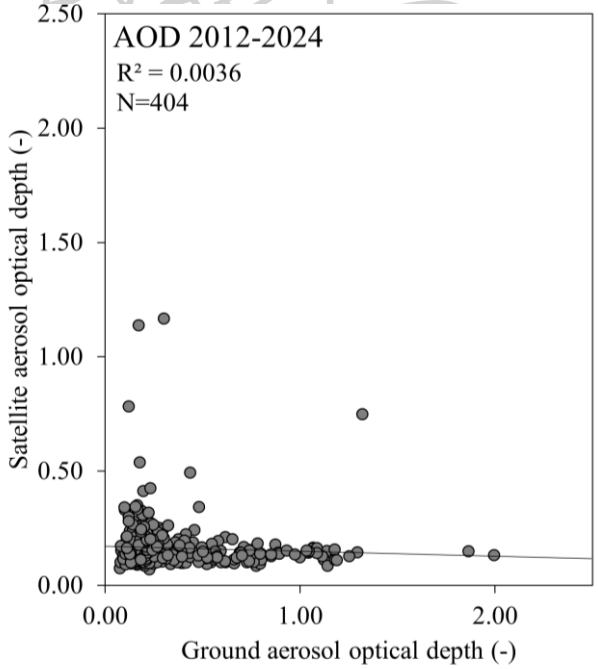


Figure 78 Comparison of AERONET aerosol optical depth and MODIS aerosol optical depth.

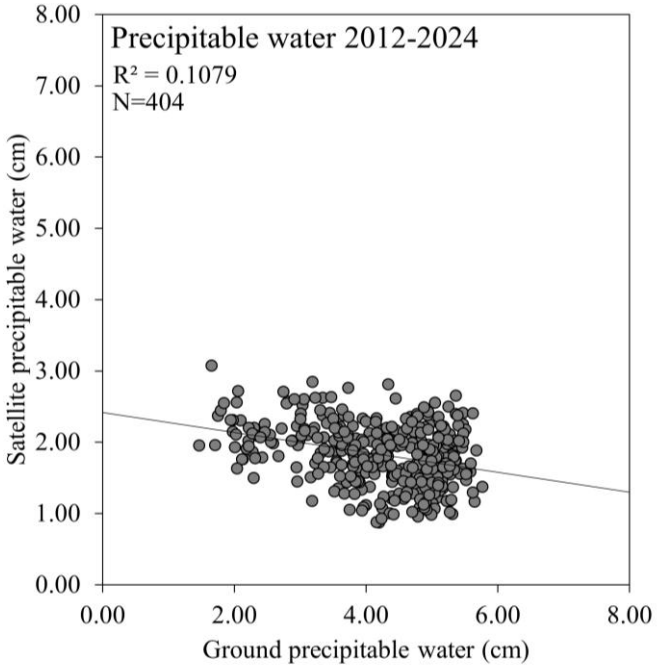


Figure 79 Comparison of AERONET precipitable water and MODIS precipitable water.

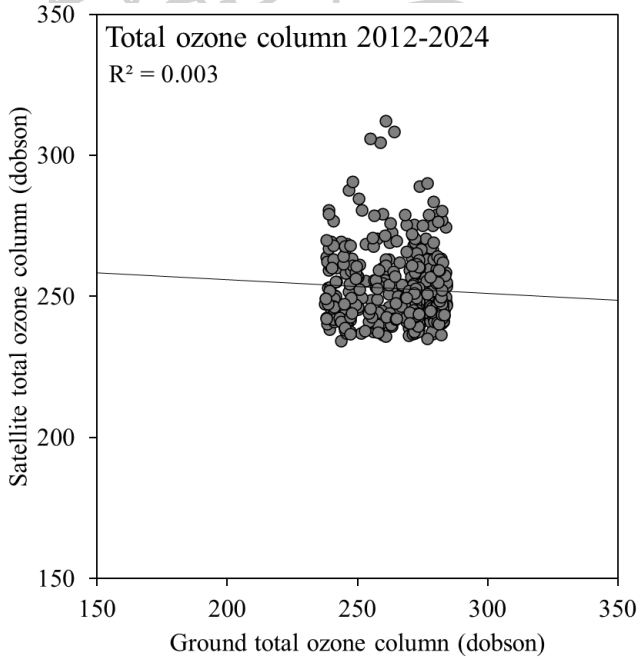


Figure 80 Comparison of AERONET total ozone column and MODIS total ozone column.

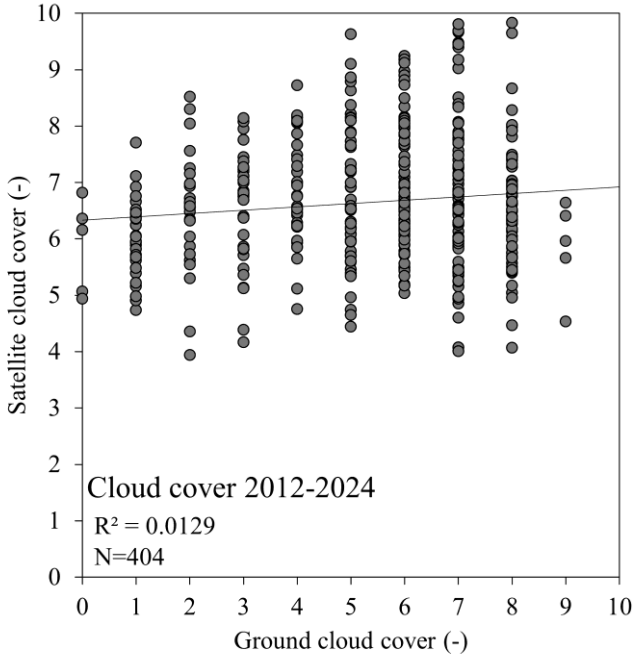


Figure 81 Comparison of TMD cloud cover and MODIS cloud fraction.

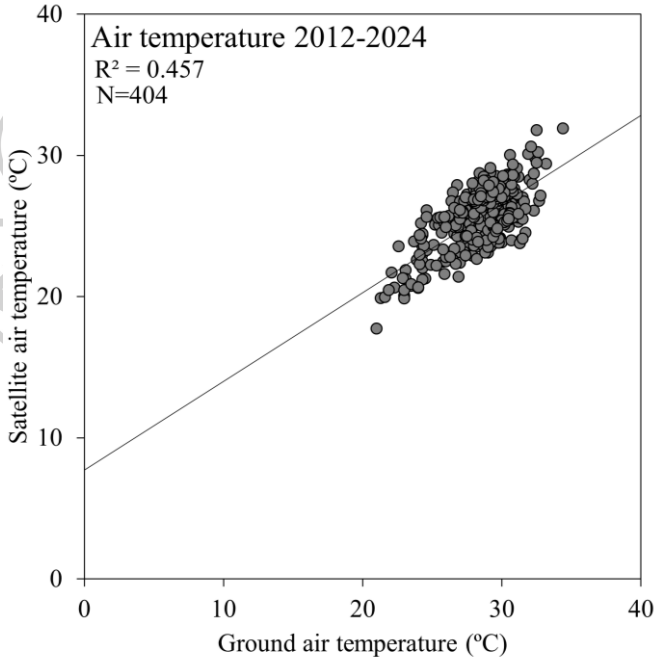


Figure 82 Comparison of TMD air temperature and NCEP/NCAR air temperature.

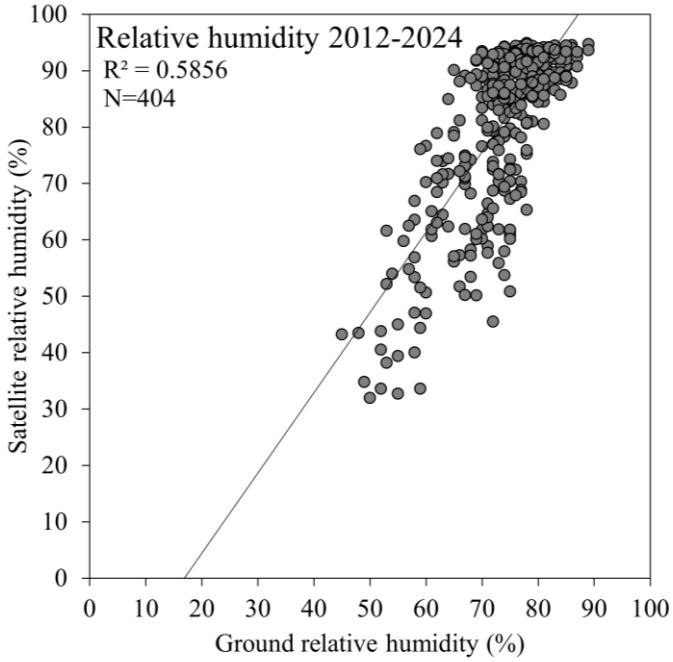


Figure 83 Comparison of TMD relative humidity and NCEP/NCAR relative humidity.

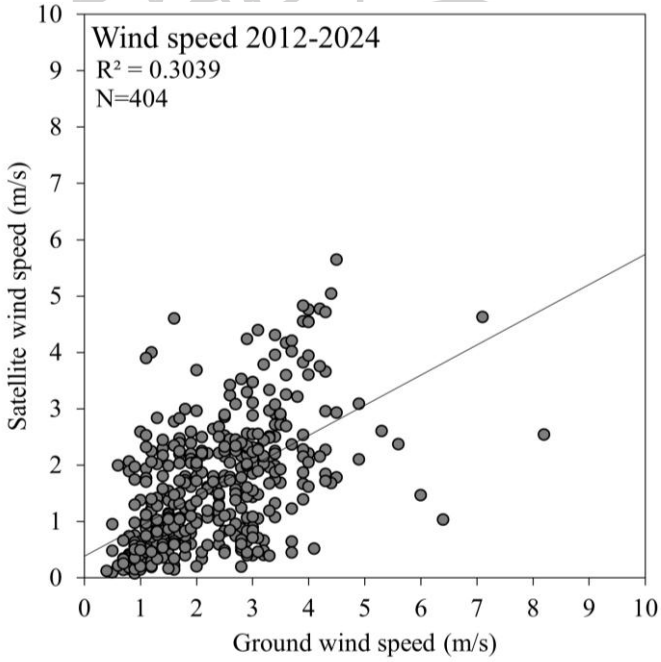


Figure 84 Comparison of TMD wind speed and NCEP/NCAR wind speed.

From the Figures 77–84, it is evident that several atmospheric parameters derived from satellite observations differ significantly from those obtained through ground-based measurements. These errors are reflected in the wide data dispersion and the lack of alignment observed in the comparison graphs. Therefore, prior to

using satellite-derived data for modeling, it is necessary to apply the correction to align them with ground-based observations.

To address the discrepancy between satellite-derived and ground-based data, the Quantile Mapping (QM) method was applied. QM is a statistical bias correction technique that adjusts the distribution of satellite-based measurements so that they closely match the distribution corresponding to ground-based observations. Unlike simpler correction methods that only shift the mean, QM corrects the entire distribution including the variance and skewness of the distribution curve. The core principle of QM is to use the cumulative distribution functions (CDFs) of the two datasets. Let $F_{sat}(x)$ is the CDF of the satellite data, $F_{obs}^{-1}(p)$ is the inverse CDF (quantile function) of the ground-based data, p is a result of $F_{sat}(x)$ function in the probability. For each satellite observation x , the corrected value x_{qm} is given by equation (48).

$$x_{qm} = F_{obs}^{-1}\left(F_{sat}(x)\right) \tag{48}$$

This equation means that the percentile rank (quantile) of the satellite value x is first determined using its own CDF and then the corresponding ground-based value is obtained by looking up that quantile in the inverse CDF of the ground data.

This approach is particularly powerful when systematic differences exist between the two datasets due to difference measurement techniques, atmospheric penetration depths, or temporal/spatial resolutions. The corrected results showed in the Figures 85–92.

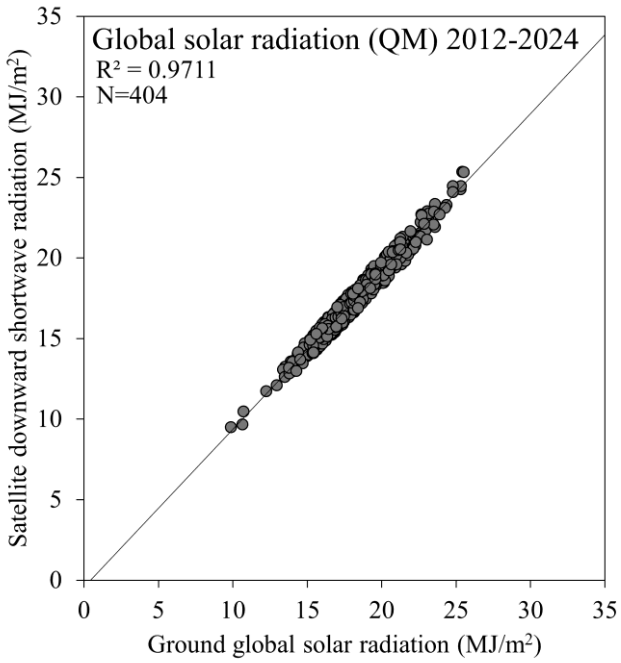


Figure 85 Comparison of ground-based global solar radiation and MODIS downward shortwave solar radiation after applying quantile mapping.

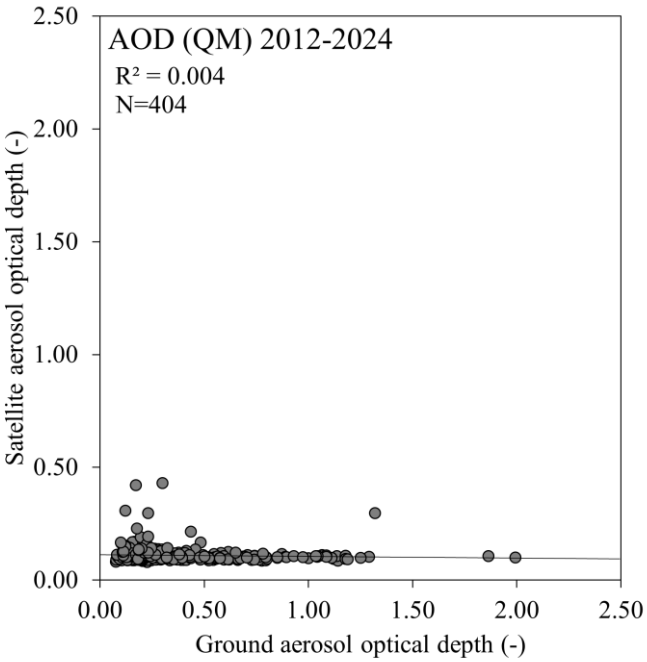


Figure 86 Comparison of AERONET aerosol optical depth and MODIS aerosol optical depth after applying quantile mapping.

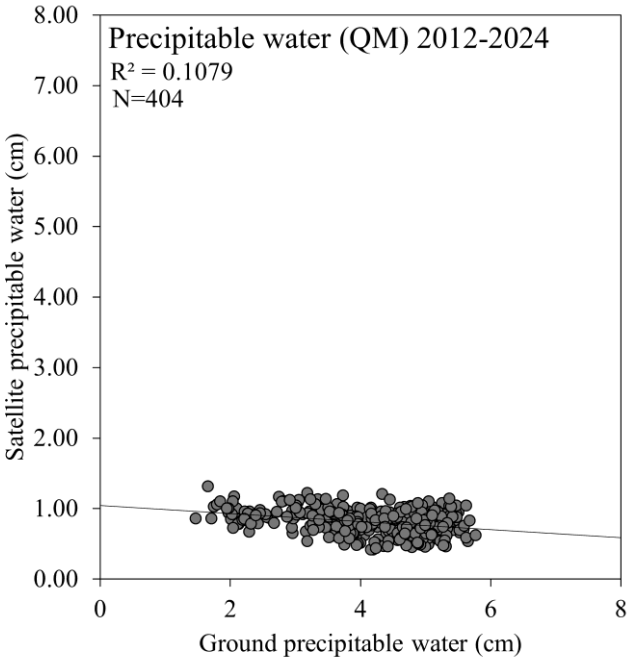


Figure 87 Comparison of AERONET precipitable water and MODIS precipitable water after applying quantile mapping.

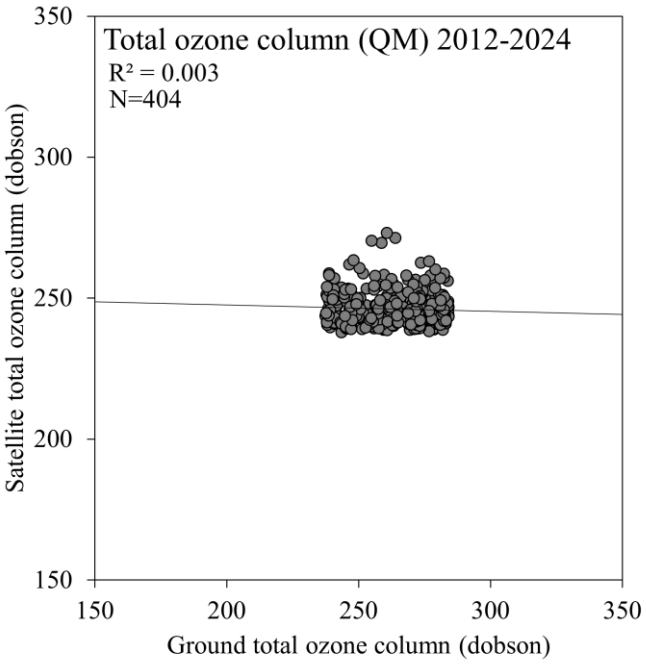


Figure 88 Comparison of AERONET total ozone column and MODIS total ozone column after applying quantile mapping.

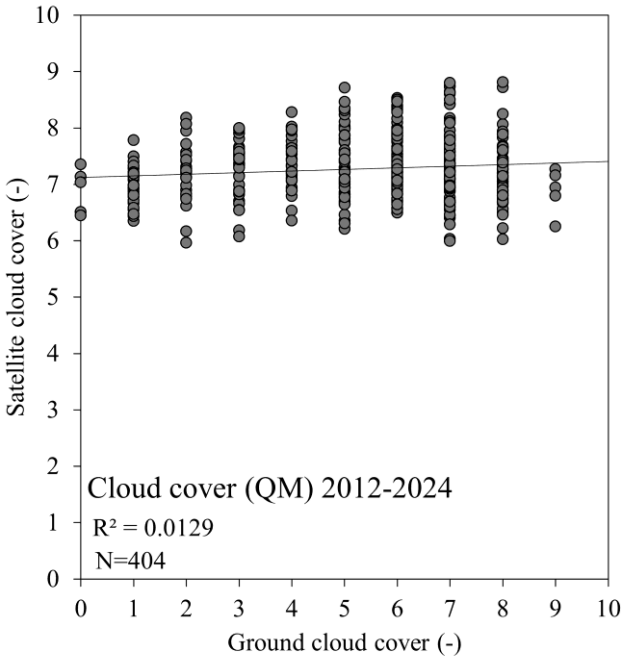


Figure 89 Comparison of TMD cloud cover and MODIS cloud fraction after applying quantile mapping.

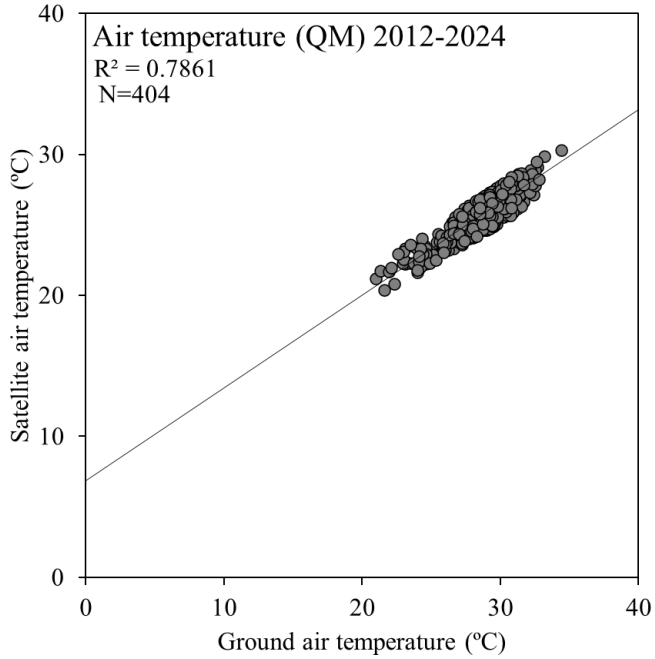


Figure 90 Comparison of TMD air temperature and NCEP/NCAR air temperature after applying quantile mapping.

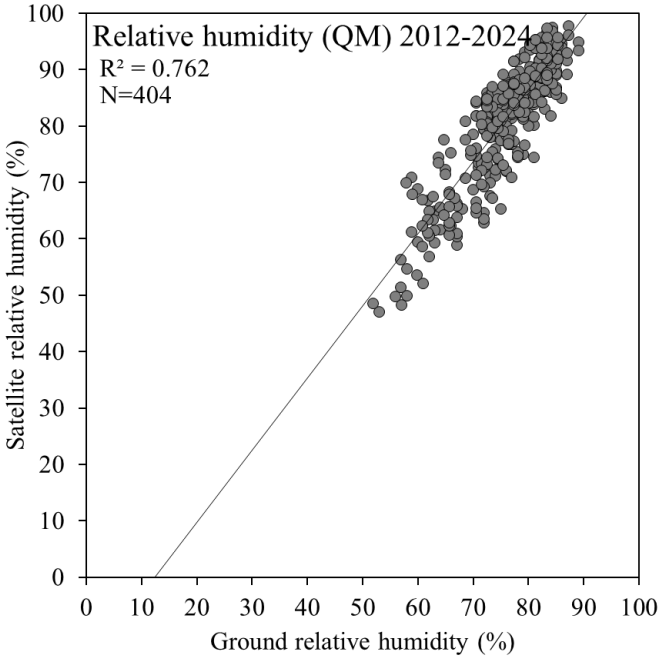


Figure 91 Comparison of TMD relative humidity and NCEP/NCAR relative humidity after applying quantile mapping.

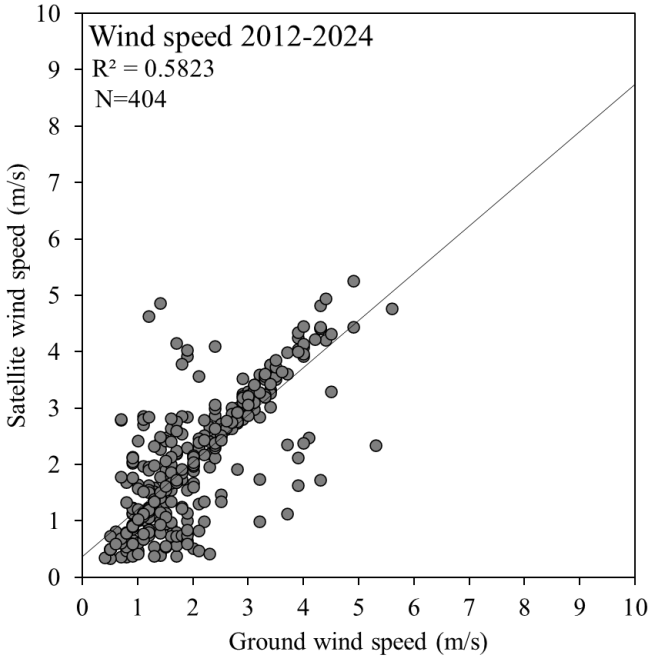


Figure 92 Comparison of TMD wind speed and NCEP/NCAR wind speed after applying quantile mapping.

Figures 85–92 present the results after applying the Quantile Mapping method, demonstrating improved data quality and greater reliability.

3.2.2 Evaluation of atmospheric parameters for model selection

After collecting and adjusting the satellite-derived data using the Quantile Mapping (QM) method, the development of a diffuse fraction model based on the clearness index can be further improved by combining relevant atmospheric parameters. In this study, the influence of each parameter is evaluated to determine its suitability for delivering in the baseline model. The outcome of this analysis guides the selection of variables for the satellite-based model ensuring that the final model integrates the most significant inputs to enhance its accuracy and reliability in estimating the diffuse solar radiation.

To determine a significant contribution of atmospheric parameters for obtaining the diffuse fraction, a statistical approach based on the t-statistic and p-value was applied. The t-statistic for each parameter were calculated using the formula from Witte and Witte (2017) expressed in Equation (49).

$$t_i = \frac{\hat{\beta}_i}{SE(\hat{\beta}_i)} \tag{49}$$

Where t_i is the t-statistic value, $\hat{\beta}_i$ is the estimated regression coefficient and $SE(\hat{\beta}_i)$ is its standard error. A high absolute t-value indicates a stronger relationship between the parameter and the diffuse fraction.

In addition, the p-value was computed to assess the statistical significance of each parameter. It represents the probability of observing a t-statistic as extreme as the one calculated, assuming the null hypothesis $H_0: \beta_i = 0$ is true. The p-value is calculated from the t-distribution using Moore et al. (2009).

$$p - values = 2 \cdot P(T > |t_i|) \tag{50}$$

For this study, the critical t-value at a 95% confidence level (α = 0.05, two-tailed) is approximately 1.96. Therefore, any parameter with an absolute t-statistic greater than 1.96 or a p-value less than 0.05 is considered statistically significant. The results of the t-statistic and p-values are presented in Table 3.

Table 3 t-statistics and p-values of each atmospheric parameter.

Atmospheric parameters	variable	t-stat	p-value
Clearness index	$\overline{K_T}$	–11.58	0.00
Aerosol optical depth	$\overline{AOD}$	0.89	0.37
Precipitable water	$\overline{w}$	0.05	0.96
Total ozone column	$\overline{O_3}$	–0.30	0.76
Cloud cover	$\overline{CC}$	–0.18	0.86
Air temperature	$\overline{T_a}$	5.30	0.00
Relative humidity	$\overline{RH}$	2.44	0.01
Wind speed	$\overline{ws}$	–1.25	0.21

As shown in Table 3, the t-statistics and p-values indicate that the clearness index, air temperature, and relative humidity passed the test for statistical significance at the 95% confidence level. These variables demonstrated strong relationships with the diffuse fraction and were therefore selected as the core atmospheric parameters to be included in the baseline model for satellite data.

3.2.3 Model development and performance evaluation

Before developing the diffuse fraction model and generating the spatial distribution maps, all atmospheric parameters were normalized to ensure a consistency across the different variables. This step is important because each parameter such as temperature, humidity, or aerosol optical depth, has different units and value ranges. Normalizing the data, usually by adjusting it to have an average of zero and a standard deviation of one, helping a balance of the influence of each parameter in the model. It also improves the accuracy and stability of the model when combining many variables with different scales. Therefore, normalization is a necessary step to support reliable and accurate estimation of the diffuse solar radiation in various regions.

To develop the model, satellite-based data from 2012 to 2022 were used as training dataset, while data from 2023 to 2024 were used as testing dataset. The baseline model was developed using multiple linear regression, cross validation and artificial neuron network method. In addition, non-significant parameters were added step-by-step in the subset selection process to evaluate their influence and optimize the model. After identifying the optimized model, it was compared with models from previous studies to confirm its reliability. The model with the most accuracy was applied to generate a monthly diffuse solar radiation map over Thailand.

To evaluate models, the accuracy and performance of the model and reliability of the diffuse solar radiation map were evaluated and validated using three statistical indicators, namely the mean bias difference (MBD), the root mean square difference (RMSD), and the index of agreement (IOA).

The MBD shows the bias of the diffuse fraction calculated from the model or diffuse solar radiation gathering from the map to the measurements. A positive value represents an overestimation, and a negative value presents an underestimation. The MBD can be calculated from the formula:

$$MBD = \frac{\left[\frac{1}{N}\sum_{i=1}^{N} E_i - O_i\right]}{\bar{O}} \times 100\% \tag{51}$$

where E_i are the estimated values O_i is the measured value, $\bar{O}$ is the averaged estimated value, and N is the amount of data.

The RMSD performs the deviation of the measurement from the model or map and can be calculated from:

$$RMSD = \frac{\sqrt{\frac{1}{N}\sum_{i=1}^{N}(E_i - O_i)^2}}{\bar{O}} \times 100\% \tag{52}$$

The IOA is used for quantifying the degree of prediction error in models ranging between 0 and 1, where a value of 1 signifies a perfect match between model predictions or map and observed data, while a value of 0 indicates no agreement. The IOA is calculated using the equation below (Willmott, 1981):

$$IOA = 1.0 - \frac{\sum_{i=1}^{N}(E_i - O_i)^2}{\sum_{i=1}^{N}(\,|E_i - \bar{O}| + |E_i - \bar{O}|\,)^2} \tag{53}$$

A multiple linear regression (MLR) is a widely used statistical method for investigating the relationship between a dependent variable and one or more independent variables. In this study, MLR was first applied to develop a baseline model for estimating the diffuse fraction based on the clearness index. This initial model is also referred to simple regression or ordinary least squares (OLS). However, to improve the model's accuracy, additional atmospheric parameters were introduced as predictors. Thus, MLR was used to create an empirical equation relating the diffuse fraction to these parameters, where each parameter has its own coefficient and interception. The coefficients in the MLR model were determined using the OLS method as described by Kutner et al. (2005), resulting in a robust empirical model.

To evaluate the performance of the model, a cross-validation (CV) technique was applied. This approach combines mathematical modeling with machine learning techniques. The data from 2012 to 2024 were split into three subsets: training, validation, and testing. The data from 2012 to 2022 was used for training and validating the model. The data from 2023 to 2024 was reserved for testing.

During the CV process, the modeling dataset was further divided into ten equal subgroups (each containing 10% of the data). In each iteration, 90% of the data was used for training and 10% for validation. This process was repeated ten times with each subgroup used once as a validation set. The model was fine-tuned during these iterations by adjusting its hyperparameters. The final CV model was then tested on the testing dataset. The detail of the cross-validation method described by Irizarry (2019).

In addition, an artificial neural network (ANN) was also employed. ANN is a machine learning algorithm inspired by the structure of biological neural networks. The ANN used in this study consists of three components: an input layer, one or more hidden layers, and an output layer. The input layer receives atmospheric parameters. The hidden layers apply a nonlinear activation function typically the sigmoid function. Each node in the hidden layer computes an output using associated weights and biases. Weights adjust the strength of each input, while biases help fine-tune the output. The output from each node is calculated using Equation (54).

$$y = F\left[\sum_{i=1}^{N} w_i x_i + b\right] \tag{54}$$

where y is the output (monthly average diffuse fraction), x_i is the input (all predictors), w_i is the weight for each predictor, b is the bias, and F is the sigmoid function.

The result is produced in the output layer. The training process begins with a feedforward pass, where input data moves through the network. A backpropagation algorithm is then applied to adjust the weights and biases by minimizing the error between the predicted and actual values using a loss function. This continuous adjustment improves the model's predictive capability over time (Dangeti, 2017).

To assess the impact of different atmospheric parameters on the accuracy of diffuse fraction estimation, multiple linear regression models were constructed using satellite-derived variables. The baseline model (M1) incorporates three statistically significant parameters: clearness index, air temperature, and relative humidity. Additional parameters (aerosol optical depth, precipitable water, total ozone column, cloud cover, and wind speed) were added sequentially to the baseline using a subset selection approach, resulting in extended models up to M32. This method aimed to identify the optimal parameter combination for maximizing model accuracy. Each model configuration was evaluated using three statistical indicators, enabling a comprehensive performance comparison. The statistical developed models and their corresponding metrics are presented in Table 4. The resulting comparisons between the diffuse fraction calculated from the model and that obtained from the measurement for the best model M6 is shown in Figures 93.

Table 4 Summary of regression models (M1–M32) using satellite-derived parameters corresponded to different input variables and evaluation statistics (MBD, RMSD and IOA).

Model ID	Input Variables	MBD (%)	RMSD (%)	IOA
M1	$\overline{K_T}, \overline{T_a}, \overline{RH}$	5.01	15.80	0.920
M2	M1+ $\overline{AOD}$	4.90	15.91	0.913
M3	M1+ $\overline{w}$	5.52	16.46	0.909
M4	M1+ $\overline{O_3}$	6.53	16.60	0.907
M5	M1+ $\overline{CC}$	5.28	16.01	0.913
M6	M1+ $\overline{ws}$	4.71	14.15	0.933
M7	M1+ $\overline{AOD}, \overline{w}$	5.41	16.60	0.913
M8	M1+ $\overline{AOD}, \overline{O_3}$	6.30	16.61	0.913
M9	M1+ $\overline{AOD}, \overline{CC}$	5.17	16.24	0.916
M10	M1+ $\overline{AOD}, \overline{ws}$	4.89	15.74	0.921
M11	M1+ $\overline{w}, \overline{O_3}$	6.77	17.09	0.909
M12	M1+ $\overline{w}, \overline{CC}$	5.60	16.48	0.915
M13	M1+ $\overline{w}, \overline{ws}$	5.54	16.28	0.917
M14	M1+ $\overline{O_3}, \overline{CC}$	6.72	16.79	0.911
M15	M1+ $\overline{O_3}, \overline{ws}$	6.28	16.29	0.916
M16	M1+ $\overline{CC}, \overline{ws}$	5.20	15.78	0.921
M17	M1+ $\overline{AOD}, \overline{w}, \overline{O_3}$	6.52	17.12	0.908
M18	M1+ $\overline{AOD}, \overline{w}, \overline{CC}$	5.48	16.67	0.912
M19	M1+ $\overline{AOD}, \overline{w}, \overline{ws}$	5.40	16.44	0.915
M20	M1+ $\overline{AOD}, \overline{O_3}, \overline{CC}$	6.40	16.87	0.910
M21	M1+ $\overline{AOD}, \overline{O_3}, \overline{ws}$	5.95	16.29	0.916
M22	M1+ $\overline{AOD}, \overline{CC}, \overline{ws}$	5.09	16.02	0.918
M23	M1+ $\overline{w}, \overline{O_3}, \overline{CC}$	6.85	17.12	0.909
M24	M1+ $\overline{w}, \overline{O_3}, \overline{ws}$	6.52	16.79	0.912
M25	M1+ $\overline{w}, \overline{CC}, \overline{ws}$	5.57	16.30	0.917
M26	M1+ $\overline{O_3}, \overline{CC}, \overline{ws}$	6.46	16.48	0.915
M27	M1+ $\overline{AOD}, \overline{w}, \overline{O_3}, \overline{CC}$	6.54	17.19	0.908
M28	M1+ $\overline{AOD}, \overline{w}, \overline{O_3}, \overline{ws}$	6.17	16.81	0.912
M29	M1+ $\overline{AOD}, \overline{w}, \overline{CC}, \overline{ws}$	5.44	16.50	0.915
M30	M1+ $\overline{AOD}, \overline{O_3}, \overline{CC}, \overline{ws}$	6.10	16.55	0.914
M31	M1+ $\overline{w}, \overline{O_3}, \overline{CC}, \overline{ws}$	6.58	16.83	0.912
M32	M1+$\overline{AOD}, \overline{w}, \overline{O_3}, \overline{CC}, \overline{ws}$	6.23	16.89	0.911

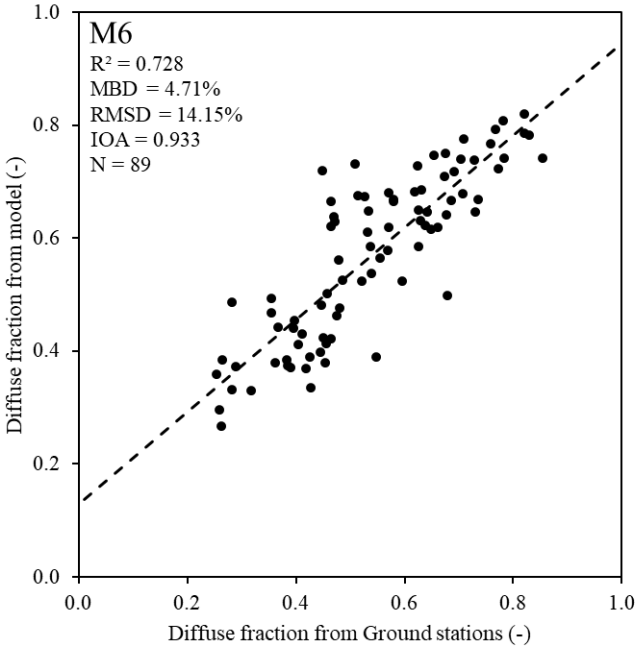


Figure 93 Comparison between observed and estimated diffuse fraction using Model M6.

From Table 4, the performance evaluation of 32 multiple linear regression models (M1–M32) developed using different combinations of satellite atmospheric parameters are presented. The baseline model (M1), which includes a clearness index, air temperature, and relative humidity shows great accuracy with an MBD of 5.01%, RMSD of 15.80%, and IOA of 0.920. Among all models that added a single parameter to the baseline, only M6, which added only wind speed, showed improved performance reducing RMSD to 14.15% and increasing IOA to 0.933. This highlights wind speed as the only parameter with a strong correlation to the diffuse fraction. In contrast, M1–M5 is increased MBD and RMSD with reducing IOA. Especially, the total ozone column (O_3) in model M4 gives the worst result. Furthermore, models that added two or more variables beyond the baseline model do not lead to better accuracy than model M6. Models M10, M13 and M16, which wind speed is the component of this combination, show slightly better results than the baseline model but worse than model M6. Moreover, the performance of all models that add more than two parameters is decreased. That show adding more non-significant parameters may add noise, often resulting in higher RMSD and lower IOA instead of improving model quality.

After identifying Model M6 as the optimal model based on its strong statistical performance, it was further compared with the diffuse fraction models from previous studies. These prior models are empirical and were developed using data from different geographic locations with distinct atmospheric and climatic conditions. In addition to this comparison, the M6 model was also implemented using different modeling approaches: k-fold cross-validation (M6A) and artificial neural networks (ANN) (M6B). The schematic structures of the M6A and M6B models are shown in Figure 94 and 95, respectively.

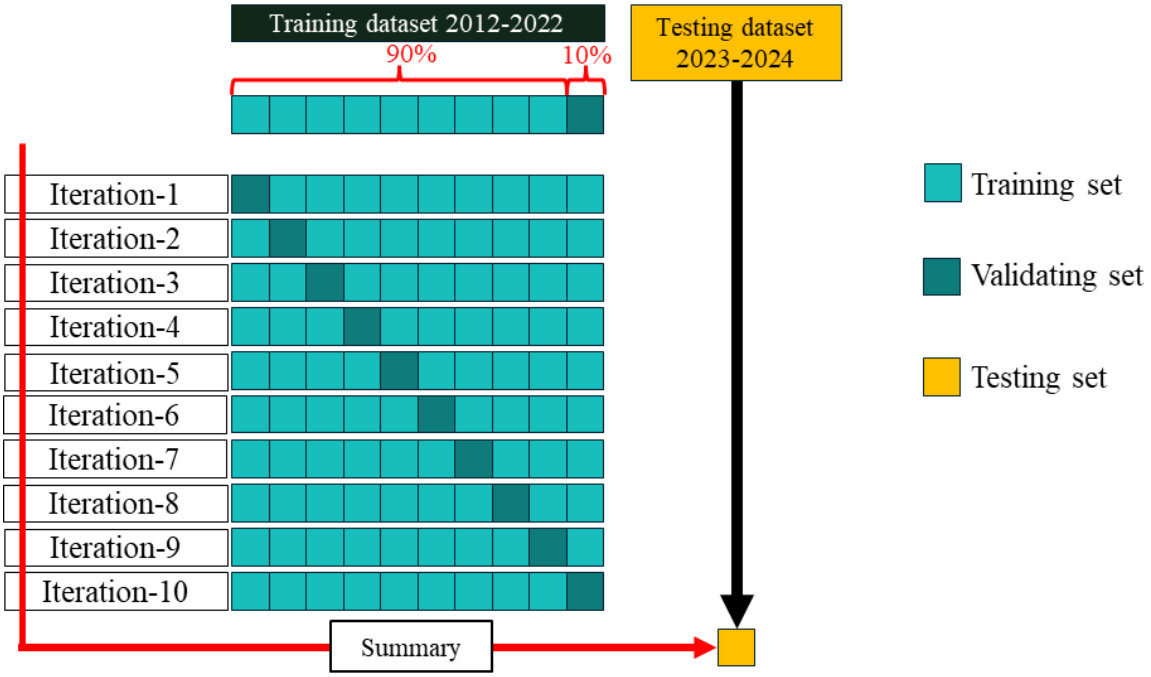


Figure 94 The structure of 10-fold cross-validation model (M6A).

The structure of the k-fold cross-validation used in M6A is illustrated in Figure 94. The dataset from 2012 to 2022 was divided into ten equal subsets. In each iteration, one subset was used as the validation set, and the remaining nine subsets were used for training. This process was repeated for ten iterations, and the results were averaged to ensure model reliability. The independent dataset from 2023 to 2024 was reserved for final testing.

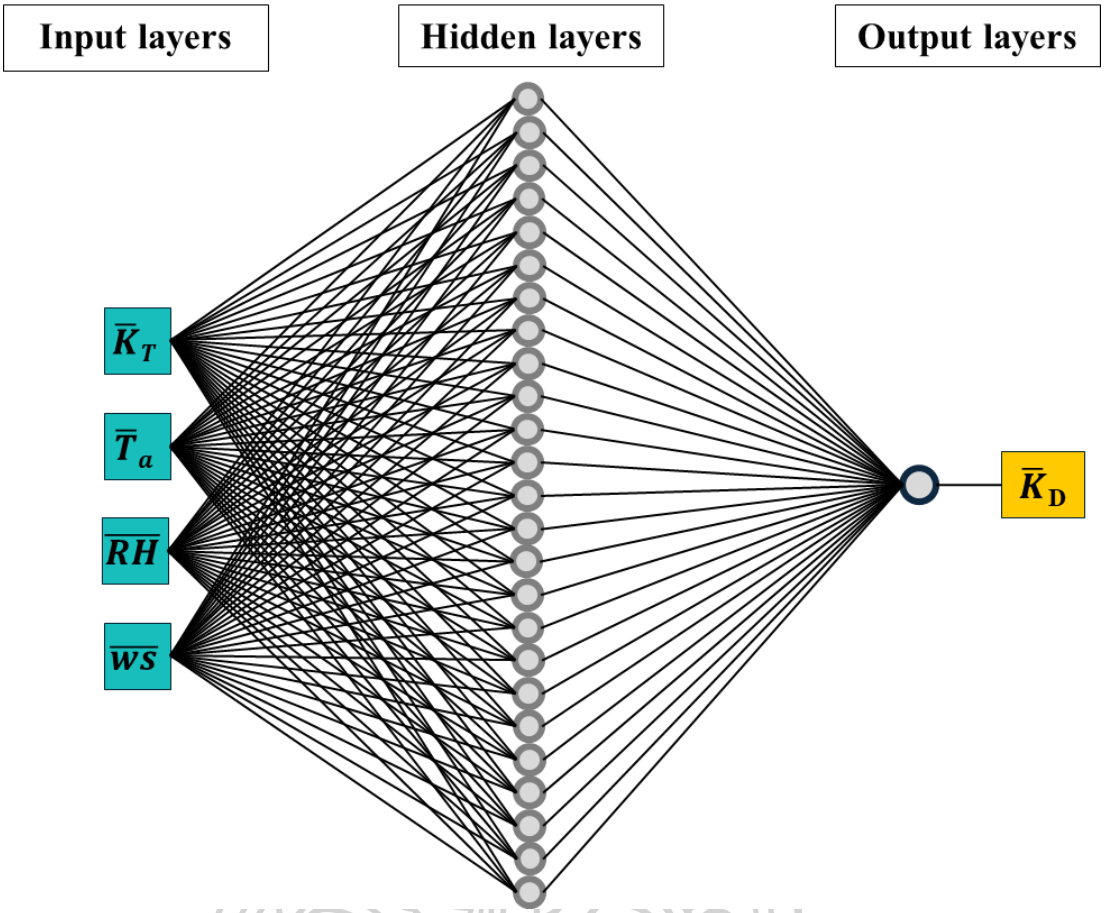


Figure 95 The structure of Artificial neuron network model (M6A).

Figure 95 presents the architecture of the ANN model (M6B), which consists of four input variables such as monthly average clearness index ($\overline{K}_T$), air temperature ($\overline{T}_a$), relative humidity ($\overline{RH}$), and wind speed ($\overline{ws}$) are connected to a single hidden layer comprising 25 neurons. The output layer provides the predicted monthly average daily diffuse fraction ($\overline{K}_D$). The network was trained using supervised learning by minimizing the prediction error between observed and predicted values.

To ensure a fair comparison, all models were evaluated using the same dataset from Thailand encompassing the period of 2012–2022 used for training and 2023–2024 used for testing. The model performance was assessed using the same three statistical indicators: MBD, RMSD and IOA. The results of this comparison are presented in Table 5.

Table 5 Performance comparison of diffuse fraction models with previous studies and different methods.

Model ID	Model's formula	Reference	MBD (%)	RMSD (%)	IOA
O1	$\overline{K}_D = a_0 + a_1\overline{K}_T$	Oliveira et al. 2002 and EI-Sebaii and Trabea. 2003	6.56	16.62	0.905
O2	$\overline{K}_D = a_0 + a_1\overline{K}_T + a_2\overline{K}_T^2$	Barbaro et al. 1981	6.48	16.63	0.906
O3	$\overline{K}_D = a_0 + a_1\overline{K}_T + a_2\overline{K}_T^2 + a_3\overline{K}_T^3$	Ulgen and Hepbasli 2009	6.38	16.42	0.907
O4	$\overline{K}_D = a_0 + a_1\overline{K}_T + a_2\overline{K}_T^2 + a_3\overline{K}_T^3 + a_4\overline{K}_T^4$	Bamiro 1983	6.15	16.34	0.907
O5	$\overline{K}_D = a_0 + \exp(a_1\overline{K}_T)$	Lealea and Tchinda 2013	7.98	20.77	0.752
O6	$\overline{K}_D = a_0\exp(a_1\overline{K}_T)$	Boukelia et al. 2014	6.85	18.05	0.883
O7	$\overline{K}_D = a_0 + a_1 log\overline{K}_T)$	Bailek et al. 2018	6.46	16.49	0.907
O8	$\overline{K}_D = \log(a_0 + a_1\overline{K}_T)$	Bailek et al. 2018	6.56	16.30	0.905
O9	$\overline{K}_D = \ln(a_0 + a_1\overline{K}_T)$	Lealea and Tchinda 2013	6.45	16.23	0.909
O10	$\overline{K}_D = a_0 + a_1\overline{K}_T + a_2\overline{RH}$	Mubiru and Banda 2007	4.78	15.84	0.920
O11	$\overline{K}_D = a_0 + a_1\overline{K}_T + a_2\overline{T}_a + a_3\overline{RH}$	Li et al. 2011	5.01	15.80	0.920
M6	$\overline{K}_D = a_0 + a_1\overline{K}_T + a_2\overline{T}_a + a_3\overline{RH} + a_4\overline{ws}$	The purposed model	4.71	14.15	0.933
M6A	k-fold cross validation (M6)	The purposed model	2.81	13.49	0.957
M6B	$\overline{K}_D = F[\sum_{i=1}^{N} w_i(\overline{T}_a, \overline{RH}, \overline{ws}) + b$	The purposed model	5.51	13.72	0.946

Table 5 presents a performance comparison between the proposed models developed using different methods (MLR (M6), CV (M6A), and ANN (M6B)) and existing diffuse fraction models from previous studies. Most of the earlier models were based on the relationship between the diffuse fraction and clearness index using linear or polynomial equations. Models O1 to O4 demonstrate moderate accuracy with MBD around 6.0–6.5%, RMSD around 16.5%, and IOA slightly below 0.910. Models O5 to O9 utilized logistic functions. Among these, the exponential models (O5 and O6) perform poorly, while the logarithmic models (O7 to O9) show the performance compared to linear and polynomial models. The multiple linear regression models (O10, O11, and M6), which include additional atmospheric parameters, demonstrate the improved accuracy with MBD under 6%, RMSD under 17%, and IOA above 0.90. Comparatively, models developed using cross-validation (M6A) and ANN (M6B) outperform the standard multiple linear model (M6) highlighting the potential of deep learning to further enhance model accuracy. The resulting plots for the best performance models M6A are shown in Figure 96.

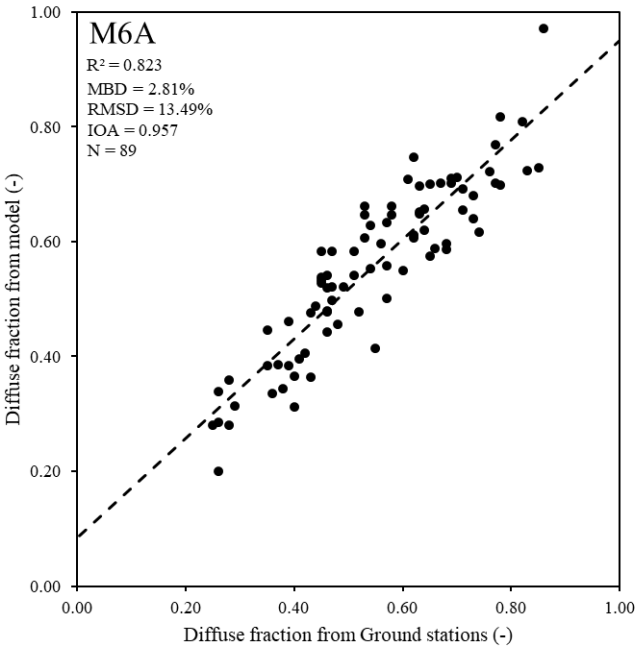


Figure 96 Comparison between observed and estimated diffuse fraction using Model M6A from k-fold cross-validation method.

Based on the comparing results, the k-fold cross-validation model (M6A) demonstrates the highest performance, with the MBD of 2.81%, the RMSD of 13.49%, and the IOA of 0.957. Consequently, this model was selected for generating the diffuse solar radiation map. Therefore, our purpose model in this work is expressed in Equation (55).

$$\overline{K_D} = 0.7742 - 1.5904\overline{K_T} + 0.7427\overline{T_a} + 0.0056\overline{RH} - 0.1756\overline{ws} \quad (55)$$

3.3 Satellite-based diffuse solar radiation map

3.3.1 Preparation of satellite-based data

As shown in Section 3.1.2, the satellite-based datasets used in this study come from various sources and differ in both spatial resolution and temporal intervals. Prior to generating the diffuse solar radiation maps, all datasets were preprocessed to ensure consistency across pixels.

First, this study used Python for all data processing and analysis. Several satellite-based datasets were originally provided as satellite images in various coordinate systems. To ensure consistency, the spatial reference of all datasets was converted to the standard WGS84 (EPSG:4326) system. The satellite image and reprojection image are demonstrated in Figure 97 and 98 respectively.

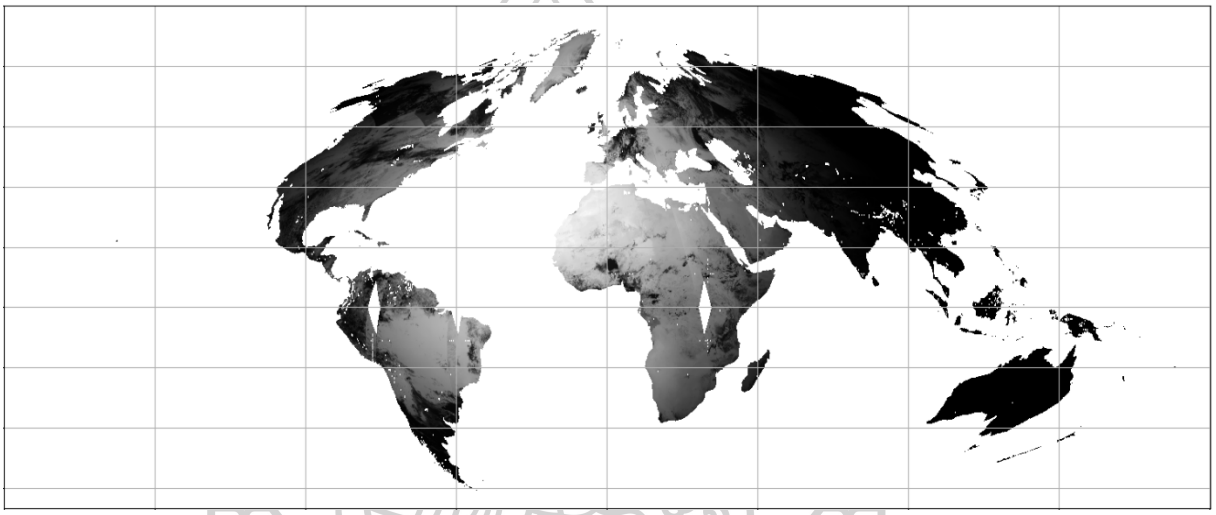


Figure 97 Example of satellite image from MODIS MCD18A1.

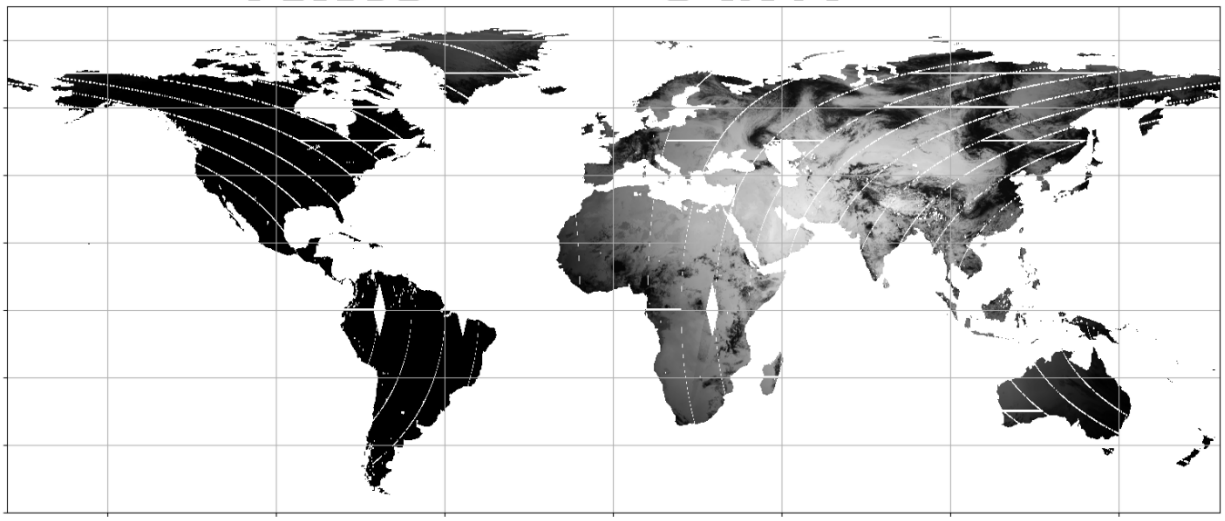


Figure 98 Reprojection image by WGS84 (EPSG:4326) system.

Following the reprojection, the datasets were cropped to specifically focus on a study domain, which covers Thailand between latitudes 5°N and 21°N and longitudes 97°E and 107°E. This reduced the size of the datasets and helped the analysis in the desired area. The cropped map is presented in Figure 99.

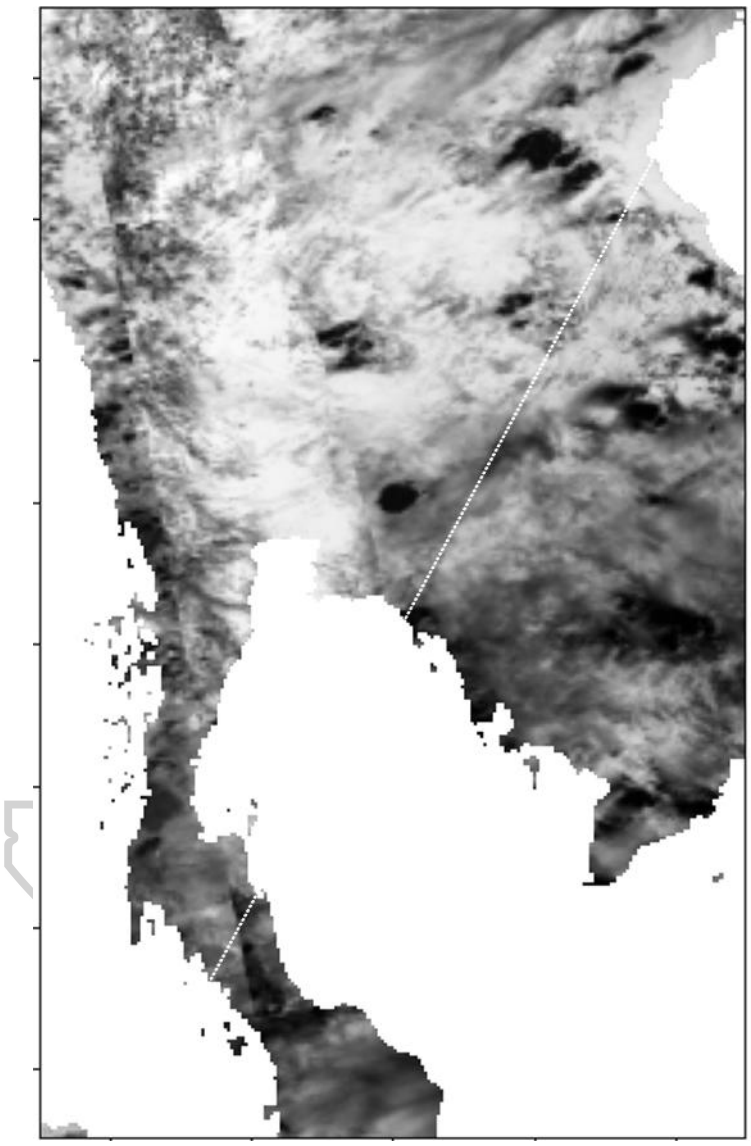


Figure 99 Cropped image of the study domain for this study.

The temporal resolution was standardized to match the 3-hourly intervals with the MODIS downward shortwave radiation data linearly interpolated to hourly values from 00:00 to 23:00. These hourly values were then aggregated into daily totals and subsequently averaged to produce monthly mean daily radiation data for use in the modeling and mapping process. some of the datasets from the satellite contained missing values caused by clouds or limitations from the satellite's orbit. In this work, a nearest neighbor interpolation was applied to fill in the data gaps and maintain spatial completeness. The result of interpolation showed as Figure 100.



Figure 100 Interpolated image for filling the gap of filled the missing data.

After the interpolation, as each satellite product comes with a different native resolution (5km, 2.5º, 1º, 0.25º, 0.01º), the datasets were then resampled to a common grid of 0.01° by 0.01°. The resample satellite image is shown in Figure 101.

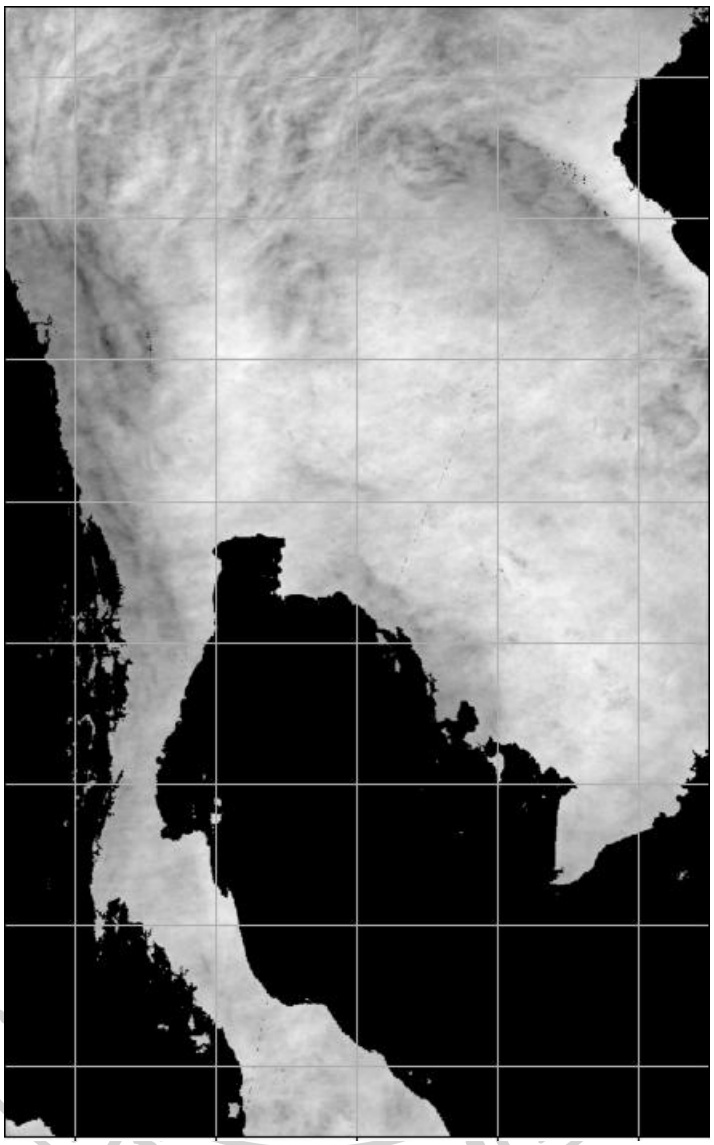


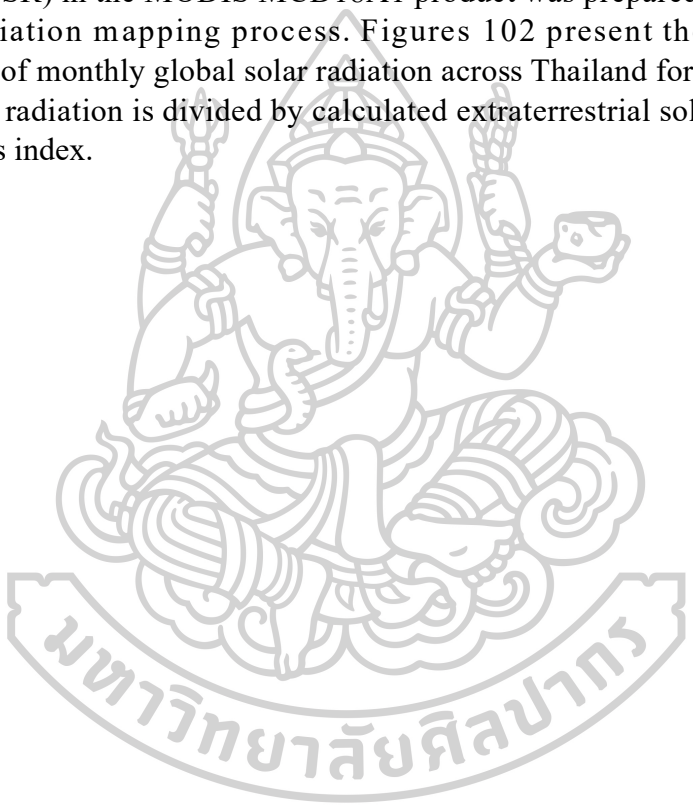
Figure 101 Resampled image with the resolution of 0.01º×0.01º.

After completing these preparation steps (reprojecting, cropping, interpolating, and resampling), the satellite data were ready to be used in the purpose model. Each pixel within the domain contained a full set of standardized atmospheric parameters, which were used to calculate the diffuse fraction and generate monthly diffuse solar radiation maps over Thailand. Finally, the diffuse solar radiation maps were evaluated by comparing the map results with the data from indirect measurement stations. This comparison will confirm the reliability of the estimated diffuse solar radiation.

3.3.2 Mapping diffuse solar radiation

To generate the monthly average daily diffuse solar radiation map, k-fold cross-validation was applied to estimate the monthly average daily diffuse fraction using satellite-derived atmospheric parameters. This diffuse fraction was then multiplied by monthly average daily global solar radiation to calculate the monthly average daily diffuse solar radiation. Before performing the calculations for each pixel, all input atmospheric parameters were preprocessed and standardized. The mapping was conducted over the study domain, covering Thailand (latitude 5° to 21°N and longitude 97° to 107°E) with a spatial resolution of 0.01°×0.01°.

The monthly global solar radiation data derived from downward shortwave radiation (DSR) in the MODIS MCD18A1 product was prepared as an input for the diffuse radiation mapping process. Figures 102 present the example spatial distribution of monthly global solar radiation across Thailand for the year 2024. The global solar radiation is divided by calculated extraterrestrial solar radiation to find the clearness index.



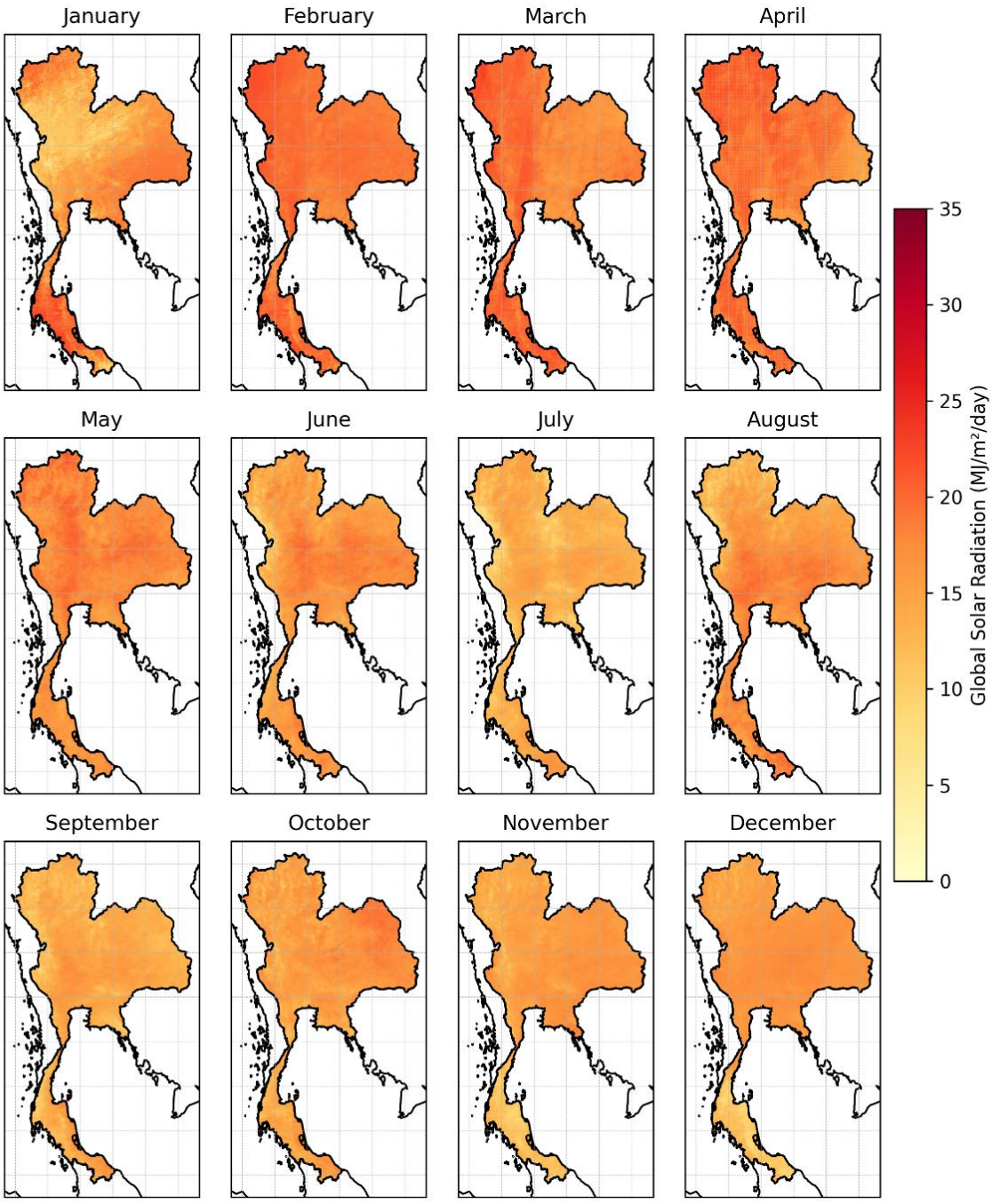


Figure 102 Monthly global solar radiation maps from MODIS for the year 2024.

The first atmospheric parameters, the monthly air temperature data obtained from NCEP/NCAR was prepared as input for the mapping process. Figure 103 present the example spatial distribution of monthly air temperature across Thailand for the year 2024.

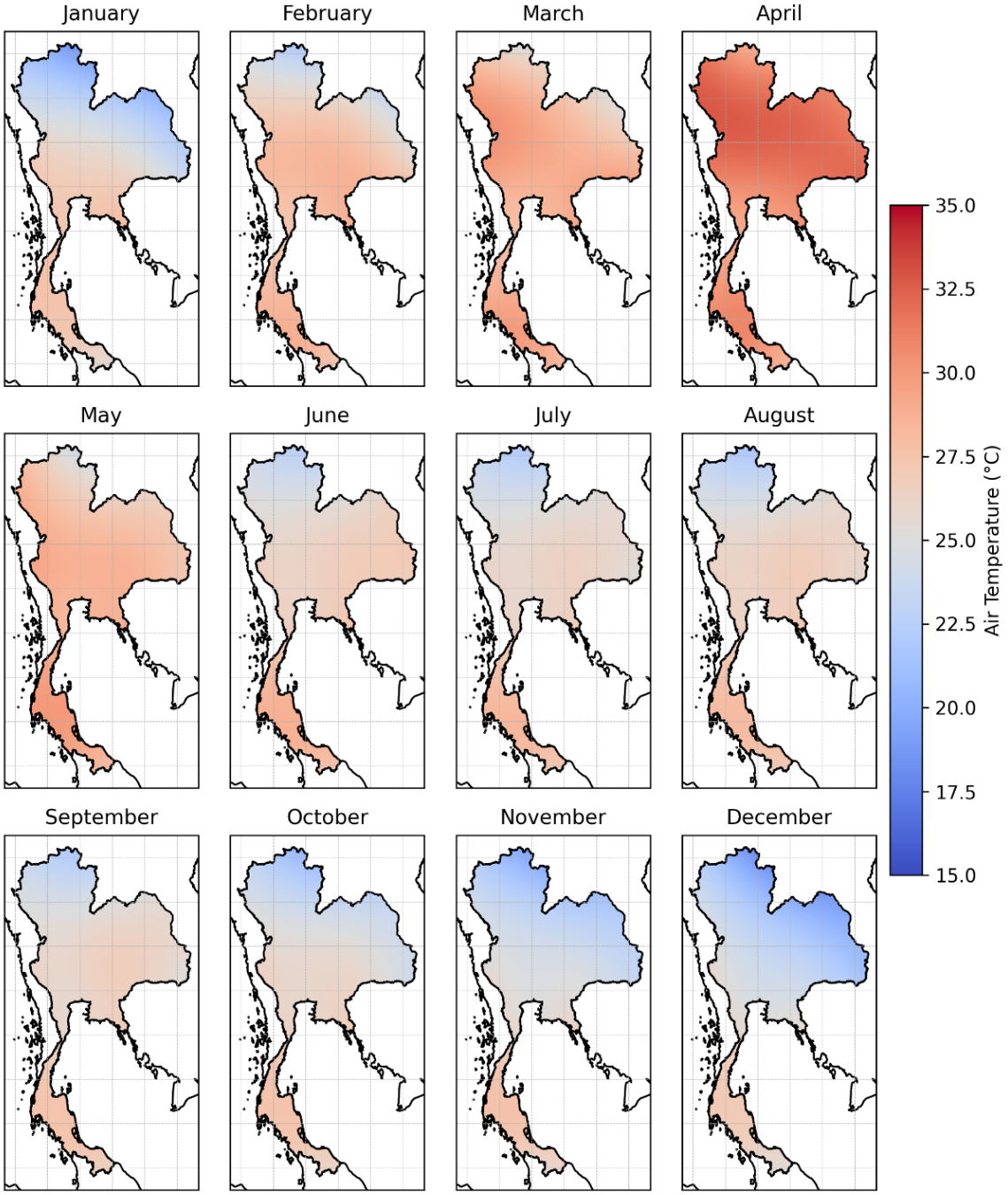


Figure 103 Monthly air temperature maps from NCEP/NCAR for the year 2024.

The monthly average daily relative humidity data from NCEP/NCAR was prepared as inputs for mapping process. Figures 104 present the example spatial distribution of monthly relative humidity across Thailand for the year 2024.

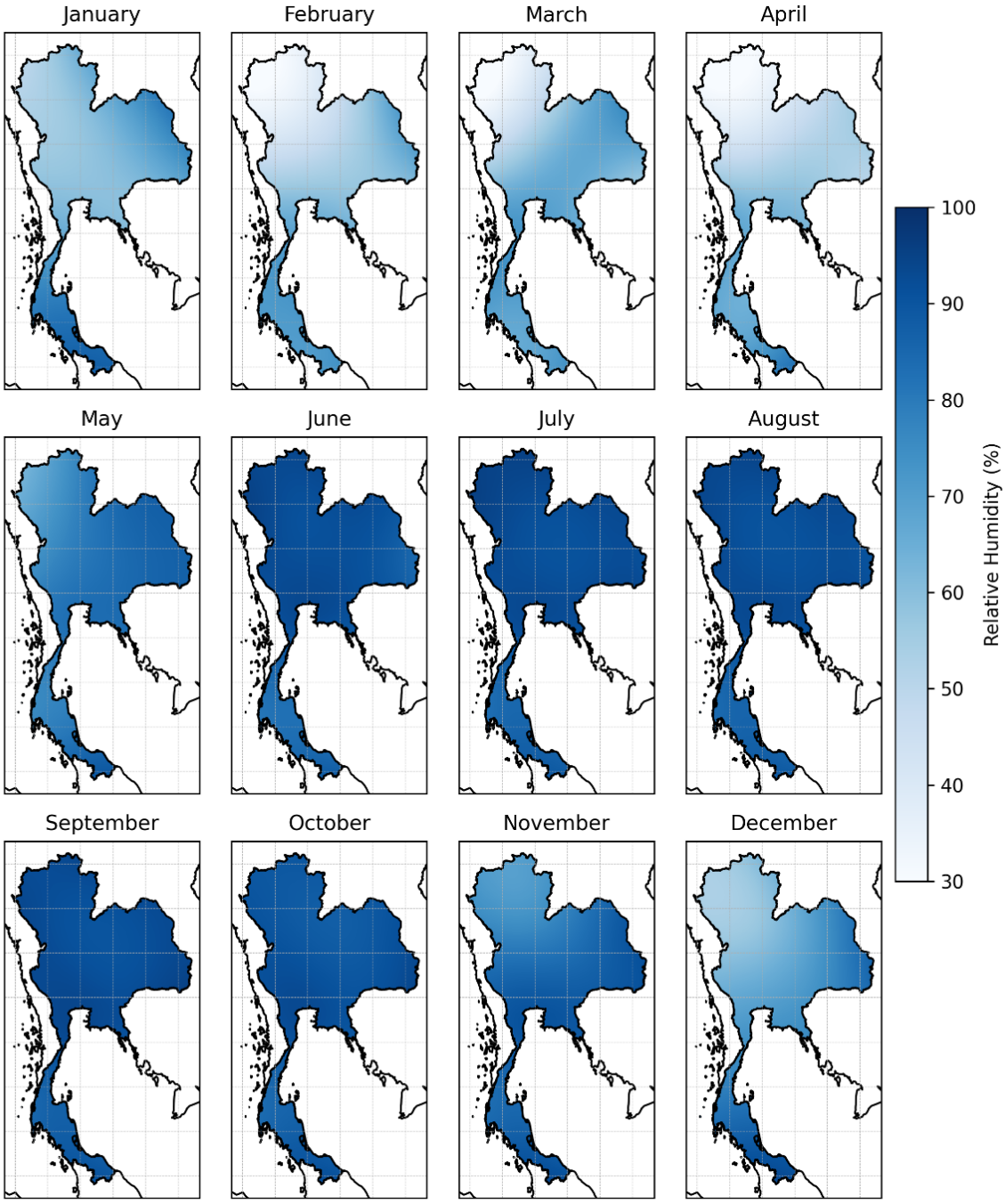


Figure 104 Monthly relative humidity maps from NCEP/NCAR for the year 2024.

The monthly average daily wind speed data from CCMP was prepared as inputs for mapping process. Figures 105 present the example spatial distribution of monthly wind speed and wind direction across Thailand for the year 2024.

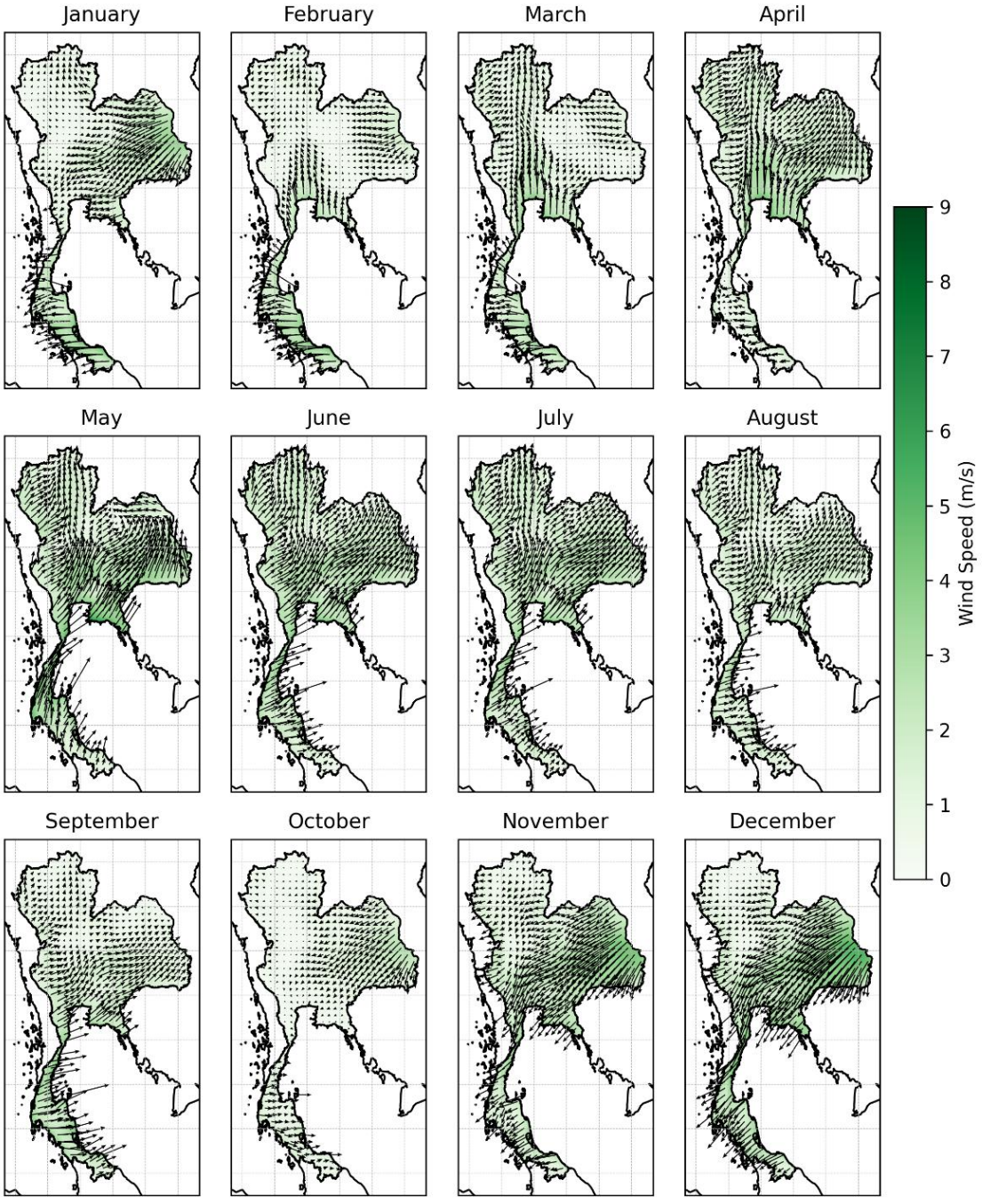


Figure 105 Monthly wind speed and wind direction maps from CCMP for the year 2024.

After preparing all spatial atmospheric data, the diffuse fraction was calculated for each pixel using the proposed cross-validation model the corresponding expression is shown in Equation (54). The diffuse solar radiation was then obtained by multiplying the estimated diffuse fraction by the corresponding global solar radiation. The results for the validating period (2023–2024) are presented in Figures 106 and 107.

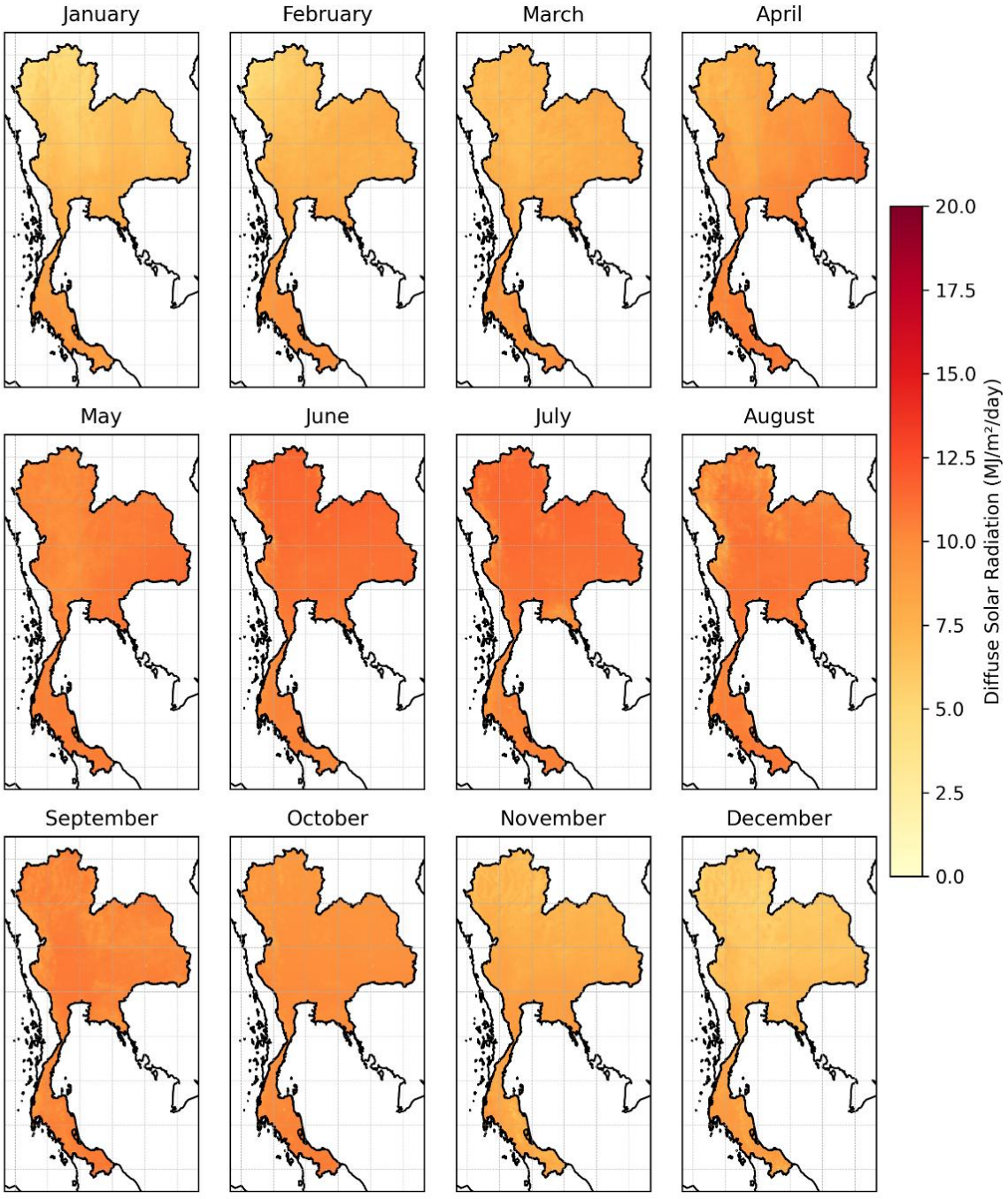


Figure 106 Monthly average daily diffuse solar radiation maps for the year 2023.

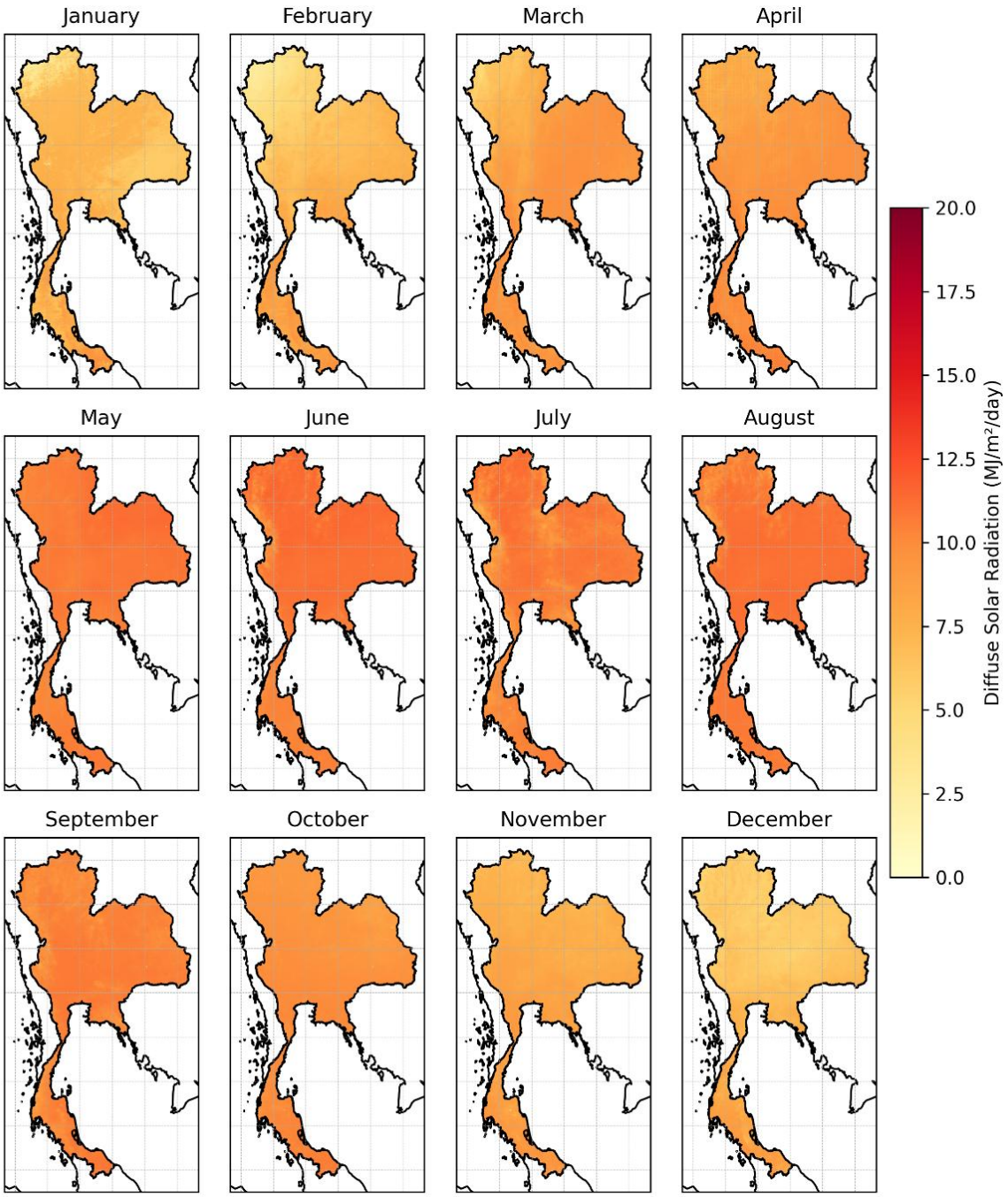


Figure 107 Monthly average daily diffuse solar radiation maps for the year 2024.

Figures 106 and 107 show the final diffuse solar radiation maps over Thailand created using the cross-validation model. The maps clearly present the spatial distributions of the diffuse solar radiation, and it changes with the seasons. The maps demonstrate that the diffuse solar radiation varies with the seasons, being higher during May to October (rainy season) due to an increase in cloud occurring in the sky and lowest during November to February (winter) when the skies are generally clearer. To verify the accuracy of the maps, ground-based independent data from four stations indirectly measured the diffuse solar radiation was used for the validation.

These stations located at different regions of Thailand are Phayao, Uthai Thani, Udon Thani, and Nakhon Si Thammarat. The comparison represented the model performance between the diffuse solar radiation extracted from the diffuse map and that collected from the ground-based measurement is shown in Figure 108.

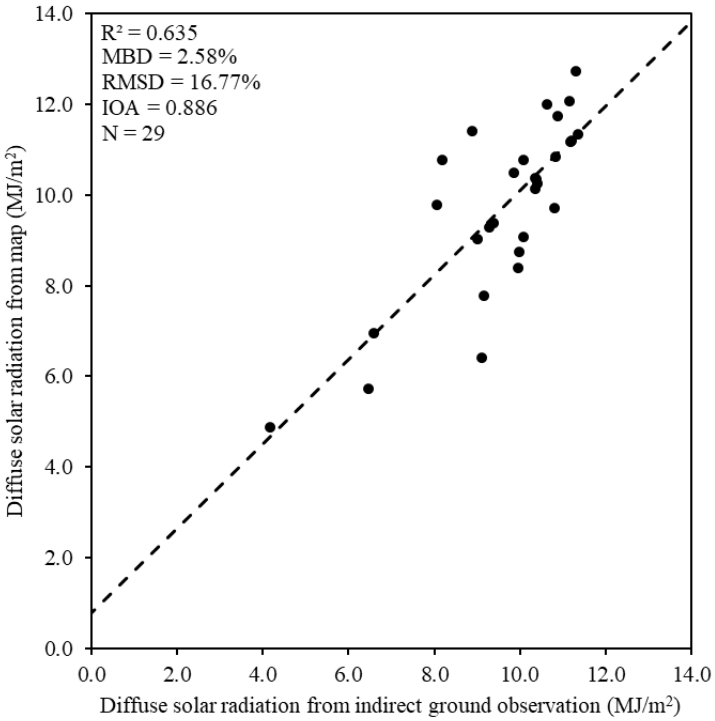


Figure 108 The validation of diffuse solar radiation from the map generated against indirectly measured values from ground-based measurement.

From the model was developed based on a k-fold cross-validation relating the diffuse fraction to the clearness index, with additional inputs of air temperature, relative humidity, and wind speed to improve accuracy. This model was successfully used to generate the diffuse solar radiation map. The validation shown in Figure 195 presents a good agreement between the diffuse solar radiation from the resulted map and the ground-based measurement with a discrepancy in terms of MBD of 2.58%, RMSD of 16.77%, and an IOA of 0.886. This evaluation confirm that the map can reliably represent the spatial distribution of the diffuse solar radiation across Thailand.

Chapter 4
Conclusions

This study aims to develop a model for estimating monthly average daily diffuse solar radiation and to generate spatial maps of the diffuse solar radiation across Thailand. Observations were conducted using data from four main ground-based stations located in different regions such as Chiang Mai, Nakhon Pathom, Ubon Ratchathani, and Songkhla. The diffuse solar radiation at each station was measured using a CM11 pyranometer mounted on a two-axis suntracker (2AP) with a shading ball from KIPP & ZONEN. Global solar radiation was measured using a CM21 pyranometer also manufactured by KIPP & ZONEN. Data collected over the period from 2012 to 2024 was processed and filtered for a future analysis. The frequency distribution of the global solar radiation generally peaks around 17–18 MJ/m², while diffuse solar radiation peaks near 8 MJ/m². However, the Chiang Mai station showed different results with a slightly lower global radiation peak around 16 MJ/m² and a higher diffuse radiation peak around 10 MJ/m², likely due to an increasing of aerosol concentrations in the region. Additionally, the diffuse solar radiation at four other stations was indirectly measured in 2024 by measuring both global and direct solar radiation and these data were used to validate the generated diffuse solar radiation maps.

The ground atmospheric parameters were retrieved from two sources; aerosol optical depth, precipitable water, and total ozone column were measured by CIMEL-318 from AERONET; cloud cover, air temperature, relative humidity, and wind speed from Thai Meteorological Department (TMD). The satellite-based atmospheric parameters were obtained from multiple sources aligned with ground-based observations. The downward shortwave radiation used as a proxy for global solar radiation was derived from the MODIS MCD18A1 product. Aerosol optical depth, precipitable water, total ozone column, and cloud fraction used as cloud cover were extracted from the MODIS MYD08 product. Air temperature and relative humidity data were sourced from NCEP/NCAR, while wind speed was obtained from the CCMP dataset.

To estimate the diffuse solar radiation, the relationship between the diffuse fraction and the clearness index was applied as the foundation of the model. Results from four main ground-based measurements showed good agreement with this approach. Since the objective of the modeling was to generate diffuse solar radiation maps at the Earth's surface, ground-based observations were used as reference data to correct satellite-derived parameters through the quantile mapping method. The results demonstrated that the satellite data adjusted with quantile mapping showed better consistency with the ground measurements.

After preparing the satellite-based data, the selection of parameters for modeling of monthly average daily diffuse solar radiation was carried out using t-statistics and p-values. In this analysis, parameters with a t-statistic greater than 1.96 and a p-value less than 0.05 were considered statistically significant. The results showed that only three parameters (clearness index, air temperature, and relative

humidity) passed the test. These three were therefore used to formula the baseline model, named M1. The remaining parameters were included in a subset selection process to identify the best combination of variables. This process produced models M2 through M32 by using multiple linear regression. Each model was evaluated using three statistical indicators, namely mean bias difference (MBD), root mean square difference (RMSD), and index of agreement (IOA). The results indicated that Model M6, which added wind speed to the baseline model achieved the highest accuracy with MBD of 4.71%, RMSD of 14.15%, and IOA of 0.933.

After identifying Model M6 as the optimal baseline model, it was further evaluated using two additional methods such as k-fold cross-validation (M6A) and artificial neural networks (M6B). The performance of these models was then compared with empirical models from previous studies (O1–O11). The results showed that the cross-validation model (M6A) achieved the highest accuracy, with the MBD of 2.81%, RMSD of 13.49%, and IOA of 0.957.

Model M6A was then selected to generate the monthly average daily diffuse solar radiation map. All satellite-based atmospheric parameters were preprocessed into the same format (monthly average daily values) cropped to the domain of Thailand (latitudes 5° to 21°N and longitudes 97° to 107°E) and resampled to a uniform resolution of 0.01° × 0.01°. These prepared parameters were then used to calculate the diffuse solar radiation at each pixel using the cross-validation model (M6A). The resulting maps illustrate the spatial distribution of monthly average daily diffuse solar radiation across Thailand. Furthermore, the maps were validated using ground-based data from indirect measurements at four independent stations such as Phayao, Uthai Thani, Udon Thani, and Nakhon Si Thammarat. The validation showed strong agreement, with the MBD of 2.58%, RMSD of 16.71%, and IOA of 0.886, confirming that the maps reliably represent the spatial characteristics of the diffuse solar radiation for Thailand. This diffuse solar radiation obtained from the map was the utilized for different applications in solar energy technologies or other related works.

Appendices

Appendix A: Diffuse fraction model results

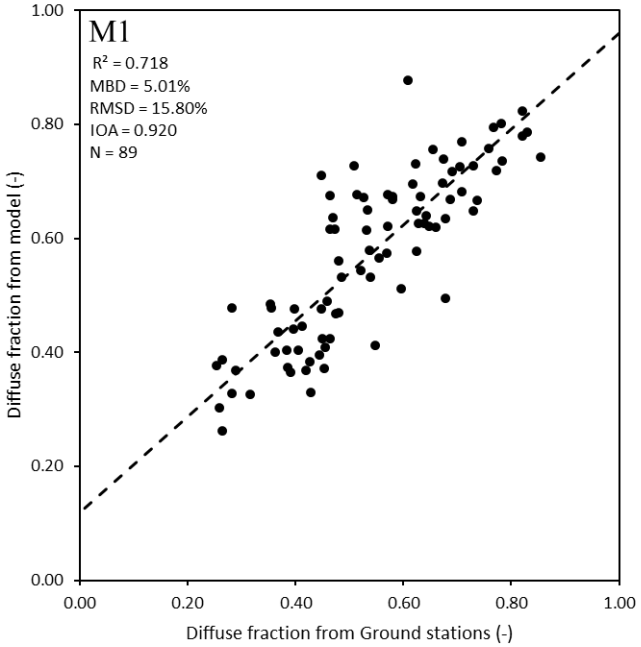


Figure 109 Comparison between observed and estimated diffuse fraction using Model M1.

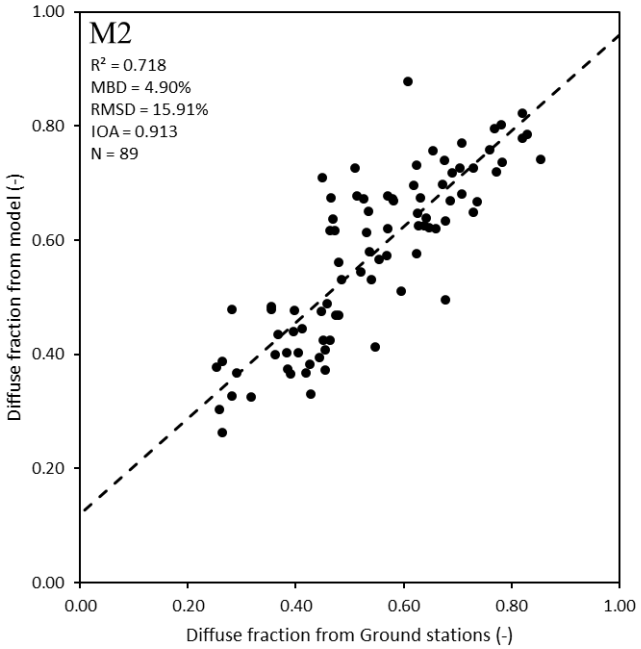


Figure 110 Comparison between observed and estimated diffuse fraction using Model M2.

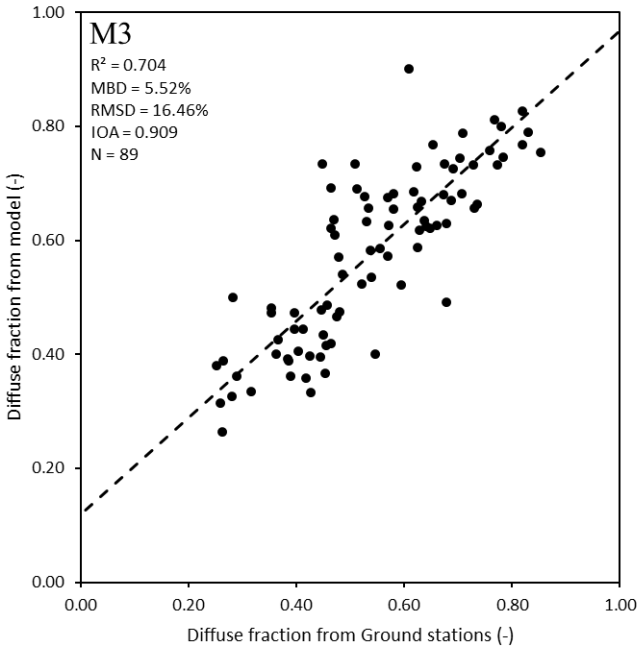


Figure 111 Comparison between observed and estimated diffuse fraction using Model M3.

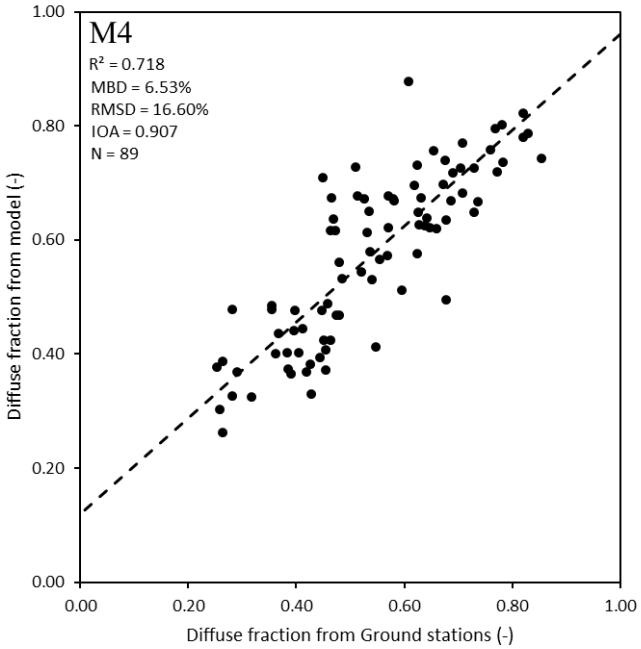


Figure 112 Comparison between observed and estimated diffuse fraction using Model M4.

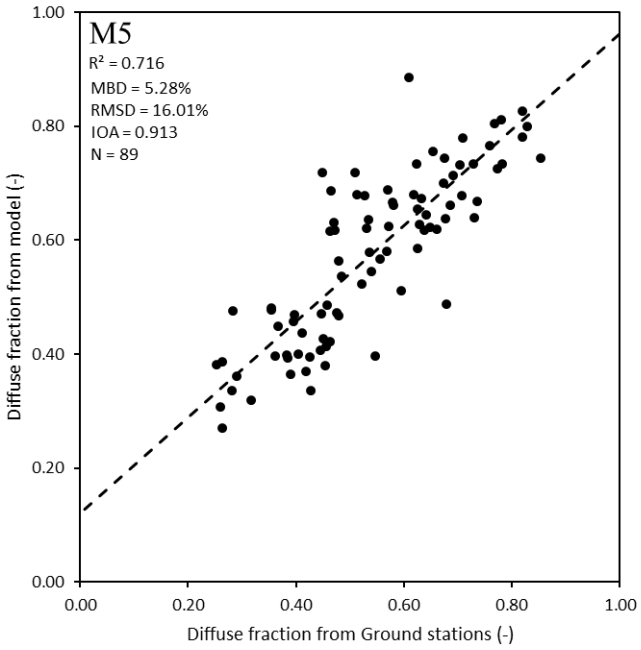


Figure 113 Comparison between observed and estimated diffuse fraction using Model M5.

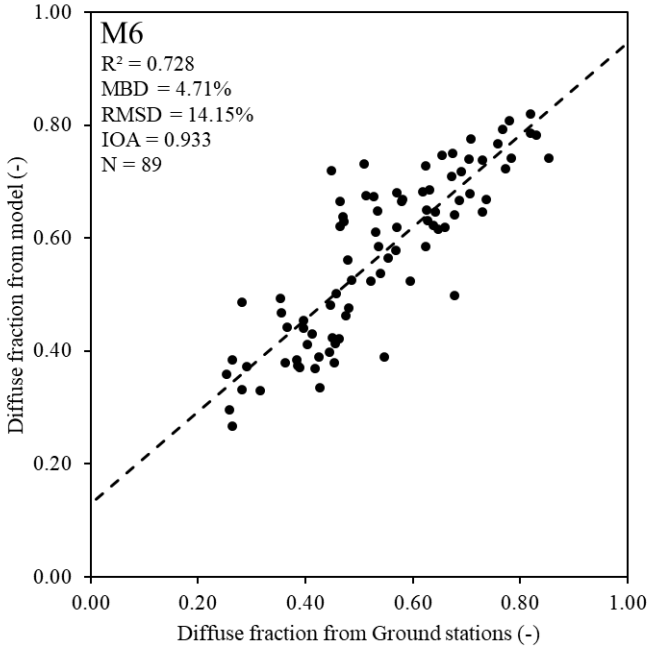


Figure 114 Comparison between observed and estimated diffuse fraction using Model M6.

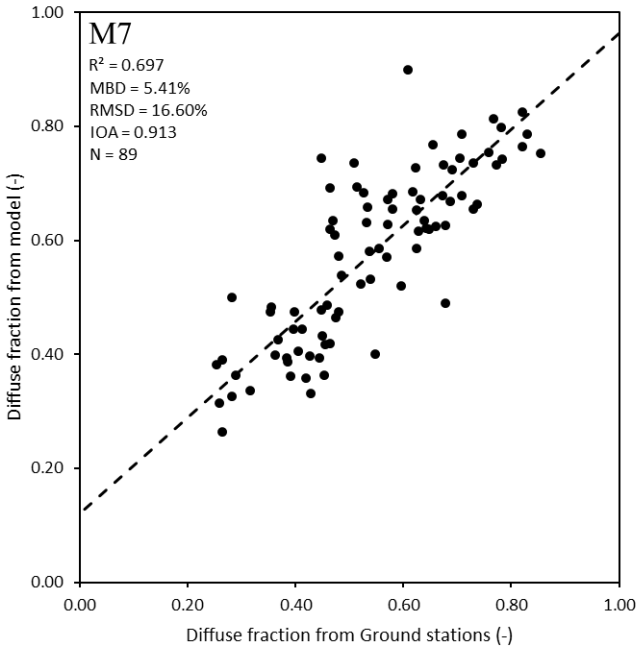


Figure 115 Comparison between observed and estimated diffuse fraction using Model M7.

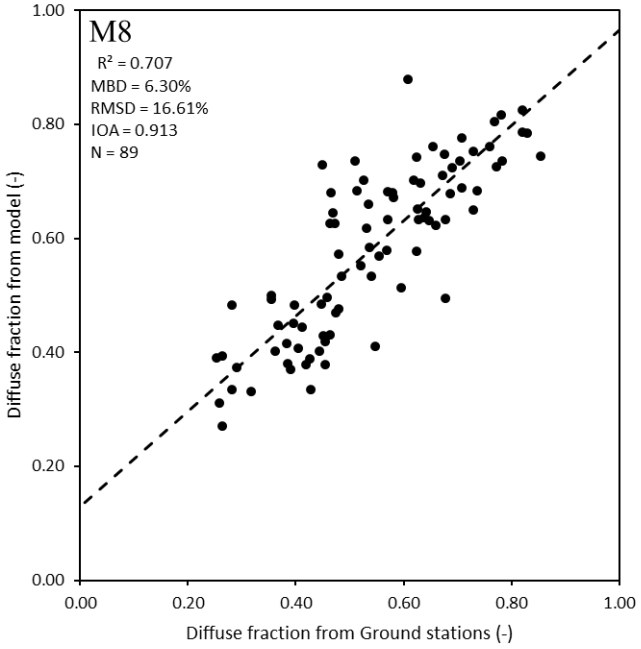


Figure 116 Comparison between observed and estimated diffuse fraction using Model M8.

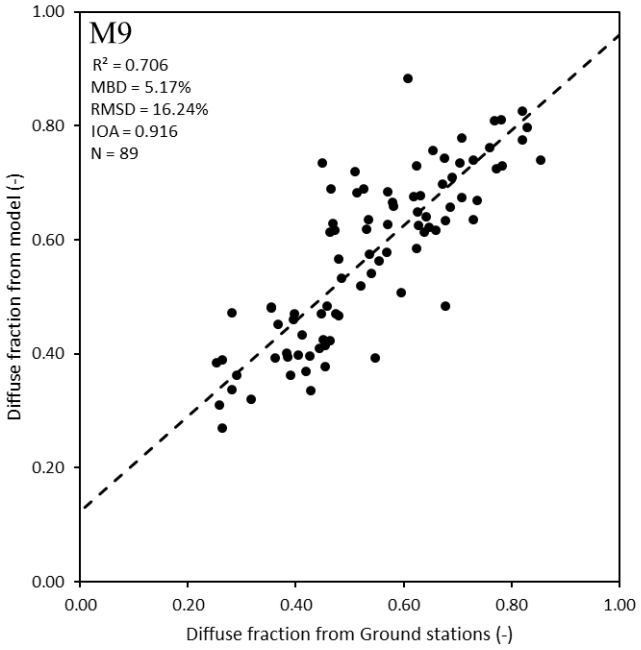


Figure 117 Comparison between observed and estimated diffuse fraction using Model M9.

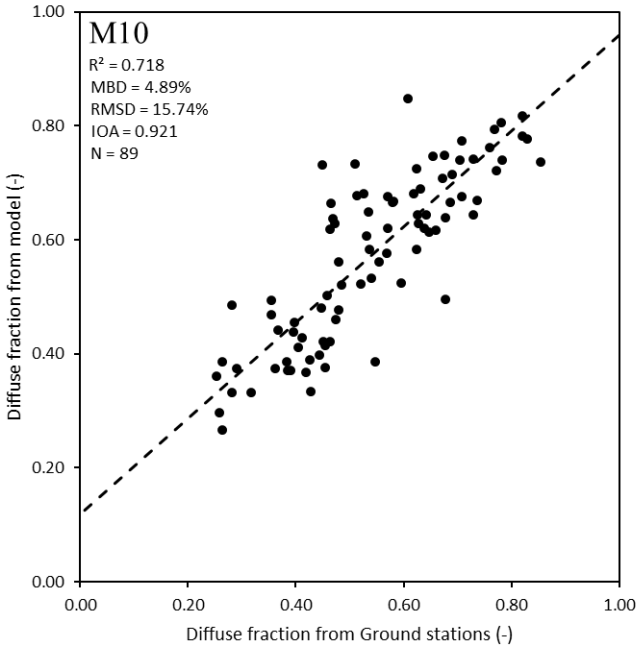


Figure 118 Comparison between observed and estimated diffuse fraction using Model M10.

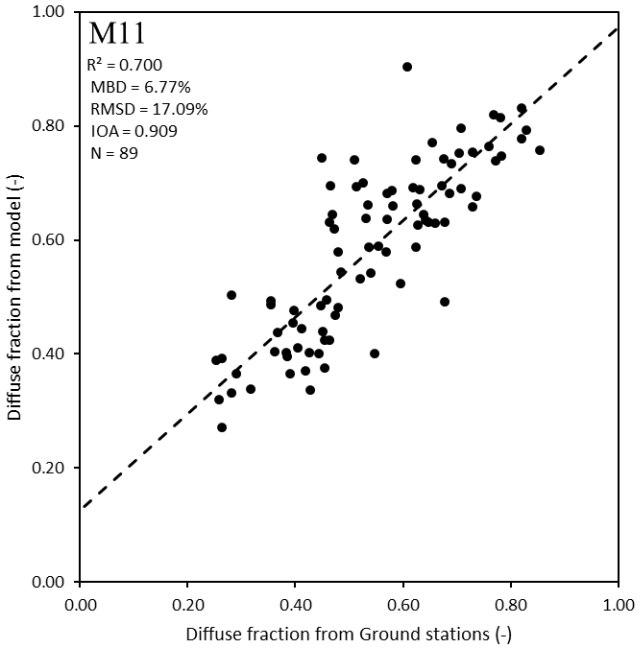


Figure 119 Comparison between observed and estimated diffuse fraction using Model M11.

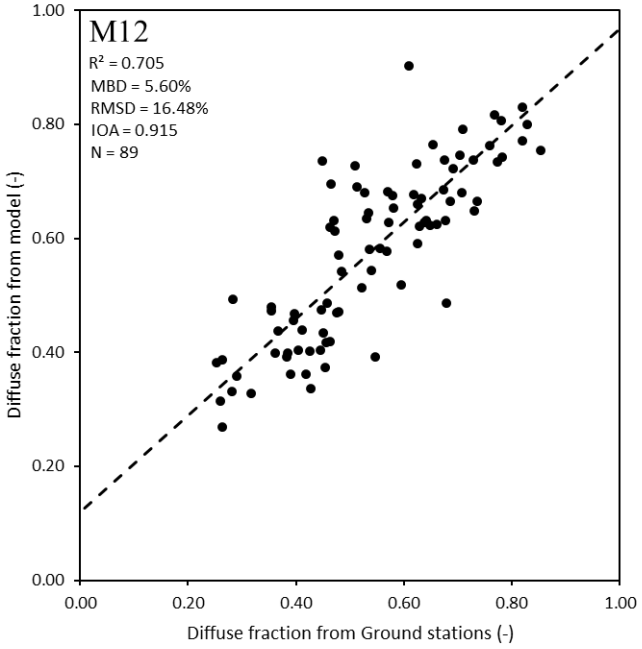


Figure 120 Comparison between observed and estimated diffuse fraction using Model M12.

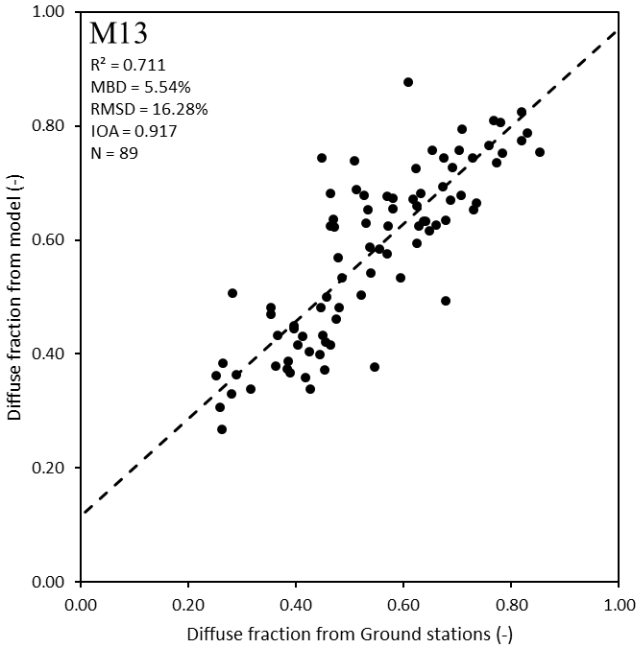


Figure 121 Comparison between observed and estimated diffuse fraction using Model M13.

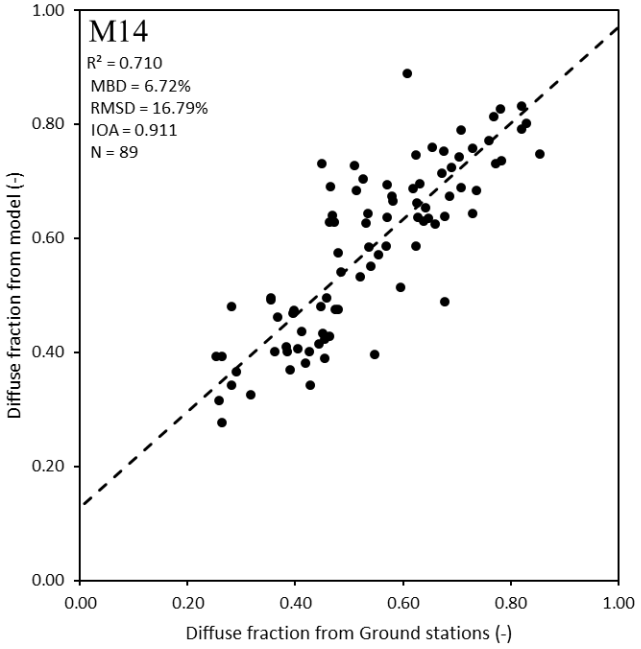


Figure 122 Comparison between observed and estimated diffuse fraction using Model M14.

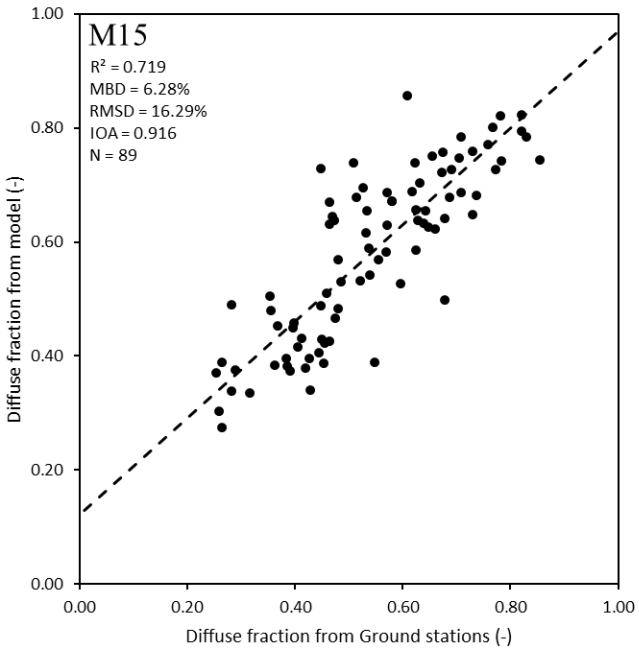


Figure 123 Comparison between observed and estimated diffuse fraction using Model M15.

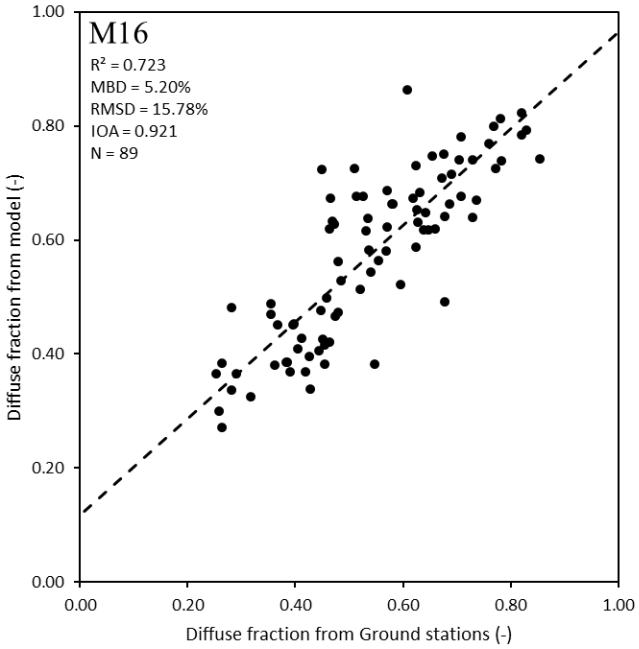


Figure 124 Comparison between observed and estimated diffuse fraction using Model M16.

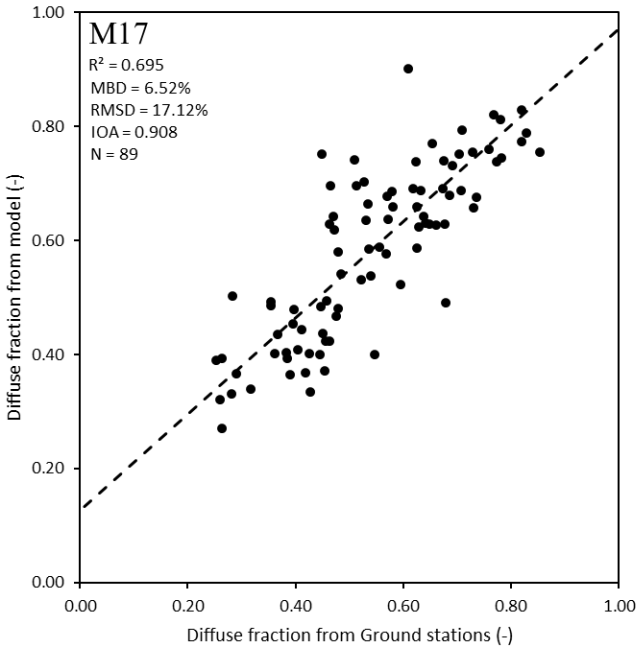


Figure 125 Comparison between observed and estimated diffuse fraction using Model M17.

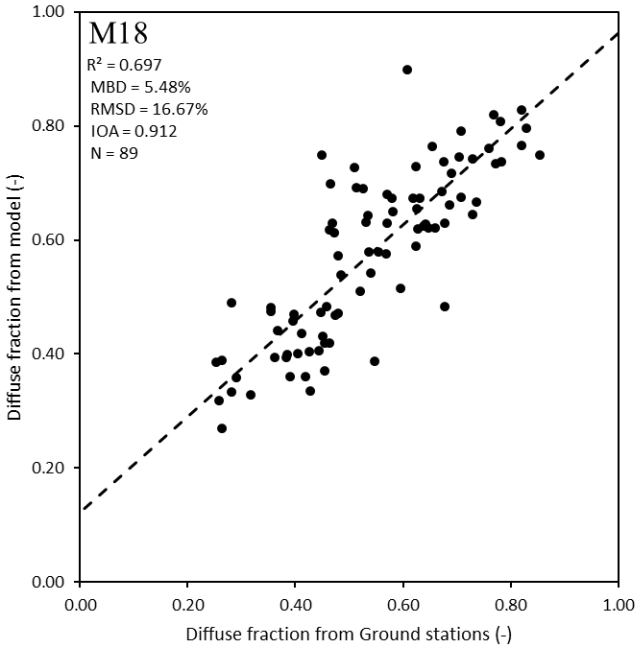


Figure 126 Comparison between observed and estimated diffuse fraction using Model M18.

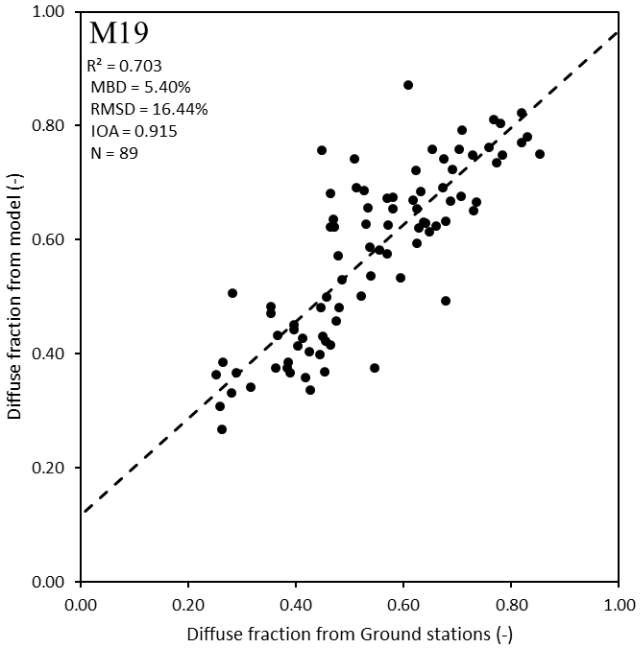


Figure 127 Comparison between observed and estimated diffuse fraction using Model M19.

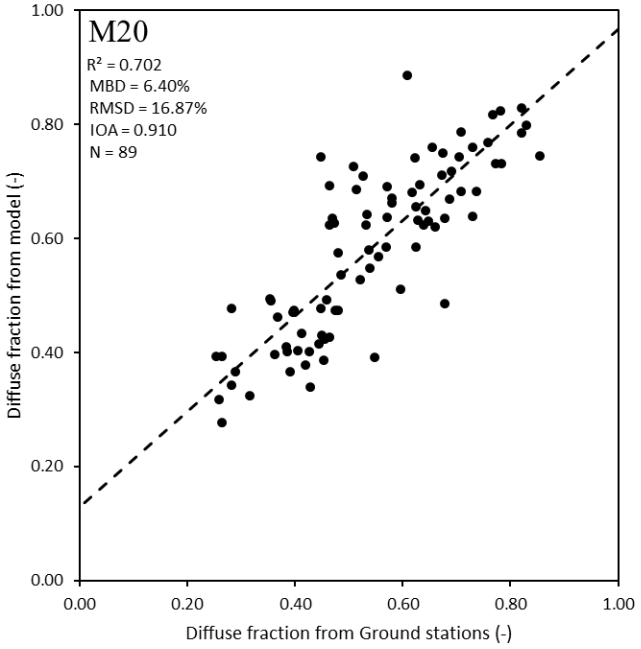


Figure 128 Comparison between observed and estimated diffuse fraction using Model M20.

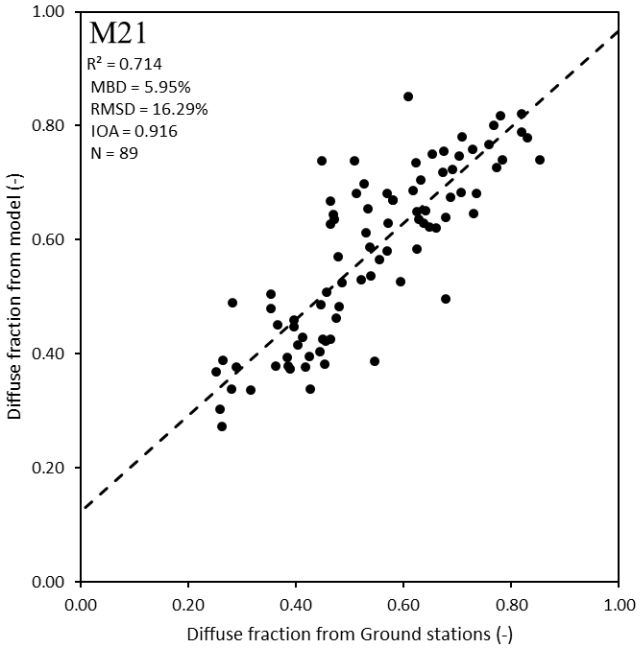


Figure 129 Comparison between observed and estimated diffuse fraction using Model M21.

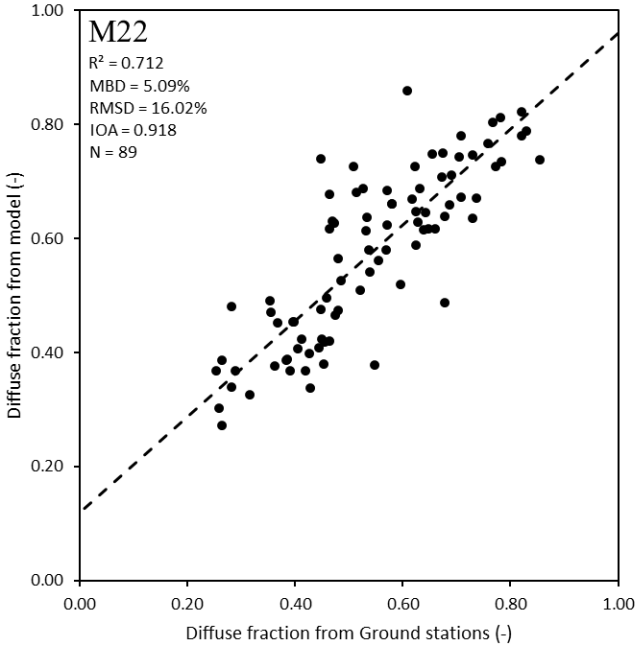


Figure 130 Comparison between observed and estimated diffuse fraction using Model M22.

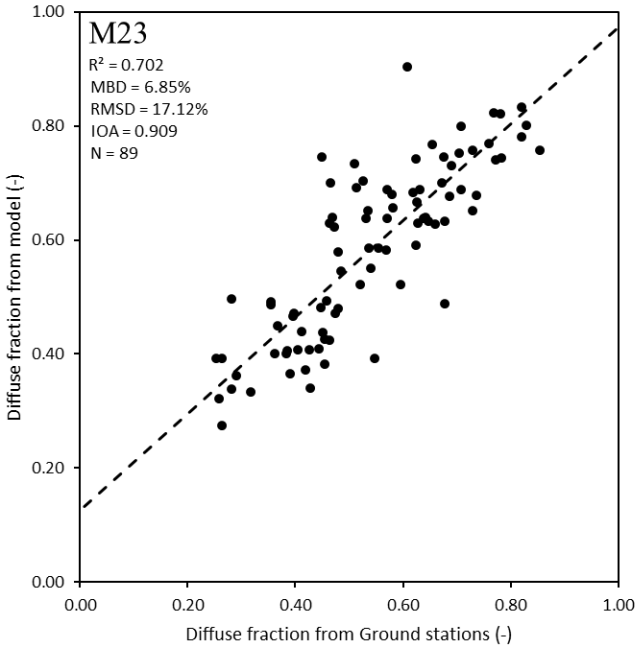


Figure 131 Comparison between observed and estimated diffuse fraction using Model M23.

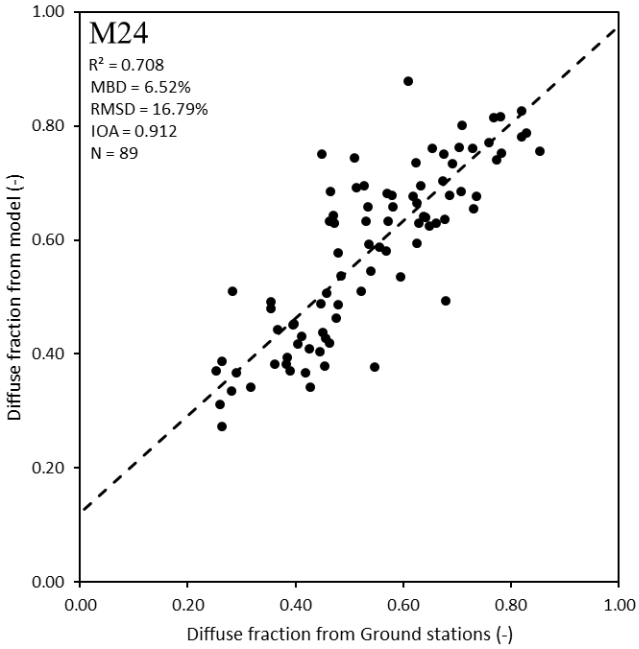


Figure 132 Comparison between observed and estimated diffuse fraction using Model M24.

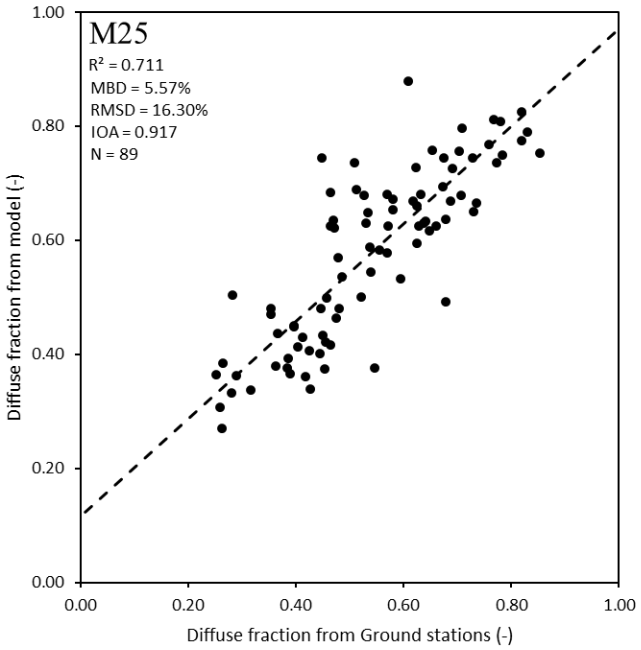


Figure 133 Comparison between observed and estimated diffuse fraction using Model M25.

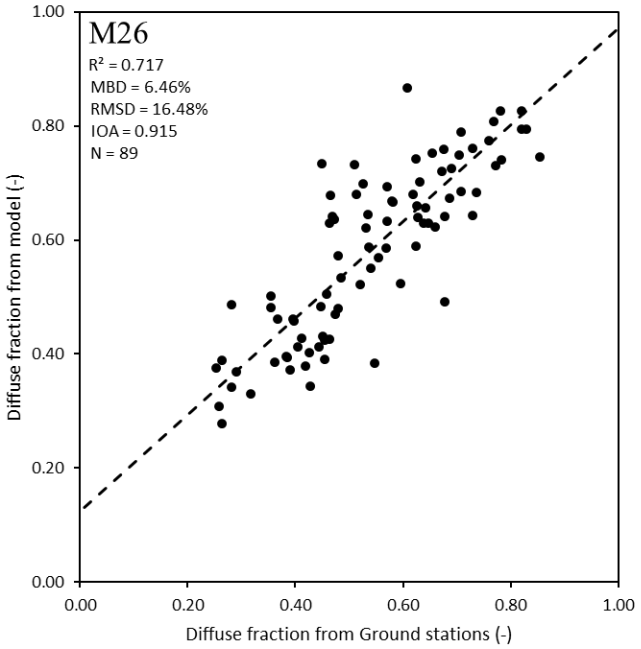


Figure 134 Comparison between observed and estimated diffuse fraction using Model M26.

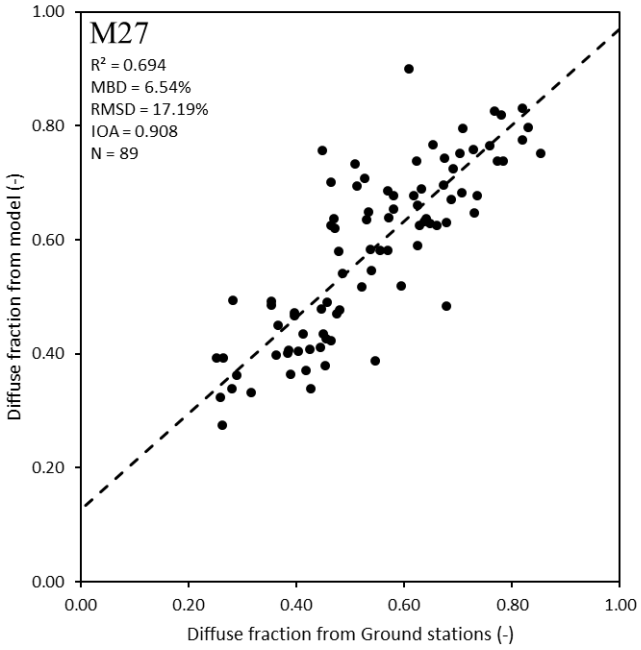


Figure 135 Comparison between observed and estimated diffuse fraction using Model M27.

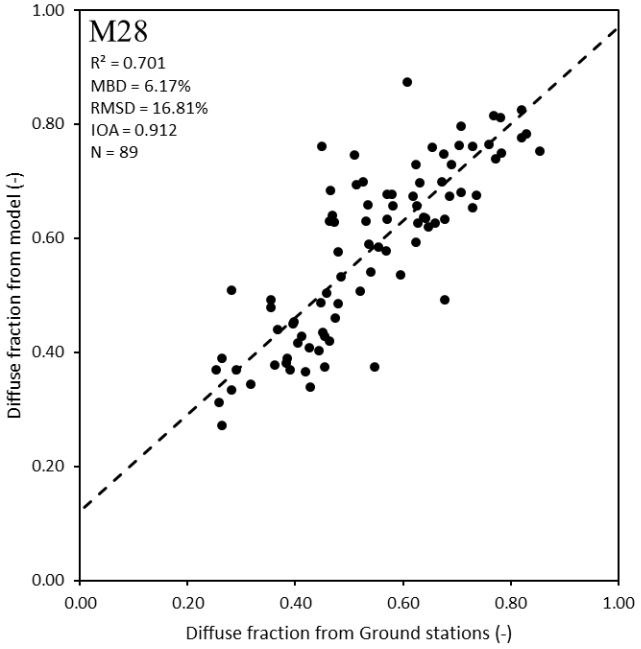


Figure 136 Comparison between observed and estimated diffuse fraction using Model M28.

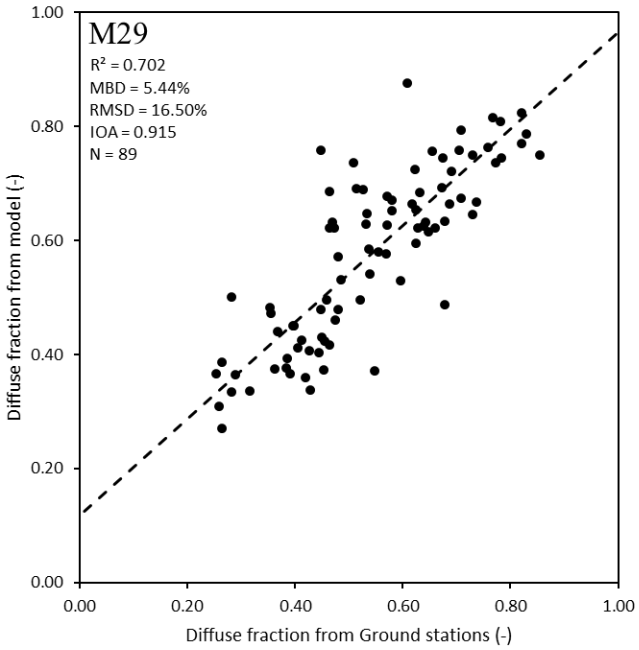


Figure 137 Comparison between observed and estimated diffuse fraction using Model M29.

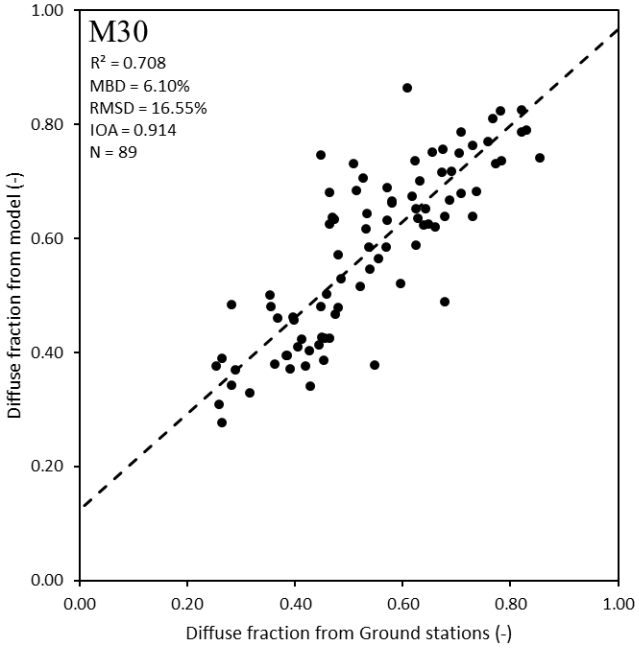


Figure 138 Comparison between observed and estimated diffuse fraction using Model M30.

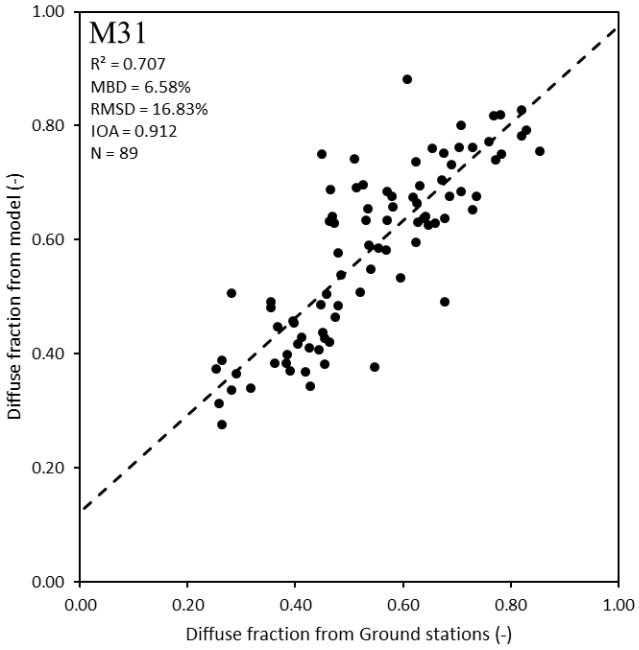


Figure 139 Comparison between observed and estimated diffuse fraction using Model M31.

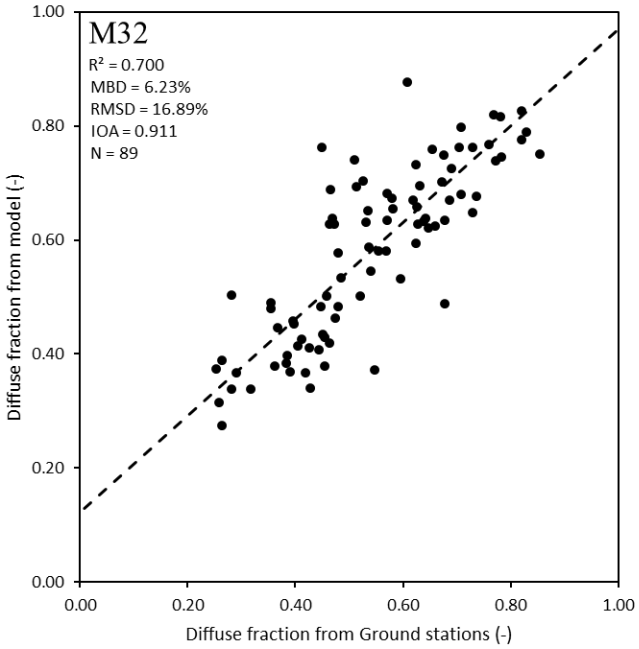


Figure 140 Comparison between observed and estimated diffuse fraction using Model M32.

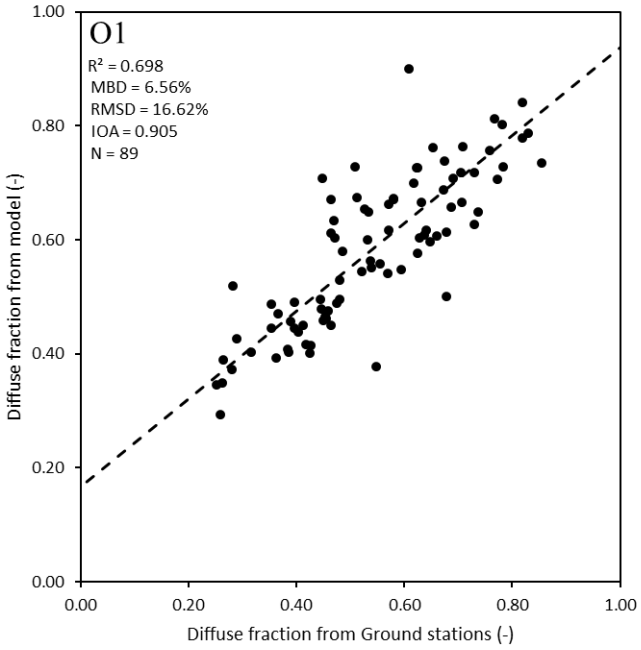


Figure 141 Comparison between observed and estimated diffuse fraction using Model O1 from Oliveira et al. (2002) and El-Sebaii and Trabea (2003).

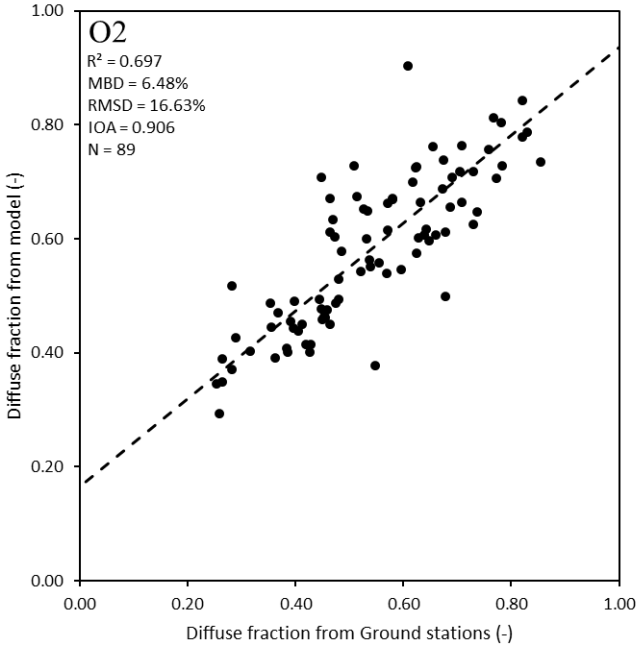


Figure 142 Comparison between observed and estimated diffuse fraction using Model O2 from Barbaro et al. (1981).

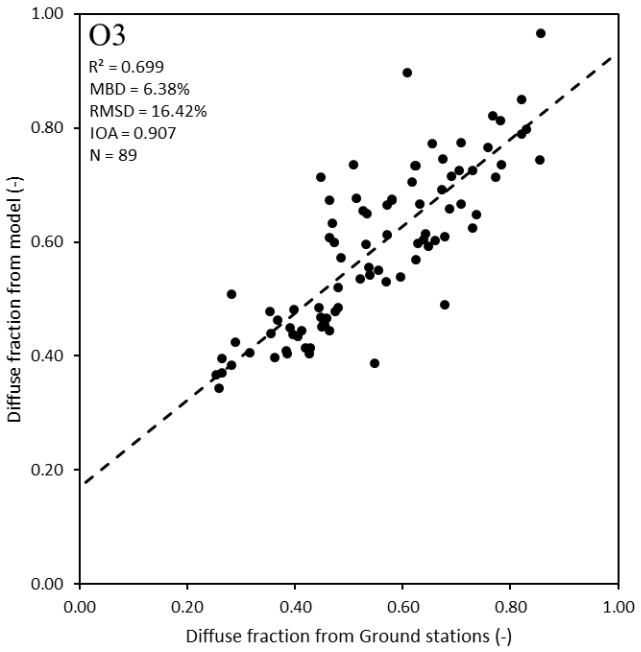


Figure 143 Comparison between observed and estimated diffuse fraction using Model O3 from Ulgen and Hepbasli (2009).

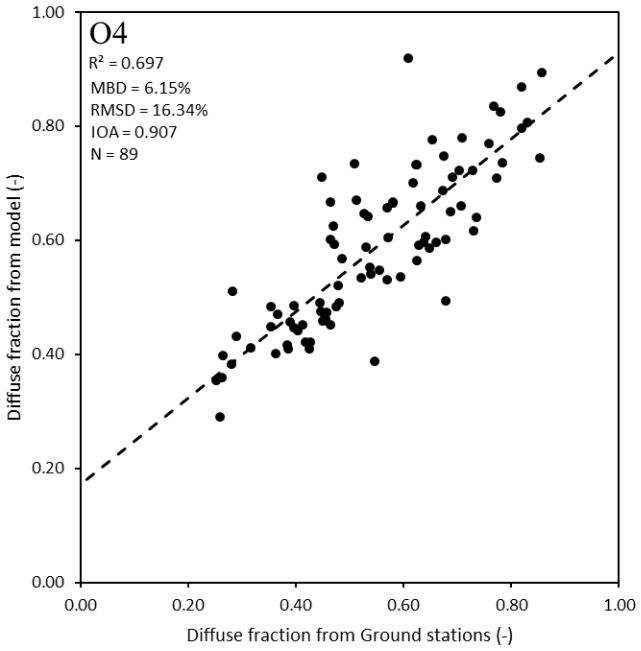


Figure 144 Comparison between observed and estimated diffuse fraction using Model O4 from Bamiro (1983).

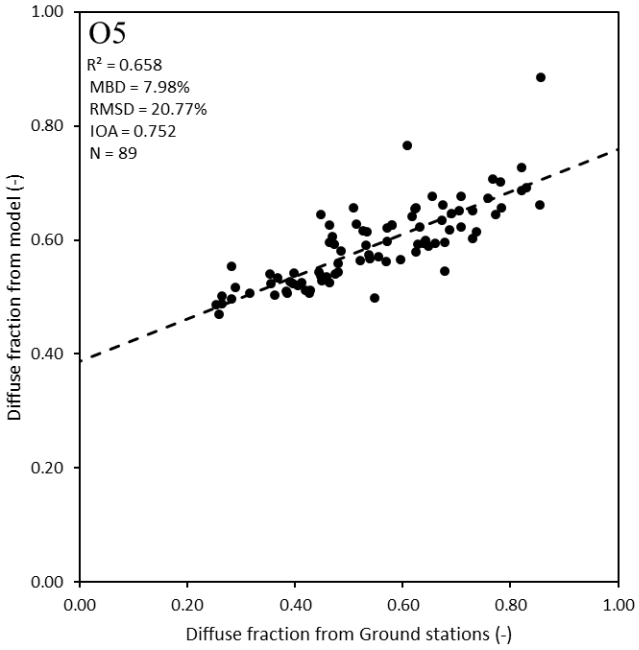


Figure 145 Comparison between observed and estimated diffuse fraction using Model O5 from Lealea and Tchinda (2013).

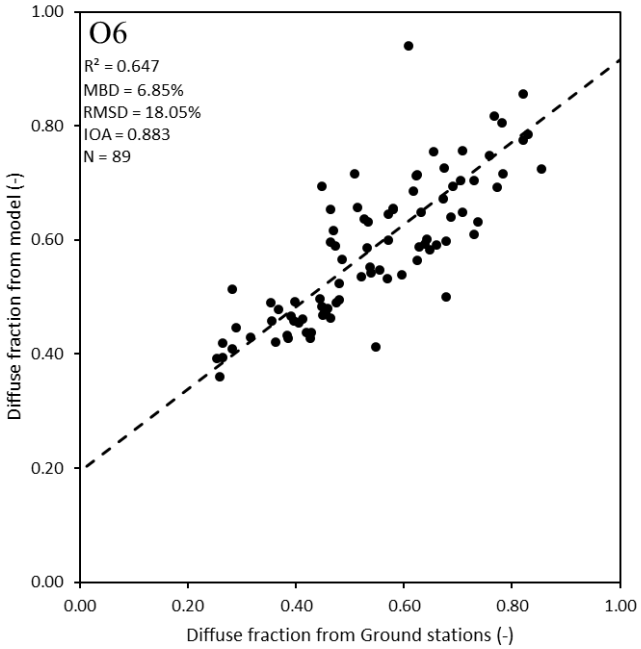


Figure 146 Comparison between observed and estimated diffuse fraction using Model O6 from Boukelia et al. (2014).

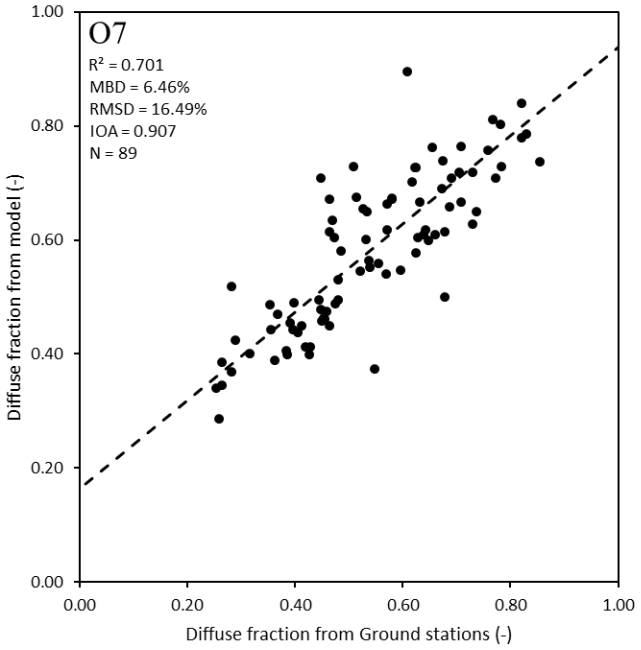


Figure 147 Comparison between observed and estimated diffuse fraction using Model O7 from Bailek et al. (2018).

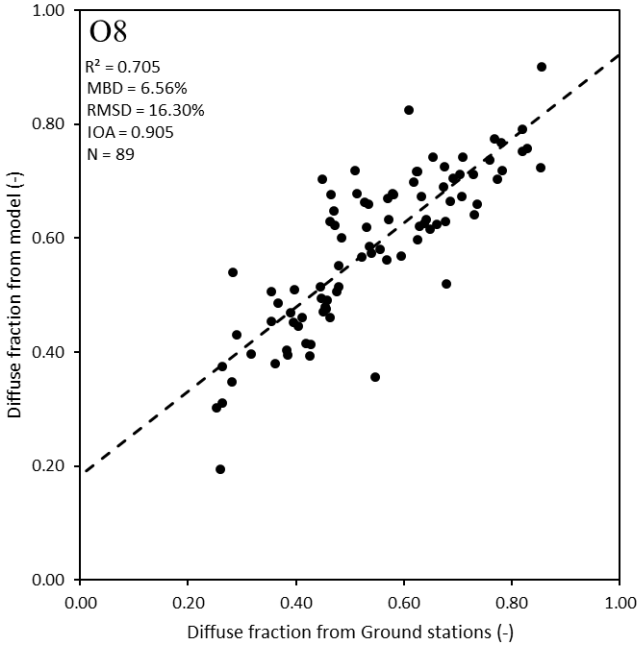


Figure 148 Comparison between observed and estimated diffuse fraction using Model O8 from Bailek et al. (2018).

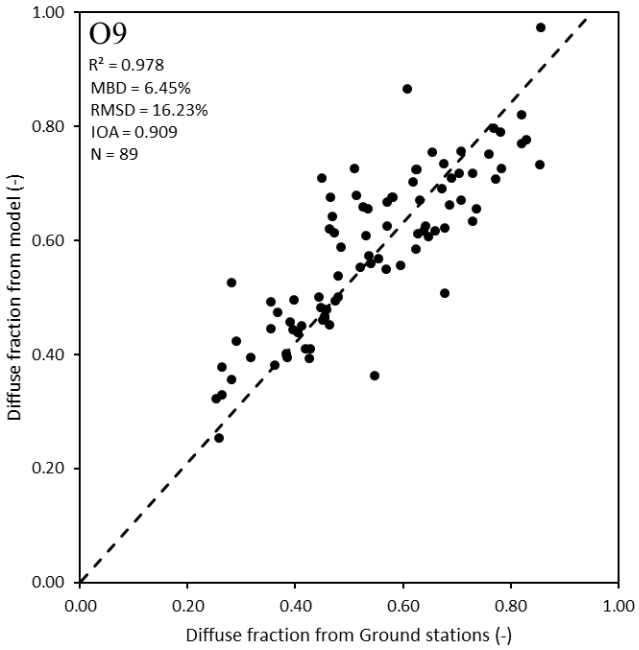


Figure 149 Comparison between observed and estimated diffuse fraction using Model O9 from (Lealea & Tchinda, 2013).

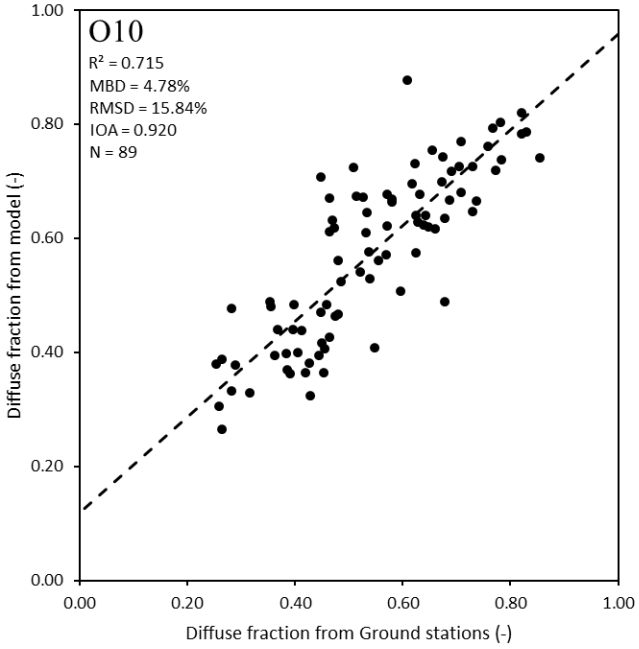


Figure 150 Comparison between observed and estimated diffuse fraction using Model O10 from Mubiru and Banda (2007).

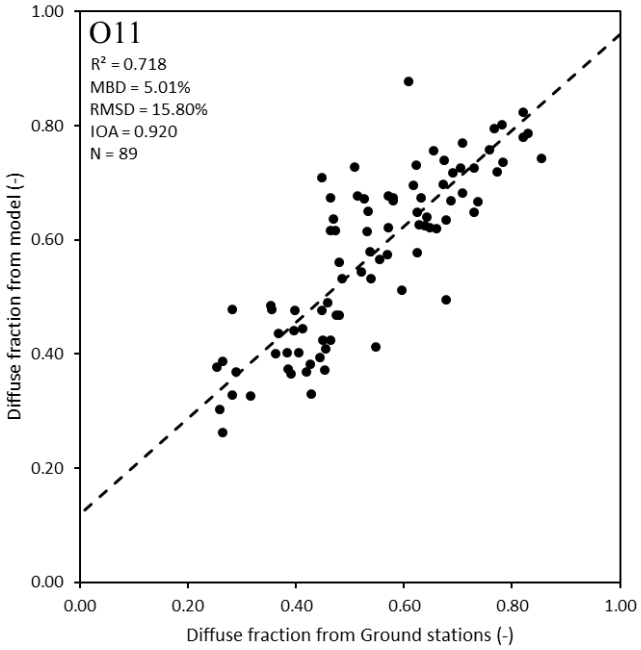


Figure 151 Comparison between observed and estimated diffuse fraction using Model O11 from Li et al. (2011).

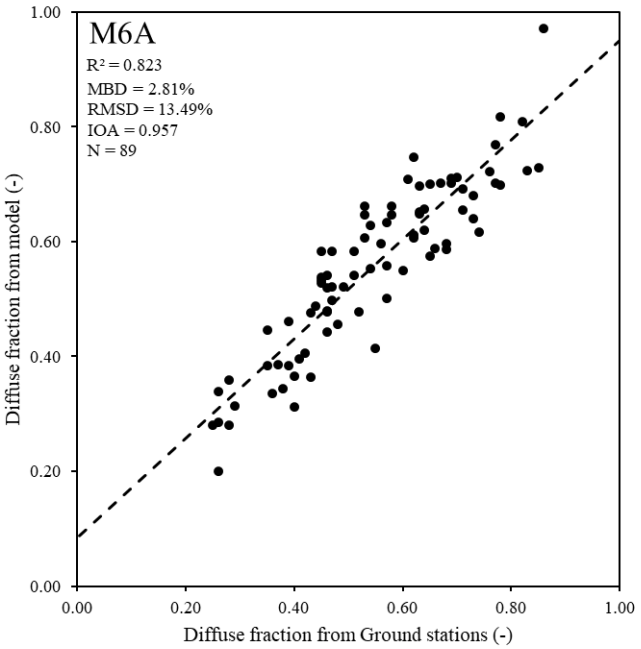


Figure 152 Comparison between observed and estimated diffuse fraction using Model M6A from k-fold cross-validation method.

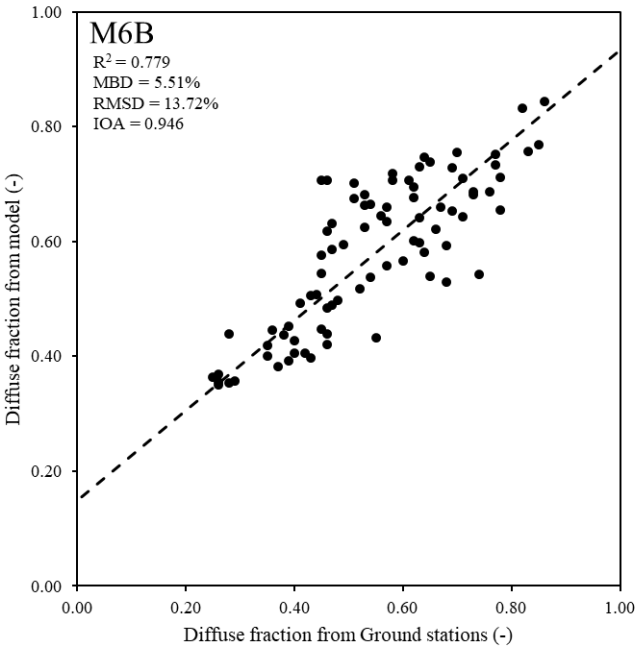


Figure 153 Comparison between observed and estimated diffuse fraction using Model M6B from artificial neurons network method.

Appendix B: Input data for generating diffuse solar radiation maps

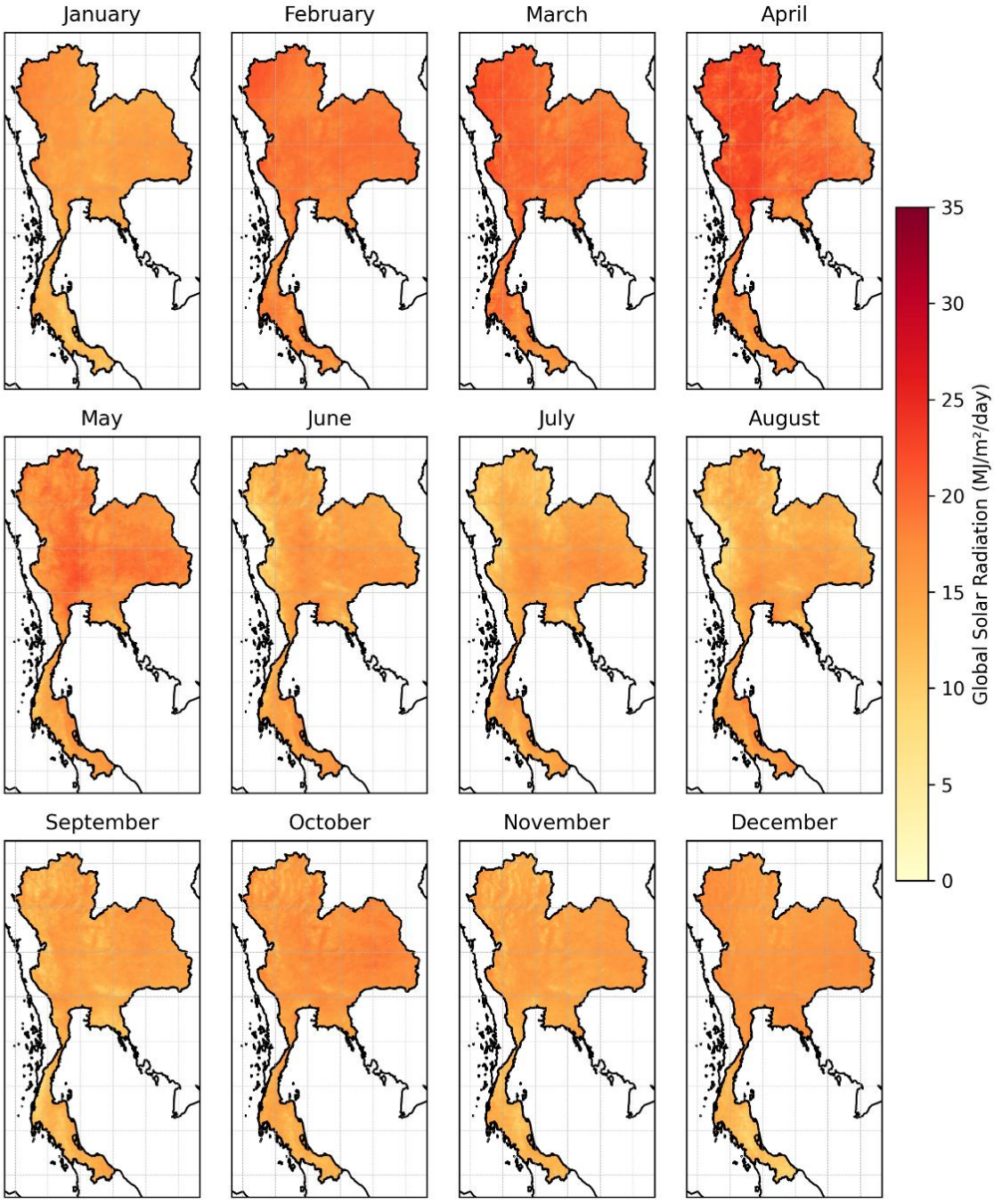


Figure 154 Monthly global solar radiation maps from MODIS for the year 2012.

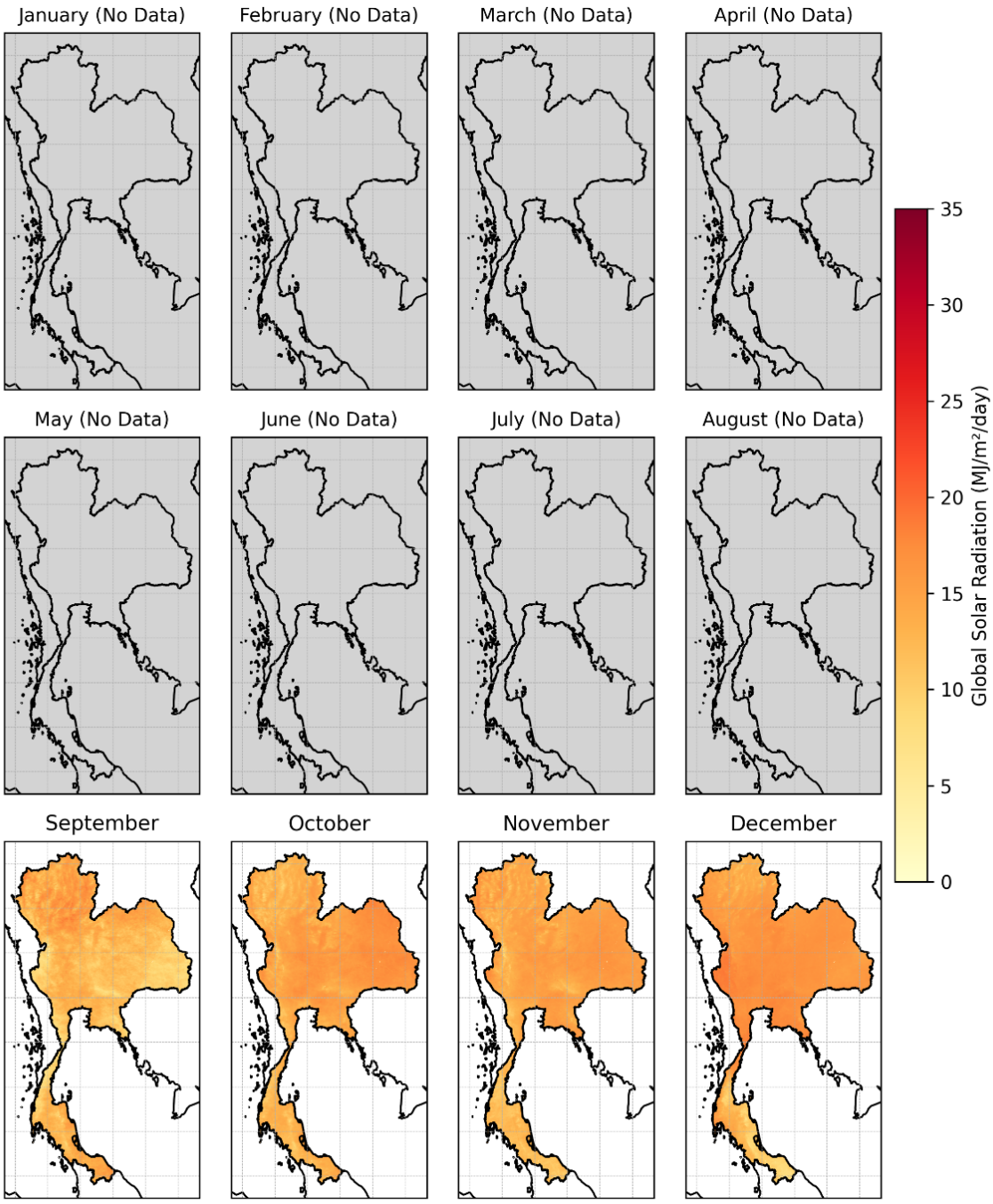


Figure 155 Monthly global solar radiation maps from MODIS for the year 2013.

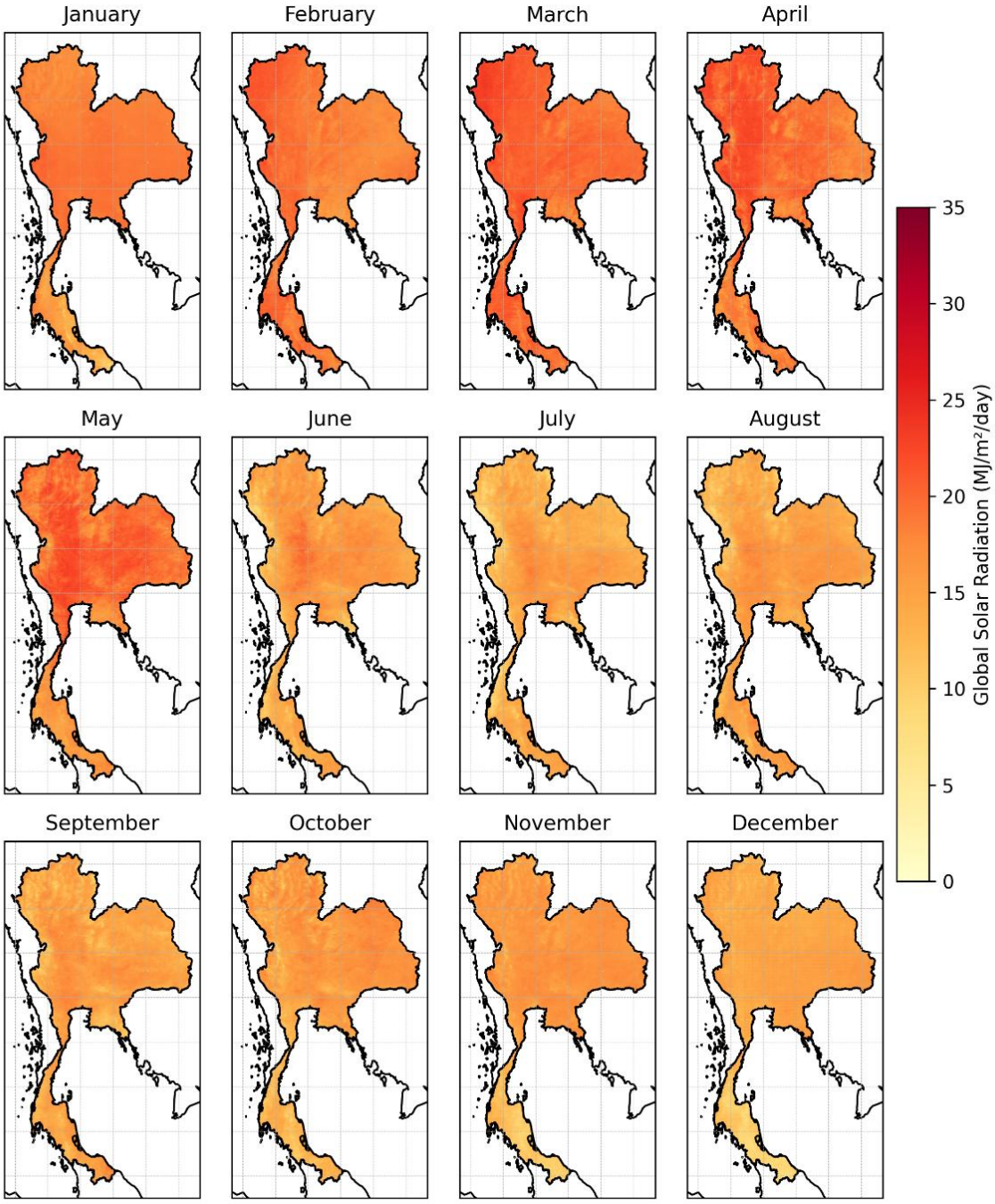


Figure 156 Monthly global solar radiation maps from MODIS for the year 2014.

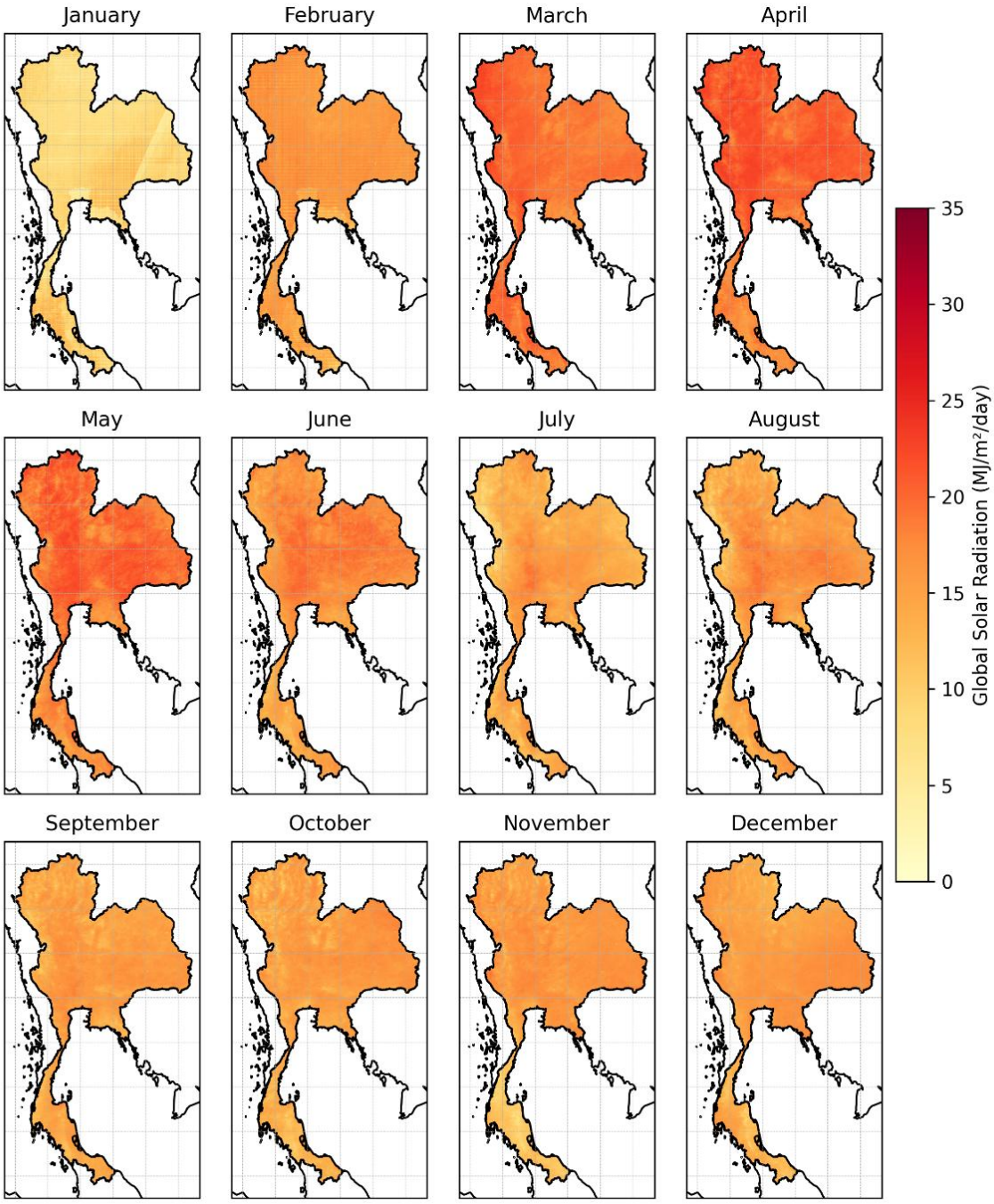


Figure 157 Monthly global solar radiation maps from MODIS for the year 2015.

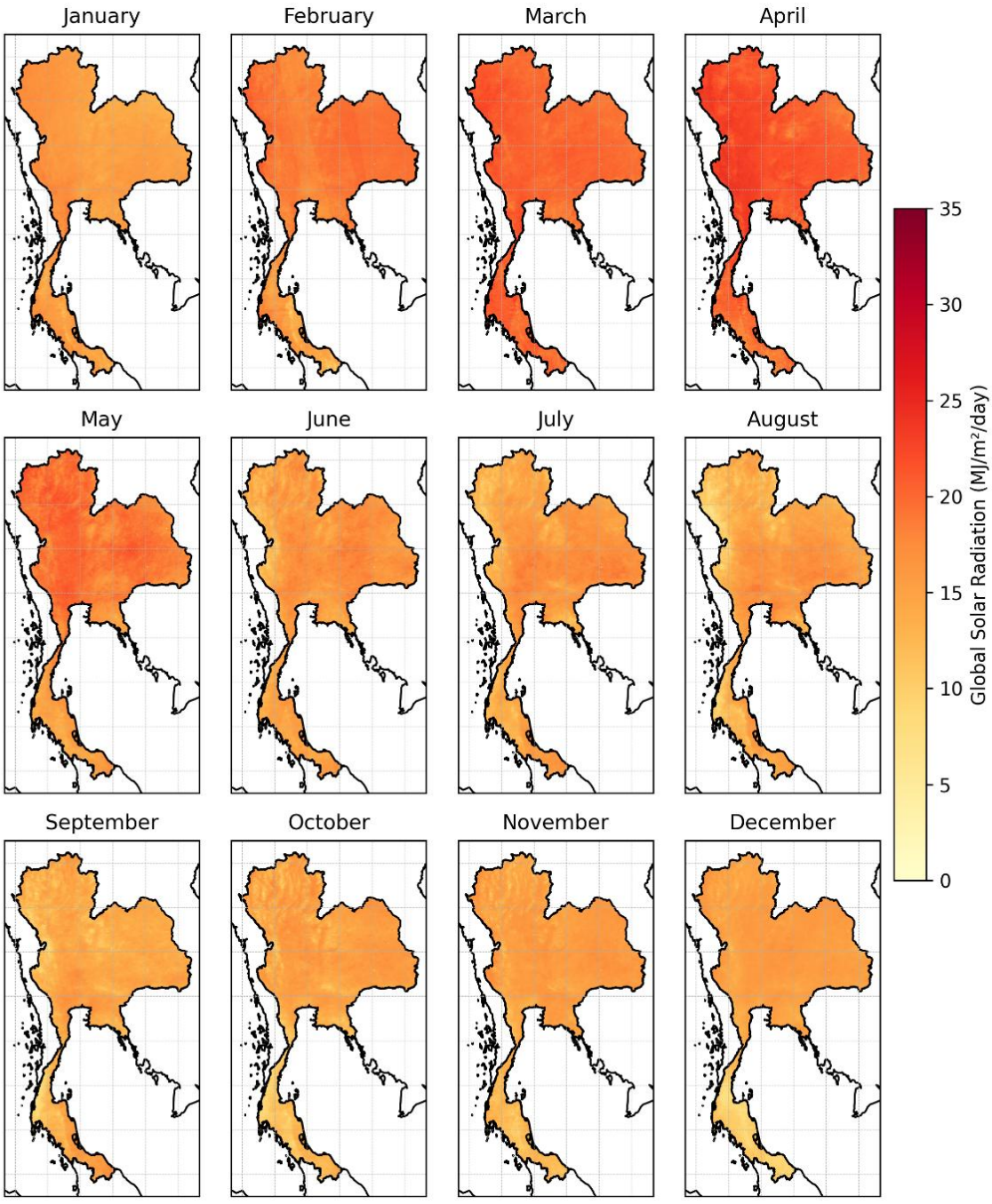


Figure 158 Monthly global solar radiation maps from MODIS for the year 2016.

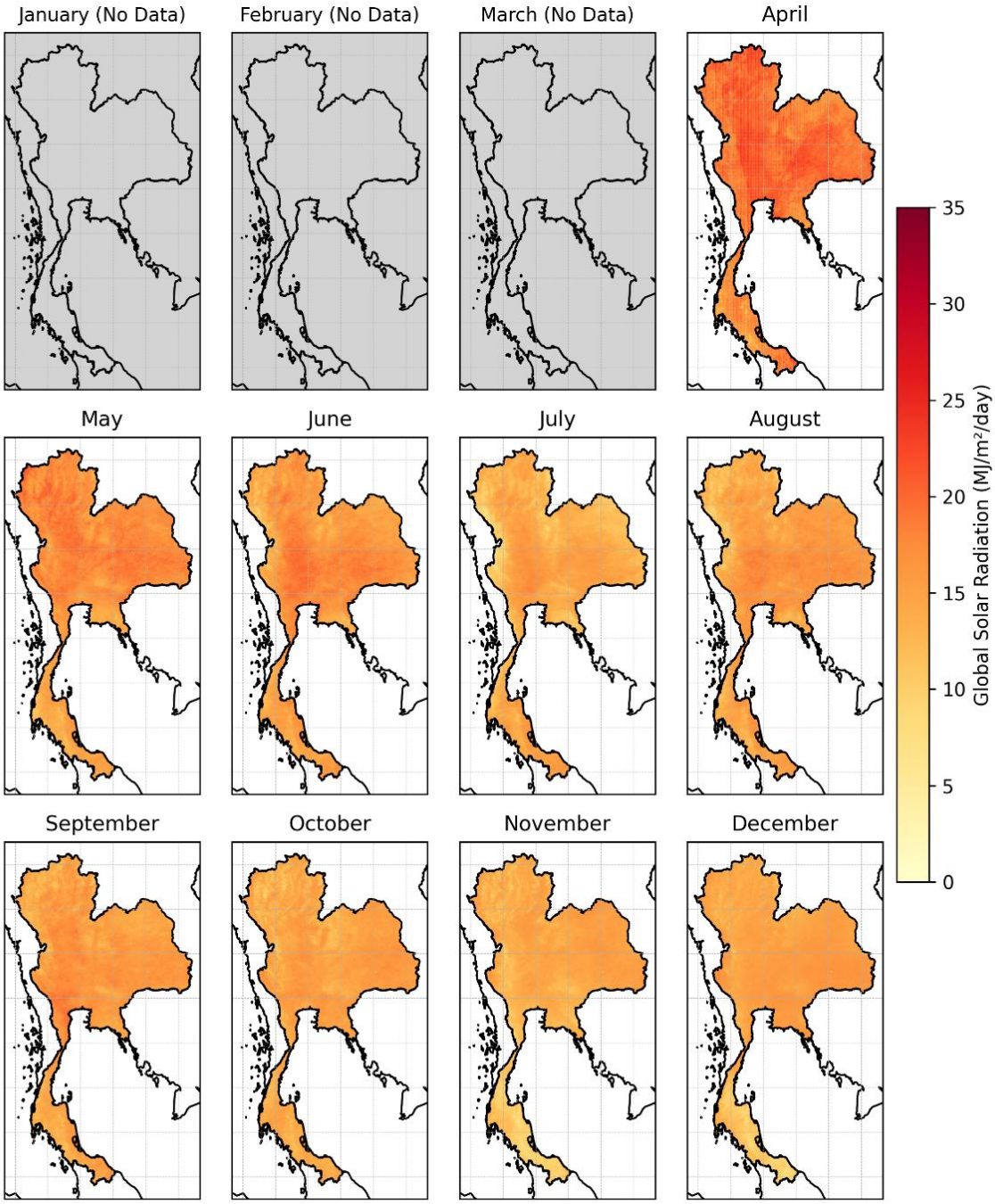


Figure 159 Monthly global solar radiation maps from MODIS for the year 2017.

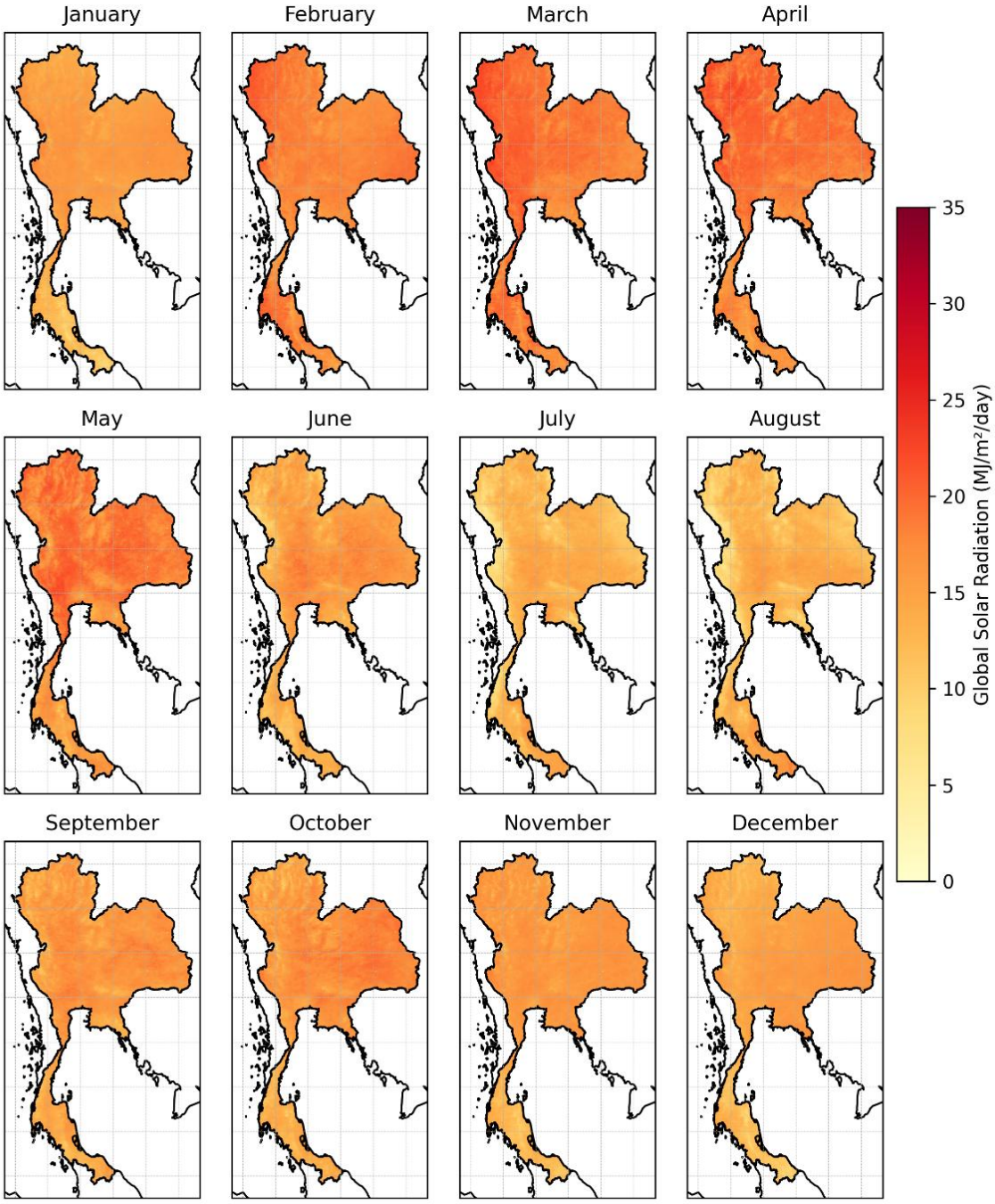


Figure 160 Monthly global solar radiation maps from MODIS for the year 2018.

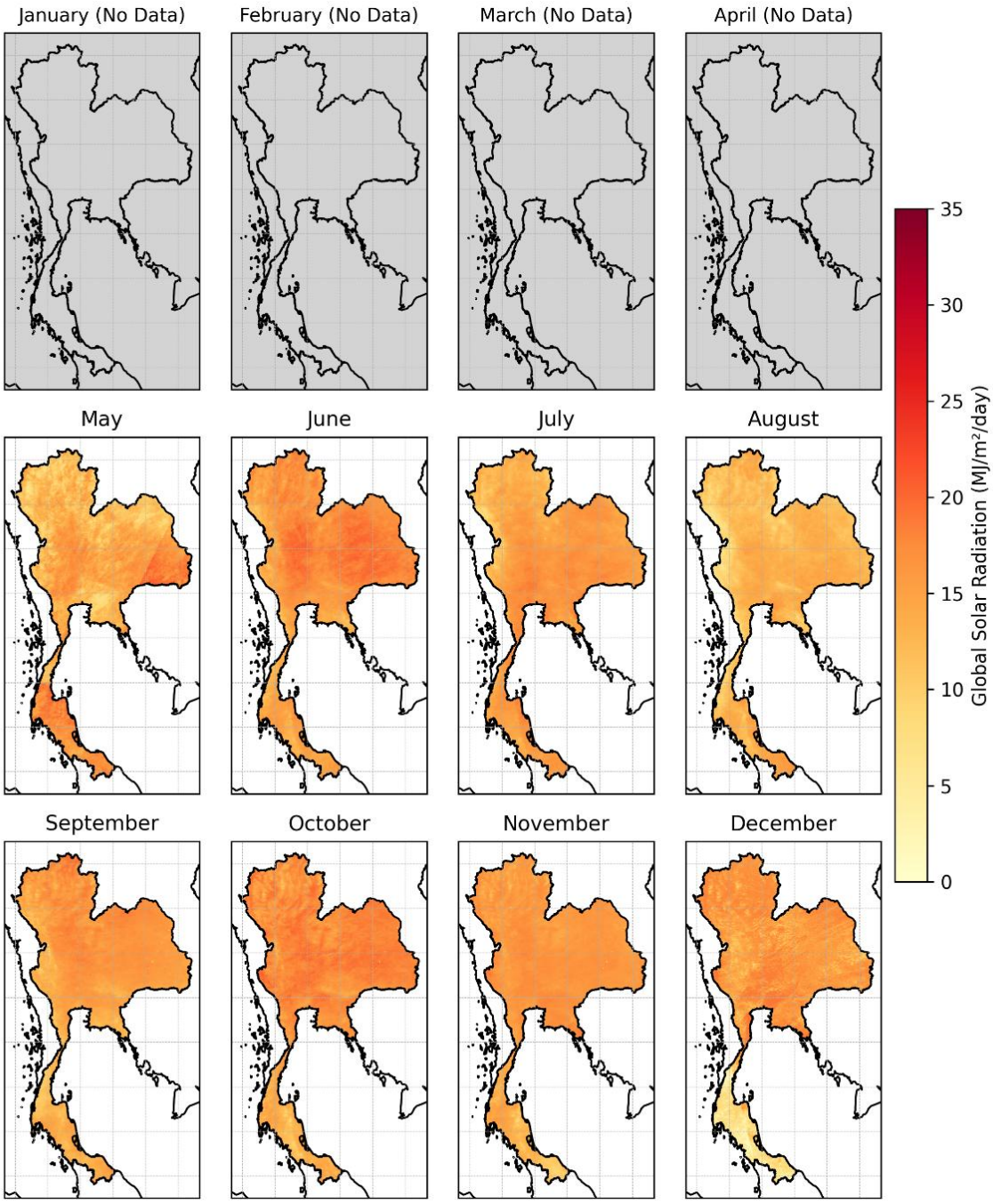


Figure 161 Monthly global solar radiation maps from MODIS for the year 2019.

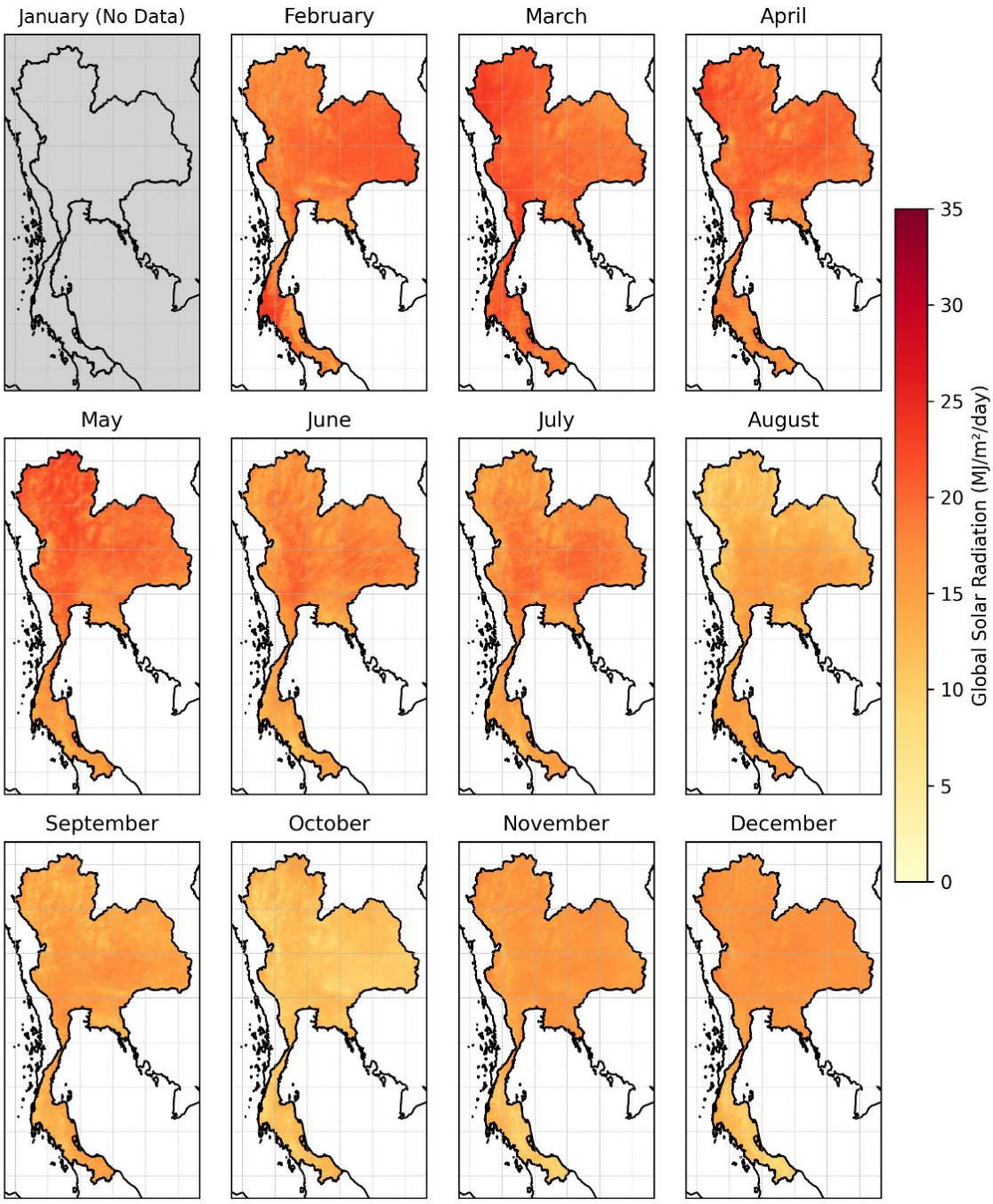


Figure 162 Monthly global solar radiation maps from MODIS for the year 2020.

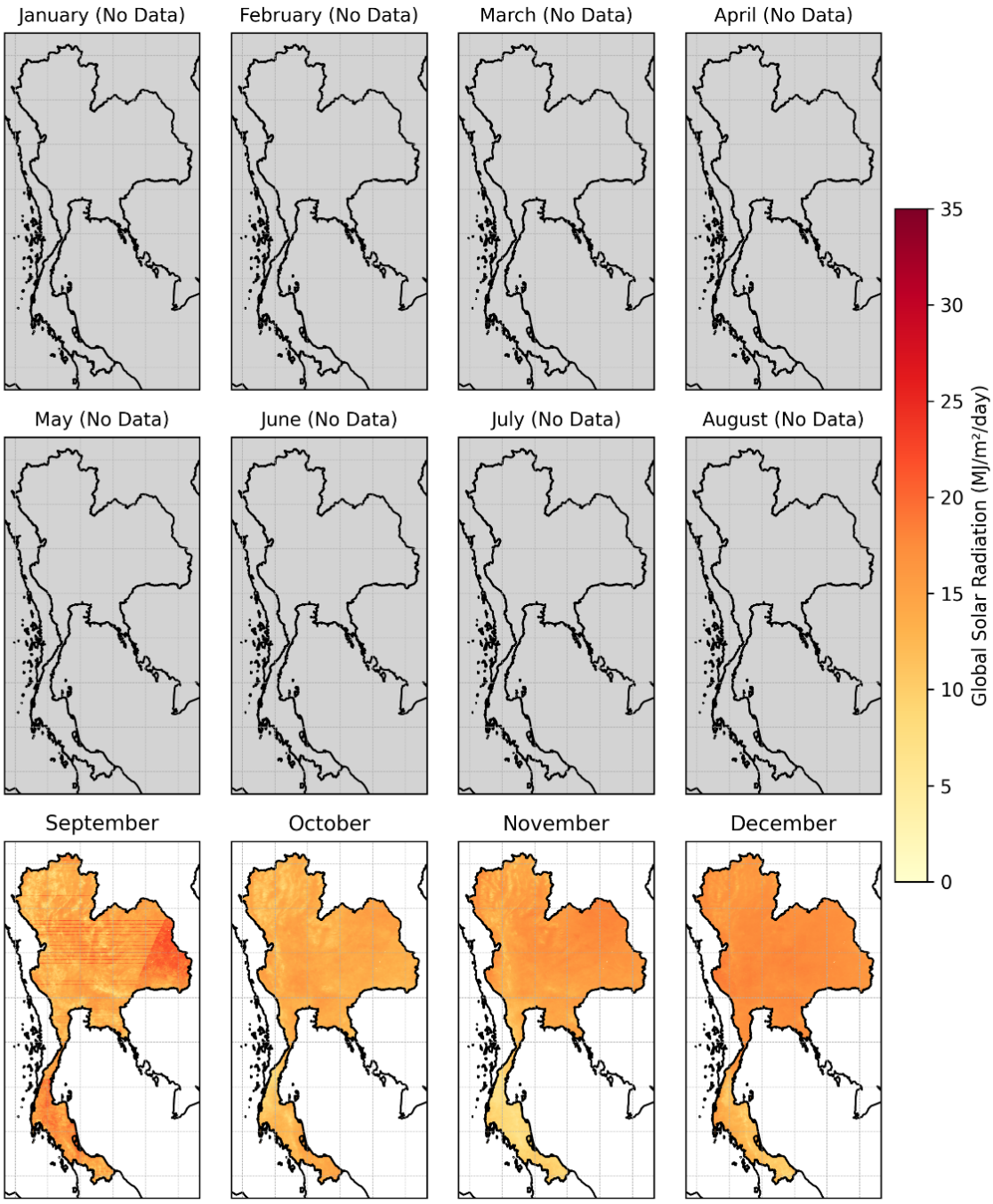


Figure 163 Monthly global solar radiation maps from MODIS for the year 2021.

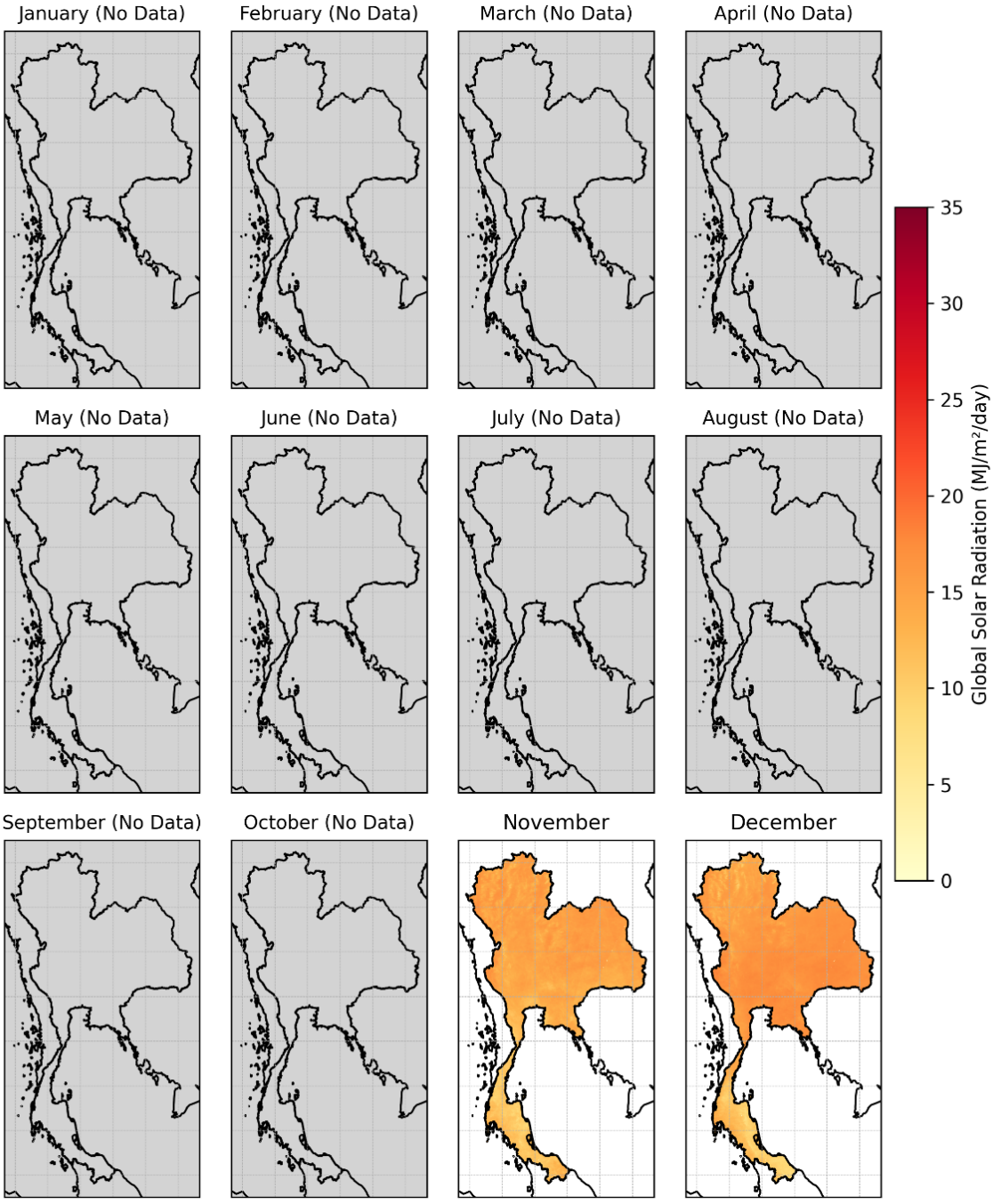


Figure 164 Monthly global solar radiation maps from MODIS for the year 2022.

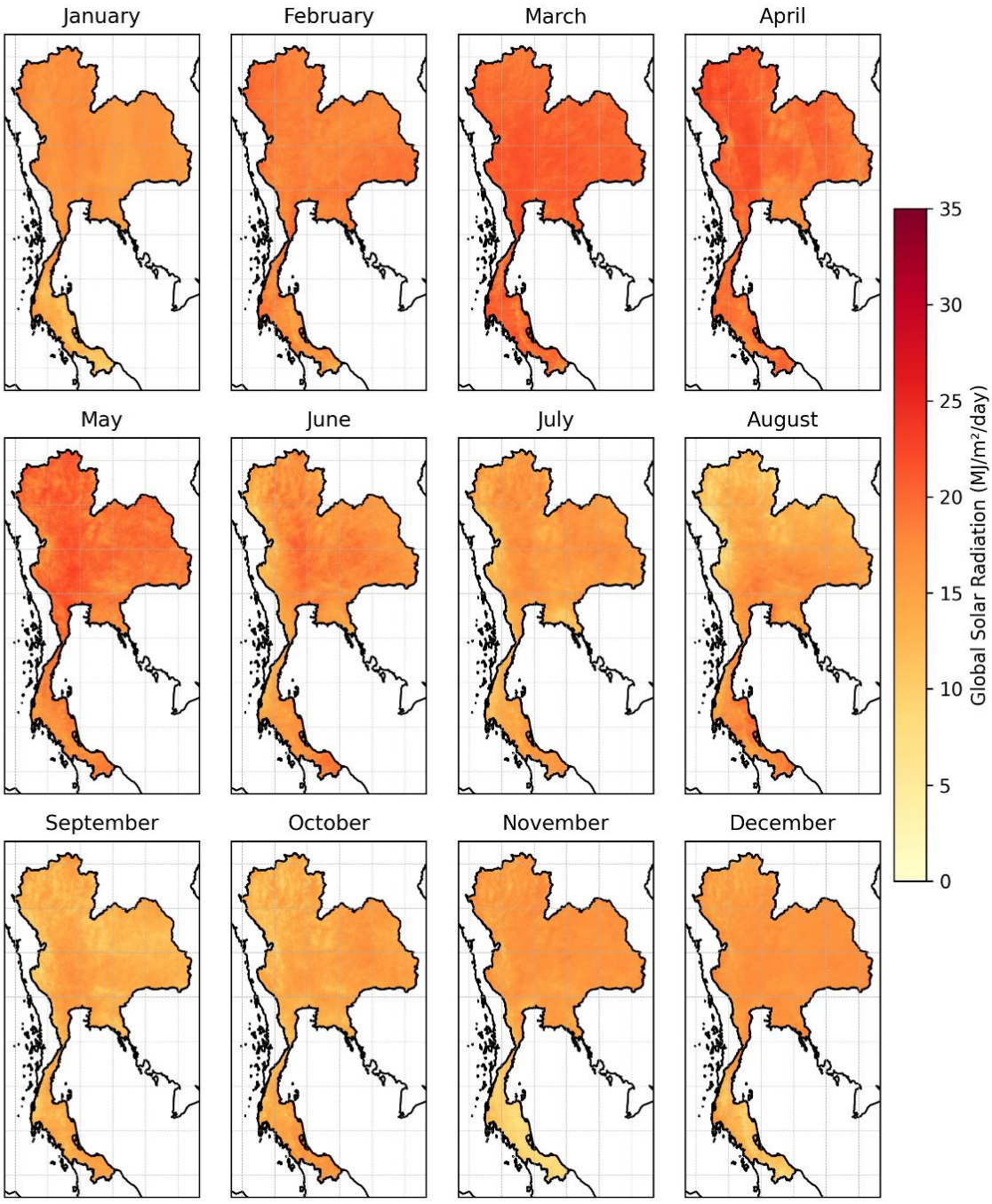


Figure 165 Monthly global solar radiation maps from MODIS for the year 2023.

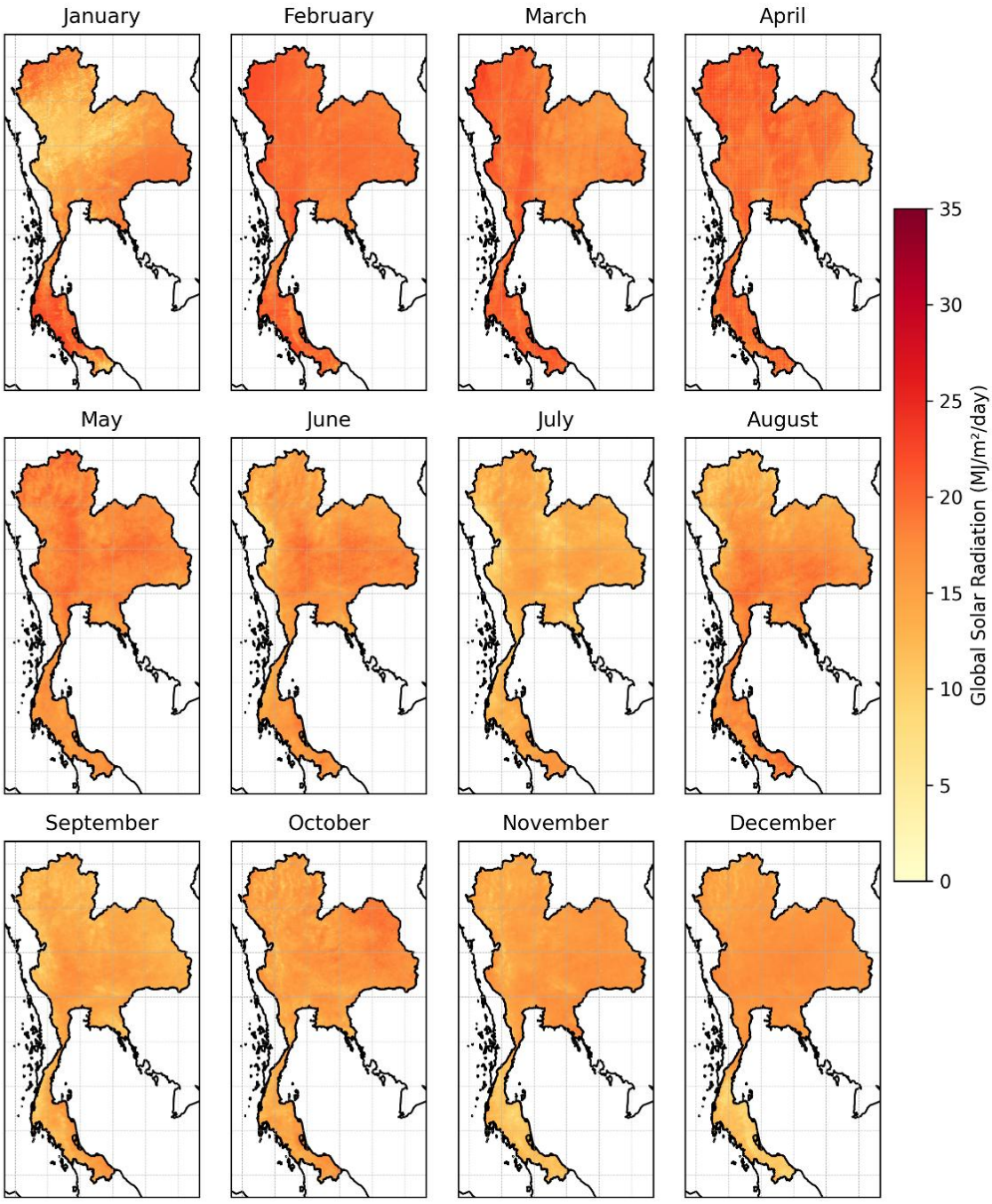


Figure 166 Monthly global solar radiation maps from MODIS for the year 2024.

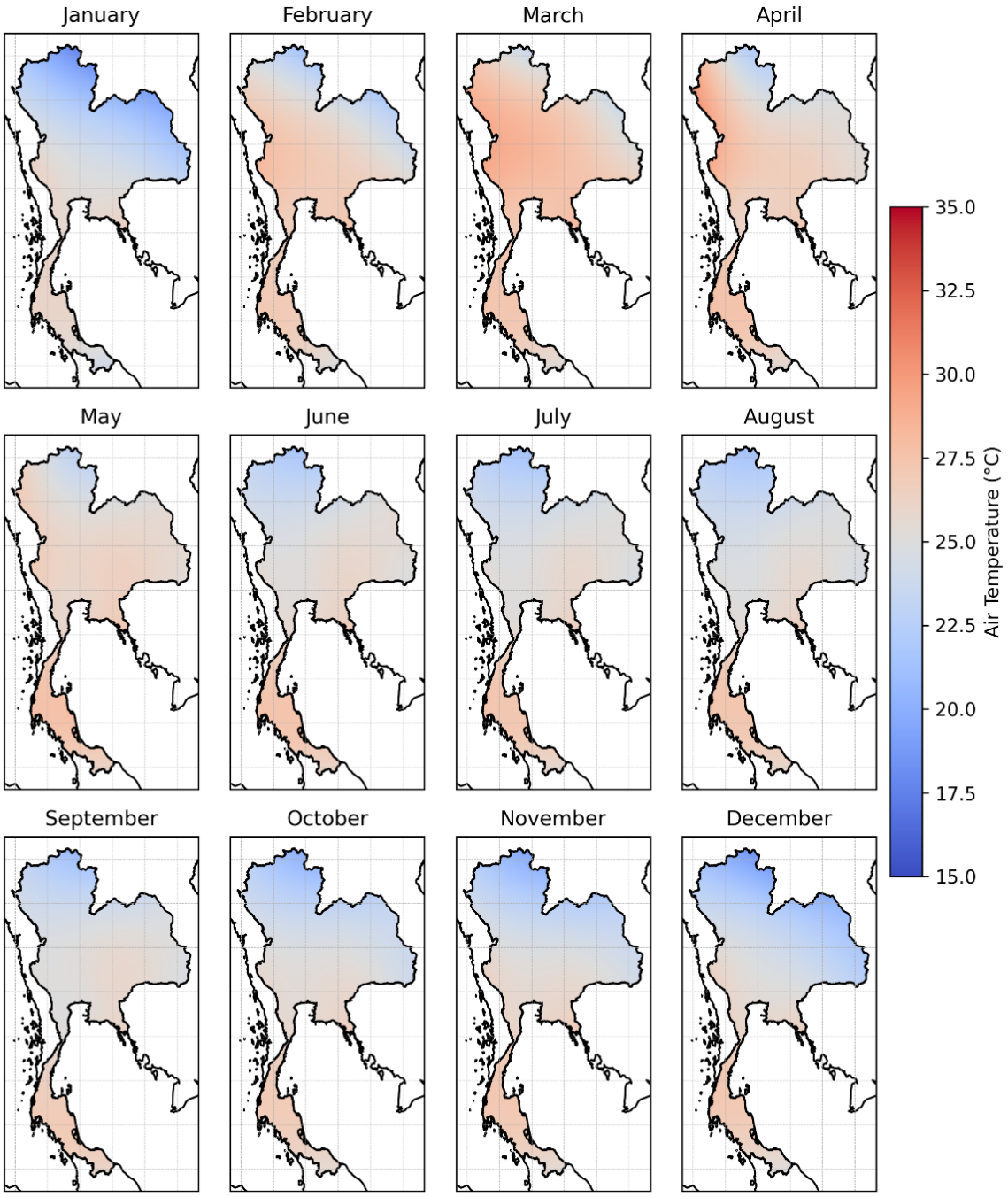


Figure 167 Monthly air temperature maps from NCEP/NCAR for the year 2012.

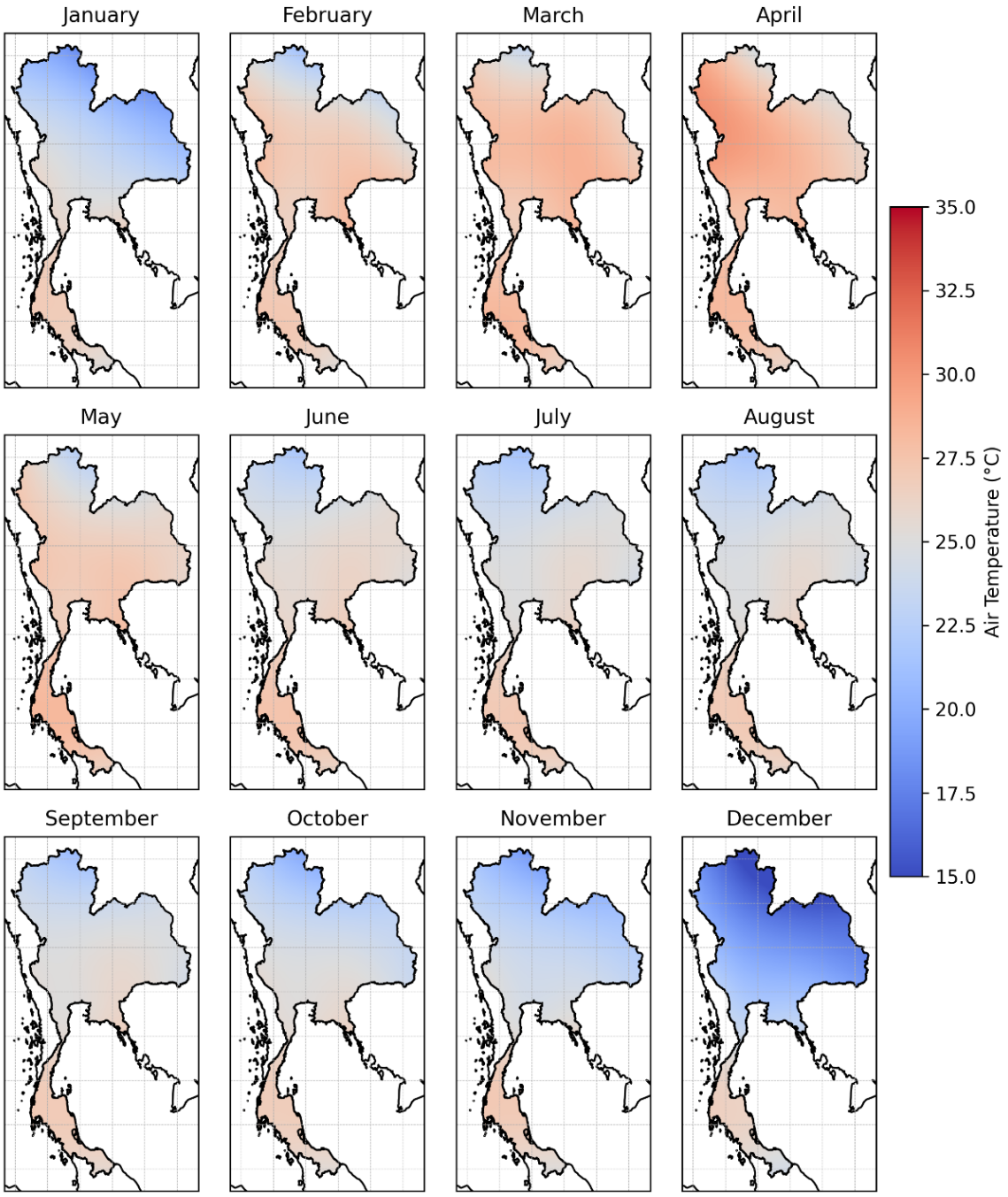


Figure 168 Monthly air temperature maps from NCEP/NCAR for the year 2013.

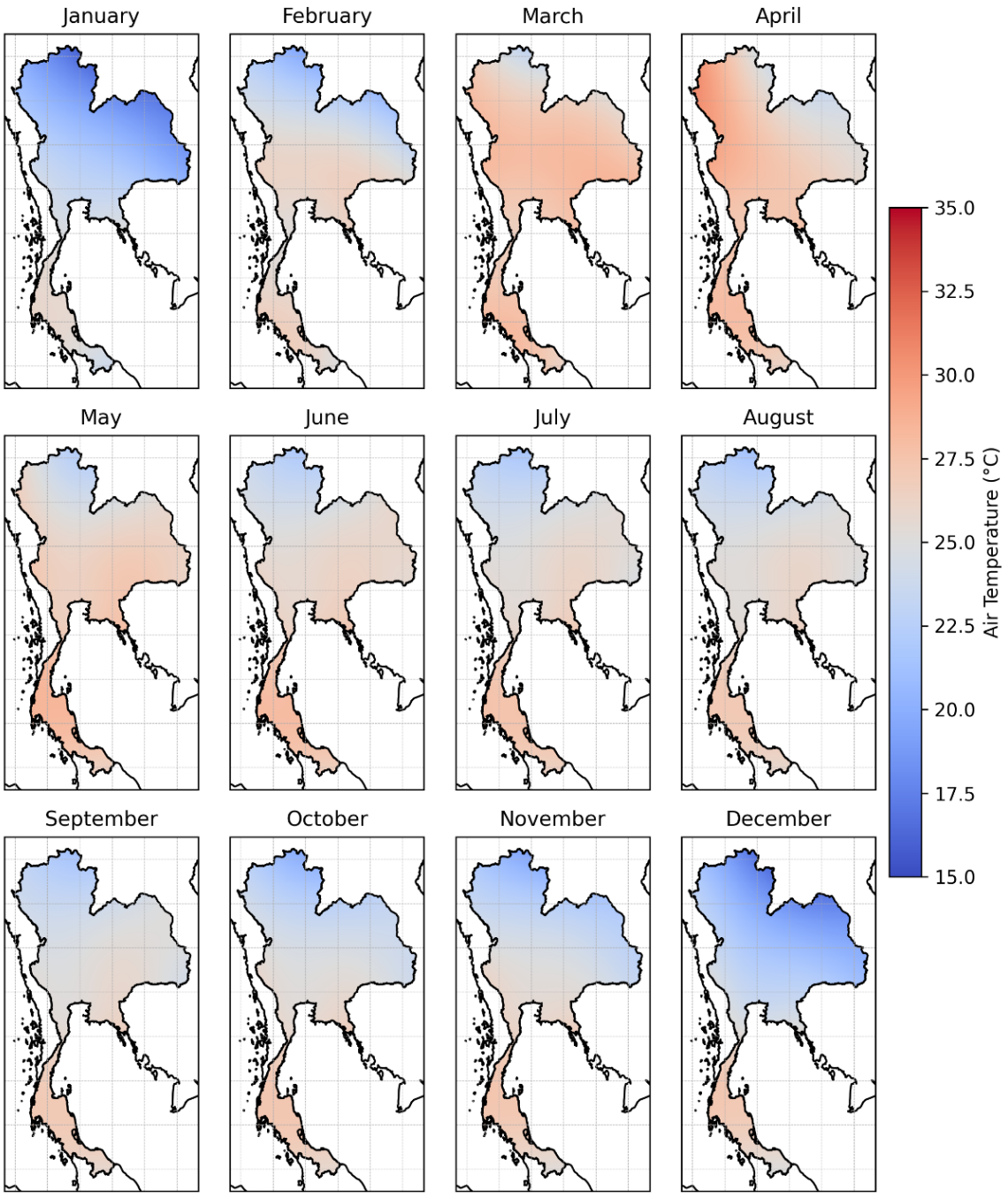


Figure 169 Monthly air temperature maps from NCEP/NCAR for the year 2014.

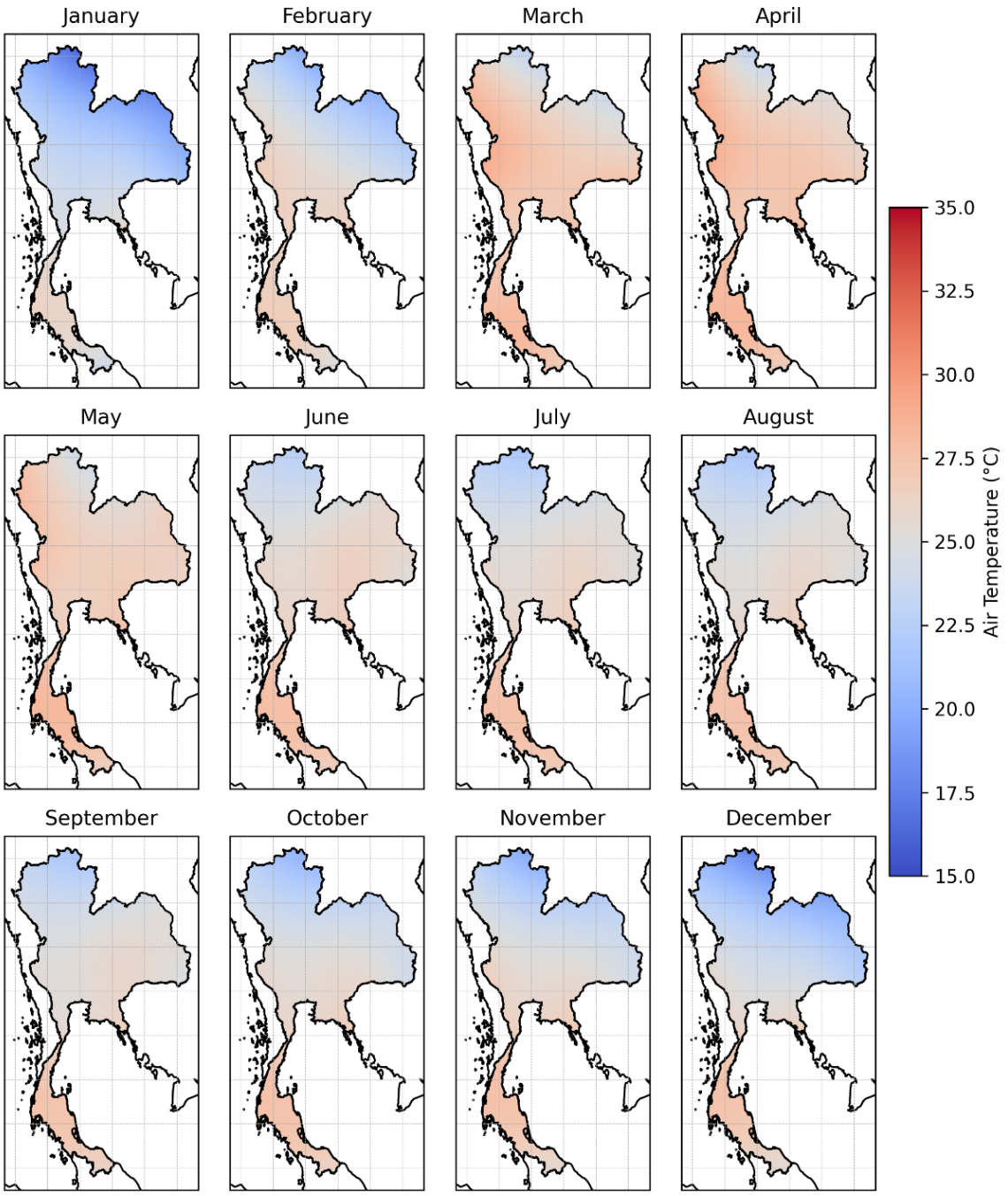


Figure 170 Monthly air temperature maps from NCEP/NCAR for the year 2015.

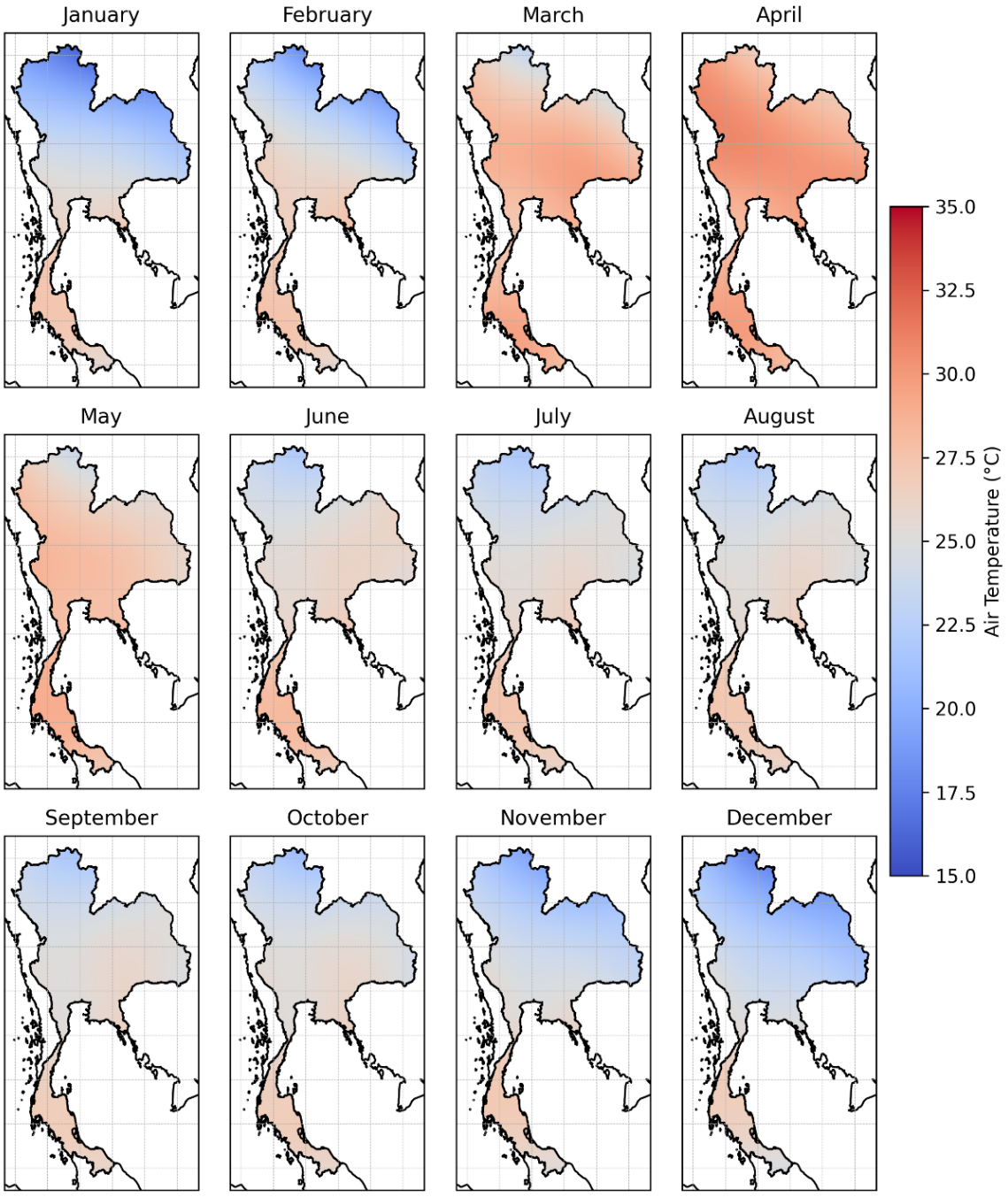


Figure 171 Monthly air temperature maps from NCEP/NCAR for the year 2016.

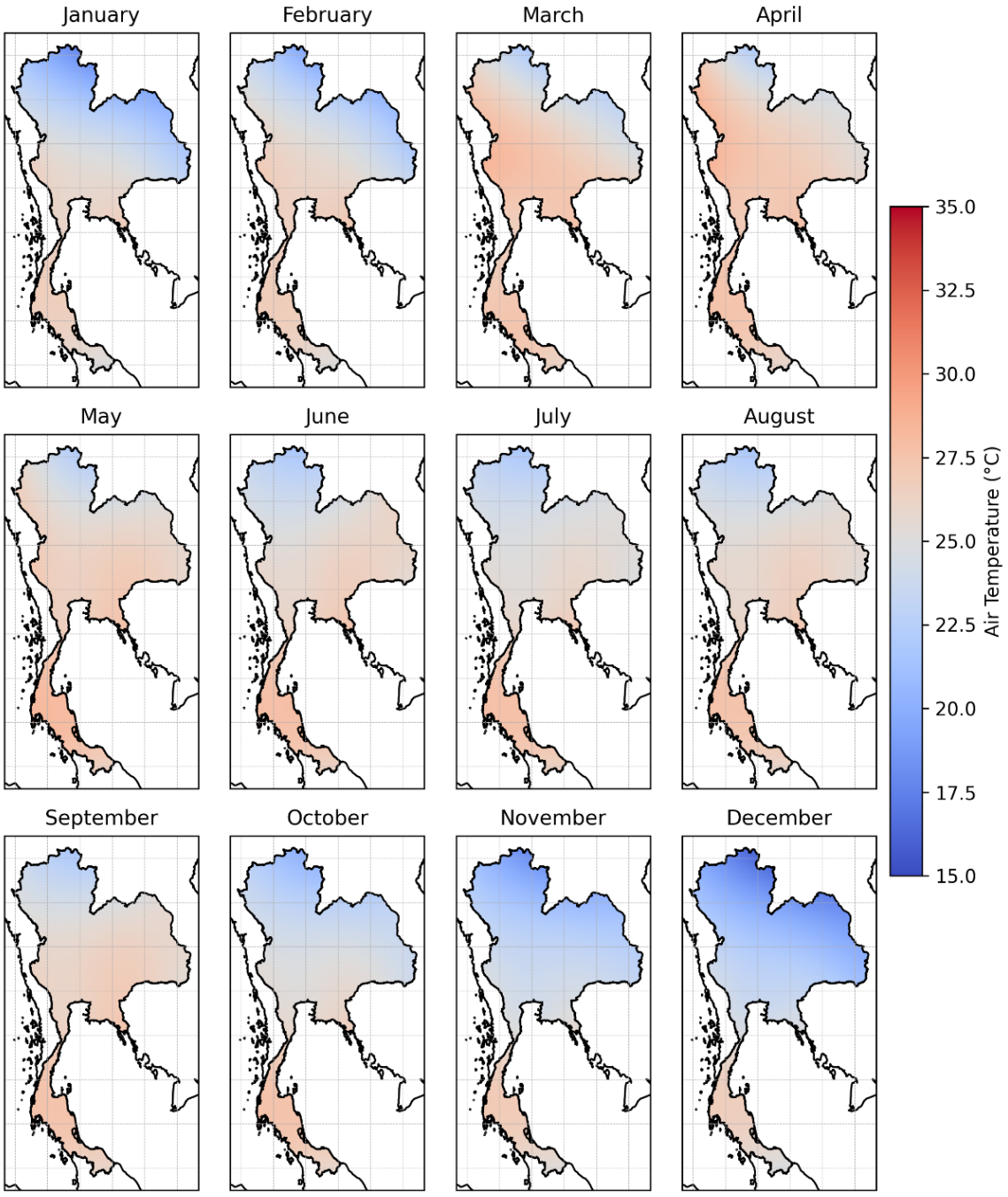


Figure 172 Monthly air temperature maps from NCEP/NCAR for the year 2017.

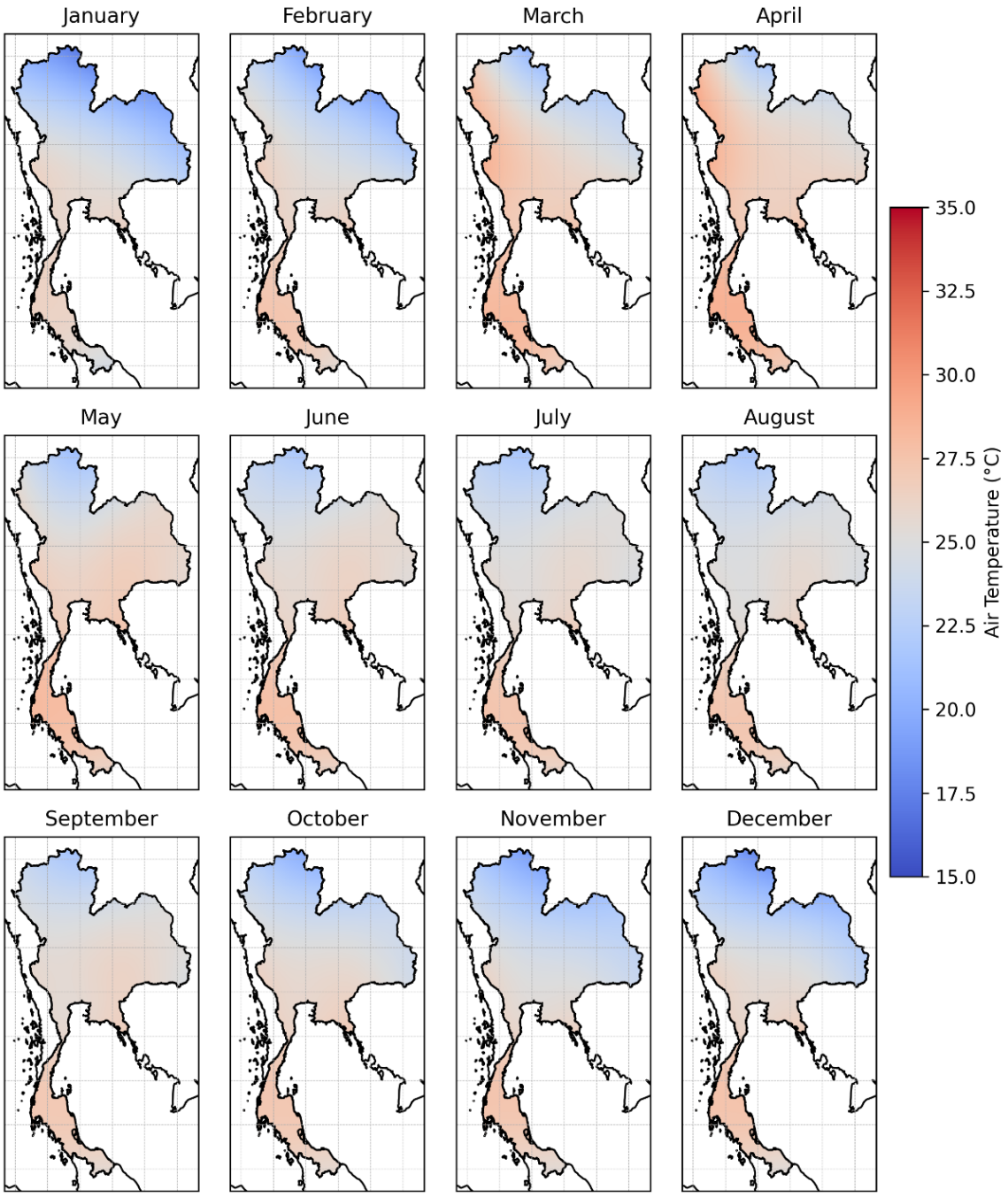


Figure 173 Monthly air temperature maps from NCEP/NCAR for the year 2018.

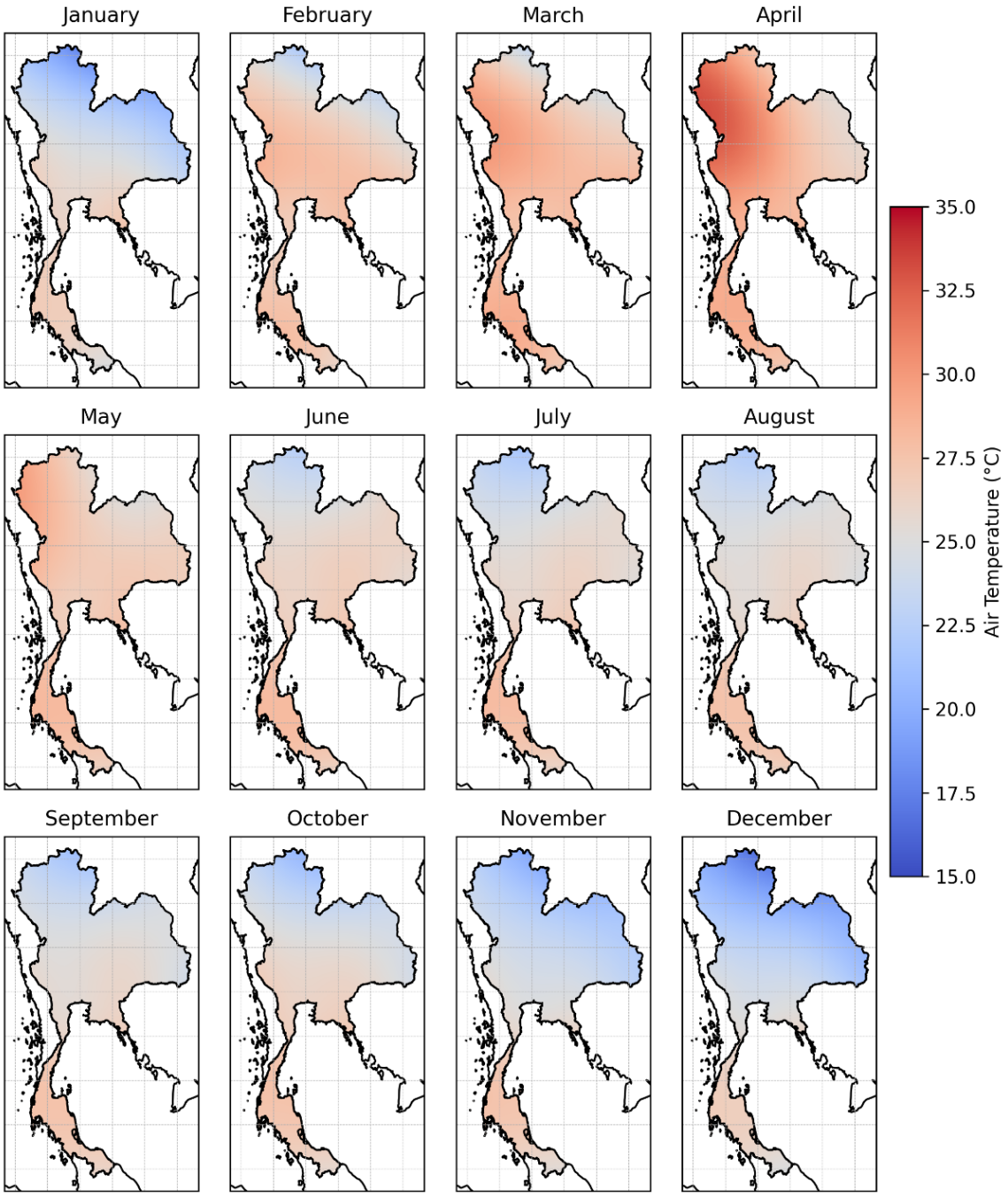


Figure 174 Monthly air temperature maps from NCEP/NCAR for the year 2019.

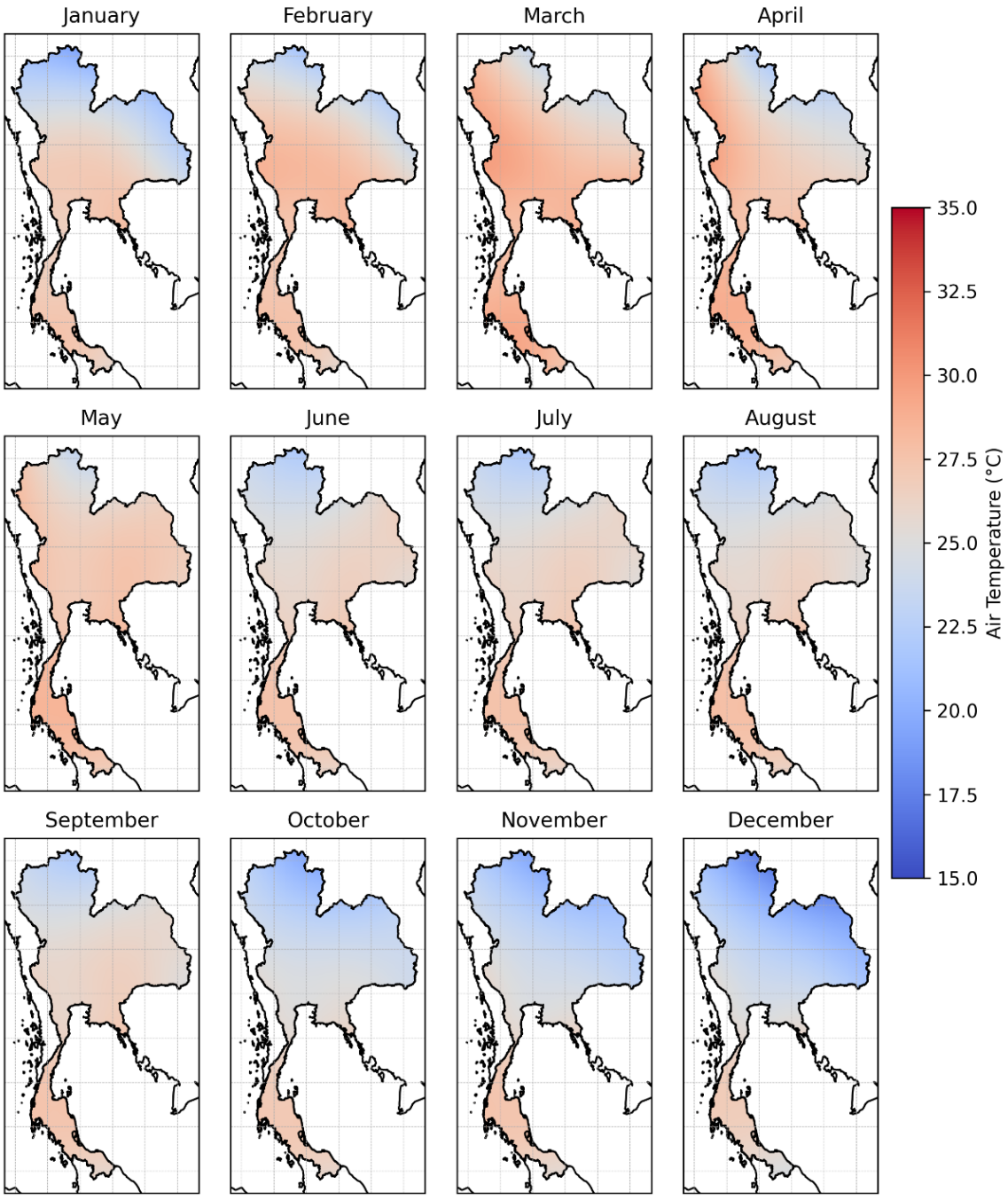


Figure 175 Monthly air temperature maps from NCEP/NCAR for the year 2020.

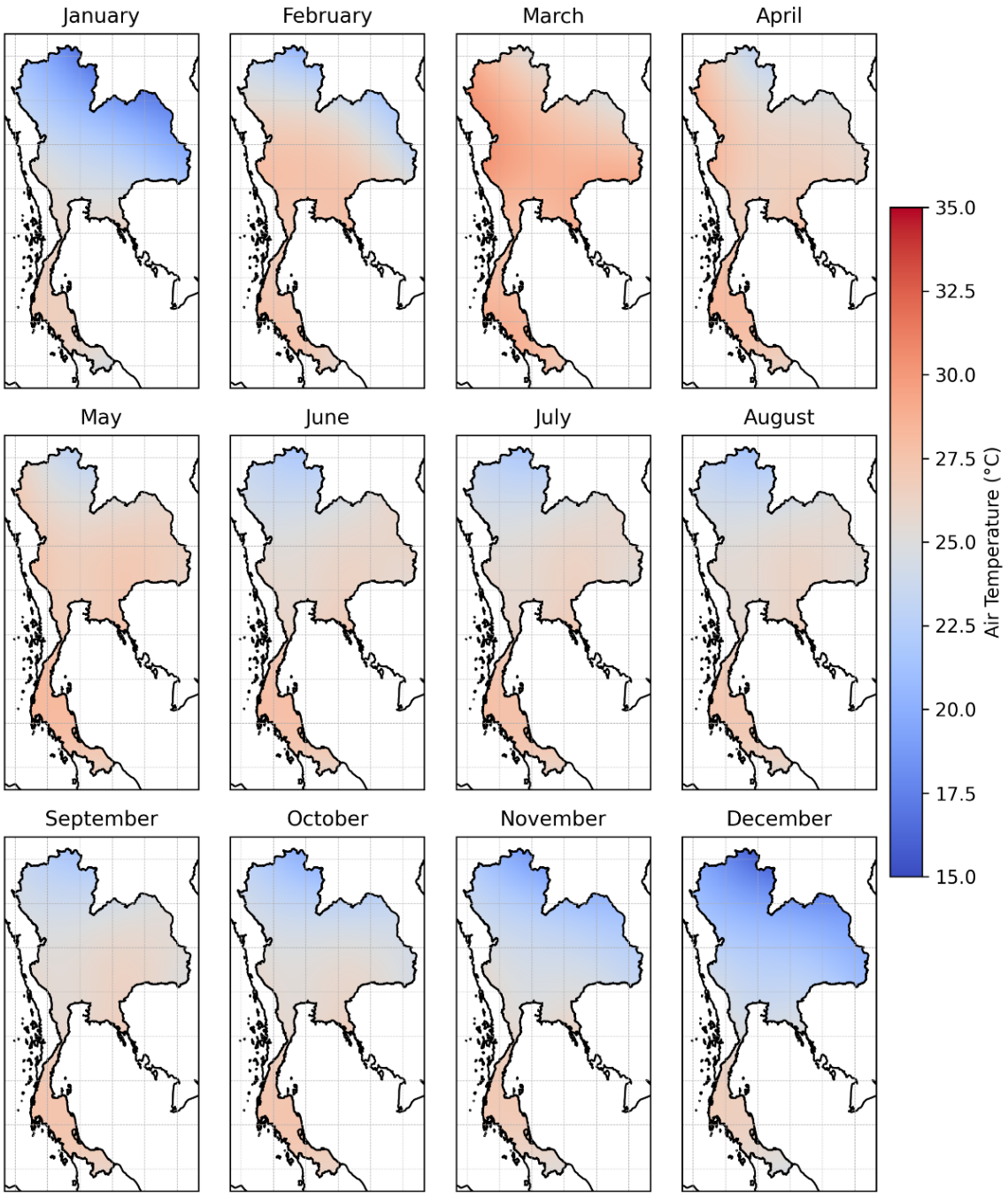


Figure 176 Monthly air temperature maps from NCEP/NCAR for the year 2021.

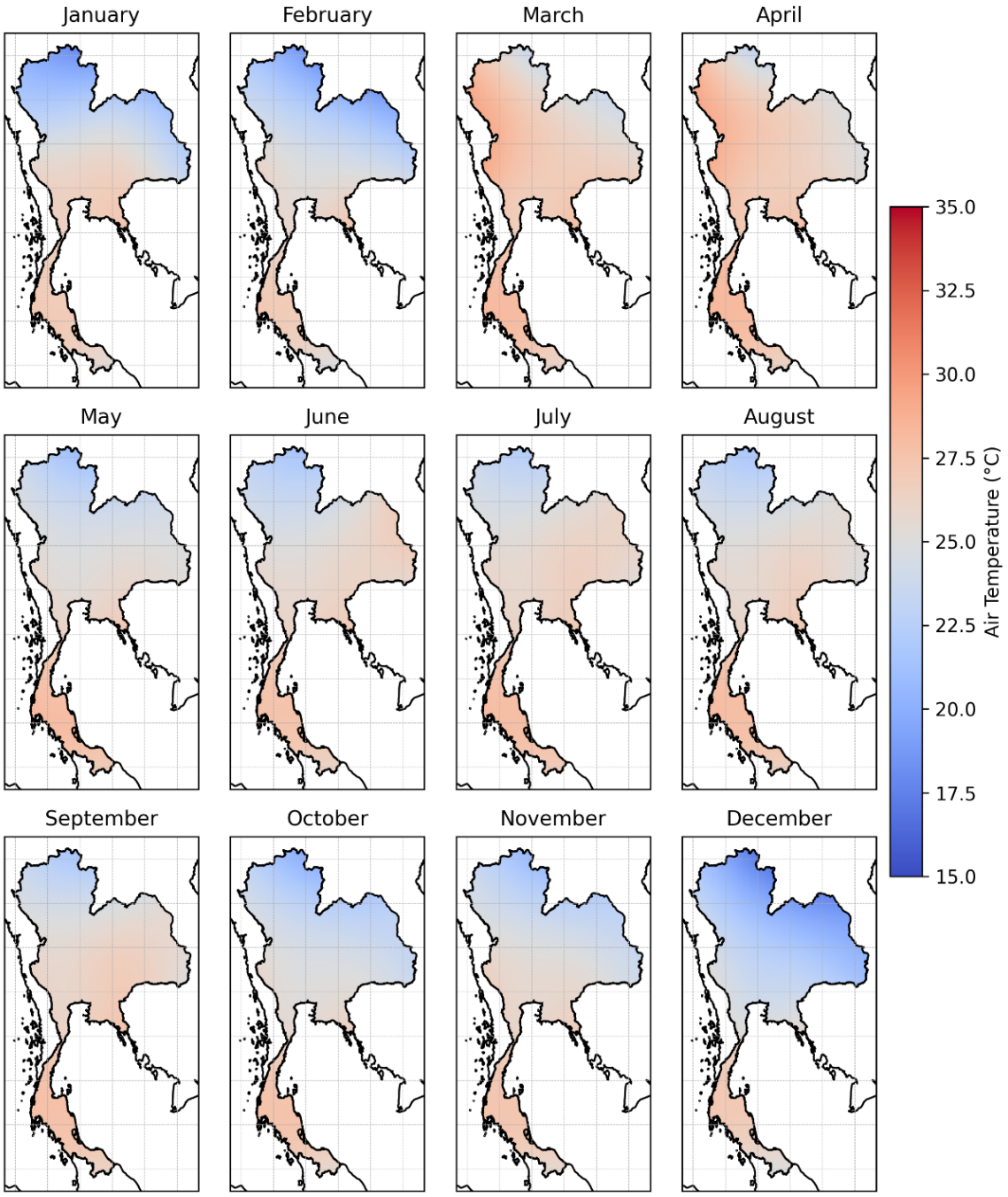


Figure 177 Monthly air temperature maps from NCEP/NCAR for the year 2022.

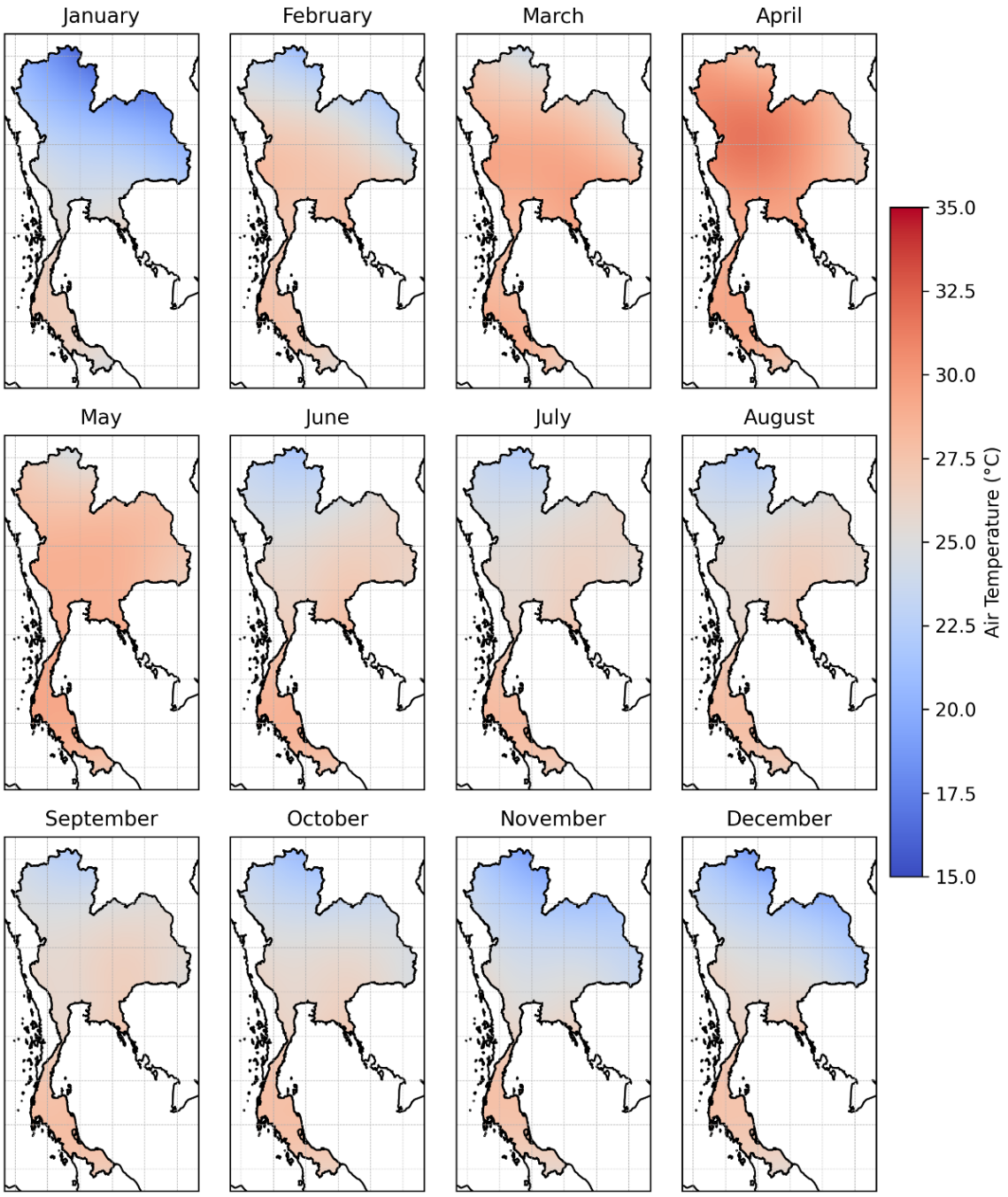


Figure 178 Monthly air temperature maps from NCEP/NCAR for the year 2023.

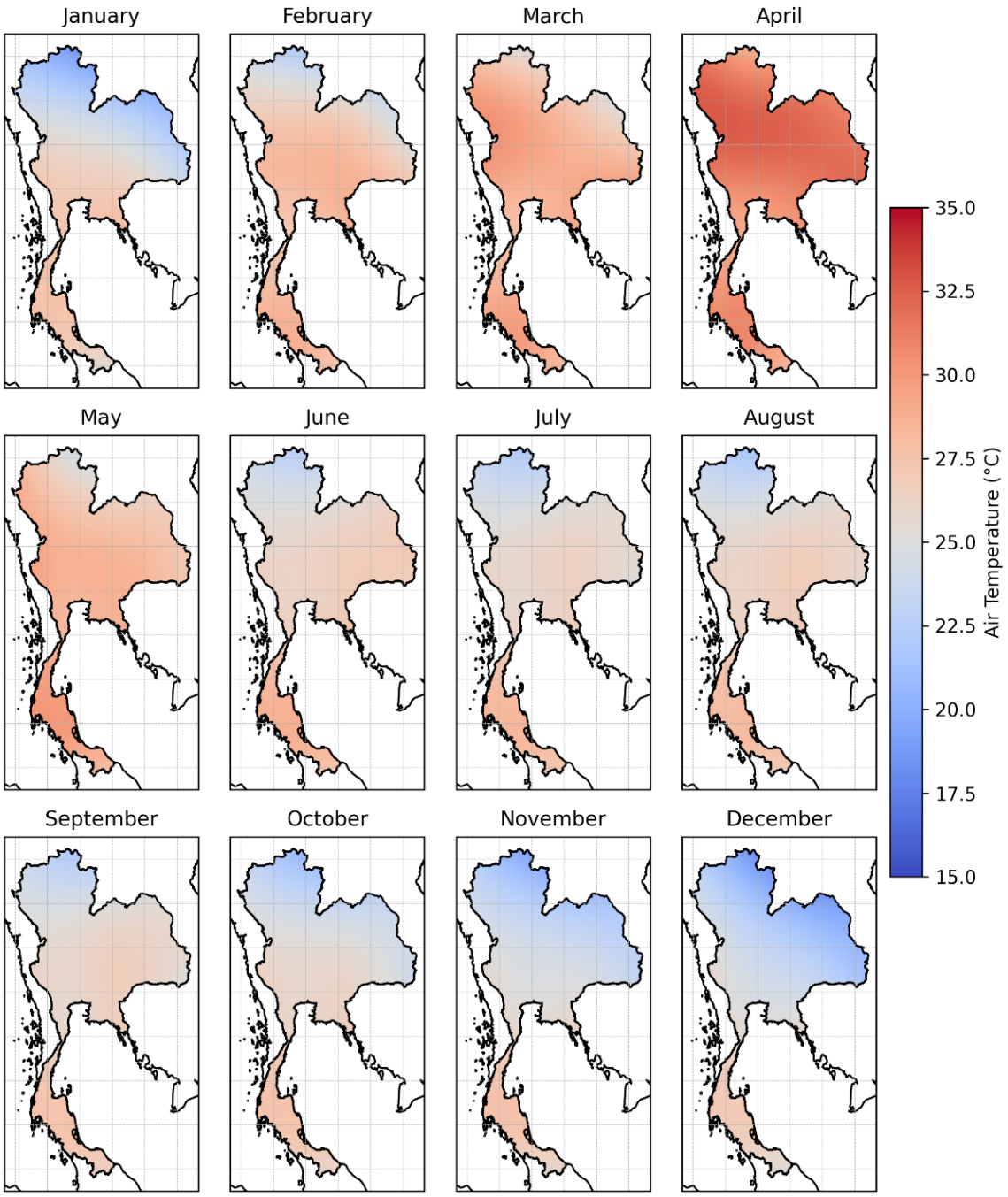


Figure 179 Monthly air temperature maps from NCEP/NCAR for the year 2024.

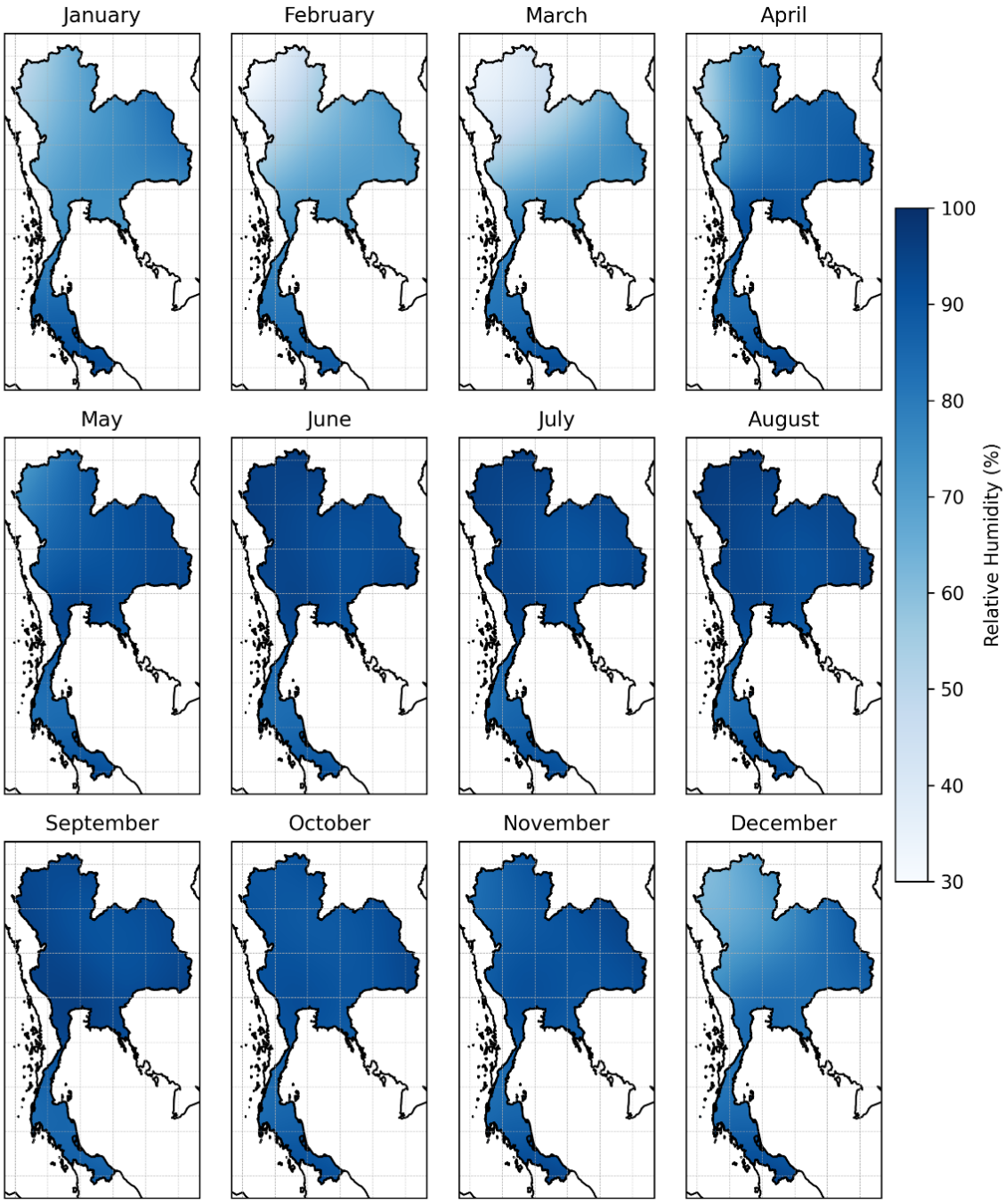


Figure 180 Monthly relative humidity maps from NCEP/NCAR for the year 2012.

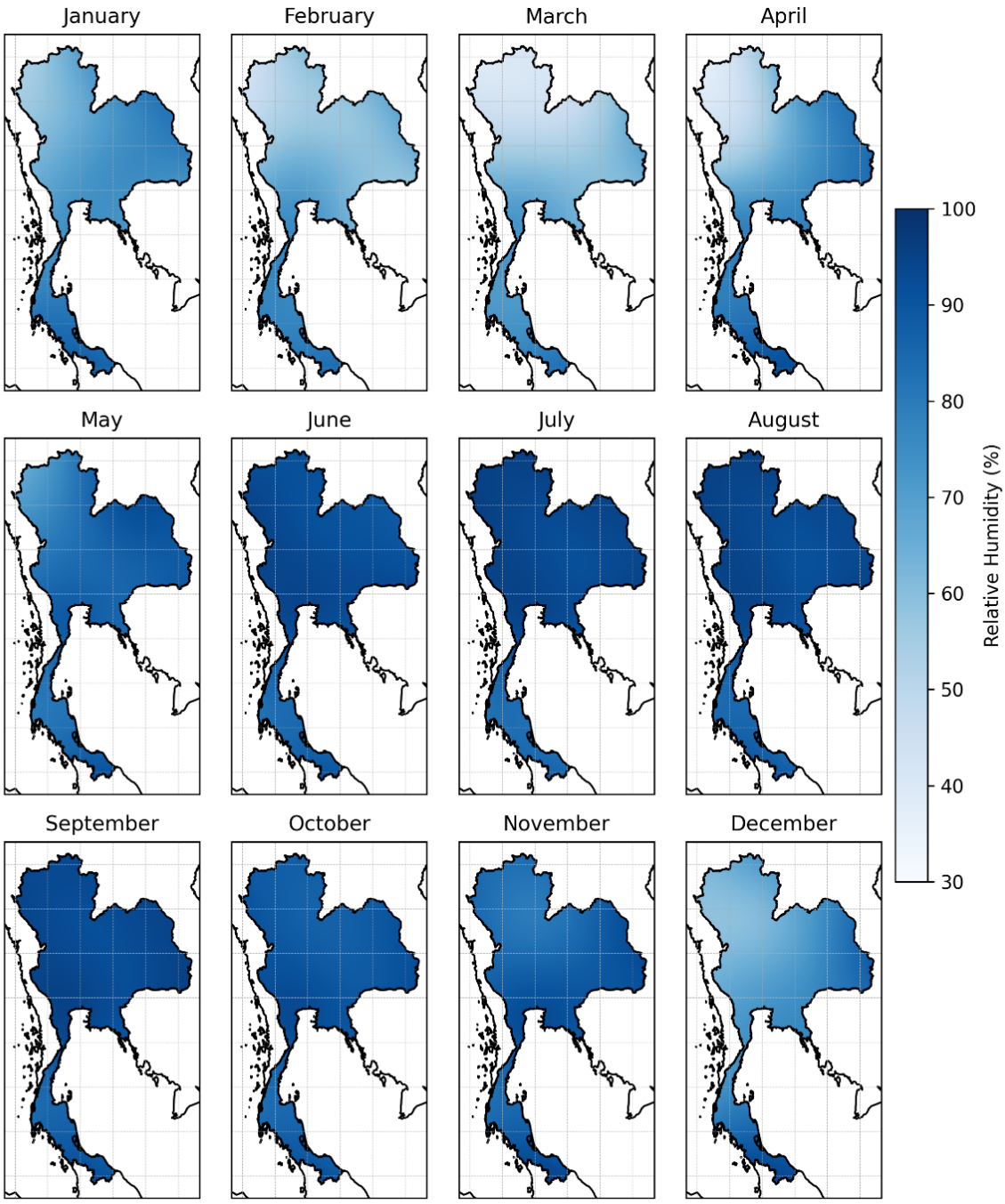


Figure 181 Monthly relative humidity maps from NCEP/NCAR for the year 2013.

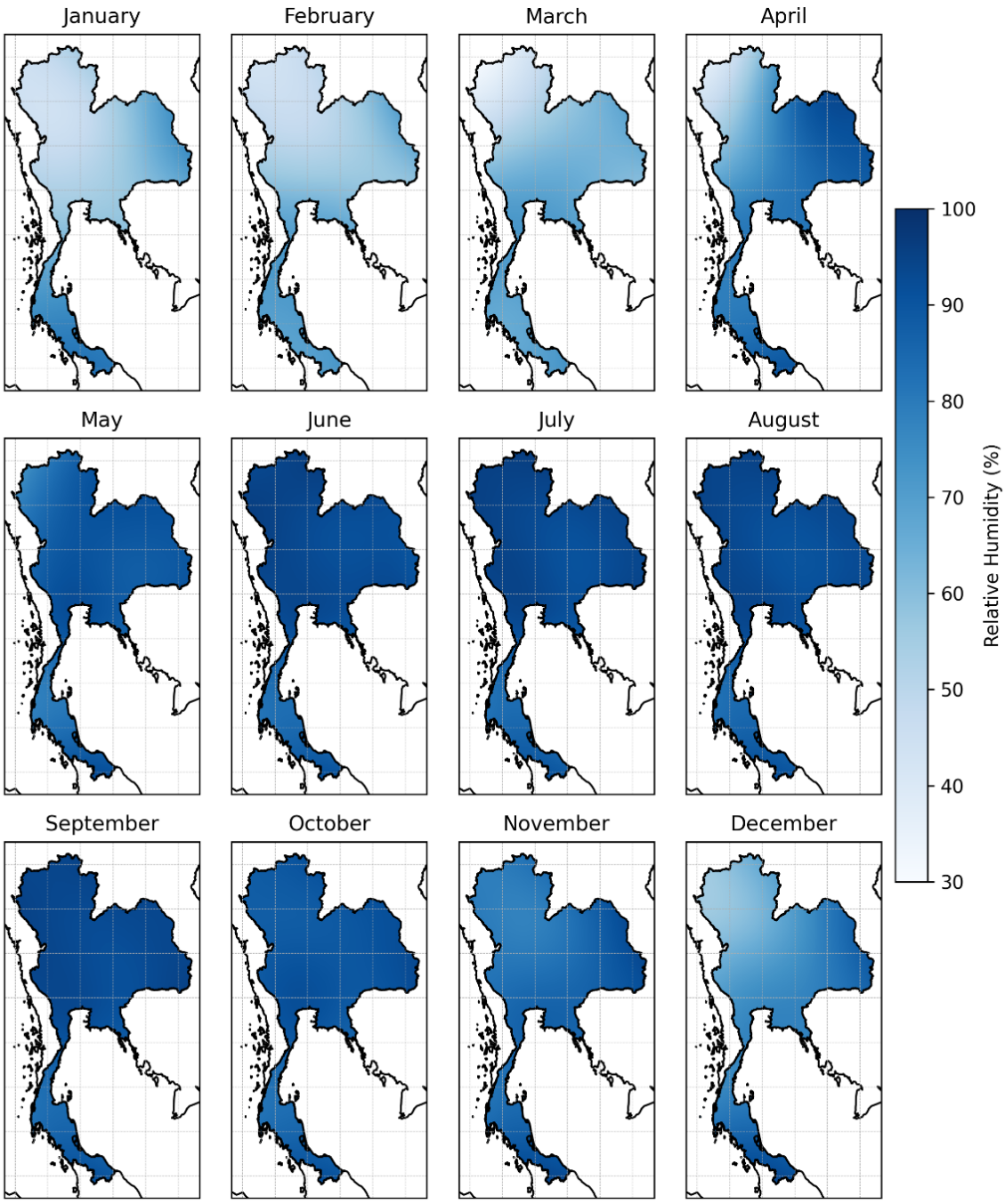


Figure 182 Monthly relative humidity maps from NCEP/NCAR for the year 2014.

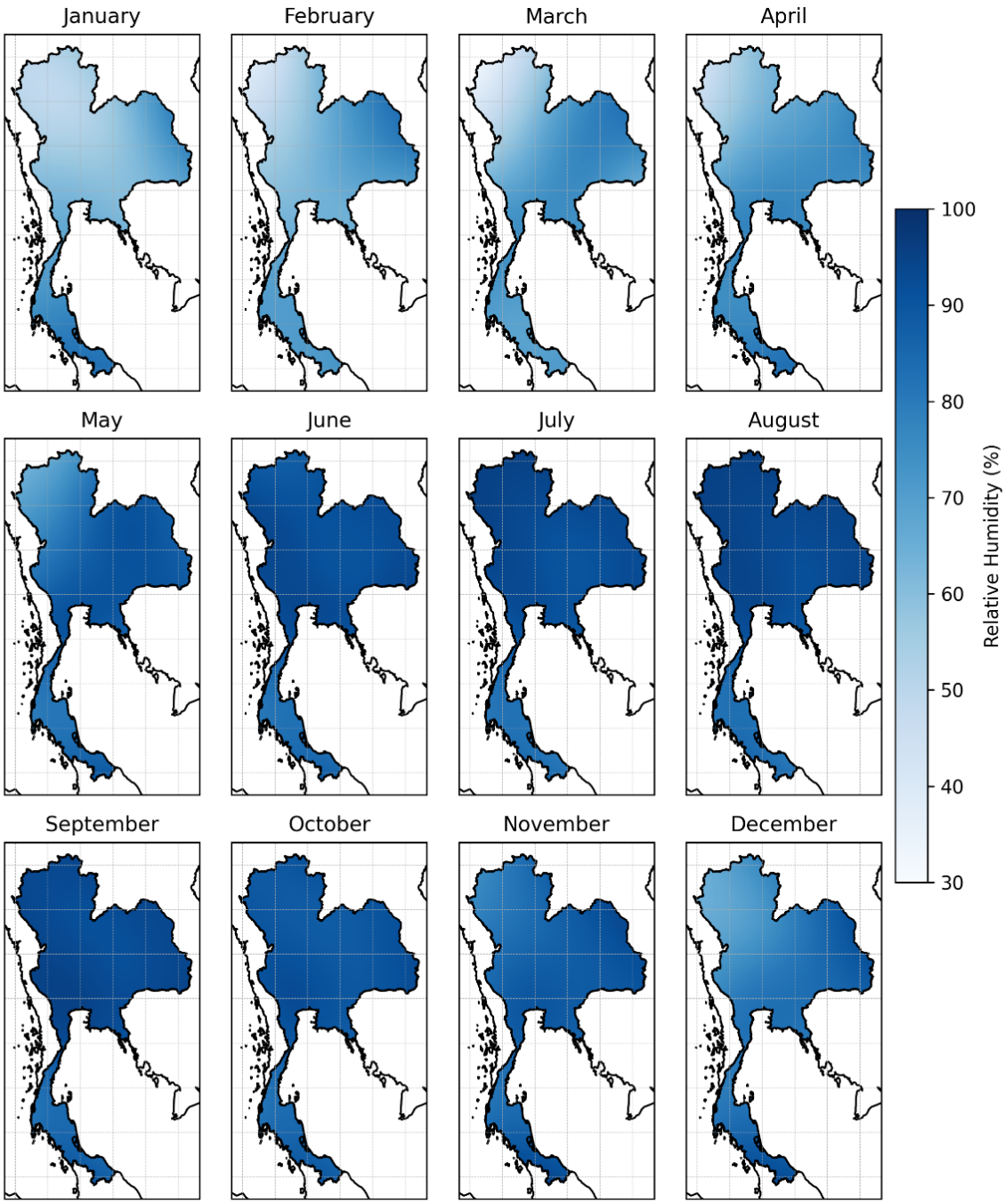


Figure 183 Monthly relative humidity maps from NCEP/NCAR for the year 2015.

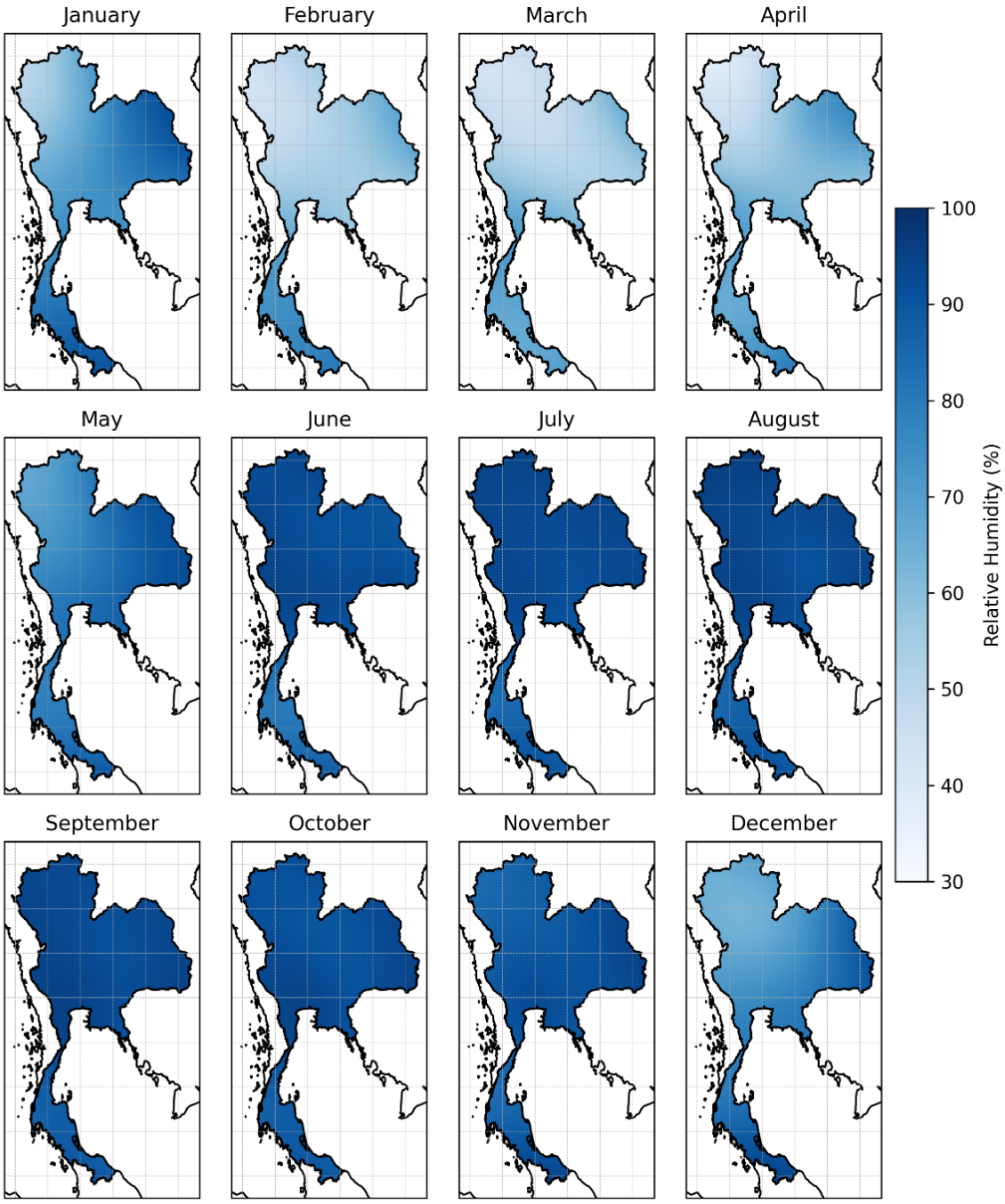


Figure 184 Monthly relative humidity maps from NCEP/NCAR for the year 2016.

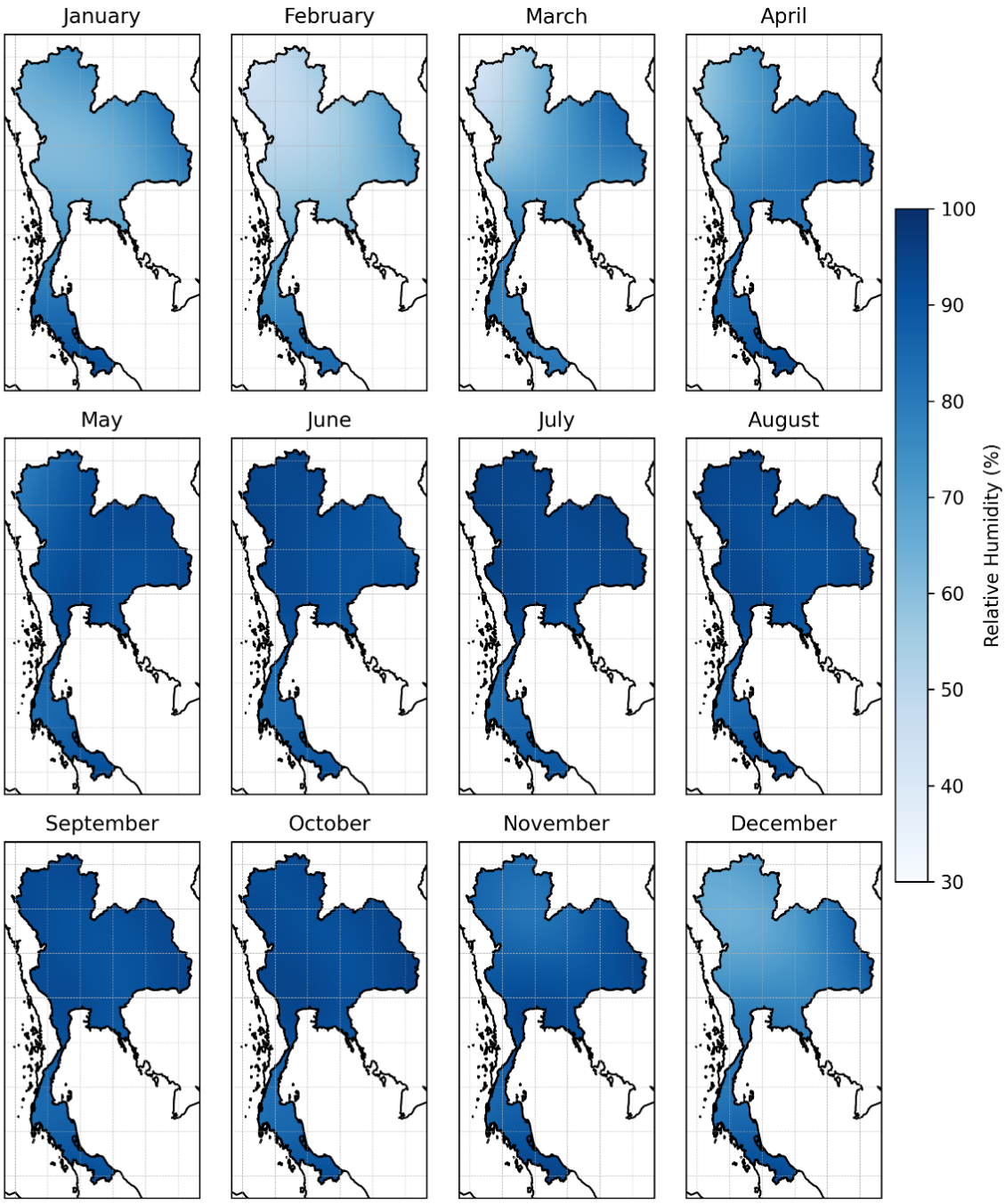


Figure 185 Monthly relative humidity maps from NCEP/NCAR for the year 2017.

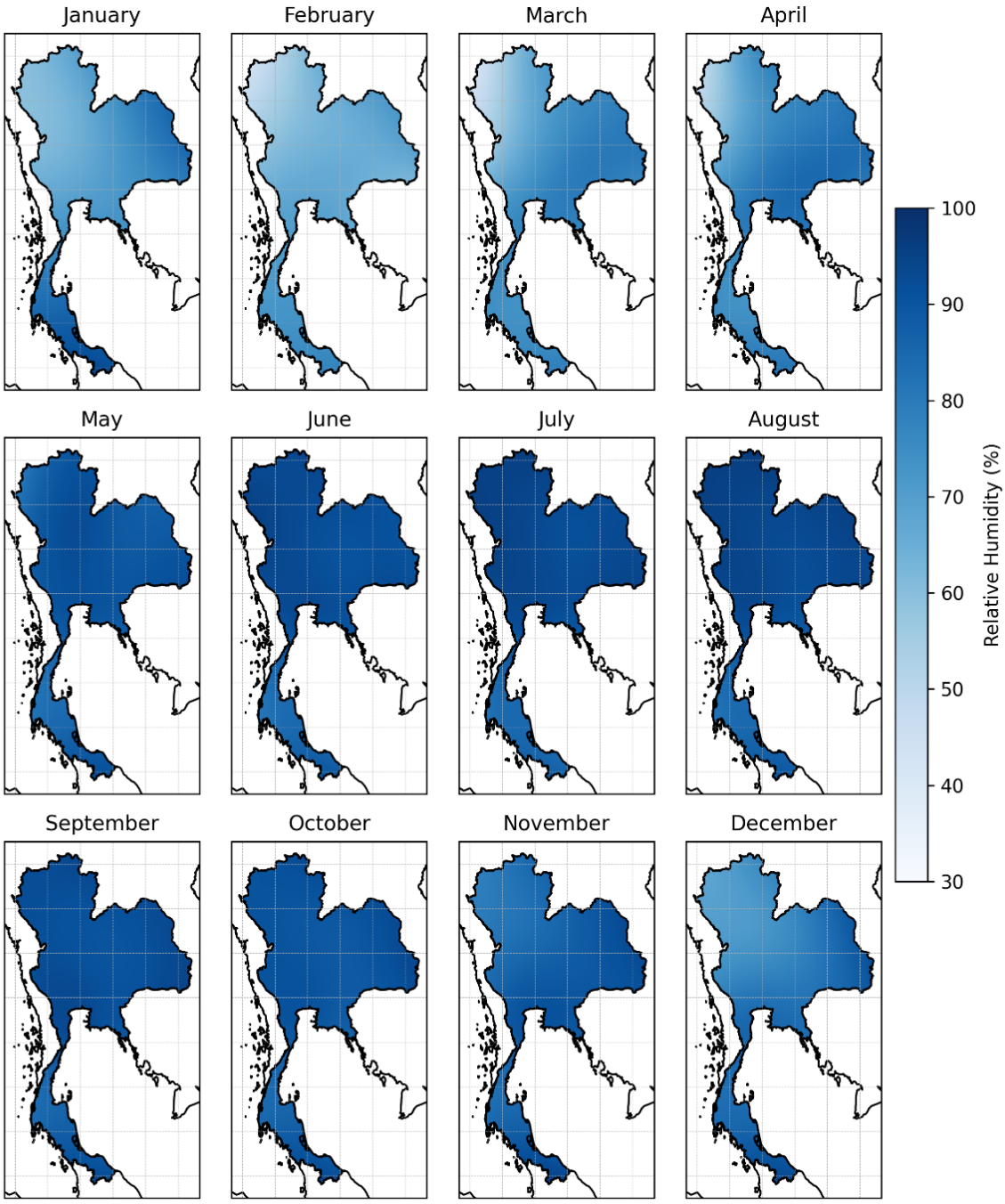


Figure 186 Monthly relative humidity maps from NCEP/NCAR for the year 2018.

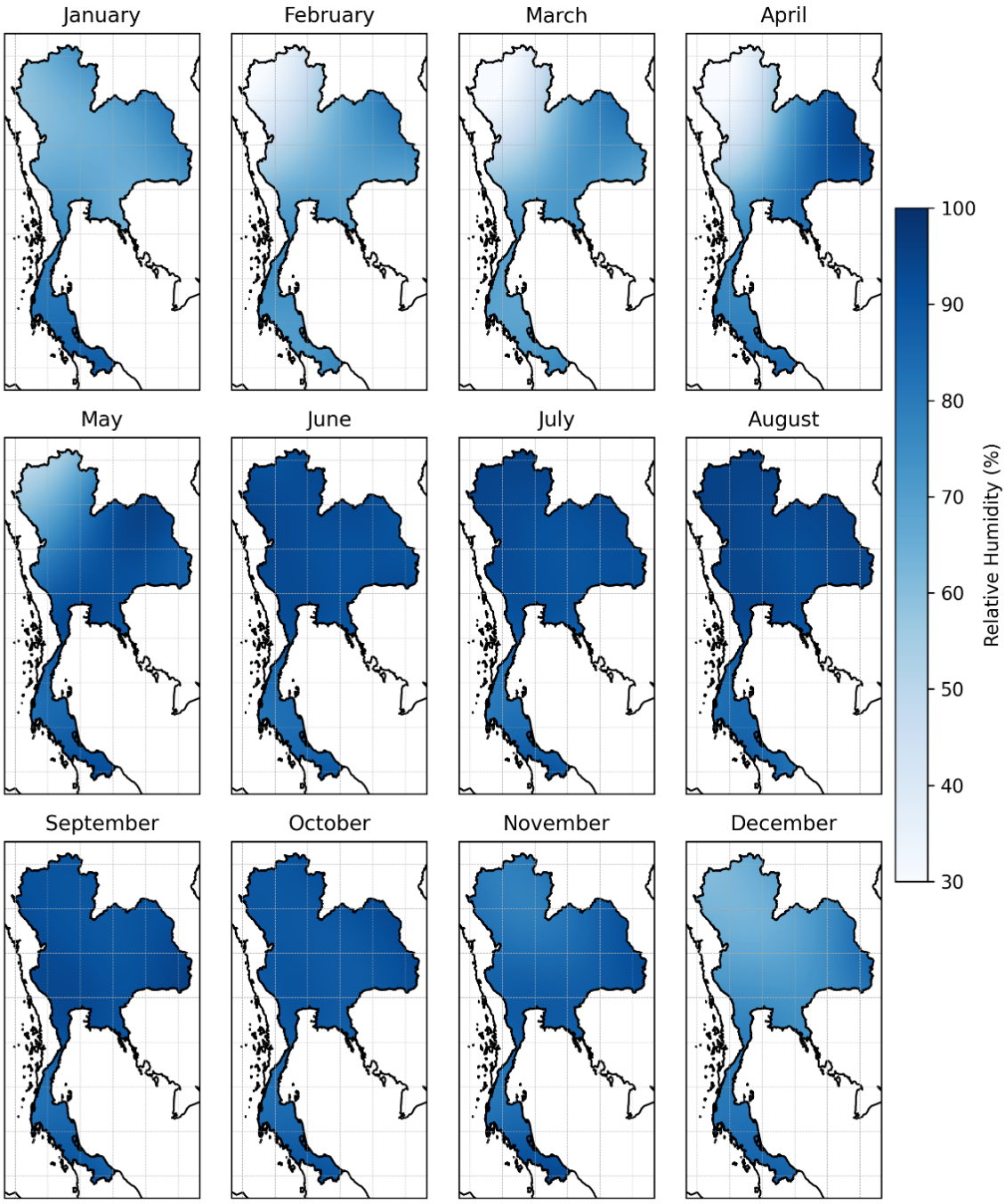


Figure 187 Monthly relative humidity maps from NCEP/NCAR for the year 2019.

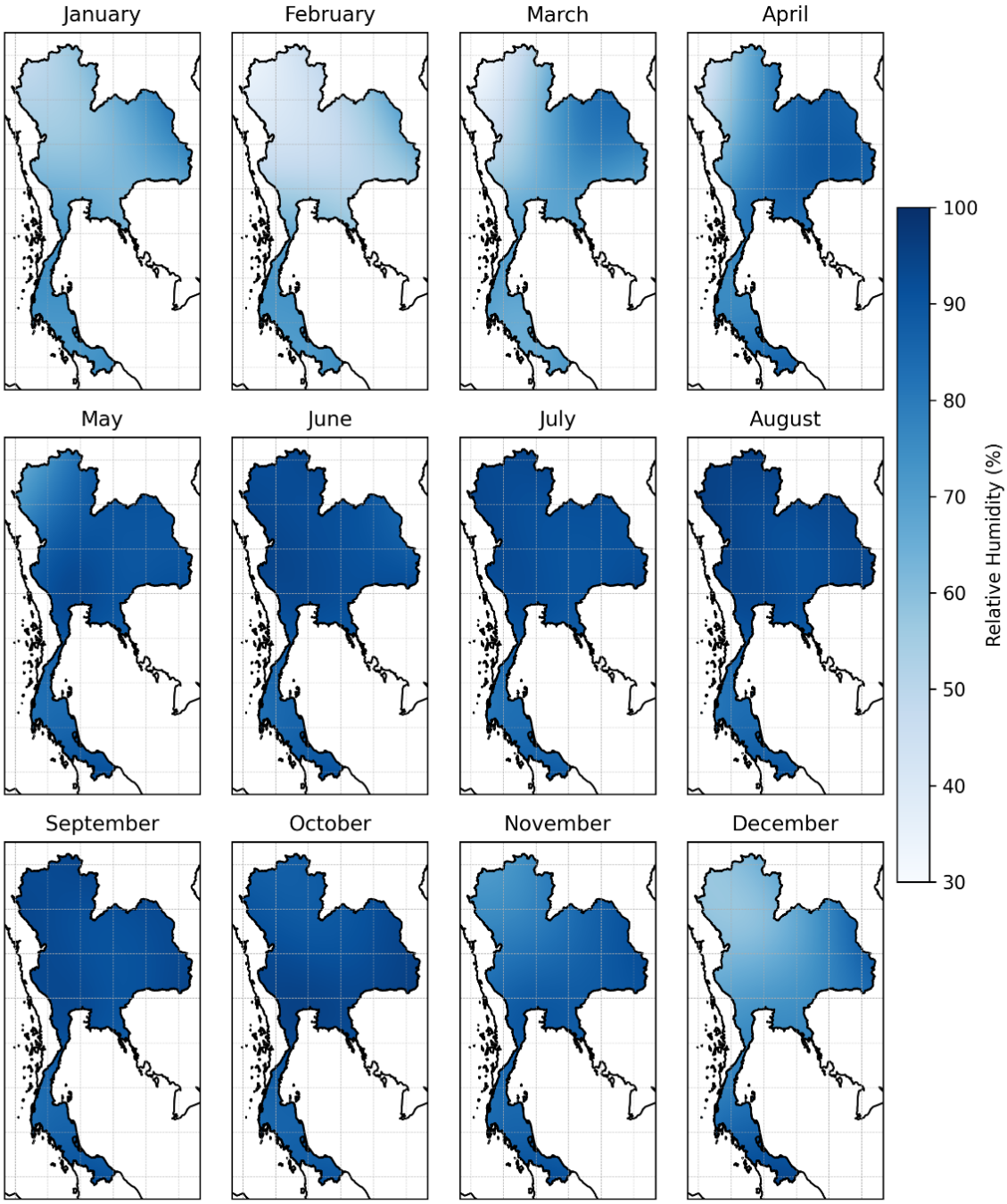


Figure 188 Monthly relative humidity maps from NCEP/NCAR for the year 2020.

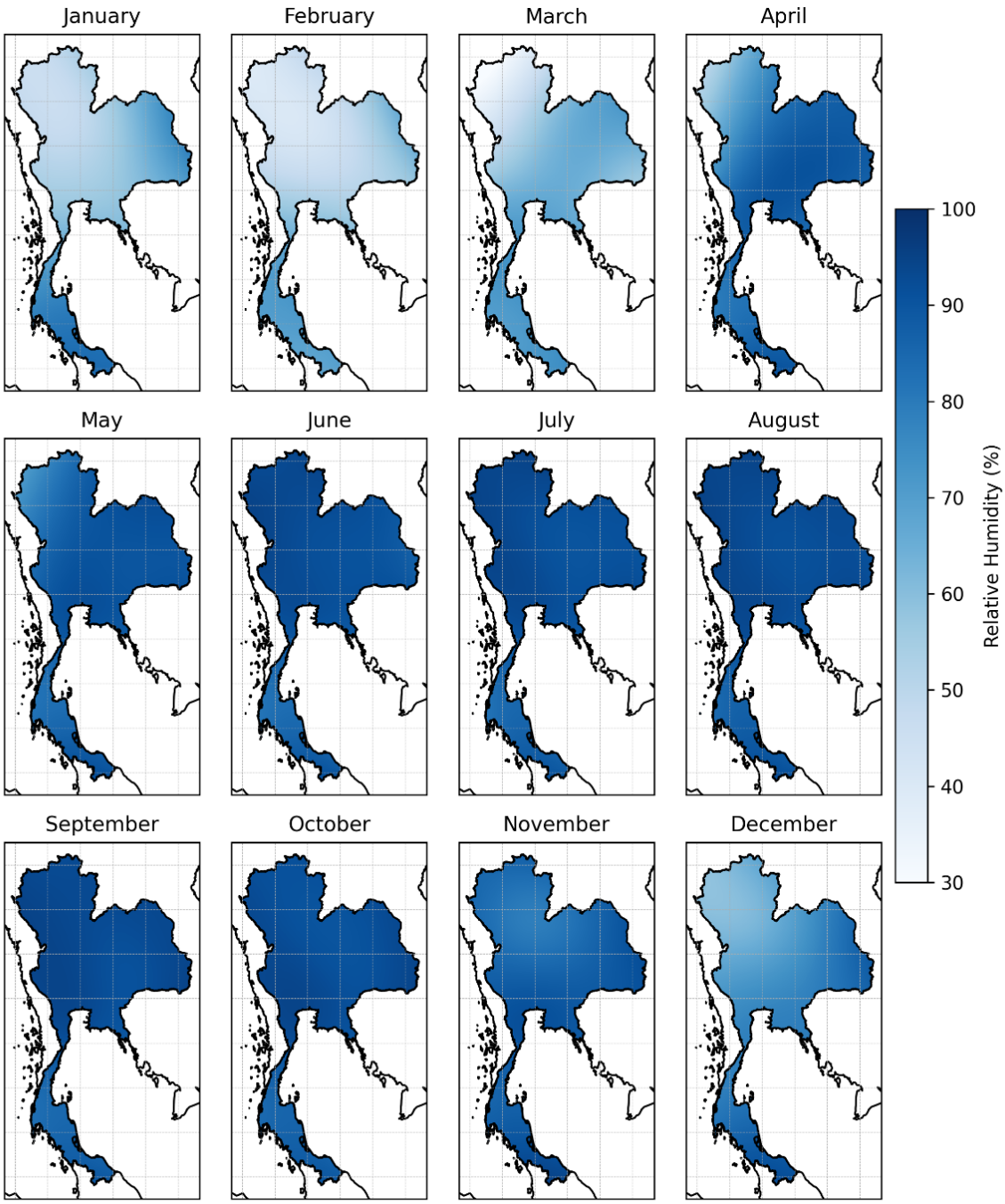


Figure 189 Monthly relative humidity maps from NCEP/NCAR for the year 2021.

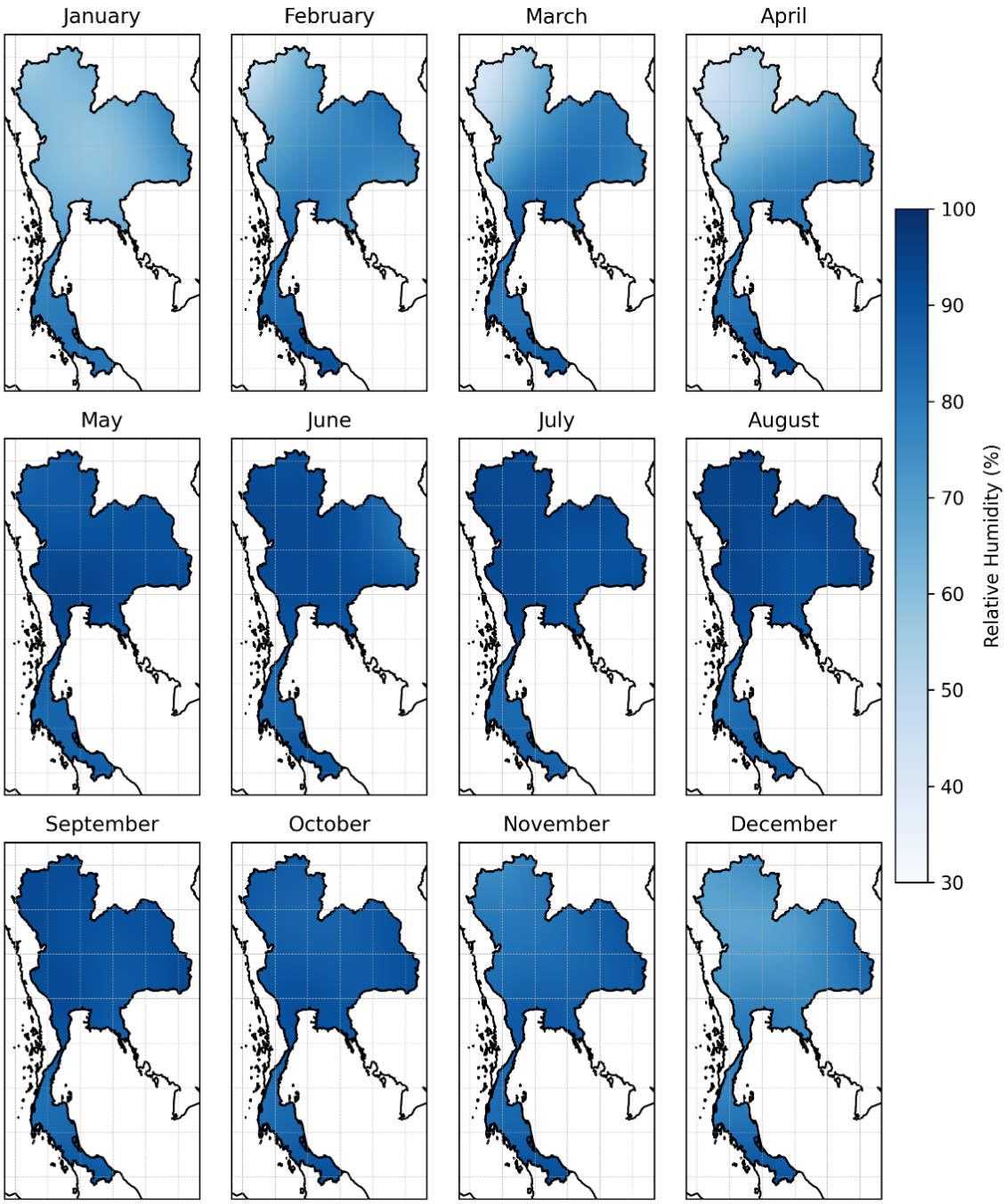


Figure 190 Monthly relative humidity maps from NCEP/NCAR for the year 2022.

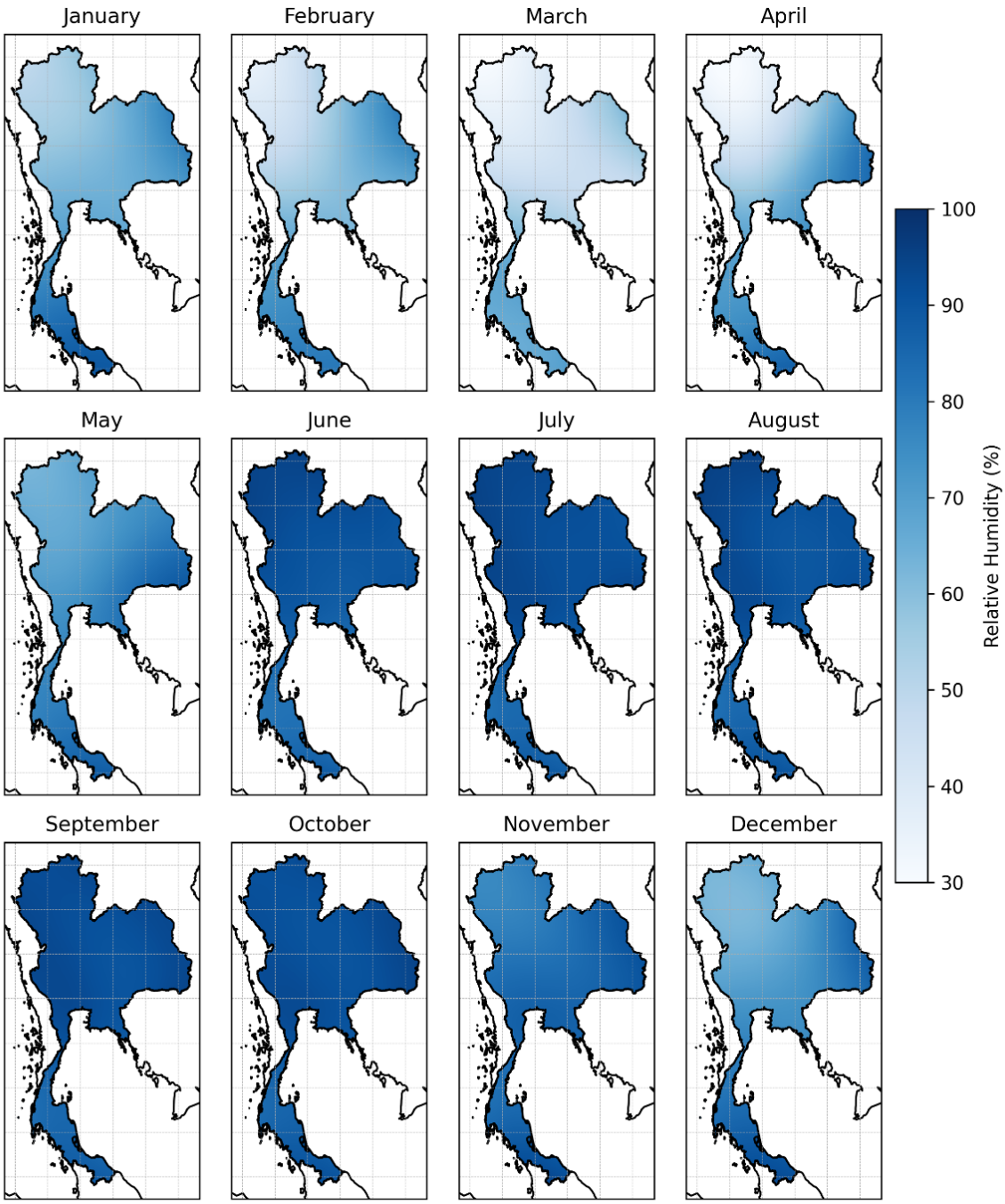


Figure 191 Monthly relative humidity maps from NCEP/NCAR for the year 2023.

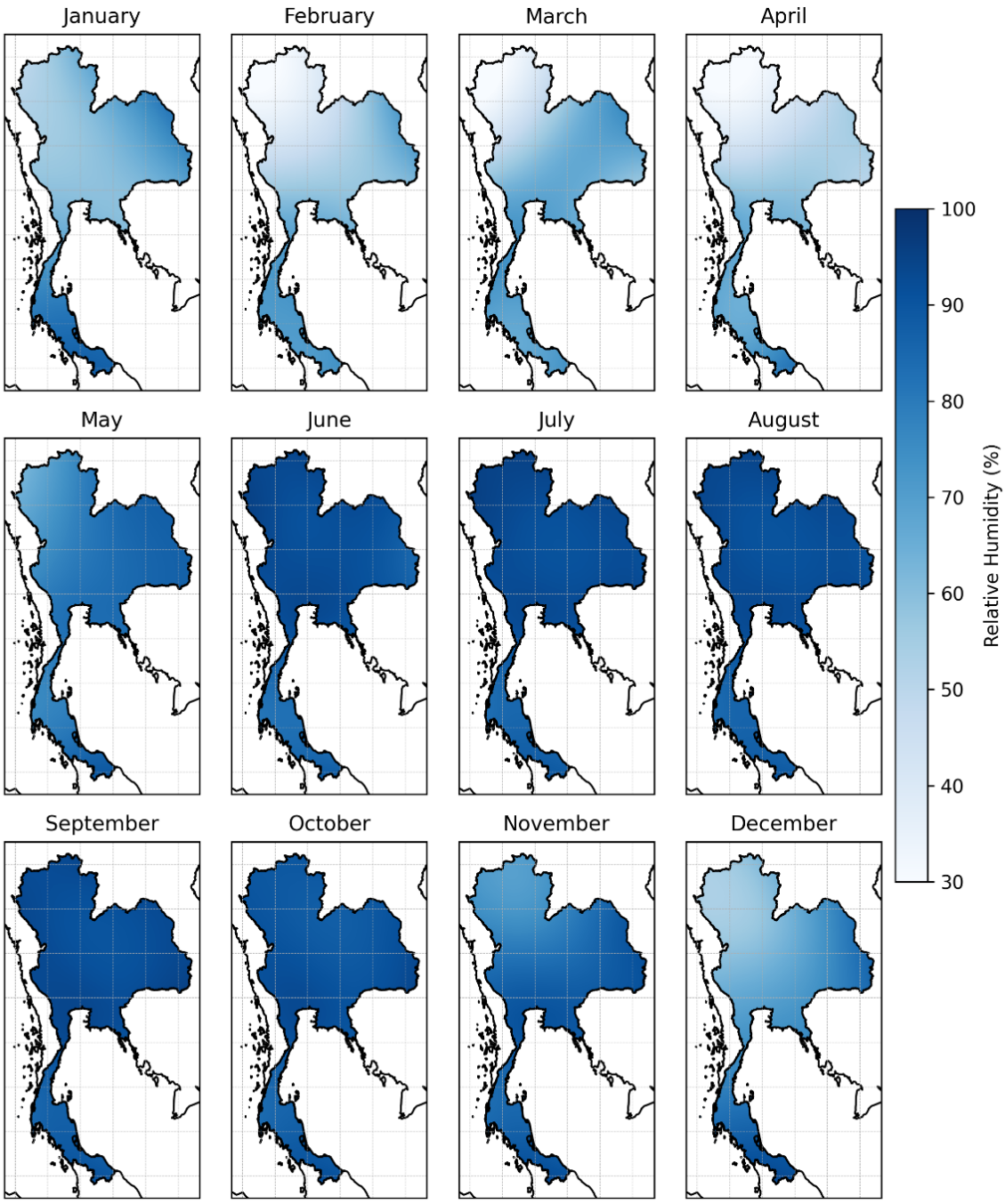


Figure 192 Monthly relative humidity maps from NCEP/NCAR for the year 2024.

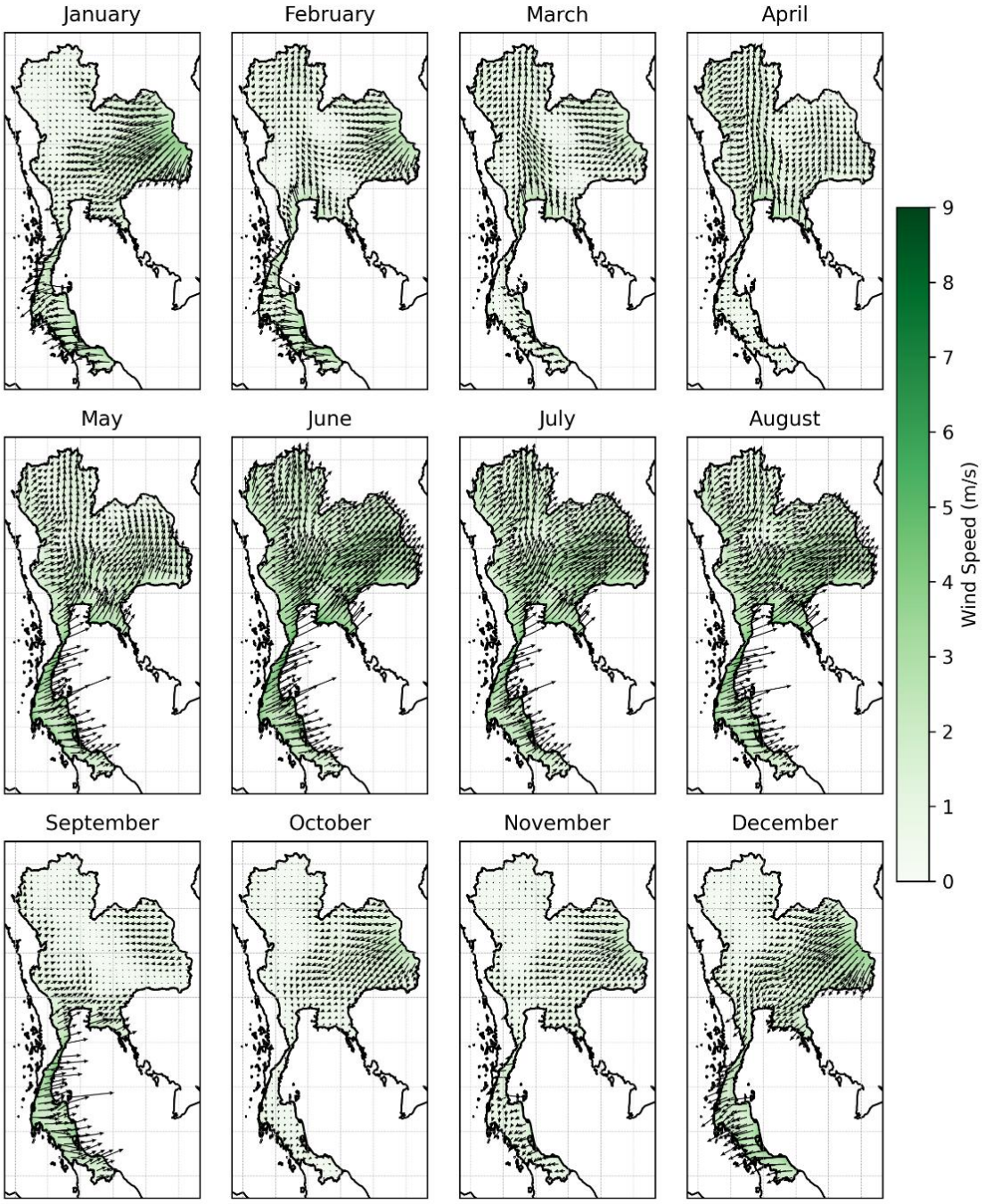


Figure 193 Monthly wind speed and wind direction maps from CCMP for the year 2012.

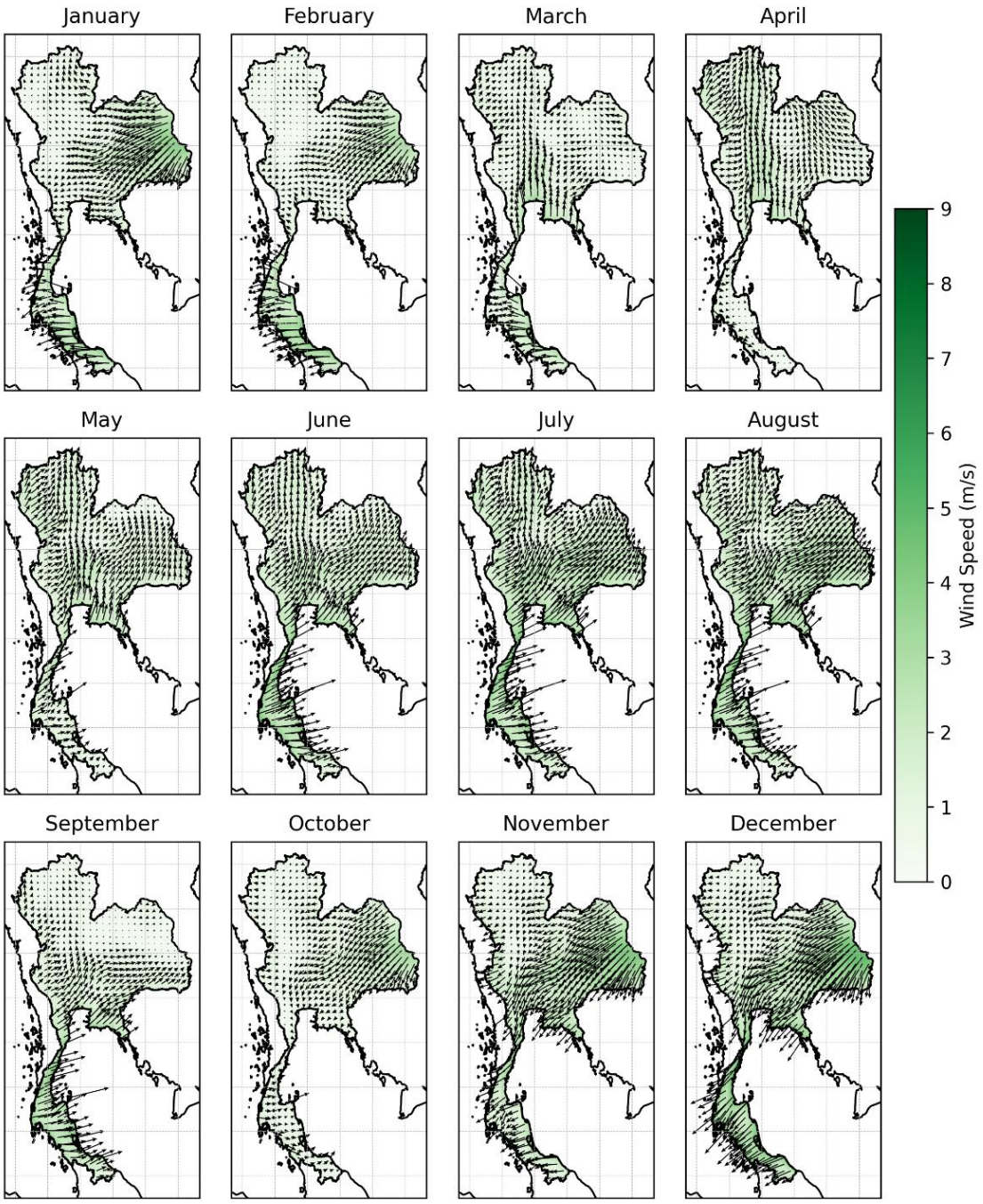


Figure 194 Monthly wind speed and wind direction maps from CCMP for the year 2013.

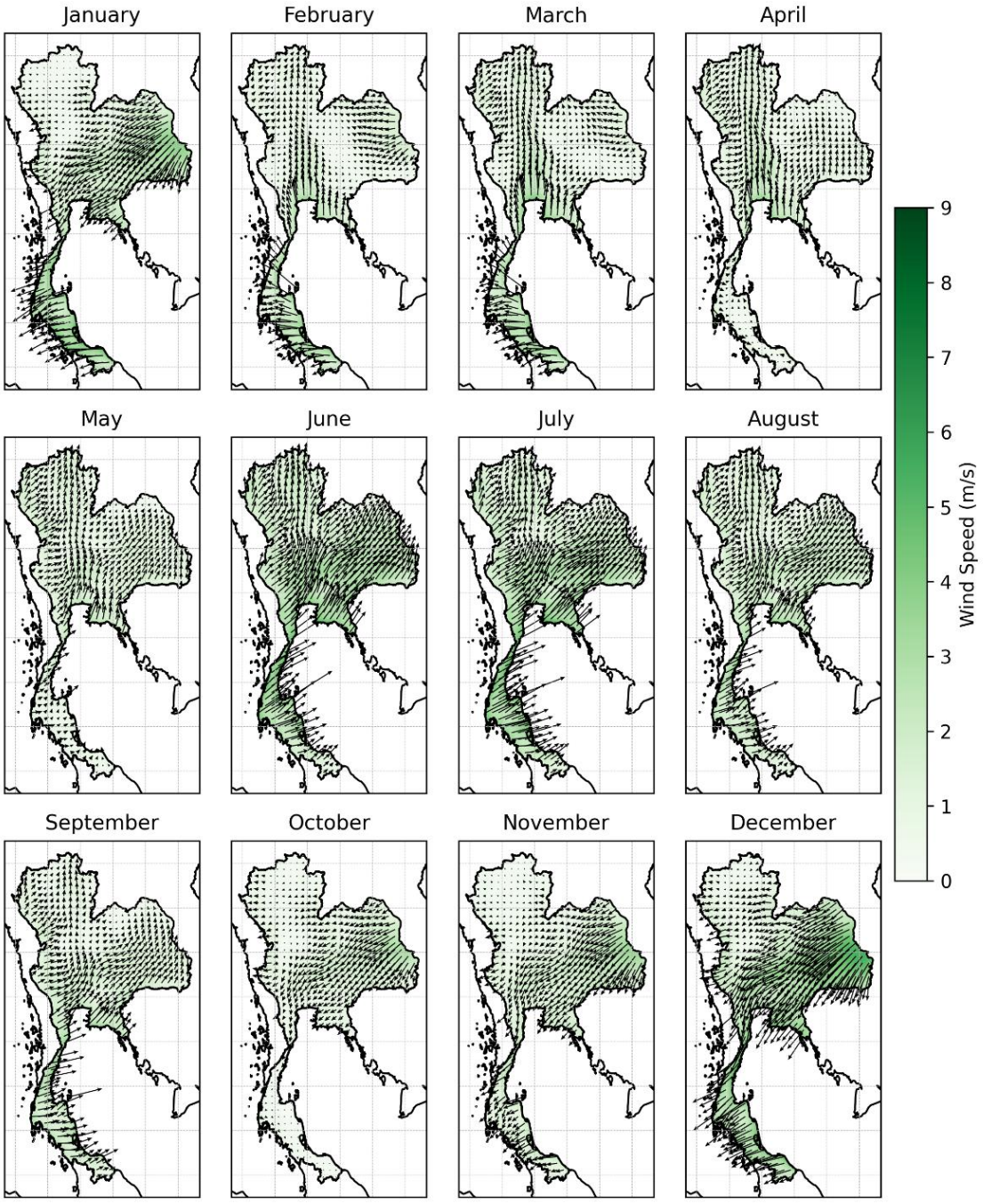


Figure 195 Monthly wind speed and wind direction maps from CCMP for the year 2014.

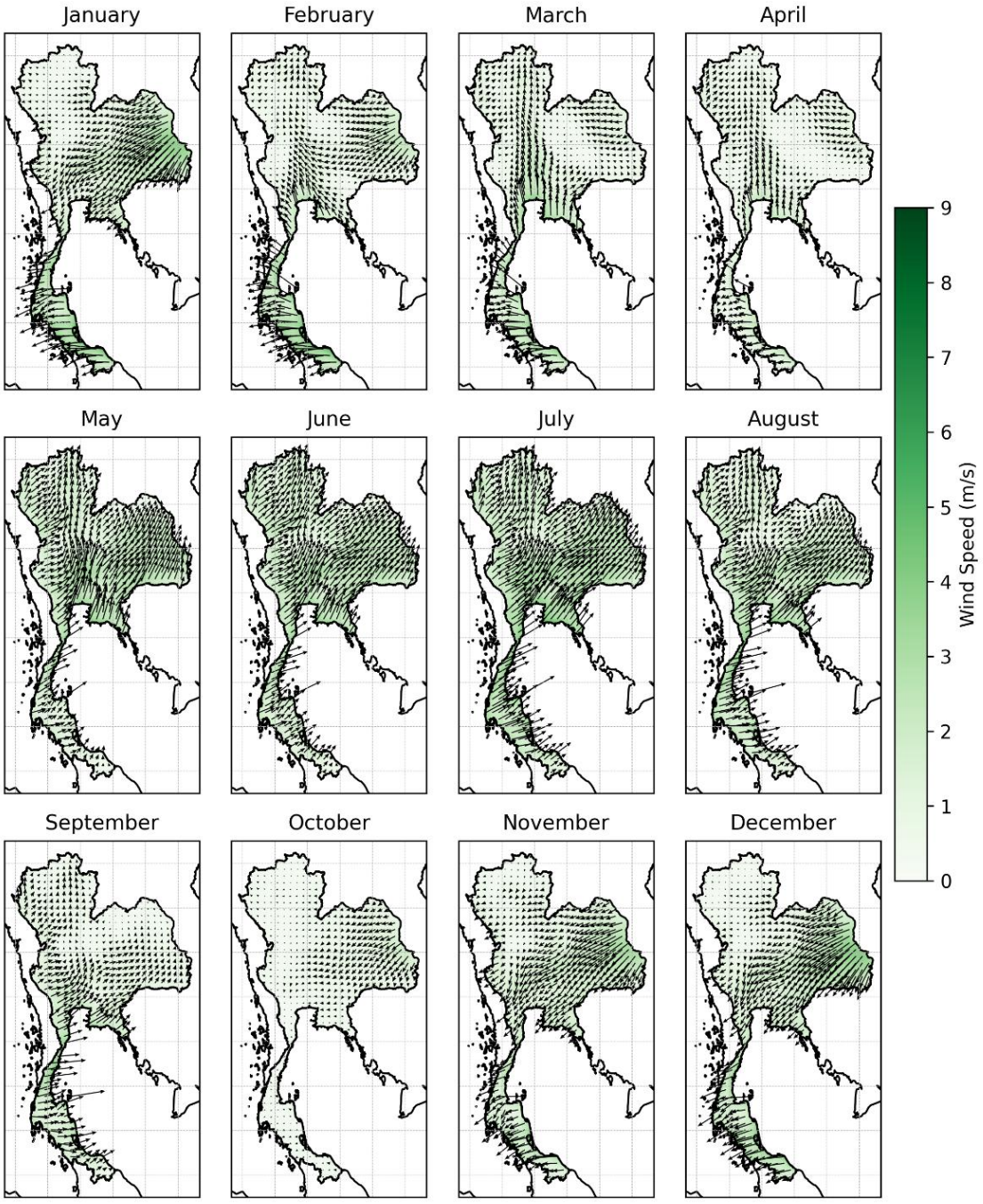


Figure 196 Monthly wind speed and wind direction maps from CCMP for the year 2015.

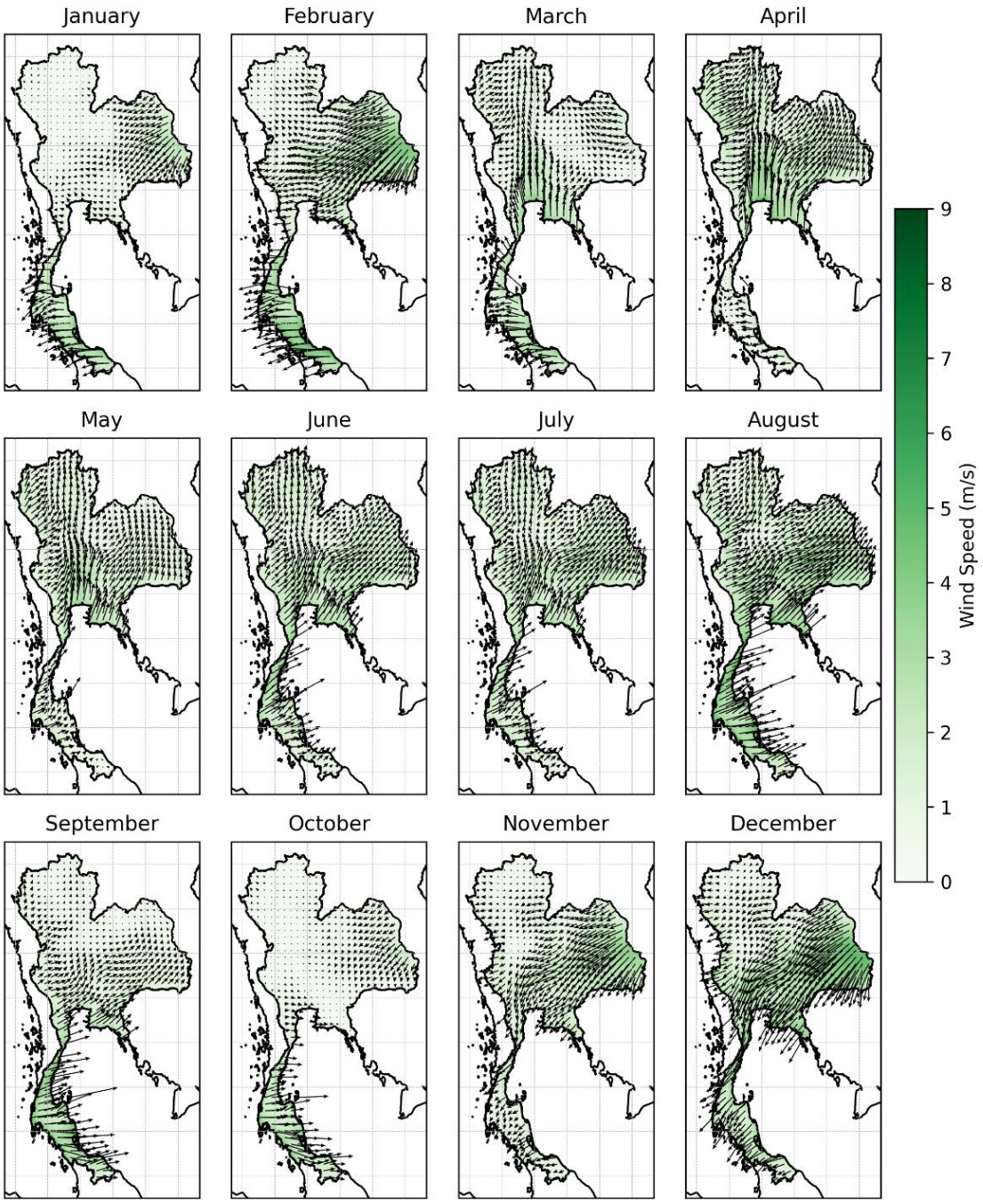


Figure 197 Monthly wind speed and wind direction maps from CCMP for the year 2016.

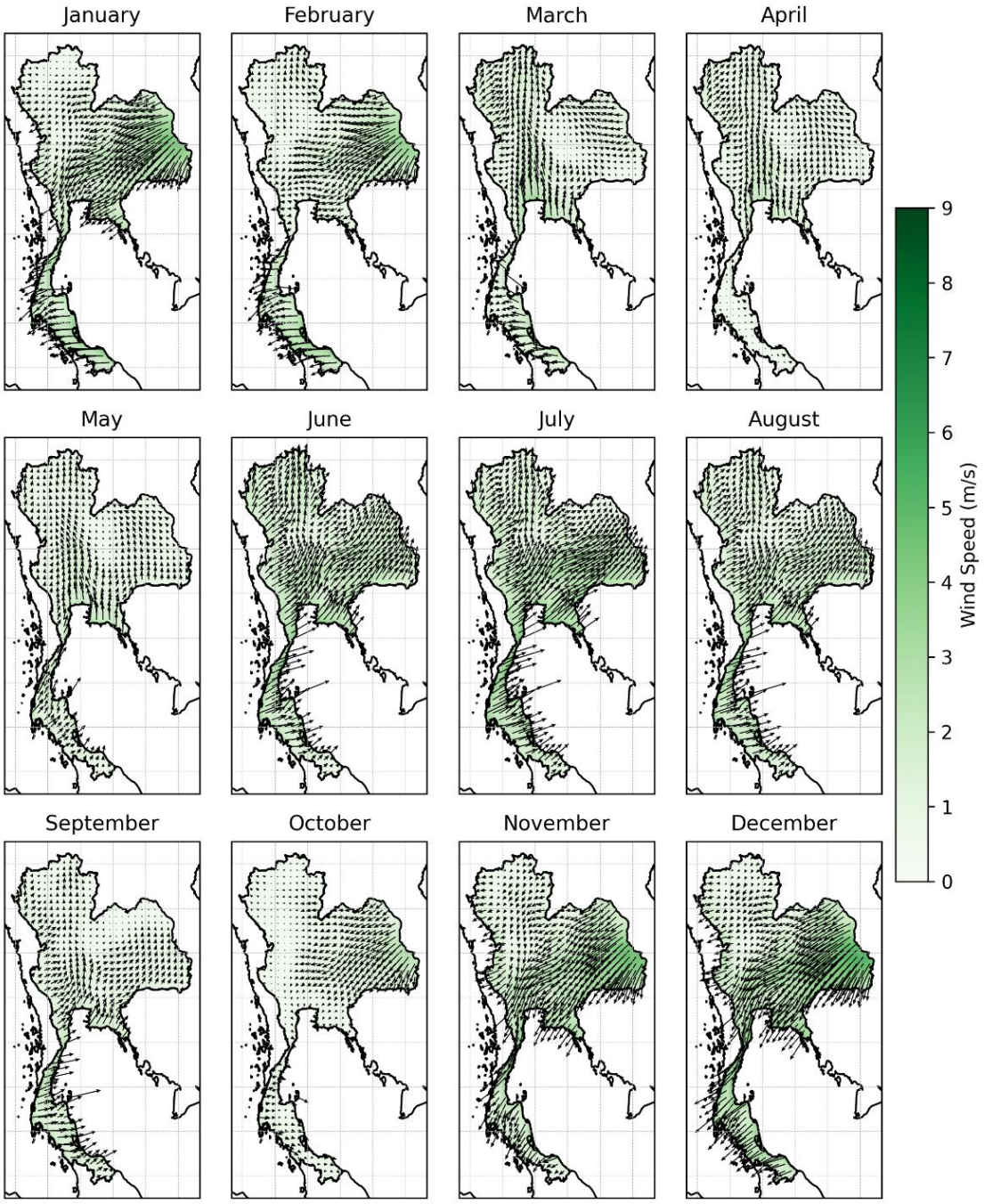


Figure 198 Monthly wind speed and wind direction maps from CCMP for the year 2017.

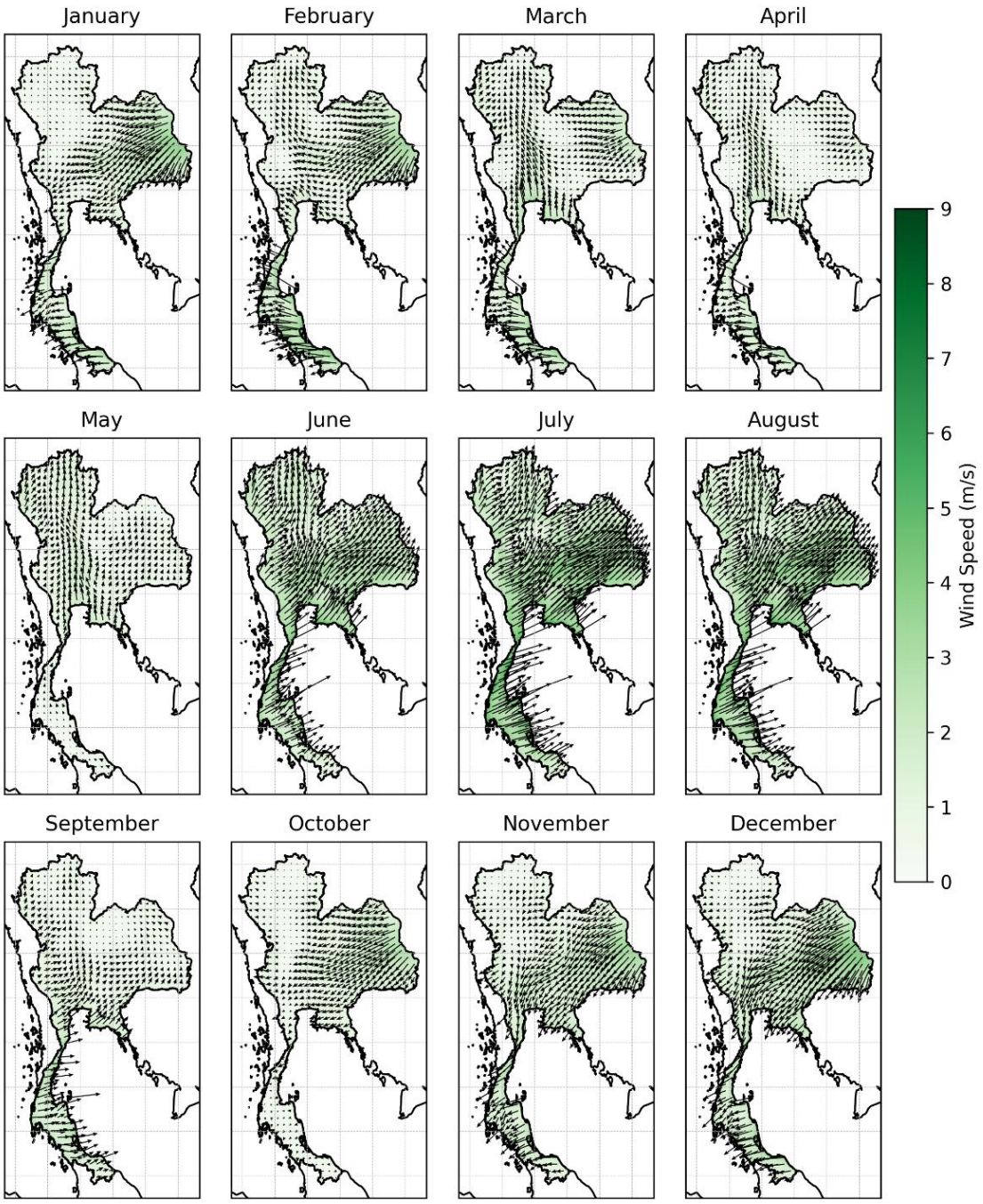


Figure 199 Monthly wind speed and wind direction maps from CCMP for the year 2018.

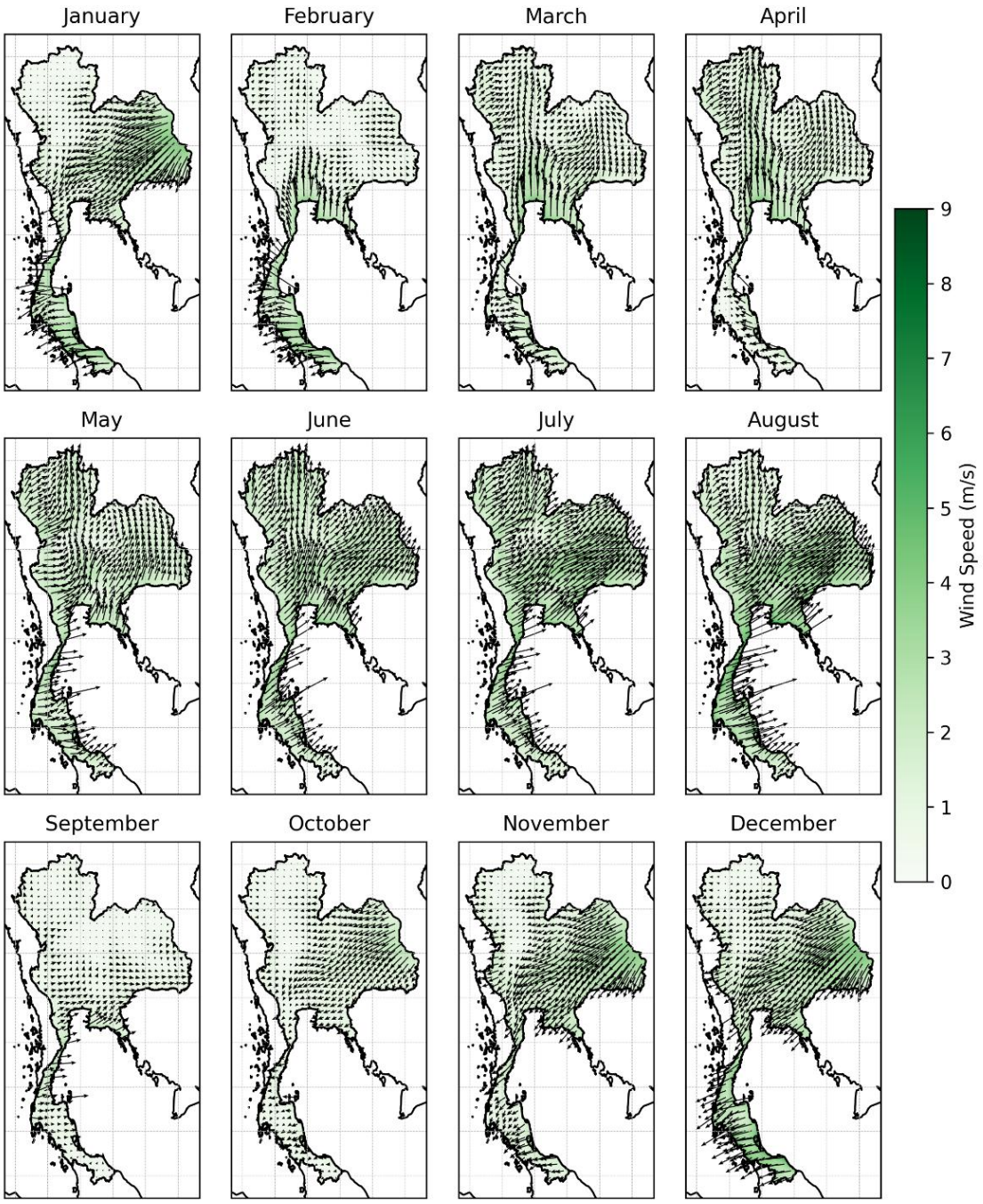


Figure 200 Monthly wind speed and wind direction maps from CCMP for the year 2019.

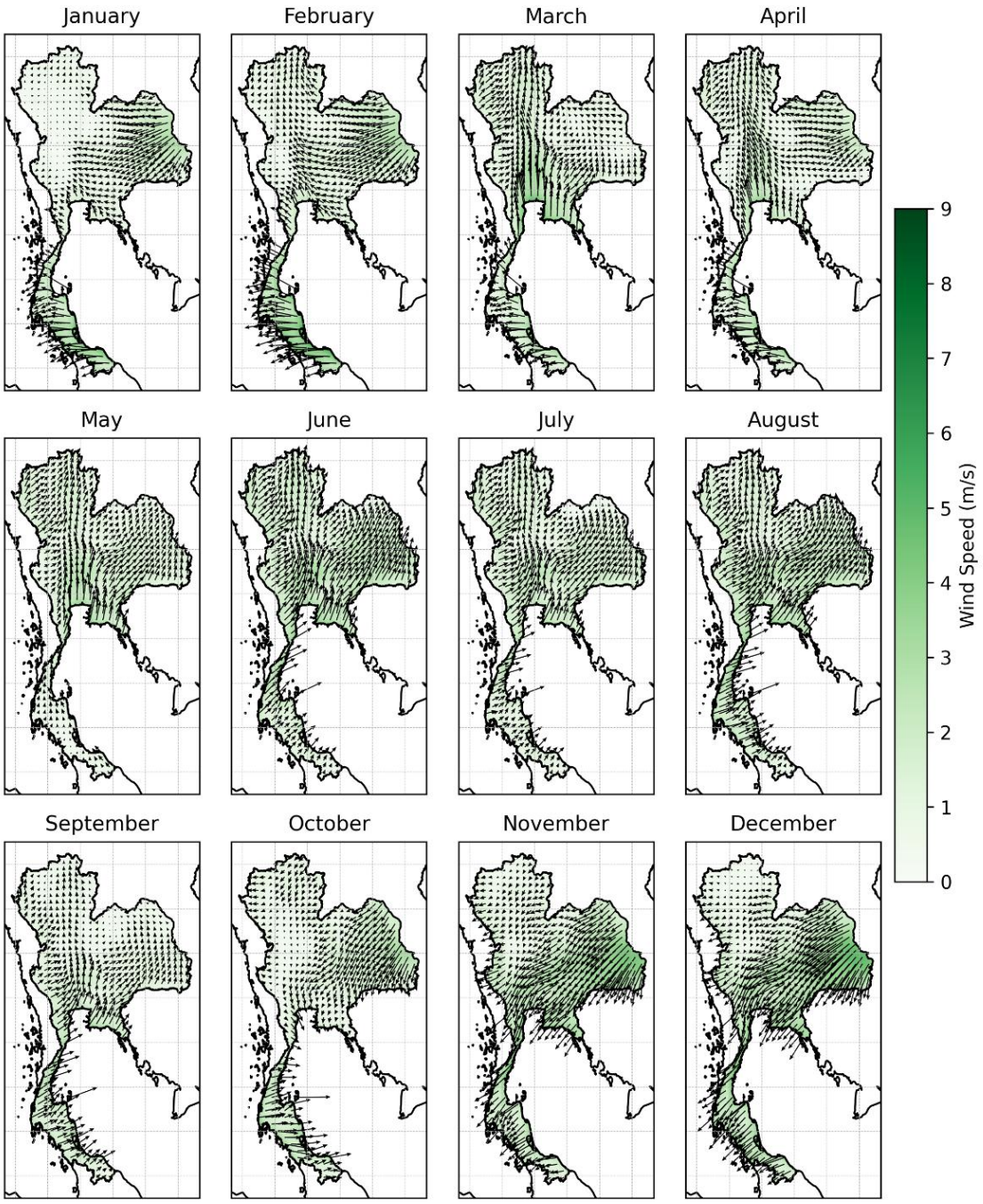


Figure 201 Monthly wind speed and wind direction maps from CCMP for the year 2020.

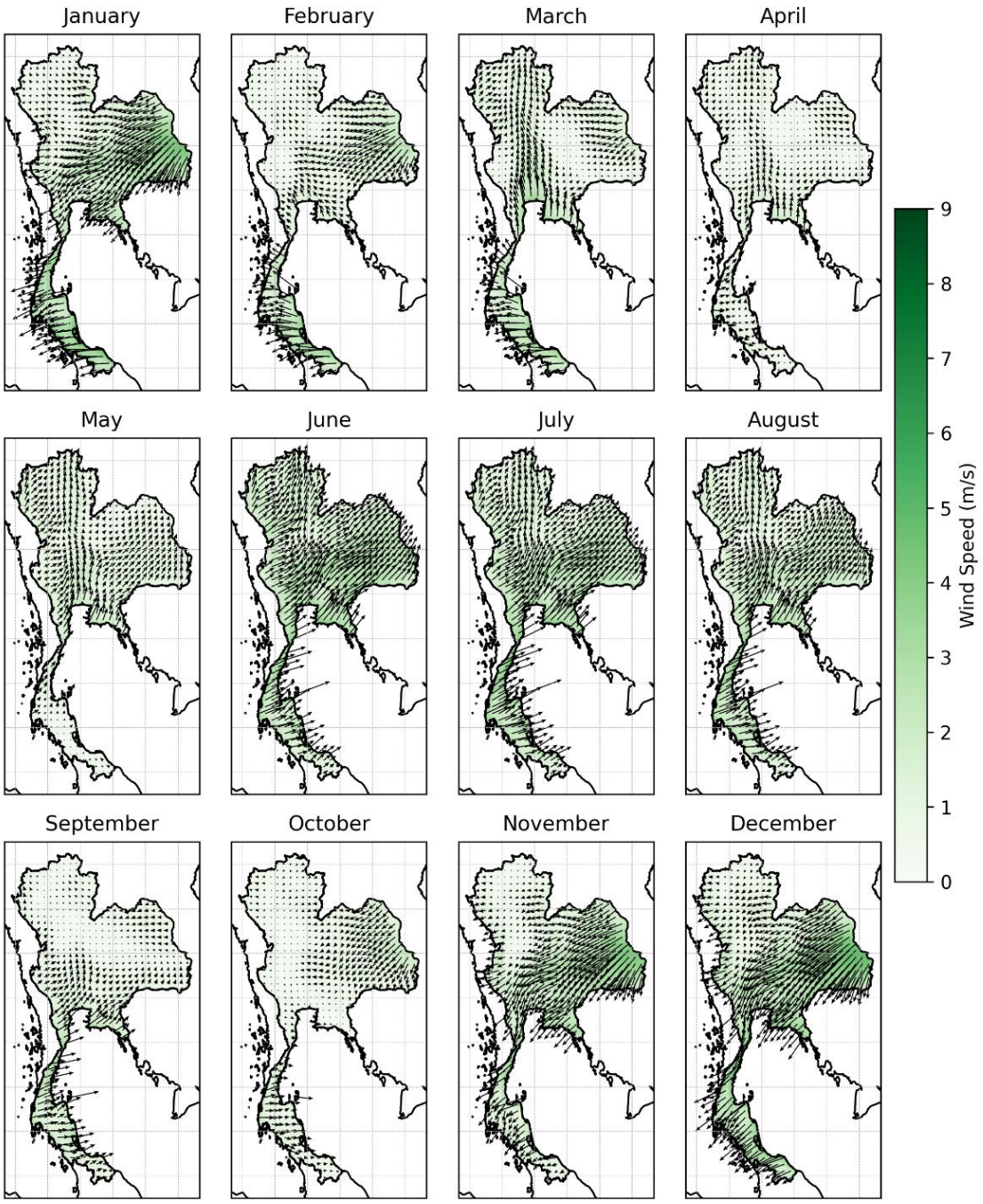


Figure 202 Monthly wind speed and wind direction maps from CCMP for the year 2021.

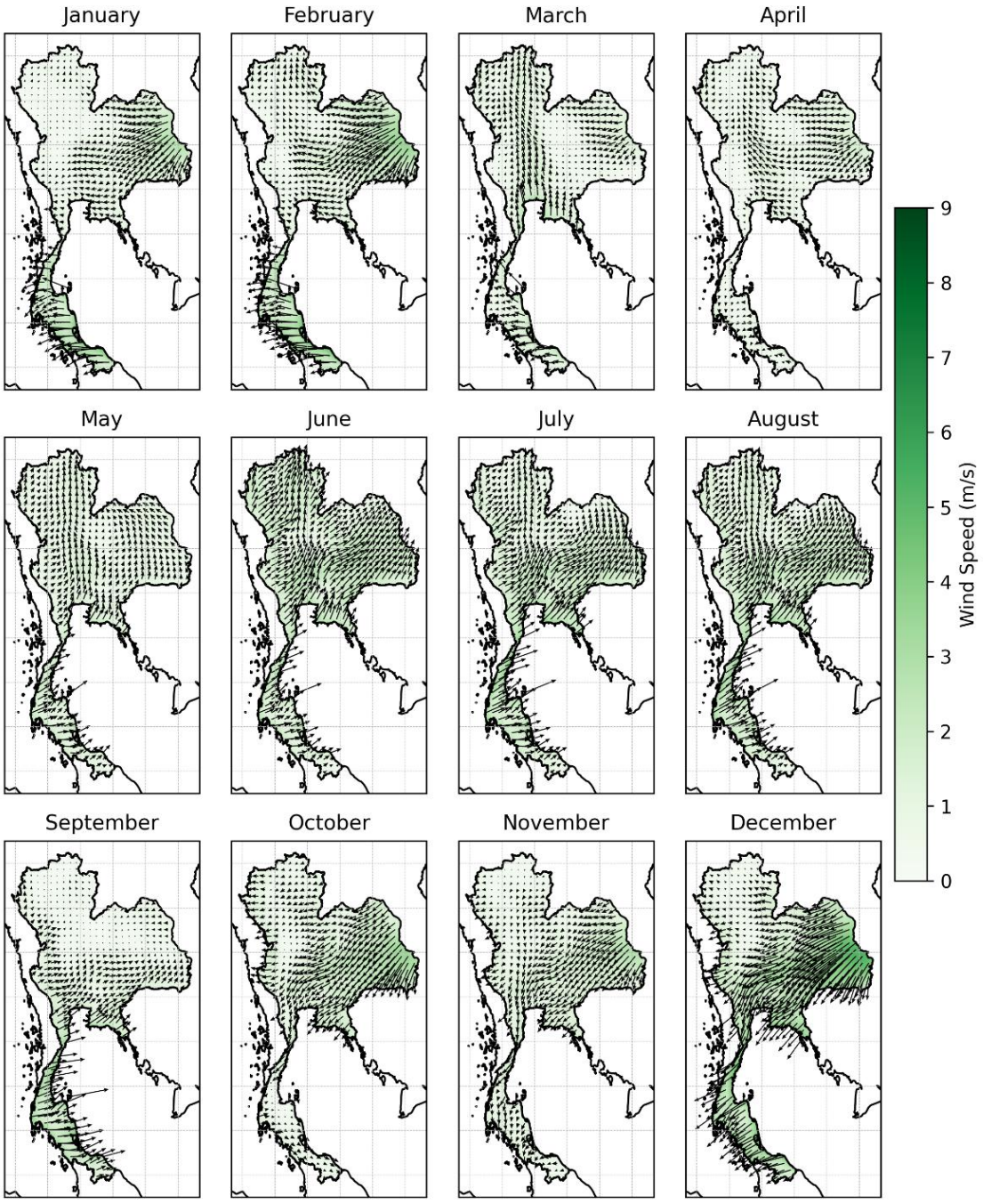


Figure 203 Monthly wind speed and wind direction maps from CCMP for the year 2022.

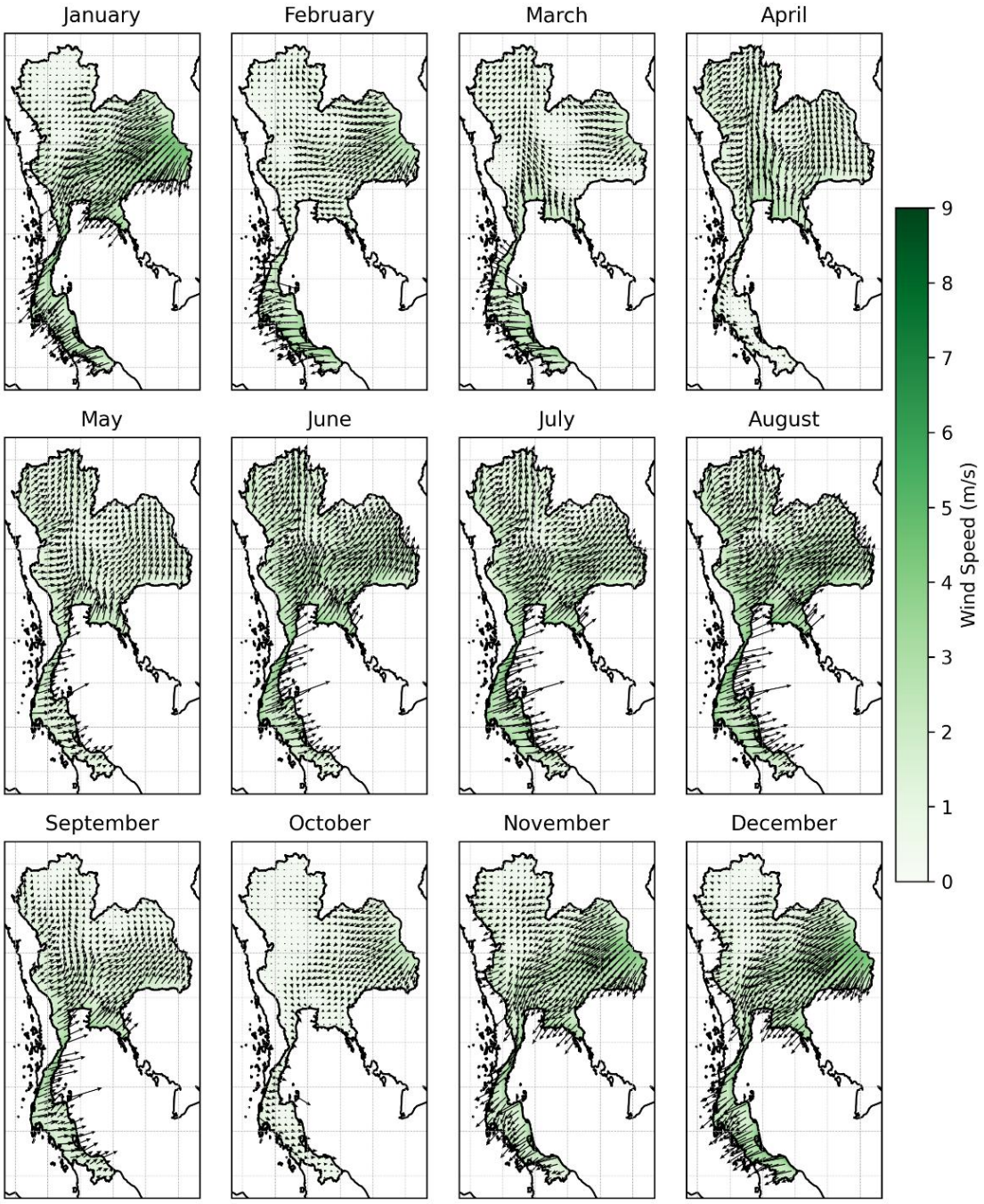


Figure 204 Monthly wind speed and wind direction maps from CCMP for the year 2023.

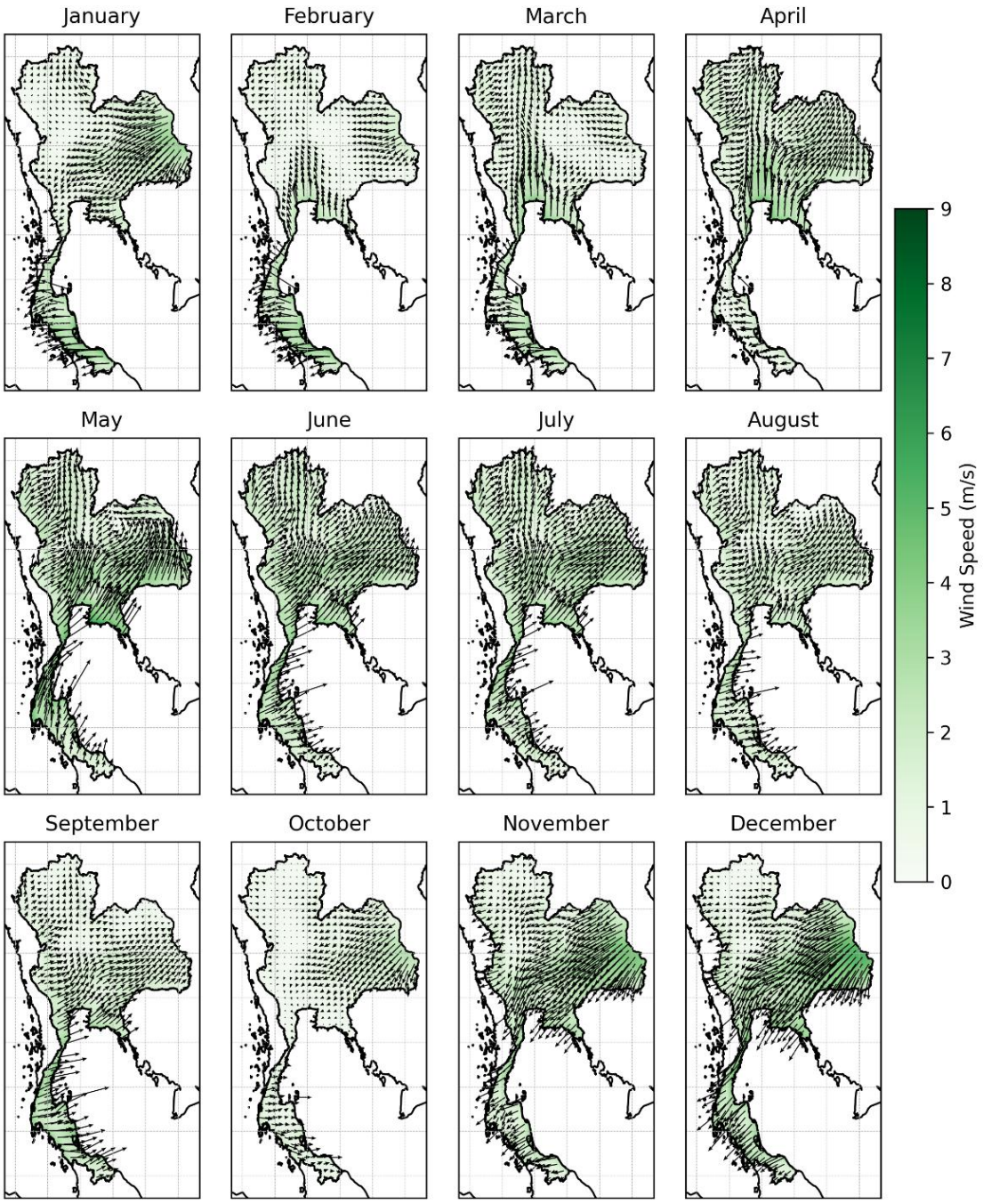


Figure 205 Monthly wind speed and wind direction maps from CCMP for the year 2024.

REFERENCES

Abal, G., Aicardi, D., Suárez, R. A., & Laguarda, A. (2017). Performance of empirical models for diffuse fraction in Uruguay. *Solar energy*, *141*, 166-181.

Ahwide, F., Spena, A., & El-Kafrawy, A. (2013). Correlation for the average daily diffuse fraction with clearness index and estimation of beam solar radiation and possible sunshine hours fraction in Sabha, Ghdames and Tripoli-Libya. *APCBEE procedia*, *5*, 208-220.

Ångström, A. (1929). On the atmospheric transmission of sun radiation and on dust in the air. *Geografiska Annaler*, *11*(2), 156-166.

Antuña-Marrero, J. C., Cachorro Revilla, V., García Parrado, F., de Frutos Baraja, Á., Rodríguez Vega, A., Mateos, D., Estevan Arredondo, R., & Toledano, C. (2018). Comparison of aerosol optical depth from satellite (MODIS), sun photometer and broadband pyrheliometer ground-based observations in Cuba. *Atmospheric Measurement Techniques*, *11*(4), 2279-2293.

Atlas, R., Hoffman, R., Ardizzone, J., Leidner, S., & Jusem, J. (2009). Development of a new cross-calibrated, multi-platform (CCMP) ocean surface wind product. AMS 13th Conference on Integrated Observing and Assimilation Systems for Atmosphere, Oceans, and Land Surface (IOAS-AOLS),

Ayegba, A., Jegede, J. O., & Odoma, A. N. (2017). A Study of the Global Solar Radiation of Makurdi, Benue State, Nigeria. *American International Journal of Research in Science, Technology Engineering and Mathematics*, *18*(1), 70-75.

Bailek, N., Bouchouicha, K., Al-Mostafa, Z., El-Shimy, M., Aoun, N., Slimani, A., & Al-Shehri, S. (2018). A new empirical model for forecasting the diffuse solar radiation over Sahara in the Algerian Big South. *Renewable Energy*, *117*, 530-537.

Bakirci, K. (2015). Models for the estimation of diffuse solar radiation for typical cities in Turkey. *Energy*, *82*, 827-838.

Bakirci, K. (2021). Prediction of diffuse radiation in solar energy applications: Turkey case study and compare with satellite data. *Energy*, *237*, 121527.

Bamiro, O. (1983). Empirical relations for the determination of solar radiation in Ibadan, Nigeria. *Solar energy*, *31*(1), 85-94.

Barbaro, S., Cannata, G., Coppolino, S., Leone, C., & Sinagra, E. (1981). Diffuse solar radiation statistics for Italy. *Solar energy*, *26*(5), 429-435.

Behr, H. D. (2022). Trends and interdependence of solar radiation and air temperature—a case study from Germany. *Meteorology*, *1*(4), 341-354.

Bempah, K. O., Kwon, K., & Kim, K. A. (2019). Experimental study of photovoltaic panel mounting configurations for tube-shaped structures. *Applied Energy*, *240*, 754-765.

Benard, R., Menguy, G., & Schwartz, M. (1980). *Le Rayonnement Solaire: Conversion Thermique et Application*. Technique et Documentation.

Bett, P. E., & Thornton, H. E. (2016). The climatological relationships between wind and solar energy supply in Britain. *Renewable Energy*, *87*, 96-110.

Bilbao, J., Román, R., Yousif, C., Mateos, D., & De Miguel, A. (2014). Total ozone column, water vapour and aerosol effects on erythemal and global solar irradiance in Marsaxlokk, Malta. *Atmospheric Environment*, *99*, 508-518.

Boucher, O. (2015). *Atmospheric aerosols*. Springer.

Boukelia, T. E., Mecibah, M.-S., & Meriche, I. E. (2014). General models for estimation of the monthly mean daily diffuse solar radiation (Case study: Algeria). *Energy Conversion and management*, *81*, 211-219.

Cooper, P. (1969). The absorption of radiation in solar stills. *Solar energy*, *12*(3), 333-346.

Coppolino, S. (1990). A new model for estimating diffuse solar radiation in Italy from clearness index and minimum air mass. *Solar & wind technology*, *7*(5), 549-553.

Dangeti, P. (2017). *Statistics for machine learning*. Packt Publishing Ltd.

Duffie, J. A., Beckman, W. A., & Blair, N. (2020). *Solar engineering of thermal processes, photovoltaics and wind*. John Wiley & Sons.

Earth Science Stack Exchange. (2021). *How does a whirling hygrometer work? How does it differ from static dry/wet-bulb thermometer?* Retrieved 18 June from https://earthscience.stackexchange.com/questions/21198/how-does-a-whirling-hygrometer-work-how-does-it-differ-from-static-dry-wet-bulb

El-Sebaii, A., & Trabea, A. (2003). Estimation of horizontal diffuse solar radiation in Egypt. *Energy Conversion and management*, *44*(15), 2471-2482.

Elhadidy, M., & Abdel-Nabi, D. (1991). Diffuse fraction of daily global radiation at Dhahran, Saudi Arabia. *Solar energy*, *46*(2), 89-95.

Elminir, H. K. (2007). Experimental and theoretical investigation of diffuse solar radiation: data and models quality tested for Egyptian sites. *Energy*, *32*(1), 73-82.

Erbs, D., Klein, S., & Duffie, J. (1982). Estimation of the diffuse radiation fraction for hourly, daily and monthly-average global radiation. *Solar energy*, *28*(4), 293-302.

Exell, R., & Santibuppakul, P. (1984). New estimates of mean daily diffuse solar radiation in Thailand. *Journal of the Science Society of Thailand*, *10*, 37-41.

Falkoni, A., & Krajačić, G. (2015). The Analysis of the Correlation between Wind Speed, Solar Radiation, Air Temperature and Electricity Demand of the Dubrovnik Region. 10th Conference on Sustainable Development of Energy, Water and Environment Systems–SDEWES,

Flowers, P., Theopold, K. H., Langley, R., & Robinson, W. R. (2019). *Chemistry 2e*. OpenStax Houston, TX.

Fontana, F., Lugrin, D., Seiz, G., Meier, M., & Foppa, N. (2013). Intercomparison of satellite-and ground-based cloud fraction over Switzerland (2000–2012). *Atmospheric Research*, *128*, 1-12.

Frederick, J. E. (2008). *Principles of atmospheric science*. Jones & Bartlett Learning.

Hargreaves, G. H., & Samani, Z. A. (1985). Reference crop evapotranspiration from temperature. *Applied engineering in agriculture*, *1*(2), 96-99.

Holben, B. N., & Eck, T. F. (1990). Precipitable water in the Sahel measured using sun photometry. *Agricultural and Forest Meteorology*, *52*(1-2), 95-107.

Hove, T., & Göttsche, J. (1999). Mapping global, diffuse and beam solar radiation over Zimbabwe. *Renewable Energy*, *18*(4), 535-556.

https://aeronet.gsfc.nasa.gov/. (2025). *AERONET website*. AERONET. Retrieved 18 June from (https://aeronet.gsfc.nasa.gov/, 2025)

Inn, E. C., & Tanaka, Y. (1953). Absorption coefficient of ozone in the ultraviolet and visible regions. *Journal of the optical society of America*, *43*(10), 870-873.

Iqbal, M. (2012). *An introduction to solar radiation*. Elsevier.

Irizarry, R. A. (2019). *Introduction to data science: Data analysis and prediction algorithms with R*. Chapman and Hall/CRC.

Janjai, S. (2012). Diffuse-global correlation models at four locations in Thailand. *Journal of Renewable Energy and Smart Grid Technology*, *7*(1), 11-22.

Kondrat′ev, K. I. A. k. (1999). *Climatic effects of aerosols and clouds*. Springer.

Lacis, A. A., & Hansen, J. (1974). A parameterization for the absorption of solar radiation in the earth's atmosphere. *Journal of Atmospheric Sciences*, *31*(1), 118-133.

Lealea, T., & Tchinda, R. (2013). Estimation of diffuse solar radiation in the north and far north of Cameroon. *European Scientific Journal*, *9*(18), 370-381.

Leckner, B. (1978). The spectral distribution of solar radiation at the earth's surface—elements of a model. *Solar energy*, *20*(2), 143-150.

Li, H., Ma, W., Wang, X., & Lian, Y. (2011). Estimating monthly average daily diffuse solar radiation with multiple predictors: a case study. *Renewable Energy*, *36*(7), 1944-1948.

Liang, S., & Wang, D. (2017). Moderate resolution imaging spectroradiometer (MODIS) downward shortwave radiation (MCD18A1) and photosynthetically active radiation (MCD18A2) algorithm theoretical basis document. In *Google Scholar There is no Corresponding Record for This Reference*.

Liu, B. Y., & Jordan, R. C. (1960). The interrelationship and characteristic distribution of direct, diffuse and total solar radiation. *Solar energy*, *4*(3), 1-19.

Matsumi, Y., & Kawasaki, M. (2003). Photolysis of atmospheric ozone in the ultraviolet region. *Chemical Reviews*, *103*(12), 4767-4782.

Meeus, J. (1991). Astronomical Algorithms, Willmann-Bell, Incorporated. In.

Moore, D. S., McCabe, G. P., & Craig, B. A. (2009). *Introduction to the Practice of Statistics* (Vol. 4). WH Freeman New York.

Moruno, R., San José, L., Martín, F., Núñez, R., Herrero, R., & Antón, I. (2024). Understanding the impact of sky diffuse irradiance on curved photovoltaic modules. *Solar Energy Materials and Solar Cells*, *275*, 113029.

Mubiru, J., & Banda, E. (2007). Performance of empirical correlations for predicting monthly mean daily diffuse solar radiation values at Kampala, Uganda. *Theoretical and applied climatology*, *88*(1), 127-131.

Munro Instruments. (2024). *IM147 In-line Cup Anemometer & Wind Direction Vane*. Munro Instruments Ltd. Retrieved 18 June from https://www.munroinstruments.com/product/im147-in-line-cup-anemometer-wind-direction-vane/

Oliveira, A. P., Escobedo, J. F., Machado, A. J., & Soares, J. (2002). Correlation models of diffuse solar-radiation applied to the city of Sao Paulo, Brazil. *Applied Energy*, *71*(1), 59-73.

Orgill, J., & Hollands, K. (1977). Correlation equation for hourly diffuse radiation on a horizontal surface. *Solar energy*, *19*(4), 357-359.

Pattarapanitchai, S., & Janjai, S. (2012). A semi-empirical model for estimating diffuse solar irradiance under a clear sky condition for a tropical environment. *Procedia Engineering*, *32*, 421-426.

Petty, G. W. (2006). *A first course in atmospheric radiation*. Sundog publishing.

Prasad, A. K., & Singh, R. P. (2009). Validation of MODIS Terra, AIRS, NCEP/DOE AMIP-II Reanalysis-2, and AERONET Sun photometer derived integrated

precipitable water vapor using ground-based GPS receivers over India. *Journal of Geophysical Research: Atmospheres*, *114*(D5).

Rathakrishnan, E. (2019). Applied gas dynamics.

Raziei, T., & Parehkar, A. (2021). Performance evaluation of NCEP/NCAR reanalysis blended with observation-based datasets for estimating reference evapotranspiration across Iran. *Theoretical and applied climatology*, *144*, 885-903.

Said, A. A., HassabElnaby, H. R., & Wier, B. (2003). An empirical investigation of the performance consequences of nonfinancial measures. *Journal of management accounting research*, *15*(1), 193-223.

Salloom, A. H., Abdulrazzaq, O. A., & Ismail, B. H. (2018). Assessment of the performance of bifacial solar panels. *International Journal of Engineering and Technical Research*, *8*(7), 264790.

Schaap, M., Timmermans, R., Koelemeijer, R., De Leeuw, G., & Builtjes, P. (2008). Evaluation of MODIS aerosol optical thickness over Europe using sun photometer observations. *Atmospheric Environment*, *42*(9), 2187-2197.

Sharma, S., Kumar, P., Vaishnav, R., Shukla, K., & Phanikumar, D. (2018). Analysis of total column ozone, water vapour and aerosol optical thickness over Ahmedabad, India. *Meteorological Applications*, *25*(1), 33-39.

Smart, W. M., & Green, R. M. (1977). *Textbook on spherical astronomy*. Cambridge University Press.

Spencer, J. W. (1971). Fourier series representation of the position of the sun. *Search*, *2*, 165-172.

Trabea, A. (1999). Technical note a multiple linear correlation for diffuse radiation from global solar radiation and sunshine data over Egypt. *Renewable Energy*, *17*(3), 411-420.

Ulgen, K., & Hepbasli, A. (2002). Comparison of solar radiation correlations for Izmir, Turkey. *International Journal of Energy Research*, *26*(5), 413-430.

Ulgen, K., & Hepbasli, A. (2009). Diffuse solar radiation estimation models for Turkey's big cities. *Energy Conversion and management*, *50*(1), 149-156.

van Dijk, A., Kohsiek, W., & de Bruin, H. A. (2003). Oxygen sensitivity of krypton and Lyman-α hygrometers. *Journal of Atmospheric and Oceanic Technology*, *20*(1), 143-151.

Wang, D., Liang, S., Zhang, Y., Gao, X., Brown, M. G., & Jia, A. (2020). A new set of MODIS land products (MCD18): Downward shortwave radiation and photosynthetically active radiation. *Remote Sensing*, *12*(1), 168.

Werkmeister, A., Lockhoff, M., Schrempf, M., Tohsing, K., Liley, B., & Seckmeyer, G. (2015). Comparing satellite-to ground-based automated and manual cloud coverage observations–a case study. *Atmospheric Measurement Techniques*, *8*(5), 2001-2015.

Witte, R. S., & Witte, J. S. (2017). *Statistics*. John Wiley & Sons.

WMO. (2003). World Meteorological Organization. *WMO Reactive Gases Bulletin. Highlights from the Global Atmosphere Watch Programme. https://library. wmo. int/opac/doc_num. php*.

Wu, X., Yuan, J., Wei, T., Zhang, Y., Wu, K., & Xia, H. (2022). Variation of aerosol optical depth measured by Sun photometer at a Rural site near Beijing during the 2017–2019 Period. *Remote Sensing*, *14*(12), 2908.

Yin, K., Zhang, X., Xie, J., Hao, Z., Xiao, G., & Liu, J. (2023). Modeling hourly solar diffuse fraction on a horizontal surface based on sky conditions clustering. *Energy*, *272*, 127008.

Zhou, Y., Liu, Y., Chen, Y., & Wang, D. (2019). General models for estimating daily diffuse solar radiation in China: Diffuse fraction and diffuse coefficient models. *Energy Procedia*, *158*, 351-356.

Zhu, T., Li, J., He, L., Wu, D., Tong, X., Mu, Q., & Yu, Q. (2021). The improvement and comparison of diffuse radiation models in different climatic zones of China. *Atmospheric Research*, *254*, 105505.

มหาวิทยาลัยศิลปากร

VITA

NAME	Danuch Phaisathit
INSTITUTIONS ATTENDED	Phra Pathom Wittayalai School — High School Diploma Silpakorn University — B.Sc. in Physics Silpakorn University — M.Sc. in Physics Silpakorn University — Ph.D. in Physics (Ongoing)
PUBLICATION	Tohsing, K., Phaisathit, D., Pattarapanitchai, S., Masiri, I., Buntoung, S., Aumporn, O., & Wattan, R. (2019, November). A development of a low-cost pyranometer for measuring broadband solar radiation. In Journal of Physics: Conference Series (Vol. 1380, No. 1, p. 012045). IOP Publishing. PHAISATHIT, D., & Tohsing, K. (2022). A study of diffuse solar radiation in Thailand (Doctoral dissertation, Silpakorn University). Phaisathit, D., Tohsing, K., & Janjai, S. (2023). Estimation of Diffuse Fraction from Clearness Index and Atmospheric Parameters in Thailand. CURRENT APPLIED SCIENCE AND TECHNOLOGY, e0262956-e0262956. Tohsing, K., Phaisathit, D., & Janjai, S. (2025). Appling a semi-empirical model for estimating hourly diffuse solar radiation at the main regions of Thailand. In Journal of Physics: Conference Series (Vol. 2934, No. 1, p. 012032). IOP Publishing.
AWARD RECEIVED	DPST Scholarship (Development and Promotion of Science and Technology Talents Project) Second Class Honors, B.Sc. in Physics, Silpakorn University